

# Large-Eddy Simulation of Turbulent Flow and Dispersion within Modeled Urban Environments

A Thesis Submitted to the Faculty of Graduate Studies of  
the University of Manitoba  
in Partial Fulfilment of the Requirements for the Degree of

Doctor of Philosophy

Department of Mechanical Engineering  
University of Manitoba  
Winnipeg, Manitoba

by

Mohammad Saeedi

# Abstract

In this thesis, wall-resolved and wall-modeled large-eddy simulation (LES) have been employed to investigate turbulent flow and dispersion around a single and a group of wall-mounted bluff bodies which are partially and fully submerged in developing boundary layers, respectively. The dispersion is caused by a continuous release of a passive scalar from a ground-level point source located within the matrix of obstacles. The results have been validated through comparisons against the available experimental measurement data. Thorough physical analysis including investigation of the spatial evolution and temporal cascades of the kinetic and scalar energies, flow structures and their influences on dispersion of the concentration plume in the context of highly disturbed flows, and study of turbulence statistics for the flow and concentration fields have been performed to provide deeper insights into turbulent flow and dispersion in domains with complex geometries.

An in-house code based on FORTRAN programming language, parallelized with MPI libraries has been developed, modified and optimized for conducting the simulations. The simulations have been conducted on public-domain supercomputers of West-Grid, specifically Orcinus and Grex, and also the local 256-core cluster system of the CFD LAB at the University of Manitoba.

# Acknowledgements

I would like to use this opportunity and deeply thank all the supports, patients and wonderful teaching of my advisor Professor Bing-Chen Wang. All the opportunities he generously provided for me are greatly acknowledged.

I have so much benefited through discussions and questions from Professor M. F. Tachie and Professor S. J. Ormiston who patiently answered my questions. All the guidance and help from Dr. P. P. LePoudre, Dr. E. Yee and Dr. Z. Yang are also greatly appreciated.

I also thank all my friends and fellows in the research group of Professor Wang who created a nice and friendly environment.

Last, but definitely not least, my love and appreciation go to my parents, my wife, and my son Amirali.

# Table of Contents

Abstract	i
Acknowledgements	ii
Table of Contents	iii
List of Figures	viii
Nomenclature	xvi
<b>1 Introduction</b>	<b>1</b>
1.1 Background and Motivation . . . . .	1
1.1.1 Previous Experimental Studies . . . . .	1
1.1.1.1 Single obstacle flow . . . . .	1
1.1.1.2 Flow and dispersion for a group of obstacles . . . . .	4
1.1.2 Previous numerical studies . . . . .	5
1.1.2.1 RANS and DNS of bluff body flows . . . . .	5
1.1.2.2 LES of bluff body flows . . . . .	8
1.2 Objectives of the Thesis . . . . .	12
1.3 Outline of the Thesis . . . . .	13
<b>2 Mathematical framework</b>	<b>15</b>

2.1	Governing equations . . . . .	15
2.2	Large-eddy simulation (LES) . . . . .	16
2.2.1	Governing equations for LES . . . . .	19
2.2.2	SGS stress models . . . . .	19
2.2.3	SGS scalar flux models . . . . .	21
2.3	Statistical analysis and time-averaging . . . . .	23
2.3.1	Transition from initial condition . . . . .	23
<b>3</b>	<b>Numerical algorithms</b>	<b>26</b>
3.1	Spatial discretization scheme . . . . .	26
3.1.1	Mass and momentum equations . . . . .	26
3.1.2	Scalar transport equation . . . . .	29
3.2	Time advancement . . . . .	30
3.3	Boundary conditions . . . . .	31
3.3.1	Solid wall . . . . .	32
3.3.1.1	Wall modeling . . . . .	33
3.3.2	Inflow . . . . .	39
3.3.2.1	Synthetic turbulence . . . . .	39
3.3.2.2	Deterministic computation . . . . .	41
3.3.3	Outflow . . . . .	43
3.3.4	Periodic boundary condition . . . . .	43
3.3.5	Slip boundary condition . . . . .	44
3.3.6	Boundary conditions for the scalar transport equation . . . . .	44
3.4	Parallel computing . . . . .	45
3.4.1	Supercomputers . . . . .	45

3.4.2	Message passing interface . . . . .	46
3.4.3	Parallel efficiency . . . . .	48
3.5	Preliminary tests based on plane channel flow . . . . .	50
<b>4</b>	<b>Wall-resolved LES of turbulent wake behind a surface-mounted square cylinder</b>	<b>53</b>
4.1	Test case and computational domain . . . . .	54
4.2	Results and discussions . . . . .	58
4.2.1	Flow structures . . . . .	58
4.2.2	Turbulence statistics . . . . .	71
4.2.3	SGS effects . . . . .	83
4.3	Closure . . . . .	89
<b>5</b>	<b>Wall-modeled LES of turbulent flow over a matrix of wall-mounted cubes submerged in a simulated atmospheric boundary layer</b>	<b>94</b>
5.1	Test case and computational domain . . . . .	96
5.1.1	Boundary conditions . . . . .	98
5.2	Results and discussions . . . . .	102
5.2.1	General description of the flow field . . . . .	102
5.2.2	Statistics of the velocity field . . . . .	110
5.2.3	Budget of the resolved kinetic energy . . . . .	116
5.3	Closure . . . . .	125
<b>6</b>	<b>LES of turbulent dispersion from a localized source within an urban canopy model</b>	<b>129</b>
6.1	Test case and computational domain . . . . .	129
6.2	Results and discussions . . . . .	131

6.2.1	General description of the concentration field . . . . .	131
6.2.2	Concentration statistics . . . . .	133
6.2.3	Spectra and scalar energy . . . . .	137
6.3	Closure . . . . .	145
<b>7</b>	<b>Conclusions and Future Works</b>	<b>148</b>
7.1	Computational code . . . . .	148
7.1.1	SGS stress and scalar flux models . . . . .	149
7.1.2	Wall models . . . . .	149
7.1.3	Inlet conditions . . . . .	150
7.1.4	Preliminary validation . . . . .	150
7.2	Turbulent wake of a single wall-mounted obstacle . . . . .	150
7.3	Turbulent flow over a matrix of wall-mounted obstacles . . . . .	151
7.4	Turbulent dispersion from a localized source . . . . .	153
7.5	Future works . . . . .	154
	<b>References</b>	<b>156</b>
<b>A</b>	<b>Derivation of the transport equations</b>	<b>178</b>
A.1	Resolved kinetic energy . . . . .	178
A.2	Resolved turbulent kinetic energy . . . . .	179
A.3	Resolved scalar energy . . . . .	180
A.4	Resolved scalar variance . . . . .	181
<b>B</b>	<b>Discretization of the governing equations</b>	<b>183</b>
B.1	Discretization of the momentum equation . . . . .	183
B.2	Discretization of the continuity equation . . . . .	189

B.3 Discretization of the scalar transport equation . . . . .	191
---	-----

# List of Figures

2.1	Schematic of the turbulent energy spectra. . . . .	17
2.2	Time-history of the resolved streamwise velocity component in a turbulent plane channel flow at the half channel height, evolving from the initial condition to the statistically stationary state ( $Re_\tau = 2,000$ ). . . . .	24
3.1	parallel code scalability based on the execution time required for one single time step. . . . .	46
3.2	Schematic of the physical domain of a plane channel. . . . .	47
3.3	Isopleths of the streamwise velocity in three typical $x$ - $y$ , $x$ - $z$ and $y$ - $z$ planes, respectively, at $Re_\tau = 300$ . . . . .	48
3.4	Comparison of the resolved first- and second-order turbulence statistics obtained from wall-modeled LES with the DNS results at $Re_\tau = 300$ . . . . .	49
3.5	Resolved mean streamwise velocity at $Re_\tau = 2,000$ . . . . .	52
4.1	Schematic of the computational domain and coordinate system for the wall-mounted square cylinder flow. . . . .	54
4.2	Grid distribution in streamwise, vertical and spanwise directions. . . . .	56
4.3	Time-averaged streamlines and contours of non-dimensionalized resolved streamwise velocity in $x$ - $z$ planes at two different elevations for $y/d = 0.03$ and $y/d = 3$ . . . . .	58
4.4	Top view of the instantaneous and time-averaged vector plots of the resolved velocity field in the $x$ - $z$ plane at elevation $y/d = 3$ . . . . .	60

4.5	Side view of the instantaneous and time-averaged vector plots of the resolved velocity field in the central $x$ - $y$ plane at $z/d = 0$ . . . . .	60
4.6	Spanwise profiles of the mean resolved streamwise velocity at 3 different elevations and multiple streamwise locations within the recirculation region (in order to make the figure more readable, data points are labeled using symbols at segments with the length of 3% of the total height of the frame). . . . .	62
4.7	Time-averaged streamlines and contours of the mean resolved streamwise velocity in the central $x$ - $y$ plane located at $z/d = 0$ . . . . .	63
4.8	Tip vortex shedding visualized using the instantaneous non-dimensionalized resolved pressure field in the central $x$ - $y$ plane located at $z/d = 0$ (the pressure coefficient is defined as $C_p = (\bar{p} - \bar{p}_\infty)/q_\infty$ ). The time step between the two snapshots is 0.004 s. . . . .	64
4.9	Kármán vortex shedding visualized using the instantaneous non-dimensionalized resolved pressure field near the cylinder in the $x$ - $z$ plane located at $y/d = 1$ (the pressure coefficient is defined as $C_p = (\bar{p} - \bar{p}_\infty)/q_\infty$ ). . . . .	64
4.10	Three-dimensional vortical structures in the wake region and around the cylinder edges visualized using instantaneous resolved low pressure iso-surfaces (the pressure field has been non-dimensionalized and is represented by the pressure coefficient defined as $C_p = (\bar{p} - \bar{p}_\infty)/q_\infty$ ). . . . .	66
4.11	Contours of instantaneous non-dimensionalized resolved pressure in $y$ - $z$ planes at 12 consecutive streamwise locations (the pressure coefficient is defined as $C_p = (\bar{p} - \bar{p}_\infty)/q_\infty$ ). . . . .	67
4.12	Contours of the resolved TKE production rate in two typical $x$ - $y$ and $x$ - $z$ planes (non-dimensionalized using the maximum resolved TKE production rate in the same planes, respectively). . . . .	69

4.13	Slices of resolved TKE contours along the streamwise direction (the resolved TKE value has been non-dimensionalized using $U_\infty^2$ ). . . . .	70
4.14	Time-averaged resolved streamwise and spanwise velocity profiles downstream of the obstacle at elevation $y/d = 3$ , and two streamwise locations for $x/d = 2$ and $x/d = 3.5$ . . . . .	72
4.15	Cross-stream profiles the resolved streamwise and spanwise RMS velocities at elevation $y/d = 3$ , and two streamwise locations for $x/d = 2$ and $x/d = 3.5$ . . . . .	74
4.16	Streamwise profiles of the resolved streamwise mean and RMS velocities at two different elevations in the central $x$ - $y$ plane ( $z/d = 0$ ). . .	76
4.17	Cross-stream profiles of the resolved streamwise and spanwise RMS velocities in the recirculation and far downstream regions at elevation $y/d = 2$ . Data points are labeled using symbols at segments with the length of 3% of the total height of the frame. . . . .	77
4.18	Cross-stream profiles of the non-dimensionalized mean resolved Reynolds stress component $\langle \bar{u}''\bar{w}'' \rangle$ at elevation $y/d = 3$ , and two streamwise locations for $x/d = 2$ and $x/d = 3.5$ . . . . .	79
4.19	Cross-stream profiles of the non-dimensionalized mean resolved Reynolds stress component $\langle \bar{u}''\bar{w}'' \rangle$ in the recirculation and far downstream regions at elevation $y/d = 2$ . Data points are labeled using symbols at segments with the length of 3% of the total height of the frame. . . .	80
4.20	Non-dimensionalized temporal energy spectra for the resolved streamwise velocity component in the central plane ( $z/d = 0$ ), at the elevation $y/d = 4$ and two streamwise locations $x/d = 2$ and $x/d = 3.5$ . . . . .	81
4.21	Cumulative distribution function for the resolved streamwise velocity component in the central plane ( $z/d = 0$ ), at the elevation $y/d = 4$ and two streamwise locations $x/d = 2$ and $x/d = 3.5$ . . . . .	82

4.22	Cross-stream profiles of the non-dimensionalized mean SGS shear stress $\tau_{13}$ in the recirculation and far downstream regions at elevation $y/d = 2$ . Data points are labeled using symbols at segments with the length of 3% of the total height of the frame. . . . .	84
4.23	Streamwise profiles of the mean SGS KE dissipation rate $\langle \varepsilon_{sgs} \rangle$ at different elevations downstream of the cylinder in the central plane (located at $z/d = 0$ ). All the quantities shown in the figure have been non-dimensionalized using $U_\infty^3/d$ . Data points are labeled using symbols at segments with the length of 3% of the total height of the frame. . . . .	85
4.24	Cross-stream profiles of the mean SGS KE dissipation rate $\langle \varepsilon_{sgs} \rangle$ in the recirculation and far downstream regions at elevation $y/d = 2$ . All the quantities shown in the figure have been non-dimensionalized using $U_\infty^3/d$ . Data points are labeled using symbols at segments with the length of 3% of the total height of the frame. . . . .	85
4.25	Streamwise profiles of the ratio of the SGS viscosity to the kinematic viscosity of the fluid ( $\langle \nu_{sgs} \rangle / \nu$ ) at different elevations downstream of the cylinder in the central plane (located at $z/d = 0$ ). Data points are labeled using symbols at segments with the length of 3% of the total height of the frame. . . . .	88
4.26	Cross-stream profiles of the ratio of the SGS viscosity to the kinematic viscosity of the fluid ( $\langle \nu_{sgs} \rangle / \nu$ ) at elevation $y/d = 2$ . Data points are labeled using symbols at segments with the length of 3% of the total height of the frame. . . . .	88
5.1	Schematic of the matrix of $16 \times 16$ wall-mounted cubes and the coordinate system. The side length of the cube is $d = 31.75$ mm. . . .	95

5.2	Locations in cell 1 and cell 6 selected for comparison of the predicted and measured velocity profiles. The non-dimensional coordinate ( $x/d$ ) in these two subfigures specifies the streamwise location with respect to the coordinate system defined in Fig. 5.1. . . . . .	95
5.3	Grid distribution in streamwise, vertical and spanwise directions, respectively. . . . .	97
5.4	Effects of 4 different inlet conditions on the predicted streamwise RMS velocity level at the measurement locations D1 and D6. . . . .	99
5.5	Contours of the resolved instantaneous streamwise velocity in the central $x$ - $y$ plane (located at $z/d = 0$ ). . . . .	99
5.6	Time-averaged streamlines around obstacles in different rows, demonstrated in the central $x$ - $y$ plane at $z/d = 0$ . . . . .	101
5.7	Horseshoe vortex in front of the first-row obstacle in the central column, visualized using time-averaged resolved streamwise velocity, pressure coefficient and streamlines in the $x$ - $z$ plane at elevation $y/d = 0.25$ . . . . .	102
5.8	Contours of the time-averaged resolved streamwise velocity and time-averaged streamlines in $x$ - $z$ planes at elevation $y/d = 0.5$ and different streamwise regions. . . . .	104
5.9	Top view of the time-averaged vector plot of the resolved velocity field around the last-row obstacle of the central column, in the $x$ - $z$ plane at elevation $y/d = 0.5$ . . . . .	105
5.10	Lateral view of the instantaneous and time-averaged vector plots and streamlines of the resolved velocity field inside the canyon in the self-similar region (between rows 7 and 8). The plots are made in the central $x$ - $y$ plane located at $z/d = 0$ . . . . .	107

5.11	Non-dimensionalized temporal energy spectra for the streamwise, vertical and spanwise velocity components at position $x/d = 13.5$ , $y/d = 1$ and $z/d = 0$ (located within the self-similar region between rows 7 and 8 at the rooftop elevation in the central plane of the domain).	108
5.12	Cumulative distribution function for the streamwise, vertical and spanwise velocity components, respectively, at $x/d = 13.5$ , $y/d = 1$ and $z/d = 0$ .	109
5.13	Vertical profiles of the non-dimensionalized mean streamwise velocity at different locations in cell 1.	111
5.14	Vertical profiles of the non-dimensionalized mean streamwise velocity at different locations in cell 6.	112
5.15	Vertical profiles of the non-dimensionalized RMS streamwise velocity at different locations in cell 1.	113
5.16	Vertical profiles of the non-dimensionalized RMS streamwise velocity at different locations in cell 6.	114
5.17	Budget of the time-averaged resolved kinetic energy ( $k_r$ ) at $x/d = 13.5$ within $-1 < z/d < 1$ , at three different elevations. All the quantities shown in the figures have been non-dimensionalized using $U_\infty^3/d$ .	116
5.18	Profiles of the time-averaged SGS KE dissipation rates ( $\langle \varepsilon_{sgs} \rangle$ ) at $x/d = 13.5$ within $-1 < z/d < 1$ , at three different elevations. All the quantities shown in the figures have been non-dimensionalized using the averaged viscous dissipation rate $2\nu \langle \overline{S}_{ij} \overline{S}_{ij} \rangle$ .	117
5.19	Budget of the time-averaged resolved TKE ( $k$ ) at $x/d = 13.5$ within $-1 < z/d < 1$ , at three different elevations. All the quantities shown in the figures have been non-dimensionalized using $U_\infty^3/d$ .	123
6.1	Schematic of the ground-level point source located in the central (or, eighth) column of the matrix of the obstacles.	130

6.2	Contours of the instantaneous resolved concentration field ( $\bar{c}$ ) in the $x$ - $y$ and $x$ - $z$ planes located at $z/d = 0$ and $y/d = 0.5$ , respectively. The concentration field has been non-dimensionalized using the source strength $c_s$ . . . . .	132
6.3	Contours of the time-averaged resolved concentration field ( $\langle\bar{c}\rangle$ ) in $x$ - $z$ planes at two different elevations below and above the canopy. The concentration field has been non-dimensionalized using the source strength $c_s$ . . . . .	132
6.4	Streamwise evolution of vertical profiles of the mean and standard deviation of the concentration normalized by their local maximums along the vertical lines. . . . .	134
6.5	Cross-stream profiles of the non-dimensionalized mean concentration at the elevation $y/d = 0.25$ and different streamwise locations. . . . .	135
6.6	Cross-stream profiles of the non-dimensionalized mean concentration at the elevation $y/d = 0.5$ and different streamwise locations. . . . .	136
6.7	Cross-stream profiles of the non-dimensionalized mean concentration at the elevation $y/d = 1.25$ and different streamwise locations. . . . .	137
6.8	Cross-stream profiles of the non-dimensionalized standard deviation of the concentration at the elevation $y/d = 0.25$ and different streamwise locations. . . . .	138
6.9	Cross-stream profiles of the standard deviation of the concentration at the elevation $y/d = 0.5$ and different streamwise locations. . . . .	139
6.10	Cross-stream profiles of the standard deviation of the concentration at the elevation $y/d = 1.25$ and different streamwise locations. . . . .	140
6.11	Non-dimensionalized temporal scalar energy spectra at $x/d = 13.5$ , $y/d = 1$ and $z/d = 0$ . . . . .	141
6.12	Cumulative distribution function for the resolved concentration at $x/d = 13.5$ , $y/d = 1$ and $z/d = 0$ . . . . .	141

6.13	Budget of the time-averaged resolved scalar energy ( $k_{rs}$ ) at $x/d = 13.5$ within $-1 < z/d < 1$ , at three different elevations. All the terms are non-dimensionalized using $U_\infty c_s^2/d$ . . . . .	142
B.1	Schematic of a typical computational cell, its node, faces, indices and neighbors in 2-D and 3-D configurations for the base grid. Note that in a staggered grid arrangement, the grids for storing velocity components ( $u$ , $v$ and $w$ ) are half-cell shifted in $x$ , $y$ and $z$ directions, respectively.	184

# Nomenclature

## English Symbols

$A^+$	Van Driest constant
$B$	Log law intercept
$a_j, b_j$	Base vectors
$c$	Scalar field
$C_p$	Pressure coefficient
$C_S$	SGS stress model coefficient for DSM
$C_S, C_W, C_N$	SGS stress model coefficients for DNM
$C_\theta$	SGS scalar flux model coefficients for EDM
$C_{\theta E}, C_{\theta S}$	SGS scalar flux model coefficients for DFLTDM
$d$	Side length of the square cylinder
$E_{ii}$	Different components of energy spectra: $i = 1, 2, 3$
$E_{cc}$	Spectra of concentration fluctuation
$f, g$	Arbitrary functions
$f_c$	Cut-off wave frequency
$G$	Filter function
$h$	Height of the square cylinder
$h_j$	SGS scalar flux vector
$k$	Resolved turbulence kinetic energy (TKE)
$k_r$	Resolved kinetic energy (KE)
$k_s$	Resolved fluctuating scalar energy (FSE)
$k_{rs}$	Resolved scalar energy (SE)
$k_c$	Cut-off wave number

$\mathcal{L}_j$	Vector
$\mathcal{L}_{ij}$	Leonard type stress tensor
$L_x, L_y, L_z$	Streamwise, vertical and spanwise lengths of the domain
$M_{ij}, W_{ij}, N_{ij}$	Differential tensors
$n_i$	Unit vector normal to the cell surface
$N_x, N_y, N_z$	Number of grid-points along $x$ , $y$ and $z$ axis, respectively
$p$	Pressure
$P_j, Q_j$	Differential vectors
$P_r$	TKE production rate
$Q$	A tensor invariant for vortex visualization
$q_\infty$	Free-stream dynamic pressure
$Re$	Reynolds number
$Re_\tau$	Reynolds number based on friction velocity: $u_\tau \delta / \nu$
$R_{ij}$	Temporal autocovariance
$s$	Time interval for temporal autocovariance
$S$	Cell surface
$S_{ij}$	Strain rate tensor: $(\partial u_i / \partial x_j + \partial u_j / \partial x_i) / 2$
$ S $	Norm of $S_{ij}$ : $(2S_{ij}S_{ij})^{1/2}$
$Str$	Strouhal number
$t$	Time
$t^*$	Characteristics time-scale for channel flow
$u_i$	Velocity components
$u, v, w$	Instantaneous velocity components in $x$ , $y$ and $z$ directions, respectively
$u^*$	Characteristics velocity scale for channel flow
$U_b$	Channel bulk velocity
$u_\tau$	Friction velocity
$U_\infty$	Free-stream mean velocity
$u_{rms}, v_{rms}, w_{rms}$	Streamwise, vertical and spanwise RMS velocities, respectively

$u_{  }$	Wall-parallel velocity component
$V$	Cell volume
$x, y, z$	Coordinates of a Cartesian frame

## Greek Symbols

$\alpha$	Molecular diffusivity of the fluid; or a generic mathematical variable
$\beta, \gamma, \xi$	Generic mathematical variables
$\alpha_{ij}, \lambda_{ij}, \zeta_{ij}$	Test-grid level base tensors
$\beta_{ij}, \gamma_{ij}, \eta_{ij}$	Grid level base tensors
$\delta$	Height of the plane channel; or normal distance of the first node off the wall
$\delta_{ij}$	Kronecker delta
$\Delta$	Grid size
$\Delta t$	Time step
$\Delta S$	Cell surface element
$\Delta V$	Cell volume element
$\Delta x, \Delta y, \Delta z$	Grid length in $x, y$ and $z$ directions, respectively
$\bar{\Delta}$	Grid level filter width; or cut-off length scale
$\tilde{\Delta}$	Test-grid level filter width
$\varepsilon$	Viscous dissipation rate
$\eta$	Kolmogorov length scale
$\kappa$	Karman constant
$\mu$	Molecular dynamic viscosity of the fluid
$\mu_{sgs}$	SGS dynamic eddy viscosity
$\nu$	Molecular kinematic viscosity of the fluid
$\nu_{eff}$	Effective kinematic viscosity

$\nu_t$	Turbulent eddy viscosity
$\nu_{sgs}$	SGS kinematic eddy viscosity
$\rho$	Fluid density
$\tau_{ij}$	SGS stress tensor
$\tau_w$	Wall shear stress
$\psi, \phi$	Generic flow properties
$\Omega_{ij}$	Rotation rate tensor: $(\partial u_i / \partial x_j - \partial u_j / \partial x_i) / 2$

## Subscripts and Superscripts

$\bar{(\cdot)}$	A grid level filtered quantity
$\tilde{(\cdot)}$	A test-grid level filtered quantity
$(\cdot)''$	Fluctuating quantity
$(\cdot)_{ij}^*$	A trace-free tensor: $(\cdot)_{ij}^* = (\cdot)_{ij} - (\cdot)_{kk} \delta_{ij} / 3$
$(\cdot)^n, (\cdot)^{n+1}$	Values at the previous and current time steps, respectively
$(\cdot)^*, (\cdot)^{**}$	Intermediate values between the previous and current time
$(\cdot)^+$	Wall coordinates
$(\cdot)_i, (\cdot)_j, (\cdot)_{ij}$	Vectors or second-order tensors: $i, j = 1, 2, 3$
$(\cdot)_{rms}$	RMS value
$(\cdot)_\infty$	Free-stream property
$\langle \cdot \rangle$	Time- and/or plane-averaged quantity

# Abbreviations

2-D	2-Dimensional
3-D	3-Dimensional
ABL	Atmospheric Boundary layer
AR	Aspect Ratio
CDF	Cumulative Distribution Function
CFD	Computational Fluid Dynamics
CPU	Central Processing Unit
DES	Detached Eddy Simulation
DFLTDM	Dynamic Full Linear Tensor Diffusivity Model
DSM	Dynamic Smagorinsky Model
DNM	Dynamic Nonlinear Model
DNS	Direct Numerical Simulation
EDM	Eddy Diffusivity Model
FSE	Fluctuating Scalar Energy
KE	Kinetic Energy
LAN	Local Area Network
LDV	Laser Doppler Velocimetry
LES	Large-Eddy Simulation
LSE	Linear Stochastic Estimation
MPI	Message Passing Interface
NORMA	No Remote Memory Access
NUMA	Non-Uniform Memory Access
ODE	Ordinary Differential Equation
PDE	Partial Differential Equation
PDF	Probability Density Function
PIV	Particle Image Velocimetry
POD	Proper Orthogonal Decomposition
PWA	Pulsed Wire Anemometer

RANS	Reynolds-Averaged Navier-Stokes
RMS	Root-Mean-Square
SE	Scalar Energy
SGS	Subgrid-Scale
TBLE	Thin Boundary Layer Equations
TKE	Turbulent Kinetic Energy
UMA	Uniform Memory Access

# Chapter 1

## Introduction

### 1.1 Background and Motivation

The massively developing urban areas with different buildings in proximity of each other along with the safety requirements for areas with dense human habitation, make it an important topic to study wind engineering and turbulent dispersion of contaminants in built-up (urban) environments. Intensive flow-structure interactions and complex vortical patterns, sharp local gradients in flow properties, presence of obstacles in the flow domain and dispersion of contaminant through the complex geometries are among the factors which increase the degree of challenge of wind engineering in urban environments. With respect to the importance of this topic and its inherent complexities, extensive experimental and numerical studies have been conducted to investigate turbulent flows and dispersion over a single or a group of wall-mounted obstacles and buildings.

#### 1.1.1 Previous Experimental Studies

##### 1.1.1.1 Single obstacle flow

Several experimental studies have been performed to investigate the three-dimensional (3-D) vortical structures and wakes behind bluff bodies [1–3]. Castro and Robins [4] studied the flow physics and wake characteristics of flow around a wall-mounted cube

based on wind-tunnel experiments. They examined two types of approaching flows, namely, irrotational uniform flow and turbulent shear flow, and revealed that the wake size is reduced when the approaching flow is a turbulent shear flow rather than a uniform flow. Hunt *et al.* [5] conducted a series of wind-tunnel and water-channel experiments and studied the vortical structures of turbulent wakes behind wall-mounted obstacles. They could identify the topological pattern of different vortices in the wake region of a typical surface-mounted obstacle. Based on their wind-tunnel experiment, Park and Lee [6] observed that for a circular wall-mounted cylinder, there was a direct relation between the cylinder aspect ratio and its shedding frequency. They also observed that the peaks of turbulence intensity were relocated farther from the cylinder as the cylinder aspect ratio was decreased. Sumner *et al.* [1, 3] and Adaramola *et al.* [7] conducted wind-tunnel experiments to investigate the wake structures of circular wall-mounted cylinders with different aspect ratios partially immersed in a boundary layer. They showed that the wake pattern and the power spectra exhibit similar behavior for aspect ratios between 5 and 9, but deviate significantly from those for aspect ratio 3. Hussein and Martinuzzi [8] studied the three-dimensional flow structure around a wall-mounted cube in a water-channel experiment. They defined four critical regions of the flow, i.e.: 1) upstream region in which the obstacle effect was insignificant, 2) evolving shear layer on the top edge of the cube, 3) horseshoe vortex regions in the cube's wake region, and 4) far wake region in which the flow adjusts itself to a far wake. Wang *et al.* [9] investigated the interaction between the approaching boundary layer and a wall-mounted cylinder with aspect ratio of 5 ( $AR = 5$ ) in a water-tunnel experiment. They observed that an increase in the boundary layer thickness could result in an enhanced base vortex which further acts to weaken the shear layer and tip vortex at the cylinder free-end. Later, Wang and Zhou [10] and Wang *et al.* [11] conducted follow-up experiments using particle image velocimetry (PIV) and hot-wire velocimetry to study the wake region of square cylinders of different aspect ratios. They investigated the interactions between the tip, base and Kármán vortices, and their influences on the dynamics of the wake flow. Araújo *et al.* [12] studied the effects of asymmetrically mounted trip

wires on the flow behind circular cylinders of different aspect ratios, and observed that the presence of a tripped wire could cause delay in boundary layer separation and thus alter the wake structures.

Okajima [13] investigated the velocity field and Strouhal number of rectangular cylinder flows. He studied a wide range of Reynolds numbers varying from 70 to  $2 \times 10^4$  in a water channel and a wind tunnel. In his experiments, Okajima observed that there existed a special range of Reynolds numbers and AR values, within which the flow patterns (including the vortical structures and reattachment points) abruptly changed accompanied with a discontinuity in the Strouhal number. Lim *et al.* [14] investigated the effects of Reynolds number on the characteristics of turbulent flows over a cubical bluff body based on wind-tunnel experiments. They observed that the mean flow quantities are independent of Reynolds number while the fluctuating quantities are Reynolds number dependent. Sumner *et al.* [15] studied the behavior of Strouhal number for two circular wall-mounted cylinders in different positions relative to the free-stream flow. They showed that when two cylinders were close to each other, the flow pattern was similar to a single bluff body while when cylinders were moderately separated, two different Strouhal numbers were observable depending on the incidence angle of the connecting line between two cylinders. However, when two cylinders were separated by a distance more than 2.5 cylinder diameter, the Strouhal numbers were close to that of a single cylinder. Martinuzzi *et al.* [16] studied the dynamics of turbulent flow around bluff bodies mounted in thin and thick boundary layers based on hot-wire measurements. They observed that for both boundary layers, the normalized ground plane pressure distribution in the wake region can be scaled with respect to the length scale measured from the upstream origin of the separated shear layer to the reattachment point. Based on their PIV measurements, Bourgeois *et al.* [17, 18] and Sattari *et al.* [19] investigated the large scale vortical structures and quasi periodical shedding flow pattern in the wake region of a wall mounted obstacle with  $AR = 4$ . They observed two dominant vortex shedding regimes dominated by Kármán alternating vortex shedding and two co-existing vortices in the obstacle leeward with low pressure fluctuation amplitudes. Martinuzzi and Havel [20] investigated the vortex

shedding from two surface-mounted cubes in a tandem configuration using hot-wire velocimetry in a wind tunnel. They revealed that for a specific range of separation lengths between the two cubes, the Strouhal number based on the distance between obstacles is constant due to the fact that the shedding frequency adjusts itself and typically decreases as the distance between the cubes increases.

#### **1.1.1.2 Flow and dispersion for a group of obstacles**

In order to investigate the flow and pollutant dispersion in urban environments, a number of large-scale field experiments have been performed, including URBAN 2000 meteorological and tracer field campaign conducted in Salt Lake City, Utah [21], Basel UrBan Boundary Layer Experiment (BUBBLE) which measured the wind flow through and above a homogeneous urban area [22], and Mock Urban Setting Trial (MUST) conducted at US Army Dugway Proving Ground which studied the contaminant plume dispersing through an array of building-size obstacles [23]. Besides the MUST field trials, Yee *et al.* [24] and Hilderman and Chong [25] conducted several sets of scaled water-channel experiments to acquire high-quality data for investigation of flow and dispersion in modeled urban environments. They used fiber-optic laser Doppler anemometry (LDA) and laser induced fluorescence (LIF) to measure the velocity and concentration fields, respectively. Brown *et al.* [26] conducted a set of high resolution measurements using pulsed wire anemometer (PWA) in a boundary-layer wind tunnel over different arrays of building-like obstacles. They studied the first- and second-order flow turbulence statistics along the centerline plane of a two-dimensional (2-D) array of wide obstacles and a three-dimensional (3-D) array of cubic obstacles immersed in a simulated atmospheric boundary layer (ABL). MacDonald *et al.* [27] and MacDonald [28] derived simple empirical models for estimation of the drag force and mean velocity profile in different arrays of wall-mounted obstacles based on simplified analytic expressions. They validated their models against several experimental studies and could obtain good agreement with experimental data.

## 1.1.2 Previous numerical studies

Besides the achievements in experimental studies reviewed above, the past two decades have also witnessed a significant progress in numerical simulation of bluff body and urban flows in the context of turbulent boundary layers. Numerical simulation of turbulent flow and pollutant dispersion in an urban area has been a challenging subject owing to the fact that the geometry of the computational domain is usually complex, the Reynolds numbers of the approaching flow are typically high, and the interaction of instantaneous concentration field with the dynamically evolving coherent flow structures occur over a wide range of spatial and temporal scales. In view of these challenges, major approaches that have been used for numerical modeling of urban flow and dispersion are the Reynolds-averaged Navier-Stokes (RANS), direct numerical simulation (DNS) and large-eddy simulation (LES) approaches.

### 1.1.2.1 RANS and DNS of bluff body flows

In RANS approaches, use of numerical models has been primarily focused on prediction of the first- and second-order flow and concentration statistics. Andronopoulos *et al.* [29] investigated the dispersion field at the cross-junction of two street canyons by explicitly solving the transport equation for the concentration variance and used the so-called gradient transfer assumption for closing the concentration variance equation. Milliez and Carissimo [30] introduced an algebraic model for closure of the concentration variance equation and validated their model performance by comparing the obtained results against MUST measurement data. Wang *et al.* [31] used a non-linear  $k$ - $\epsilon$  model for simulating instantaneous release of contaminant from a ground-level point source. They proposed a so-called dissipation length-scale model required for closure of the concentration variance equation. In their follow-up study of length scale models for the concentration variance dissipation rate, Wang *et al.* [32] and Yee *et al.* [33] simulated turbulent dispersion of a passive scalar released from a continuous ground-level point source in a cubic array of obstacles using the  $k$ - $\epsilon$

approach for solving the flow field. Based on the experimental study of Brown *et al.* [26], Lien *et al.* [34] compared the predictive performances of four different  $k$ - $\epsilon$  models in their numerical simulation of disturbed flows over and through a 2-D array of rectangular buildings immersed in a deep turbulent boundary layer. They showed that the non-linear  $k$ - $\epsilon$  model had the best performance among the tested RANS models. In a follow-up simulation, Lien and Yee [35] studied turbulent flow over an array of 3-D buildings using two versions of  $k$ - $\epsilon$  model. They could obtain good agreement with the experimental results for mean velocities but underpredicted the turbulent kinetic energy (TKE) above the buildings. Santiago *et al.* [36] used the standard  $k$ - $\epsilon$  model to study the turbulent flow over a regular array of cubes submerged in a simulated urban ABL. They observed that the center of the vortex formed in the canyon region was located at 3/4 of the cube height and the downwash flow dominated the upwash flow inside the canyon region. Kim and Baik [37] used a RANS approach to investigate the effect of wind direction on the spatial distribution of a passive scalar in an idealized urban area. They showed that when the flow direction was perpendicular to windward faces of modeled building obstacles, a high concentration zone is formed right behind them, however, the mean concentration level was diagonally symmetric when the incident angle was  $45^\circ$ . Majumdar and Rodi [38] conducted numerical simulations over wall-mounted circular cylinders based on a RANS method. They were able to reproduce some important flow physical features such as horse-shoe and Kármán vortices. They also reported high sensitivity of flow patterns to the developing boundary layer, especially in the leeward of the cylinder. Hsieh and Lien [39] simulated fully developed turbulent flow over a matrix of wall-mounted obstacles using standard  $k$ - $\epsilon$  model with a length scale correction in the  $\epsilon$  equation. They compared their results with the experimental measurements of Drain and Martin [40] and observed improvement in prediction of mean flow and turbulence quantities as the result of the length scale correction.

With the fast advancement of computational technology, high-resolution 3-D numerical simulations have become more and more accessible. However, conducting DNS is still, in general, limited to flows at low and moderate Reynolds numbers. To

name some of the recent studies, we can consider the DNS studies of Saha *et al.* [41] and Saha *et al.* [42] on 2-D and 3-D vortex dynamics behind a square cylinder at low Reynolds numbers, Sohankar *et al.* [43] for turbulent flow over a wall-mounted square cylinder for  $150 \leq \text{Re} \leq 500$  under uniform inlet boundary condition and Hwang and Yang [44] who used DNS approach to investigate the effect of Reynolds number on the flow structure around a wall-mounted cube. Yakhot *et al.* [45,46] studied the turbulent wake and vortex dynamics behind a wall-mounted cube in a fully-developed channel flow using DNS based on an immersed boundary method. They thoroughly investigated the unstable interactions between two side horse-shoe vortices and the arch-type vortex tube behind the cube. Saeedi *et al.* [47] conducted DNS to study turbulent wake behind a wall-mounted square cylinder with  $\text{AR} = 4$ . They could obtain very good agreement with the experimental measurement data and showed the dominance of the tip and Kármán vortices in the wake region. Dousset and Pothérat [48] performed DNS to study the shedding of hairpin vortices in the wake of a finite wall-mounted square cylinder for Reynolds numbers close to the critical threshold of the onset of vortex shedding. They could identify a series of  $\Omega$ -shaped vortices due to the streamwise orientation of the legs of hairpin vortices.

Coceal *et al.* [49] performed DNS over staggered and aligned arrays of wall-mounted cubes at a relatively low Reynolds number. They revealed the importance of the layout of obstacles and highlighted the need to consider three-dimensionality of the flow in urban-like configurations. Lee *et al.* [50] conducted DNS to investigate the 3-D turbulent boundary layer roughened with a staggered array of cubes and compared that with a boundary layer flow over a 2-D rod roughened wall. It was shown in their study that the friction velocity over a wall with 3-D roughness elements was smaller than that with 2-D roughness. Lee *et al.* [50] conducted DNS to investigate a 3-D turbulent boundary layer roughened with a staggered array of cubes and compared their test case with the flow over a 2-D rod-roughened wall of Ashrafian *et al.* [51]. It was shown in their study that the friction velocity of the cube-roughened wall is smaller than that of the rod-roughened wall, and correspondingly, the downshift of the mean streamwise velocity profile from the conventional log law of the wall

(characteristic of a zero-pressure gradient boundary flow) is smaller in the cube-roughened case.

#### 1.1.2.2 LES of bluff body flows

As reviewed above, traditionally, numerical studies have mainly relied on the RANS approach, which however, cannot provide detailed temporal and spatial information of the dynamically evolving flow and concentration fields. Also, in spite of some previous studies based on DNS of turbulent flows around a single or a group of bluff bodies, conducting DNS of urban flows at high Reynolds numbers of practical interest can be prohibitively expensive due to the very high computational demand for spatial and temporal resolutions. Furthermore, detailed flow information at the finest Kolmogorov scales obtained from DNS is not always necessary in engineering practice. In view of this, LES can be considered as an optimum tool for transient simulation of turbulent flow and dispersion over an idealized urban area. Rodi [52] conducted a comparative study on the performances of LES and RANS in numerical simulation of turbulent flows over wall-mounted square cylinders. In this early work of Rodi, he showed that the turbulent fluctuations were severely underpredicted when a RANS method was used while LES could capture more flow details as a transient simulation tool. Cheng *et al.* [53] compared the effectiveness of LES and RANS approaches in their numerical study of turbulent flow over a matrix of cubes at a relatively low Reynolds number. They observed a better performance of LES over RANS especially in terms of the prediction of the resolved Reynolds stresses and spanwise mean velocity. Salim *et al.* [54] compared the predictive performances of the RANS and LES approaches in their study of a concentration field released from two parallel line sources within an urban street canyon. They observed that the LES results tend to have a better agreement with wind-tunnel data in terms of the predicted mean concentration profiles. Schmidt and Thiele [55] studied complex 3-D flow structures over wall-mounted cubes using different modeling approaches (including RANS, LES and detached eddy simulation (DES)), and demonstrated the

effectiveness of DES in resolving the dominant flow patterns. Xie and Castro [56] compared the performances of LES and RANS in numerical simulation of turbulent flow over staggered and random arrays of wall-mounted cubes and reported that the RANS results were not satisfactory as those of LES due to the inherent unsteadiness of the flow. They also concluded that turbulent flow over building-like obstacles is mainly large-scale dependent rather than viscous scale dependent (except in regions very close to the wall) and consequently, even at low Reynolds numbers, a wide range of inertial subrange could be observed.

Shah and Ferziger [57] studied the flow over a wall-mounted cube (with  $AR=1$ ) at high Reynolds numbers using LES, and compared their simulation results against the experimental measurement data of Martinuzzi and Tropea [58] and demonstrated the capability of LES in solving complex 3-D bluff body flows. Fröhlich *et al.* [59] conducted LES of flow past a circular cylinder at Reynolds number 140,000 (based on the cylinder diameter and free-stream mean velocity) which was, at its time, the highest Reynolds number for this type of simulation. They showed an excellent agreement between their numerical results and experimental data, and demonstrated the superiority of LES over RANS in simulating turbulent flows over bluff bodies. In a follow-up study, Fröhlich and Rodi [60] performed LES of turbulent flow over a circular cylinder at a lower Reynolds number 43,000 (based on the cylinder diameter and free-stream mean velocity) with  $AR = 2.5$ . They studied the vortex dynamics behind the cylinder and revealed that the relatively low aspect ratio of the cylinder caused the Kármán vortices to bend and distort downstream of the cylinder. Breuer [61] investigated the effects of different discretization schemes and subgrid-scale (SGS) models on the predicted turbulence statistics for the flow over a circular cylinder with a relatively low Reynolds number (i.e.  $Re = 3,900$  based on the cylinder diameter and free-stream mean velocity). He could obtain very good agreement with the existing experimental data using the central differencing scheme for the convective terms and the dynamic Smagorinsky model as the SGS stress model. Later, Breuer [62] showed that the dynamic Smagorinsky model also performed well for a high Reynolds number flow (i.e.  $Re = 140,000$ ) over a circular cylinder. Catalano *et al.* [63] conducted LES

of turbulent flow over a circular cylinder at very high Reynolds numbers up to  $2 \times 10^6$  which was possible with the aim of wall modeling. They reported that the LES was able to correctly predict the boundary layer separation point and the lift and drag coefficients of the cylinder. Kim *et al.* [64] performed LES of turbulent flow past a square cylinder confined in a channel. They reported that compared to the cylinder flow in an infinite domain, the size of the recirculation region behind the cylinder was decreased and a higher drag force was observed in the confined cylinder flow. Afgan *et al.* [65] conducted LES of turbulent flow over a wall-mounted circular cylinder with aspect ratios 6 and 10, and showed that the effect of the downwash flow at the cylinder free-end on the wake region was stronger for lower aspect ratios. Lysenko *et al.* [66] performed LES to study turbulent flow structures past a circular cylinder and found good agreement with the available experimental and DNS data.

Niéno *et al.* [67] studied the flow over a matrix of wall-mounted heated cubes using LES and showed that the total heat transfer from the cubes to the fluid is significantly influenced by the coherent vortical structures around the cubes. Hanna *et al.* [68] performed LES of turbulent flows over different types of arrays of wall-mounted cubic obstacles immersed in a fully-developed boundary layer. They compared regular and staggered arrays of obstacles and showed that the flow quickly approached a quasi-equilibrium state in both configurations after the third or fourth row. Shi *et al.* [69] performed LES of wind field over a group of modeled building obstacles in a staggered arrangement and observed that the predicted turbulent fluctuations would be considerably lower than the experimental values if no perturbation was used at the inlet of the computational domain. As a remedy to this problem, they imposed time-correlated random fluctuations on the inlet boundary following the approach of Hanna *et al.* [68]. Liu *et al.* [70] conducted LES to predict the flow field and pollutant dispersion from ground-level line-sources located in 2-D modeled street canyons. They observed a higher pollutant concentration inside street canyons when the aspect ratio of obstacles was increased. In their follow-up LES study, Cheng and Liu [71] further investigated the pollutant dispersion in a 2-D urban model with a distributed ground-level pollutant source.

It should be noted that for wall-resolved LES, the grid resolution requirement is as demanding as DNS in the near-wall regions, as in both approaches, the near-wall flow field must be fully resolved (at viscous scales). In fact, conducting wall-resolved LES of turbulent flow and dispersion in a complex urban environment at Reynolds numbers of practical interests is still prohibitively expensive. Although LES has been used by a number of researchers to study urban flow and dispersion, some of the studies reviewed above are not rigorous in terms of the grid resolution required for resolving near-wall dynamics. For example, in the LES study of Shi *et al.* [69], only 7 grid points were used across an individual obstacle for a highly-turbulent flow at  $Re=22,400$  (defined based on the mean velocity and the obstacle height). In the LES study of Niceno *et al.* [67], the computational expenses have been significantly reduced by considering a portion of a full array of obstacles submerged in the boundary layer. This is based on the observation that flow quickly becomes self-similar after the first several rows of obstacles; such that use of the assumption of fully-developed boundary-layer flow is justified and periodic boundary conditions can be applied to both the streamwise and spanwise directions. In view of the high demands involved in wall-resolved LES for either complex flows or high Reynolds number flows, the method of wall-modeled LES has been developed and become more and more popular over the past two decades [72–76]. Although wall modeling has been primarily used in simple geometries such as plane channel flows and flat-plate boundary layer flows [73, 76, 77], a number of attempts have been also made towards applications to more complex geometries with flow separations. For instance, Mason and Callen [72] proposed a wall model for rough surfaces, Wang and Moin [75] applied a stress-balance model with and without the pressure gradient term for simulating turbulent flow over an asymmetric airfoil with strong streamwise pressure gradient, and Xie and Castro [56] utilized the log-law to infer boundary condition on the shear stresses over an array of wall-mounted cubes.

## 1.2 Objectives of the Thesis

The major objectives of this research have been summarized as:

- Establishing, testing and validating the computational code required for conducting numerical simulation (including DNS and LES) of turbulent flow and dispersion in complex geometries (namely modeled urban environments). This objective also includes reviewing, testing and assessment of numerical schemes and models such as subgrid-scale models, wall models and inlet boundary conditions.
- Testing different subgrid-scale models for LES of turbulent flow and dispersion in various configurations of bluff body flows.
- Studying different wall models which have been used for LES of turbulent flows in different configurations. Since we aim at performing LES of turbulent flows over wall-mounted obstacles which include complex vortical patterns and flow separation, it will be tried to select a wall model appropriate for the specific flow conditions considered in the current research.
- Studying the currently available methodologies of producing inlet conditions required for LES of turbulent flows over a group of wall-mounted obstacles. Different methodologies based on synthetic turbulence and physical inlet conditions will be studied and tested in the context of bluff body flows. With respect to the very high turbulence level of flows over urban canopy models, a method for reproducing physical turbulence at the inlet boundary of this type of flows will be also proposed.
- Conducting thorough physical analysis of turbulent wakes of wall-mounted obstacles, partially and fully immersed in turbulent boundary layers. In this step, the physics of turbulent flows which are highly influenced by the presence of a single or a group of wall-mounted obstacles will be investigated. Characteristics of turbulent wakes behind bluff bodies will be investigated

using different approaches to provide a deep physical insight of turbulent flows associated with interactions between the wind fields and human-made objects.

- Testing different discretization schemes for discretizing the passive scalar transport equation in the context of turbulent dispersion from a localized source. Turbulent dispersion from a localized source deals with the special challenge of very high local gradient around the point source, which needs special treatments in discretizing the passive scalar transport equation. Thus, a number of existing schemes will be studied to select the optimum one for the specific configuration used in the current research.
- providing solid and in-depth understanding into the physics of turbulent dispersion from a localized source located within a matrix of wall-mounted cubes. In this step, the concentration field over a matrix of wall-mounted obstacles will be investigated from different points of view. The evolution of dispersion field and its physical characteristics will be thoroughly studied.

### 1.3 Outline of the Thesis

The remaining of this thesis is organized as following:

in chapter 2, the mathematical formulations and governing equations will be introduced including the Navier-Stokes and scalar transport equations, filtering operation and filtered governing equations for LES, subgrid-scale models and a brief discussion on turbulence statistics and time-averaging.

In chapter 3, the numerical algorithms applied in our computational code will be demonstrated including the discretization schemes, integration schemes of the partial differential equations, boundary conditions and validation of the LES code based on bench-mark test cases. A brief review of parallel computing will be also provided.

In chapter 4, turbulent wake behind a wall-mounted obstacle will be analyzed using wall-resolved LES approach.

In chapter 5, wall-modeled LES approach will be used to thoroughly investigate the turbulent flow over a matrix of regular wall-mounted cubes and demonstrate the capability of our LES code in simulating turbulent flows over complex geometries.

In chapter 6, turbulent dispersion from a ground-level localized source located within a matrix of regular wall-mounted cubes (the same configuration used in chapter 5) will be investigated using LES approach.

Chapter 7, provides a summary of the main findings and outcomes of this research, and introduces suggested steps for continuing the research on the topic of turbulent flow and dispersion in urban areas and complex geometries.

# Chapter 2

## Mathematical framework

### 2.1 Governing equations

The continuity and momentum equations, as two coupled partial differential equations (PDEs), and also the passive scalar transport equation for a Newtonian fluid, together, form a system of governing equations which, for an incompressible flow, takes the following form in a Cartesian coordinate system (see for example Mathieu and Scott [78]).

$$\frac{\partial u_i}{\partial x_i} = 0 \quad , \quad (2.1)$$

$$\frac{\partial u_i}{\partial t} + \frac{\partial}{\partial x_j}(u_i u_j) = -\frac{1}{\rho} \frac{\partial p}{\partial x_i} + \nu \frac{\partial^2 u_i}{\partial x_j \partial x_j} \quad , \quad (2.2)$$

$$\frac{\partial c}{\partial t} + \frac{\partial}{\partial x_j}(u_j c) = \alpha \frac{\partial^2 c}{\partial x_j \partial x_j} \quad , \quad (2.3)$$

in which  $u_i$ ,  $p$  and  $c$  represent the velocity, pressure and scalar fields, respectively,  $x_i$  represents coordinates,  $\rho$  and  $\nu$  are the density and kinematic viscosity of the fluid, respectively, and  $\alpha$  is the molecular diffusivity of the scalar. The above system of transport equations can fully determine the velocity, pressure and passive scalar fields for turbulent flow and dispersion without the need to any modeling or extra equation. In fact, for DNS of turbulent heat and fluid flow, one should solve the above system of equations with proper boundary conditions and grid resolution. Among different approaches for numerical simulation of turbulent flows, DNS provides

the most accurate and reliable results which can be used for the most sophisticated physical analysis of the flow field.

With the presence of variety of well-established numerical methods for solution of the above system of equations in different geometries and under different circumstances (see for example [79–81]), conducting a DNS may seem to be a straightforward task to implement. However, there are special challenges for conducting DNS of turbulent flows (e.g., proper inflow boundary conditions, minimizing numerical dissipation and capturing all the scales of the flow) which make it an open subject to many researchers in the area of fluid dynamics. DNS is very intensive in computation as all turbulent scales need to be directly resolved temporally and spatially. In fact, conducting DNS at a high Reynolds number of practical interest can be prohibitively expensive due to the demand for high-resolution mesh required for capturing all the scales of fluid motion. Furthermore, detailed flow information at the finest Kolmogorov scales obtained from DNS is not always necessary in engineering practice. In view of this, the idea of LES looks to be an optimum approach for conducting three-dimensional unsteady flow simulations with a considerably reduced computational demand. In the next section, the basic principles of LES and its governing equations have been introduced.

## **2.2 Large-eddy simulation (LES)**

The main goal of large-eddy simulation (LES) is to obtain simulation data of turbulent flows based on transient 3-D simulations at considerably lower computational costs in comparison with that of DNS. As such, the majority of the computational load should be removed which makes the use of models a necessary part of LES. Fortunately, in a fully resolved simulation (i.e., DNS), the major computational cost is spent to solve the small scales of the flow field which are nearly isotropic and very universal in character [82]. The idea of LES is to separate the scales of the flow to the small scales (or the so-called subgrid scales (SGS)), which are assumed to be universal, isotropic

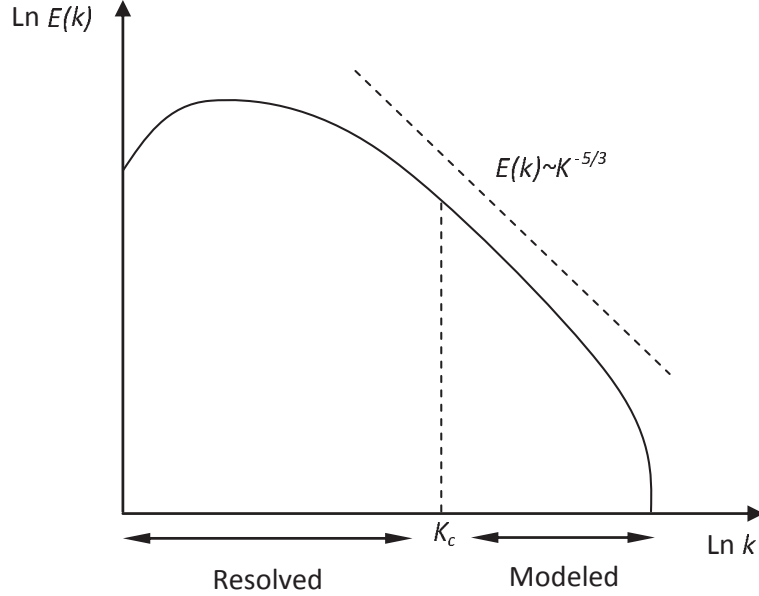


FIGURE 2.1: Schematic of the turbulent energy spectra.

and independent of the flow boundary conditions, and large scales which are mainly dominated by the geometry and boundary conditions of the flow. For the small scales with universal and non geometry-dependent behavior, a model can be used to describe their behavior and to reproduce their net effect without directly solving the flow at these scales. This will lead to a high computational saving for LES compared to DNS in which all the scales of the flow should be directly resolved. Thus, in LES of turbulent flows, the large energy-containing scales of the flow at low wave numbers are directly resolved and the effects of the high-wave-number small scales (the SGS part of the flow) are modeled. Figure 2.1 schematically shows the turbulent energy spectra and the cut-off wave number at which the resolved and modeled scales are separated in LES.

The separation of the flow scales can be accomplished by applying a low-pass spatial filter to the governing equations of fluid flow. The classical definition of a filtered quantity [83], denoted by an overbar, is

$$\bar{\phi}(\alpha) = \int_{-\infty}^{+\infty} G(\alpha - \beta)\phi(\beta)d\beta \quad , \quad (2.4)$$

where  $G(\alpha - \beta)$  is the kernel function which specifies the type of the filter. Since

equation 2.4 is a non-local operator, it is necessary to define a local discrete approximation to make it applicable for numerical simulations. In view of this, the Taylor expansion of  $\phi(\beta)$  around the point  $\alpha$  can be introduced as

$$\phi(\beta) = \phi(\alpha) + \sum_{i=1}^{\infty} \frac{(\beta - \alpha)^i}{i!} \phi(\alpha)^{(i)} \quad , \quad (2.5)$$

in which  $\phi(\alpha)^{(n)}$  is the  $n^{\text{th}}$  derivative of  $\phi$  at point  $\alpha$ . Inserting the expression 2.5 into the equation 2.4 will result in the following differential form

$$\bar{\phi}(\alpha) = \phi(\alpha) + \sum_{i=1}^{\infty} \frac{M_i}{i!} \phi(\alpha)^{(i)} \quad , \quad (2.6)$$

where  $M_n$  is the moment of the order  $n$  of the kernel  $G$  defined as

$$M_n = \int_{-\infty}^{+\infty} G(\xi) \xi^n d\xi \quad . \quad (2.7)$$

The differential form of the filter given in equation 2.6 is well-posed if and only if  $|M_n| < \infty$  for all values of  $n$ . Assuming  $\bar{\Delta}$  to be the cut-off length scale (associated with the cut-off wave number) in LES, two classical filters which are commonly used in LES [83] and satisfy the above condition are the box filter defined as

$$G(\alpha - \beta) = \begin{cases} \frac{1}{\bar{\Delta}} & \text{if } |\alpha - \beta| \leq \frac{\bar{\Delta}}{2} \\ 0 & \text{otherwise} \end{cases} \quad , \quad (2.8)$$

and the Gaussian filter defined as

$$G(\alpha - \beta) = \left( \frac{\gamma}{\pi \bar{\Delta}^2} \right) \exp \left( \frac{-\gamma |\alpha - \beta|^2}{\bar{\Delta}^2} \right) \quad . \quad (2.9)$$

For all the simulations presented in the current thesis, the box filter has been used for conducting the filtering process in LES studies.

### 2.2.1 Governing equations for LES

Theoretically, by applying a filter to the fluid flow governing equations introduced in the previous section, the filtered continuity, momentum and scalar transport equations will be obtained as

$$\frac{\partial \bar{u}_i}{\partial x_i} = 0 \quad , \quad (2.10)$$

$$\frac{\partial \bar{u}_i}{\partial t} + \frac{\partial \bar{u}_i \bar{u}_j}{\partial x_j} = -\frac{1}{\rho} \frac{\partial \bar{p}}{\partial x_i} + \nu \frac{\partial^2 \bar{u}_i}{\partial x_j \partial x_j} - \frac{\partial \tau_{ij}}{\partial x_j} \quad , \quad (2.11)$$

$$\frac{\partial \bar{c}}{\partial t} + \frac{\partial}{\partial x_j} (\bar{u}_j \bar{c}) = \alpha \frac{\partial^2 \bar{c}}{\partial x_j \partial x_j} - \frac{\partial h_j}{\partial x_j} \quad , \quad (2.12)$$

in which  $\bar{u}_i$ ,  $\bar{p}$  and  $\bar{c}$  represent the filtered velocity, pressure and scalar fields respectively, and  $\tau_{ij}$  and  $h_j$  are the so-called SGS stress tensor and SGS scalar flux vector, respectively. The SGS stress and scalar flux are appearing in the governing system of equation as results of the filtering process and are defined as  $\tau_{ij} = \overline{u_i u_j} - \bar{u}_i \bar{u}_j$  and  $h_j = \overline{u_j c} - \bar{u}_j \bar{c}$ . In order to close the above system of governing equations, we essentially need to model the SGS stress tensor and SGS scalar flux vector. In the next subsections, the SGS models considered in this research are briefly introduced.

### 2.2.2 SGS stress models

Accurate prediction of the SGS stress tensor is crucial for reliable and robust LES of turbulent flows. Several SGS stress models have been proposed during the past decades (see for example [84], [85], [86] and [87]), and many comparative studies have been conducted to investigate the performances of different SGS models in different flow conditions [88–92]. In this research, two SGS stress models have been considered which are presented in the following.

#### (1) Dynamic Smagorinsky model (DSM)

The DSM proposed by Lilly [93] and Germano *et al.* [94], is the most widely used SGS stress model in LES of turbulent flows due to its mathematical simplicity, robustness

and self-calibrating mechanism. The DSM expresses the SGS stress tensor as

$$\tau_{ij}^* \stackrel{\text{def}}{=} \tau_{ij} - \frac{\tau_{kk}}{3} \delta_{ij} = -2C_s \bar{\Delta}^2 |\bar{S}| \bar{S}_{ij} \quad , \quad (2.13)$$

where  $\bar{S}_{ij} \stackrel{\text{def}}{=} (\partial \bar{u}_i / \partial x_j + \partial \bar{u}_j / \partial x_i) / 2$  is the filtered strain rate tensor,  $|\bar{S}| \stackrel{\text{def}}{=} \sqrt{2\bar{S}_{ij}\bar{S}_{ij}}$  is the norm of  $\bar{S}_{ij}$ ,  $\delta_{ij}$  is the Kronecker delta, and the asterisk superscript denotes the trace-free form of a tensor. The dynamic model coefficient  $C_s$  can be obtained using the least squares method, viz.

$$C_s = -\frac{M_{ij}\mathcal{L}_{ij}}{M_{mn}M_{mn}} \quad , \quad (2.14)$$

where  $\mathcal{L}_{ij}$  is the resolved Leonard type stress defined as  $\mathcal{L}_{ij} \stackrel{\text{def}}{=} \widetilde{\bar{u}_i \bar{u}_j} - \tilde{u}_i \tilde{u}_j$ , and  $M_{ij} \stackrel{\text{def}}{=} \alpha_{ij} - \tilde{\beta}_{ij}$  is a differential tensor. Here,  $\alpha_{ij} \stackrel{\text{def}}{=} 2\tilde{\Delta}^2 |\tilde{S}| \tilde{S}_{ij}$  and  $\beta_{ij} \stackrel{\text{def}}{=} 2\bar{\Delta}^2 |\bar{S}| \bar{S}_{ij}$  are the test-grid and grid level base stress tensors, respectively. The resolved quantities at the grid level are denoted using an overbar, while quantities filtered at the test-grid level for the dynamic procedure are denoted using a tilde. In order to perform the dynamic modeling procedure, the filter size ratio between the grid and test-grid levels is set to 2, i.e.  $\tilde{\Delta} / \bar{\Delta} = 2$ .

## (2) Dynamic nonlinear model (DNM)

The DNM proposed by Wang and Bergstrom [95] is based on an explicit nonlinear quadratic tensorial polynomial constitutive relation originally proposed by Speziale [96] for modeling the Reynolds stress tensor in the Reynolds-averaged Navier-Stokes (RANS) approach. It employs three model coefficients dynamically calibrated using the local instantaneous velocity field. The DNM models the SGS stress tensor as

$$\tau_{ij}^* = -C_S \beta_{ij} - C_W \gamma_{ij} - C_N \eta_{ij} \quad , \quad (2.15)$$

where the base tensors are defined as  $\gamma_{ij} \stackrel{\text{def}}{=} 4\bar{\Delta}^2 (\bar{S}_{ik} \bar{\Omega}_{kj} + \bar{S}_{jk} \bar{\Omega}_{ki})$  and  $\eta_{ij} \stackrel{\text{def}}{=} 4\bar{\Delta}^2 (\bar{S}_{ik} \bar{S}_{kj} - \bar{S}_{mn} \bar{S}_{nm} \delta_{ij} / 3)$  (analogous to the definition of  $\beta_{ij}$ ). Here,  $\bar{\Omega}_{ij} \stackrel{\text{def}}{=} (\partial \bar{u}_i / \partial x_j - \partial \bar{u}_j / \partial x_i) / 2$  is the filtered rotation rate tensor. Following the least squares

procedure, the local dynamic model coefficients can be obtained, viz.

$$\begin{bmatrix} M_{ij}M_{ij} & M_{ij}W_{ij} & M_{ij}N_{ij} \\ W_{ij}M_{ij} & W_{ij}W_{ij} & W_{ij}N_{ij} \\ N_{ij}M_{ij} & N_{ij}W_{ij} & N_{ij}N_{ij} \end{bmatrix} \cdot \begin{bmatrix} C_S \\ C_W \\ C_N \end{bmatrix} = - \begin{bmatrix} \mathcal{L}_{ij}^* M_{ij} \\ \mathcal{L}_{ij}^* W_{ij} \\ \mathcal{L}_{ij}^* N_{ij} \end{bmatrix}, \quad (2.16)$$

where  $W_{ij} \stackrel{\text{def}}{=} \lambda_{ij} - \tilde{\gamma}_{ij}$  and  $N_{ij} \stackrel{\text{def}}{=} \zeta_{ij} - \tilde{\eta}_{ij}$  are differential tensors, respectively (analogous to the definition of  $M_{ij}$ ); and  $\lambda_{ij} \stackrel{\text{def}}{=} 4\tilde{\Delta}^2(\tilde{S}_{ik}\tilde{\Omega}_{kj} + \tilde{S}_{jk}\tilde{\Omega}_{ki})$  and  $\zeta_{ij} \stackrel{\text{def}}{=} 4\tilde{\Delta}^2(\tilde{S}_{ik}\tilde{S}_{kj} - \tilde{S}_{mn}\tilde{S}_{nm}\delta_{ij}/3)$  are base tensors at the test-grid level.

The constitutive relation of Eq. (2.15) includes three tensorial constituent components, i.e.,  $\beta_{ij}$ ,  $\gamma_{ij}$  and  $\eta_{ij}$ . The first term  $\beta_{ij}$  is the well-known Smagorinsky component that primarily relates to the SGS dissipation and forward scatter of kinetic energy (KE) from the filtered to SGS motions; the second term,  $\gamma_{ij}$ , does not make any contribution to the KE transfer between the filtered and subgrid scales, but it significantly improves the correlation between the exact  $\tau_{ij}$  extracted from a DNS database and that predicted by the nonlinear model; and the third term  $\eta_{ij}$  contributes considerably to the backscatter of KE from the subgrid to the filtered scales [95]. The three features mentioned above; namely, an adequate SGS dissipation level, a high correlation coefficient between the modeled and exact SGS stresses in *a priori* LES test, and a realistic representation of the KE backscatter, are among the most important criteria for developing a high-fidelity SGS stress model. It has been observed that owing to its robustness, the DNM can be applied locally without any local averaging (or, clipping) techniques in calculation of its three coefficients in several test cases for low Reynolds number turbulent channel flows with and without heat transfer [97–99], for turbulent flows under system rotations [100], and for unsteady pulsatile transitional flows [101].

### 2.2.3 SGS scalar flux models

In order to close the filtered scalar transport equation, the so-called SGS scalar flux vector should be modeled. Two SGS scalar flux models considered in this research

have been presented in the following.

### (1) Eddy diffusivity model (EDM)

The EDM proposed by Moin *et al.* [102] is based on a linear constitutive relation analogous to Fourier's law for describing molecular heat conduction, and assumes that the SGS scalar flux vector is instantaneously proportional to and aligned with the negative of the resolved temperature gradient. The EDM expresses the SGS scalar flux vector as

$$h_j = -C_\theta \bar{\Delta}^2 |\bar{S}| \frac{\partial \bar{c}}{\partial x_j} . \quad (2.17)$$

Following the dynamic procedure, the model coefficient can be obtained as

$$C_\theta = -\frac{\mathcal{L}_j M_j}{M_i M_i} , \quad (2.18)$$

in which  $\mathcal{L}_j \stackrel{\text{def}}{=} \widetilde{u_j \bar{c}} - \tilde{u}_j \tilde{\bar{c}}$  is the resolved scalar flux vector which can be directly computed from the filtered scalar field and  $M_j \stackrel{\text{def}}{=} a_j - \tilde{b}_j$  is a differential vector in which  $b_j$  and  $a_j$  are two base vectors at the grid-level and test-grid-level, respectively, defined as  $b_j \stackrel{\text{def}}{=} \bar{\Delta}^2 |\bar{S}| \frac{\partial \bar{c}}{\partial x_j}$  and  $a_j \stackrel{\text{def}}{=} \tilde{\Delta}^2 |\tilde{S}| \frac{\partial \tilde{\bar{c}}}{\partial x_j}$ .

### (2) Dynamic full linear tensor diffusivity model (DFLTDM)

The DFLTDM proposed by Wang *et al.* [103] is based on a combination of the EDM and a dynamic homogeneous linear tensor diffusivity model and expresses the SGS scalar flux vector as

$$h_j = -C_{\theta E} \bar{\Delta}^2 |\bar{S}| \frac{\partial \bar{c}}{\partial x_j} - C_{\theta S} \bar{\Delta}^2 \bar{S}_{jk} \frac{\partial \bar{c}}{\partial x_k} .$$

The dynamic model coefficients can be obtained by minimizing the residual of the Germano identity using the least-square approach as

$$\begin{bmatrix} P_j P_j & P_j Q_j \\ Q_j P_j & Q_j Q_j \end{bmatrix} \cdot \begin{bmatrix} C_{\theta E} \\ C_{\theta S} \end{bmatrix} = - \begin{bmatrix} \mathcal{L}_j P_j \\ \mathcal{L}_j Q_j \end{bmatrix} , \quad (2.19)$$

where  $P_j \stackrel{\text{def}}{=} a_j^E - \tilde{b}_j^E$  and  $Q_j \stackrel{\text{def}}{=} a_j^S - \tilde{b}_j^S$  are two differential vectors. The grid-level and test-grid-level base vectors are defined as  $b_j^E \stackrel{\text{def}}{=} \bar{\Delta}^2 |\bar{S}| \frac{\partial \bar{c}}{\partial x_j}$ ,  $b_j^S \stackrel{\text{def}}{=} \bar{\Delta}^2 \bar{S}_{jk} \frac{\partial \bar{c}}{\partial x_k}$ ,  $a_j^E \stackrel{\text{def}}{=} \tilde{\Delta}^2 |\tilde{S}| \frac{\partial \tilde{c}}{\partial x_j}$  and  $a_j^S \stackrel{\text{def}}{=} \tilde{\Delta}^2 \tilde{S}_{jk} \frac{\partial \tilde{c}}{\partial x_k}$ .

## 2.3 Statistical analysis and time-averaging

In order to analyze the results obtained from transient numerical simulation (specifically LES) of turbulent flows, the instantaneous and averaged results can be investigated. However, as pointed out by Durbin and Pettersson Reif [104], turbulent phenomena are reproducible and subject to systematic studies at the statistical level. Thus, different averaged quantities are used for describing turbulent flows and providing physical insights and robust understanding into the mechanisms governing the flow structures and their evolution. In the context of statistically stationary turbulence (i.e., mean quantities are invariant under any translation in time), all the mean quantities are based on time-averaging. In the next subsection, some considerations required for conducting the time-averaging are briefly discussed.

### 2.3.1 Transition from initial condition

All the turbulent flow fields considered in this thesis are statistically stationary which implies that their statistical quantities are independent of any translation in time. However, the time window used for conducting the time-averaging must be properly selected to obtain the statistical data which can represent the correct physical behavior of the flow field. One of the issues in selecting the averaging time window is the starting time for collecting the flow statistics which should not be influenced by the initial condition. In fact, one should ensure that the flow is fully developed and has reached a statistically stationary state to start collecting the flow statistics. Therefore, the unphysical initial condition must not be taken into account for conducting the time-averaging.

In order to demonstrate the evolution of the flow solution from the initial state

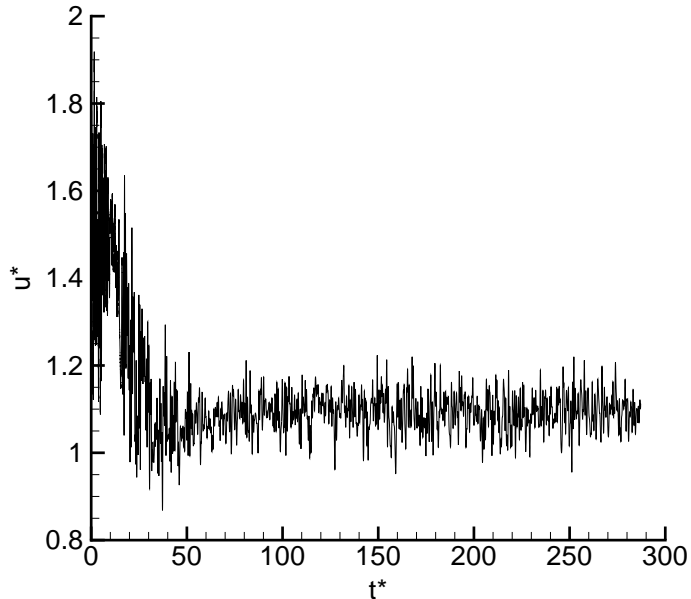


FIGURE 2.2: Time-history of the resolved streamwise velocity component in a turbulent plane channel flow at the half channel height, evolving from the initial condition to the statistically stationary state ( $Re_\tau = 2,000$ ).

to the fully-developed state, wall-modeled LES of turbulent plane channel flow at  $Re_\tau = 2,000$  has been selected. For conducting the LES, at the initial stage, the solution is started from laminar flow condition with random numbers superimposed onto the initial velocity field. The instantaneous resolved velocity at the central point of the channel has been recorded from the starting time. Figure 2.2 shows the time-history of the resolved streamwise velocity component at the central point of the channel. The resolved velocity and time have been non-dimensionalized as  $u^* = \frac{\bar{u}}{U_b}$  and  $t^* = \frac{tU_b}{\delta}$ , respectively, in which  $U_b$  is the channel bulk velocity and  $\delta$  is the half-channel height. As is evident in Fig. 2.2, it takes approximately  $60 t^*$  for the flow to pass the unphysical initial stage and evolve to the statistically stationary state. This clearly indicates that for this particular case, the flow statistics must be collected after  $t = 60 t^*$ . The same consideration has to be applied in other simulations.

Sufficient duration of the time window over which the averaging is performed is another important factor for conducting the time-averaging. Depending on the flow configuration, the duration of the time window can be characterized based on different time-scales. For instance, for a plane channel flow, the time required for the flow field

to travel the streamwise length of the channel (the so-called flow-through time), or the non-dimensional time-scale based on the channel bulk velocity and channel height ( $t^*$  in the above example) can be considered as the proper time-scale based on which the duration of the time window can be defined. For the turbulent flow around a bluff body, the duration of one vortex shedding cycle can also be considered as a proper time-scale. Typically, the time window for conducting the time-averaging must be long enough such that the time-averaged results do not change by increasing the time duration which is an indication of converged time-averaged statistics.

# Chapter 3

## Numerical algorithms

### 3.1 Spatial discretization scheme

The set of second-order non-linear partial differential equations of continuity, momentum and scalar transport, presented in the previous chapter, is very difficult to solve analytically. Only a limited number of exact solutions for this set of equations exist such as the solution of Ethier and Steinman [105] for a 3-D cavity flow under special assumptions. In order to numerically solve the governing equations of the fluid flow, a discrete system of equations analogous to the exact differential equations should be provided. The solution of the discretized equations will present an approximation of the exact solution. The accuracy level of this approximate solution depends on the discretization schemes and its local truncation error, the resolution of the discretized physical domain and boundary conditions prescribed at boundaries of the computational domain. In the following subsections, the discretization schemes for the mass, momentum and scalar transport equations will be briefly introduced.

#### 3.1.1 Mass and momentum equations

In this research, a second-order energy-conserving finite difference method proposed by Ham *et al.* [106] based on a non-uniform staggered grid system has been applied to the discretization of the governing equations. The method proposed by Ham *et al.* [106] has an advantage of conserving the kinetic energy as well as the mass

and momentum. Most of the numerical schemes only focus on conserving mass and momentum which are sufficient to provide a solution for the governing equations of fluid flow. As pointed out by Morinishi *et al.* [107], by the time of their work, none of the existing high order schemes could simultaneously conserve mass, momentum and kinetic energy. Since the kinetic energy can be derived from the momentum equation, proper selection of discrete operators can implicitly conserve both momentum and kinetic energy.

A finite difference discretization is fully conservative if it can be written as

$$\frac{\delta_1 \psi}{\delta_1 t} + \frac{\delta_1 F_i(\psi)}{\delta_1 x_i} = 0 \quad , \quad (3.1)$$

in which  $\psi$  is a typical flow property,  $F_i(\psi)$  is the flux of  $\psi$  and the one-delta ( $\delta_1$ ) is the second-order central-difference operator which is spatially defined in  $x$  direction as

$$\frac{\delta_1 \psi}{\delta_1 x} \Big|_{i,j,k} = \frac{\psi_{i+\frac{1}{2},j,k} - \psi_{i-\frac{1}{2},j,k}}{x_{i+\frac{1}{2},j,k} - x_{i-\frac{1}{2},j,k}} \quad , \quad (3.2)$$

where  $i, j, k$  represents the nodal location and  $i + \frac{1}{2}$  and  $i - \frac{1}{2}$  are the corresponding east and west faces, respectively. Similar definition can be presented for the one-delta ( $\delta_1$ ) operator in time. If the equation 3.1 is integrated over a finite volume  $V$  using discrete integration, we will obtain

$$\sum_V \left( \frac{\delta_1 \psi}{\delta_1 t} + \frac{\delta_1 F_i(\psi)}{\delta_1 x_i} \right) \Delta V = \frac{\delta_1}{\delta_1 t} \left( \sum_V \psi \Delta V \right) + \sum_S F_i(\psi) n_i \Delta S = 0 \quad , \quad (3.3)$$

where  $\Delta V$  is the cell volume element,  $\Delta S$  is the cell surface element and  $n_i$  is the unit-normal vector of the cell surface. It should be noted that in the first term of the right-hand side of the equation 3.3, the time differencing commutes with the integration and in the second term, the divergence theorem is used to convert the spatial differencing to normal flux vector. In equation 3.3, the integral of  $\psi$  over the cell volume is balanced by the net transport of  $\psi$  through all the cell surfaces which makes it spatially conservative. In the following, the interpolation operators used to discretize the governing equation will be briefly reviewed.

The interpolation schemes for a generic variable  $\psi$ , stored at cell faces, are the simple, linear and volume averaging. The simple averaging is defined as

$$\overline{\psi}^{1x} \Big|_{i,j,k,n} = \frac{\psi_{i+\frac{1}{2},j,k}^n + \psi_{i-\frac{1}{2},j,k}^n}{2} \quad , \quad (3.4)$$

in which superscript  $1x$  represents one delta operator in the  $x$  direction. The Linear or geometric interpolation is defined as

$$\overline{\psi}^{1\hat{x}} \Big|_{i,j,k,n} = \frac{(x_i - x_{i-\frac{1}{2}})\psi_{i+\frac{1}{2},j,k}^n + (x_{i+\frac{1}{2}} - x_i)\psi_{i-\frac{1}{2},j,k}^n}{x_{i+\frac{1}{2}} - x_{i-\frac{1}{2}}} \quad , \quad (3.5)$$

and volume averaging is defined as

$$\overline{\psi}^{1\check{x}} \Big|_{i,j,k,n} = \frac{(x_{i+\frac{1}{2}} - x_i)\psi_{i+\frac{1}{2},j,k}^n + (x_i - x_{i-\frac{1}{2}})\psi_{i-\frac{1}{2},j,k}^n}{x_{i+\frac{1}{2}} - x_{i-\frac{1}{2}}} \quad . \quad (3.6)$$

These operators can be applied at the node and face locations for a staggered grid arrangement. Since the node is cell-centered, these operators are all equivalent and second order in node locations. However, when evaluated at face locations, only the linear interpolation is second order accurate. It should be noted that on a non-uniform mesh, the difference and simple averaging operators only commute in different directions (e.g., in time and a spatial direction or in two different spatial directions) while the difference and linear and volume averaging operators commute in all directions.

Using the presented discrete operators, the compact discretized form of the continuity and momentum equations used in this research can be written as

$$\frac{\delta_1 u_i}{\delta_1 x_i} = 0 \quad , \quad (3.7)$$

$$\frac{\delta_1 u_i}{\delta_1 t} + \frac{\overline{\overline{\delta_1 u_j^{1\check{x}}}} \overline{\overline{\delta_1 u_i^{1\check{x}}}}}{\delta_1 x_j} = -\frac{-1}{\rho} \frac{\delta_1 \overline{p}^{1t}}{\delta_1 x_i} + \nu \frac{\delta_1}{\delta_1 x_j} \left( \frac{\delta_1 \overline{u_i}^{1t}}{\delta_1 x_j} \right) \quad . \quad (3.8)$$

If the above discretization is applied to the mass and momentum equations, the result will be a set of linear algebraic equations which can be solved by numerical solvers

(e.g., point or line iterative solvers, multigrid solvers, etc.).

### 3.1.2 Scalar transport equation

For the scalar transport equation, different discretization schemes can be applied to obtain the set of algebraic equations. Since the scalar transport equation is a linear equation without any decoupling or checkerboard problem, its discretization process and its solution are, in general, relatively straightforward in comparison with the solution of the mass and momentum equations. However, under specific configurations such as problems with very high local gradients (e.g., release of concentration from point or line sources), the solution of the passive scalar transport equation is a challenging topic. One common method for discretizing the convective and diffusive terms of the passive scalar transport equation, is the second-order central differencing scheme demonstrated by Eq. 3.2. However, for the convective terms, this scheme cannot be used in problems with high local gradient as it encounters unphysical oscillations. Pure upwinding scheme and exponential differencing schemes (based on the cell Peclet number) will not exhibit the unphysical oscillations but are first-order accurate. As a remedy to this problem, a second-order total variation diminishing (TVD) scheme [108] is used for discretizing the scalar transport equation. In the TVD scheme used in this research, the face value of the quantity is first approximated by the simple upwinding approach. The upwinding approach can be demonstrated in the  $x$  direction as

$$\psi_{i+\frac{1}{2},j,k} = \beta\psi_i + (1 - \beta)\psi_{i+1}; \quad \begin{cases} \text{if } (u < 0), & \beta = 1 \\ \text{if } (u \geq 0), & \beta = 0 \end{cases} \quad (3.9)$$

Since the upwinding scheme is only first-order accurate and consequently numerically dissipative, a so-called flux-limiter function is utilized to increase the accuracy to the second order without compromising the stability of the numerical scheme. The flux-limiter function is introduced to the source term of the discretized equation as a deferred correction term and its full description is presented in appendix B. The

compact discretized form of the scalar transport equation can be written as

$$\frac{\delta_1 c}{\delta_1 t} + \frac{\delta_1 \overline{u_j^{-1t}} \overline{c^{1t}}}{\delta_1 x_j} = \alpha \frac{\delta_1}{\delta_1 x_j} \left( \frac{\delta_1 \overline{c^{1t}}}{\delta_1 x_j} \right) . \quad (3.10)$$

In the above equation, velocity is a known value obtained from the solution of mass and momentum equations. Since the velocity is solved based on a staggered grid arrangement, it is already stored at the cell faces of the computational grid used for the scalar transport equation. As a consequence, the convective fluxes can be calculated without the need to any spatial averaging.

## 3.2 Time advancement

In this research, a fully implicit four-level fractional step method of Choi and Moin [109] coupled with a second-order Crank-Nicolson scheme has been used to advance the velocity field over a single time step. Fractional step methods are very popular in solving the unsteady Navier-Stoke equations and different variants of them have been developed (See for example Ferziger and Perić [80]). The fully implicit method allows us to use larger time steps. In comparison with semi-implicit methods, Choi and Moin [109] observed a factor of 5 in saving the CPU time required for DNS of turbulent flow over riblets when using a fully implicit method. However, the disadvantage of implicit methods compared to explicit ones is that a coupled system of linear equations has to be solved at each single time step which makes the use of efficient solvers necessary. The fully implicit fractional step method used in this thesis has been presented as follows:

$$\frac{u_i^* - u_i^n}{\Delta t} + \frac{1}{4} \frac{\partial(u_j^n + u_j^*)(u_i^n + u_i^*)}{\partial x_j} = -\frac{1}{\rho} \frac{\partial p^n}{\partial x_i} + \frac{\nu}{2} \frac{\partial^2(u_i^n + u_i^*)}{\partial x_j \partial x_j} , \quad (3.11)$$

$$\frac{(u_i^{**} - u_i^*)}{\Delta t} = \frac{1}{2\rho} \frac{\partial p^n}{\partial x_i} , \quad (3.12)$$

$$\frac{\partial^2 p^{n+1}}{\partial x_i \partial x_i} = \frac{2\rho}{\Delta t} \frac{\partial u_i^{**}}{\partial x_i} , \quad (3.13)$$

$$\frac{(u_i^{n+1} - u_i^{**})}{\Delta t} = \frac{-1}{2\rho} \frac{\partial p^{n+1}}{\partial x_i} . \quad (3.14)$$

Here,  $u_i^n$  and  $u_i^{n+1}$  are the velocities at the previous and current time steps, respectively,  $u_i^*$  and  $u_i^{**}$  are two intermediate velocity components, and  $p^n$  and  $p^{n+1}$  are the old and new pressures, respectively. In the first step, an intermediate velocity based on the pressure of the previous time step is calculated using an alternative directional implicit (ADI) solver; and then in the second step, it is further modified to a second intermediate velocity by removing half of the old pressure gradient. In the third step, the Poisson equation is solved using a four-level V-cycle multigrid method to obtain the new pressure field. Finally, half of the new pressure gradient is used to update the velocity field.

Once the velocity field is obtained, it is used to update the coefficients of the algebraic form of the scalar transport equation. Similar to the mass and momentum equations, the Crank-Nicolson time advancement scheme is used for the scalar transport equation. Only one step is required to solve the scalar transport equation which is demonstrated in the following semi-discretized (discretized in time and not in space) equation

$$\frac{c^{n+1} - c^n}{\Delta t} + \frac{1}{4} \frac{\partial(u_j^n + u_j^{n+1})(c^n + c^{n+1})}{\partial x_j} = \frac{\alpha}{2} \frac{\partial^2(c^n + c^{n+1})}{\partial x_j \partial x_j} . \quad (3.15)$$

The detailed discretization steps for the mass, momentum and scalar transport equations have been presented in appendix B.

### 3.3 Boundary conditions

Appropriate prescription of boundary conditions is critically important to obtain correct and reliable results from a numerical simulation. Different types of boundary conditions have been used in this research which are explained in the following subsections.

### 3.3.1 Solid wall

Wall boundary condition is one of the fundamental boundary conditions which is always encountered in simulation of wall-bounded flows. If the simulation is based on DNS or wall-resolved LES approaches, no-slip boundary condition has to be used at solid surfaces. With no-slip boundary condition, all the velocity components are explicitly set to zero at all solid surfaces. In DNS, the dynamics of the flow near the solid walls, like other regions of the flow field, are directly resolved. In wall-resolved LES, although the simulation is utilizing the SGS model instead of directly resolving the small scales of the flow, the near wall dynamics still has to be directly resolved. This is because SGS models are inoperative in regions close to the solid walls and can no longer provide a reduction of degrees of freedom while ensuring a proper representation of flow driving mechanisms, turbulence production and the consequent backward energy scatter near the solid walls [110].

In order to resolve the near wall dynamics, typically, the non-dimensional distance off the solid surface should be kept less than one which is computationally expensive for practical engineering problems at high Reynolds numbers. Based on an estimation of Chapman [111], the number of grid points ( $N$ ) required for conducting a wall-resolved LES of a flat-plate boundary layer is proportional to  $Re_{L_x}^{1.8}$ , while the wall-modeled LES requirement is much less demanding ( $N \propto Re_{L_x}^{0.4}$ ). Chapman's estimation was revisited by Choi and Moin [112] for a high Reynolds number boundary-layer flow. In another estimation of the resolution requirement for wall-resolved LES [113], it was estimated that the number of grid points required to conduct a wall-resolved LES on a clean wing at moderate Reynolds number is approximately  $10^{11}$ , which is a massive number regarding the current computational technology. This illustrates that conducting a wall-resolved LES will become prohibitively expensive when dealing with high Reynolds number flows. Thus, wall modeling can be considered as an affordable solution to emulate the near-wall dynamics.

### 3.3.1.1 Wall modeling

In wall modeling, the so-called wall model is used to mimic the near-wall dynamics instead of directly resolving them. Several attempts have been done during the past decades to optimally model the wall layer effects (see reviews by Cabot and Moin [114], Piomelli and Balaras [74], Piomelli [115, 116] and Spalart [117]).

There are two major approaches to model the near wall effects in LES. The first approach considers a sublayer near the solid boundary over which the RANS equations are solved to obtain an effective kinematic viscosity ( $\nu_{eff}$ ). This RANS-based  $\nu_{eff}$  is then used as the kinematic viscosity for the first node of the LES zone over which filtered Navier-Stokes equations are solved. Hybrid RANS/LES and detached-eddy simulation (DES) fall into this category. DES was first proposed by Spalart [118] and has been attracted much attention since then. Many researchers have conducted DES and hybrid RANS/LES for different applications such as turbulent flow in a cavity [119], over a hydrofoil [120] and past a circular cylinder [121]. Despite of all the advantages of DES, it has its own problems. One of the main disadvantages of DES and hybrid RANS/LES is the logarithmic mismatch [117, 122] which is caused due to an artificial buffer layer formed above the RANS zone and generally leads to underprediction of the wall shear stress [123].

The second approach for modeling the near wall effects directly deals with the wall stress and calculates the wall stress based on a simplified version of the momentum equation. This group of models shall be referred as wall-stress models. Many versions of wall-stress models are based on the assumption that the wall-parallel velocity component obeys the log law, from which the wall stress can be estimated. The log law of the wall, valid for attached zero-pressure-gradient boundary layers, expresses the non-dimensional velocity near the solid surface as

$$u^+ = \frac{1}{\kappa} \ln(y^+) + B \quad , \quad (3.16)$$

in which  $u^+ \stackrel{\text{def}}{=} \frac{u}{u_\tau}$  and  $y^+ \stackrel{\text{def}}{=} \frac{y}{\nu/u_\tau}$  are the non-dimensional velocity and wall

coordinate, respectively, with  $u_\tau$  as the friction velocity and  $\nu$  as the kinematic viscosity of the fluid.  $\kappa$  is called the Kármán constant,  $\kappa \approx 0.4$ , and  $B$  is the log law intercept,  $B \approx 5.0$  [114]. As one of the first attempts for considering the lag law in modeling the near wall dynamics, Deardorff [124], in his turbulent plane channel flow simulation, considered the following equations for the second velocity derivatives at the first node off the wall

$$\frac{\partial^2 \bar{u}}{\partial y^2} = -\frac{1}{\kappa} \frac{4}{\Delta y^2} + \frac{\partial^2 \bar{u}}{\partial z^2} \quad , \quad (3.17)$$

$$\frac{\partial^2 \bar{w}}{\partial y^2} = \frac{\partial^2 \bar{w}}{\partial x^2} \quad , \quad (3.18)$$

where  $x$ ,  $y$  and  $z$  are the streamwise, wall normal and spanwise directions, respectively, and  $u$ ,  $v$  and  $w$  are their corresponding velocity components. An overbar denotes the filtered (or large-scale) quantity. The results obtained from Deardorff's simulation did not match very well with previously reported experimental data of Laufer [125] due to lack of enough resolution [74], which was a consequence of computational restriction of his time. Schumann [126] proposed a wall model for plane channel flow simulation in which he assumed that the mean velocity field obeyed the log law and the longitudinal velocity component was in phase with the instantaneous wall shear stress. When the value of the mean wall shear stress  $\langle \tau_w \rangle$  is known *a priori* from the nominal pressure gradient, the following conditions is obtained for the first node off the wall

$$\tau_{w1}(x, z) = \frac{\bar{u}(x, \Delta y, z)}{\langle \bar{u}(x, \Delta y, z) \rangle} \langle \tau_w \rangle \quad , \quad (3.19)$$

$$\bar{v}(x, 0, z) = 0 \quad , \quad (3.20)$$

$$\tau_{w3}(x, z) = \frac{2}{Re_\tau} \left( \frac{\bar{w}(x, \Delta y, z)}{\Delta y} \right) \quad , \quad (3.21)$$

in which  $\Delta y$  is the height of the first node off the wall,  $\langle \cdot \rangle$  represents the averaged quantity in the plane parallel to the wall and  $\tau_{w1}$  and  $\tau_{w3}$  are the streamwise and spanwise components of the wall shear stress. Equation 3.19 assumes that the streamwise velocity component at the first grid point is in phase with the

instantaneous wall shear stress and equation 3.20 stands for the impermeability condition. Equation 3.21 requires the value of the pressure gradient *a priori* for specifying  $Re_\tau$ . The results reported by Schumann showed good agreement with the experimental data and was the first practical proof of the feasibility of wall-modeled LES [74]. However, the Schumann's model was only applicable for pressure driven flows in channels and annuli in which the mean wall shear stress was known *a priori*. Various modifications were proposed based on the Schumann's model to remove the limitation of knowing the pressure gradient *a priori* (e.g., Rajagopalan and Antonia [127] and Grötzbach [128]).

Mason and Callen [72] proposed the following approximate boundary condition for rough surfaces

$$\bar{u}(x, \Delta y, z) = \cos \theta [u_\tau(x, z)/k] \ln(1 + \Delta y/y_0) \quad , \quad (3.22)$$

$$\bar{v}(x, 0, z) = 0 \quad , \quad (3.23)$$

$$\bar{w}(x, \Delta y, z) = \sin \theta [u_\tau(x, z)/\kappa] \ln(1 + \Delta y/y_0) \quad , \quad (3.24)$$

in which the  $y_0$  is the roughness height,  $\Delta y$  is the height of the first grid point off the wall and  $\theta$  is the angle between the wall shear stress and the streamwise direction. It is assumed in the above model that the averaged and friction velocities are proportional. As another approximate wall boundary condition based on Schuman's model, the so-called ejection model was proposed by Piomelli *et al.* [73] for plane channel flow with and without transpiration. This model was based on the observation that the wall shear stress was significantly influenced by the high speed fluid motion toward and away from the solid wall during sweep-ejection events, and could improve the accuracy of the predicted wall shear stress. Balaras *et al.* [77] also tested the model of Piomelli *et al.* [73] for plane channel flows at high Reynolds numbers and demonstrated good agreement between the wall-modeled LES results and the experimental and DNS data.

The wall-stress models reviewed above, are based on the validity of log law in

the near wall region. In a more general approach, one can solve a simplified set of Navier-Stokes equations to obtain the wall shear stress. One of the commonly used approaches is to solve the thin boundary layer equations (TBLE) in the near wall region. TBLE, given in equation 3.25, are the simplified version of Navier-Stokes equations neglecting the wall-parallel viscous diffusion terms and fixing the pressure gradient to the outer flow value (based on the assumption of zero-pressure-gradient across the thin boundary layer). For a flat-plate boundary layer, the TBLE, for the streamwise and spanwise velocity components, take the following form [114]

$$\frac{\partial \bar{u}_i}{\partial t} + \frac{\partial \bar{u}_i \bar{u}_j}{\partial x_j} + \frac{\partial P}{\partial x_i} = \frac{\partial}{\partial y} \left[ (\nu + \nu_t) \frac{\partial \bar{u}_i}{\partial y} \right] \quad , \quad (3.25)$$

where  $\bar{u}_i$  is the velocity,  $P$  is the near wall pressure taken from the outer flow (LES solution) and  $\nu_t$  is the turbulent eddy viscosity. For calculating the  $\nu_t$ , one can use the simple mixing length model as

$$\nu_t = \kappa y u_\tau D^2, \quad D = 1 - \exp(-y^+/A^+) \quad , \quad (3.26)$$

where  $\kappa$  is the Kármán constant,  $u_\tau$  is the friction velocity,  $y^+$  is the non-dimensional normal distance from the wall, and  $A^+$  is the van Driest constant. Different values of  $A^+$  are proposed by different researchers ranging from 17 to 25. Several researchers have used TBLE in the near wall region as the wall model for LES [129–131] and obtained improved results for both attached and separated flows. For solving TBLE, no slip boundary condition is assumed at solid walls and the velocity taken from the outer LES solution is used as the boundary condition at the interface between the TBLE and LES regions. As pointed out by Cabot and Moin [114], unsteady boundary-layer equations are approximately half as expensive to solve as the full Navier-Stokes equations for the same number of grid points. In order to reduce the computational costs of TBLE models, some of the terms of the equation 3.25 can be neglected to build simpler models. If the left-hand side of the equation 3.25 is set to zero, a simplified model, the so-called stress-balance model [114], is obtained which only considers the viscous and turbulent diffusion terms. In that case, the

equation becomes an ordinary differential equation (ODE) in the form of an initial value problem assuming zero velocity at the solid wall. The stress-balance model can be written as

$$\frac{d}{dy} \left[ (\nu + \nu_t) \frac{du_{||}}{dy} \right] = 0 \quad , \quad (3.27)$$

in which  $u_{||}$  is the wall-parallel velocity component. Combining equation 3.26 and 3.27 will result in the following equation

$$u^+ = \int_0^{y^+} \frac{2dy^+}{1 + \sqrt{1 + 4\kappa^2 y^{+2} (1 - e^{-\frac{y^+}{A^+}})^2}} \quad , \quad (3.28)$$

which is an ordinary differential equation and can be easily solved using robust numerical methods such as Runge-Kutta method. Kawai and Larsson [76, 123, 132, 133] applied the stress-balance model with some conceptual modifications on a compressible turbulent boundary layer over a zero-pressure-gradient flat plate. They stated that the wall model did not necessarily need to be applied between the first grid point and the solid wall. Thus, the proper height for the wall model should be dynamically chosen based on the flow physics, and the grid resolution below this height should be refined until the numerical errors are small enough. This approach was reported to result in an improvement of the prediction of skin friction coefficient by 15% for an attached turbulent boundary layer.

Although different forms of stress-balance models look very attractive (since they can be easily implemented and are computationally inexpensive), they are not valid for flows with separation or large pressure gradients. Another approximation of the TBLE can be obtained by only considering the pressure gradient term on the left-hand side of the equation 3.25. In this case, as proposed by Wang [134] and Wang and Moin [75], the following analytical solution can be obtained for the wall shear stress

$$\tau_{wi} = \mu \frac{\partial \bar{u}_i}{\partial x_n} \Big|_{x_n=0} = \frac{\rho}{\int_0^\delta \frac{dx_n}{\nu + \nu_t}} \left( \bar{u}_{i\delta} - \frac{1}{\rho} \frac{\partial \bar{p}}{\partial x_i} \int_0^\delta \frac{x_n dx_n}{\nu + \nu_t} \right) \quad , \quad (3.29)$$

in which  $\delta$  is the height of the first grid point off the wall,  $n$  denotes the wall-normal direction,  $\bar{u}_{i\delta}$  is the wall-parallel velocity component at the height  $\delta$  taken from the

outer LES solution, and  $\nu_t$  is the turbulent eddy viscosity which can be obtained from the mixing length model given in equation 3.26. Wang [134] and Wang and Moin [75] applied the stress-balance model with and without the pressure gradient term for turbulent flow over an asymmetric airfoil with strong streamwise pressure gradient and unsteady flow separation. They showed that including the pressure gradient term will improve the results of wall-modeled LES for the separated region and a better agreement with the experimental result could be obtained. Chen *et al.* [135] applied the stress-balance model with the pressure gradient and the time derivative term into the simulation of turbulent plane channel flow at high Reynolds numbers (up to  $Re_\tau = 20,000$ ) and could obtain satisfactory results for the mean velocities and Reynolds stress components even on coarse grids.

Nicoud *et al.* [136] proposed a wall model based on optimal control theory to overcome the numerical and subgrid modeling errors in the unresolved near wall region for attached turbulent flows at high Reynolds numbers. In their approach, the LES solution from the outer layer is forced to a desired value using the nominal wall stress as the controlling parameter. Shih *et al.* [137] proposed a wall model based on the combination of the log law and pressure scaling law of Tennekes and Lumley [138] and reported a universal functionality of their model for both attached and separated flows.

In this research, we deal with turbulent flows over wall-mounted obstacles which naturally include high pressure gradients and flow separations. Also, since the Reynolds number of our test cases are typically high, the computational cost of the wall model is critically important and can have a great influence of the overall computational efficiency of simulations. In view of this, the wall model proposed by Wang and Moin [75, 134] (equation 3.29) has been chosen to be used in our wall-modeled LES studies.

### 3.3.2 Inflow

The importance of the inlet boundary condition and its influence on the accuracy of turbulent flow statistics have been numerically and experimentally studied by many researchers for different flow configurations (e.g., zero-pressure-gradient flat plate boundary layer [139], round-jet flow [140], turbulent shear-layer mixing [141] and turbulent flow over a single and an array of wall-mounted obstacles [91, 142]) and is still an open subject in the field of numerical simulation of turbulent flows. In fact, prescribing a proper inflow condition at the inlet boundary of the computational domain is a practical challenge for DNS and LES of turbulent flows. Since the exact time-dependent flow condition is not fully known at the inlet boundary, the boundary condition should be applied in such a way that ensures the most realistic statistical representation of the real turbulent flow. Several methods have been introduced to provide realistic inflow condition for DNS and LES of turbulent flows (see the review by Tabor and Baba-Ahmadi [143]) which will fall into one of these major categories: (1) imposing synthesized turbulence at the inlet boundary, also known as stochastic reconstruction from one-point statistics, and, (2) deterministic computation which is based on the use of a separate solution of Navier-Stokes equations at the inlet boundary. These two approaches are reviewed in the following subsections.

#### 3.3.2.1 Synthetic turbulence

In this approach, a synthesized fluctuating field is generated based on the known first- and second-order statistical properties of the turbulent flow field. Lee *et al.* [144] developed a method for generating stochastic inflow condition with a prescribed power spectrum. In their approach, the flow was assumed to be spatially developing in the streamwise direction and homogeneous in other directions. They could obtain turbulence statistics in good agreement with the experimental measurement data for isotropic decaying turbulent flow. Lee *et al.* [145], in a DNS of turbulent flow over a backward facing step, also applied the method of Lee *et al.* [144] where the flow was not homogeneous in the vertical direction. Li and Wang [146] used

a spectral line processor to generate inflow condition for a free-surface channel flow. They considered a target energy spectra obtained from previously measured experimental data and constructed the random field such that it could reproduce the target energy spectra at the inlet plane. Smirnov *et al.* [147] proposed a method for random flow generation in which synthesized divergence-free vector field was generated based on Fourier harmonics. Their method was also applicable to non-homogeneous anisotropic flows and could satisfy the continuity equation. Hanna *et al.* [68] employed the Monte-Carlo method to generate time-correlated random fluctuations to be superimposed onto a mean power-law profile to simulate a neutrally stratified atmospheric boundary layer. In their approach, time correlation was achieved through a simple exponential autocorrelation function. Klein *et al.* [148] introduced the concept of using a digital filter to generate artificial velocity field which could be prescribed as the inflow condition. In their approach, they were able to specify the second-order one-point statistics (Reynolds stress components) as well as the autocorrelation functions. This method received much attention through the turbulence modeling community and some similar procedures have been recommended based on digital filter concepts (see works by di Mare *et al.* [149], Veloudis *et al.* [150] and Xie and Castro *et al.* [151]). Glaze and Frankel [152] proposed a version of the so-called weighted amplitude wave superposition method to generate stochastic inlet condition for a fully-developed jet flow. They compared the performance of their proposed method with that of Gaussian random forcing and reported that their method was able to reproduce the self-sustaining inlet turbulence while Gaussian random inlet fluctuations dissipated immediately. Sandham *et al.* [153] introduced a semi-stochastic method in which known dynamical features of the inner and outer regions of a boundary layer were reproduced to generate a fully-developed turbulent boundary layer within a short distance from the inlet boundary. They could obtain good agreement with the previously reported DNS results for turbulent boundary layers over flat plates. Druault *et al.* [154,155] prescribed the inflow condition for LES of turbulent flows based on interpolation and extrapolation of measured experimental data on a limited number of measuring points. Their reconstruction method was based

on linear stochastic estimation (LSE) combined with proper orthogonal decomposition (POD) to estimate the coherent structures of the velocity field based on two-point correlations and time histories obtained from the experimental. They applied this method for a plane turbulent mixing layer and showed its superiority over using simple random fluctuating field in predicting the streamwise evolution of Reynolds stress components.

### 3.3.2.2 Deterministic computation

The first approach for prescribing inflow condition discussed in the previous subsection has some disadvantages. One major problem is that the generated fluctuation field is not based on physical flow characteristics and does not satisfy the fluid flow governing equations which can potentially introduce a new source of errors to the simulation. As reported by Keating *et al.* [156] who conducted *a priori* and *a posteriori* tests on different inflow conditions for LES, it takes a relatively long distance for spatial development of the inlet fluctuations until the flow can damp out the errors (while remaining perturbed) and become physically realistic. As an example, this distance was approximately 10 step-heights in a DNS of flow over a backward facing step reported by Le *et al.* [145]. One of the remedies towards minimizing the mentioned errors is to conduct a separate simulation (the so-called precursor simulation) for generating realistic and physical inlet conditions. This procedure can almost completely eliminate the errors associated with using unphysical random numbers for generating inflow turbulence [110]. However, conducting a separate simulation may drastically increase the total cost of the simulation. This is considered as the only major drawback of using a precursor simulation for prescribing inlet boundary condition.

Several researchers have used this strategy to produce proper inlet boundary conditions for their turbulent flow simulations. Na and Moin [157] conducted DNS of a detached turbulent boundary layer over a flat plate and used an existing DNS data of a frozen field [158] for their inflow condition. They randomized the amplitude of the

existing DNS fluctuating field while kept its phase angle constant and superimposed it at the inlet boundary of the main simulation. Lund *et al.* [159] extracted instantaneous velocity fields from an auxiliary simulation of a zero-pressure-gradient boundary layer and used them as the inflow condition for a spatially developing boundary layer. The auxiliary simulation also needed prescribing a separate inlet boundary condition which was obtained by rescaling a plane of instantaneous flow field at the rear region of the domain and re-introducing that plane to the inlet boundary. Ferrante and Elghobashi [160] used a modified version of Lund’s method in which they imposed a targeted energy spectra on the plane of the instantaneous flow field extracted from the the auxiliary simulation before rescaling and re-introducing that plane to the inlet boundary. With this approach, they could produce sustained TKE production in near-wall regions. Schlüter *et al.* [161] used an unsteady RANS solver to generate inflow condition for the LES of a confined jet in an axisymmetric expansion with and without swirling. They rescaled the generated data set to account for the desired turbulence statistics and could obtain good agreement between numerical results and previously reported experimental measurement data. Wu and Moin [162, 163] conducted DNS of turbulent boundary layer over a zero-pressure-gradient flat plate with and without surface heat transfer. For the inlet boundary condition, they introduced patches of isotropic decaying turbulence to trigger the boundary layer and accelerate the transition. The isotropic decaying turbulence had been generated *a priori* using a separate simulation in which the desired energy spectra was set as the initial condition and simulation was stopped at the required turbulence intensity. Saeedi and Wang [91] conducted LES over an array of wall-mounted cubes submerged in a simulated neutrally stratified atmospheric boundary layer. They tested several inlet boundary conditions (including the use of a precursor simulation) to generate the high turbulence level of the approaching flow. However, since the approaching flow had a very high turbulence level, the conventional methods were not able to generate the desired level of sustainable turbulence. Thus, they proposed a method of generating inlet turbulence which was based on mounting a solid grid close to the inlet boundary, to trigger the flow instability, and superimposing

random fluctuations in regions above the wall-mounted obstacles. In this approach, physical flow perturbations could be obtained at the inlet boundary and the instability level could be increased in desired regions based on artificial energy injection.

In the current research, depending on the required level of inlet turbulence, the method of Hanna *et al.* [68], based on superimposing time-correlated random fluctuations on the inlet velocity profile, and the method of Saeedi and Wang [91], based on mounting a solid grid close to the inlet boundary, have been used to produce the desired level of inlet turbulence.

### 3.3.3 Outflow

If the outlet boundary has been placed sufficiently far from any source of perturbations in the flow domain, it can be assumed that the flow has reached the fully-developed state at the outlet boundary. For turbulent flow over a group of wall-mounted obstacles, the flow instabilities, separated boundary layers and vortex shedding induced from the last row of obstacles should be significantly decayed before the flow reaches the outlet boundary. In that case, the zero-gradient boundary condition (known as Neumann boundary condition) can be prescribed for the outlet boundary. In the Neumann boundary condition, the derivative of the flow properties with respect to the streamwise direction (or perpendicular to the outlet boundary) is set to zero as

$$\frac{\partial \phi}{\partial x} = 0 \quad , \quad (3.30)$$

in which the  $\phi$  is the flow property (e.g., different velocity components) and  $x$  is the streamwise direction normal to the outlet boundary.

### 3.3.4 Periodic boundary condition

If the flow is homogeneous in a specific direction, turbulence statistics are unchanged under any translation in that direction. As an example, turbulent plane channel flow is homogeneous in the streamwise and spanwise directions. In such cases, if the

flow domain is large enough to account for the largest turbulent structures and eddies, periodic boundary condition can be applied to the domain boundaries in homogeneous directions. For turbulent flows over a single or a group of wall-mounted obstacles, if the flow domain has a repeating pattern or domain boundaries are sufficiently far from the wall-mounted obstacles, periodic boundary condition can be used at the domain boundaries. The periodic boundary condition for a typical flow property can be expressed as

$$\phi_{k_{min}-1} = \phi_{k_{max}}, \quad \phi_{k_{min}} = \phi_{k_{max}+1} \quad , \quad (3.31)$$

in which  $\phi$  is the flow property and  $k$  is the grid-point index in the periodic direction. It should be noted that indices  $k_{min} - 1$  and  $k_{max} + 1$  refer to fictitious grid points outside the real flow domain.

### 3.3.5 Slip boundary condition

This type of boundary condition is usually used to describe the free-surface flow conditions such as open channels and canals. Thus, in cases such as free-surface water channel, the interface boundary between the water and the surrounding air can be described by slip boundary condition. In that case, the velocity component perpendicular to the boundary is set to zero to maintain the impermeability condition while for other velocity components, the normal gradient are set to zero as

$$\frac{\partial u}{\partial y} = 0, \quad v = 0, \quad \frac{\partial w}{\partial y} = 0 \quad , \quad (3.32)$$

in which,  $y$  is the normal direction to the slip boundary,  $v$  is the perpendicular velocity component and  $u$  and  $w$  are the velocity components parallel to the slip boundary.

### 3.3.6 Boundary conditions for the scalar transport equation

For the scalar transport equation which describes the concentration field, the value of the scalar field has been set to zero at the inlet boundary. Zero-gradient condition

has been assumed in the spanwise, upper and outlet boundaries of the domain. Zero-flux Neumann condition has been assumed at all the solid surfaces to warrant the no penetration condition.

## 3.4 Parallel computing

Within the past several decades, computational fluid dynamics (CFD) has been one of the most demanding fields of engineering and science which required significant computational power for simulating increasingly complex flows with reliable accuracy. The computational power is crucially important when dealing with three-dimensional simulation of turbulent flows at high Reynold numbers. For such cases, although LES is much more affordable than DNS as discussed in the previous chapter, it still needs a power which is beyond the capability of regular computers. As such, the employment of supercomputers is a necessary part of LES (and obviously DNS) of turbulent flows at high Reynolds numbers.

### 3.4.1 Supercomputers

Modern supercomputers generally achieve their high computational power through synergism of the power of several single computers. Different types of architectures through which the single computers are linked together can be categorized into three main groups: uniform memory access (UMA), non-uniform memory access (NUMA) and no-remote memory access (NORMA). In UMA, all the processors can have equal access to a central shared memory, while in NUMA, each processor has been assigned a local memory. At the same time and upon necessity, they are also able to have access to the non-local memory (shared or other processor's memory) which is slower than the access to their local memory. In NORMA, each processor has its own specific individual memory and the data is only transferred between the processors through explicit communications.

A common type of NORMA architecture is called “cluster” which consists of

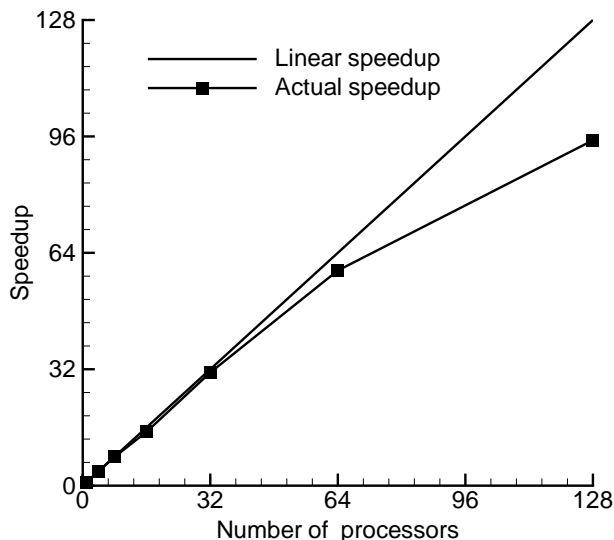


FIGURE 3.1: parallel code scalability based on the execution time required for one single time step.

several individual off-the-shelf computers connected through fast local area networks (LAN). As a rule of thumb, the computational power of single CPUs doubles in every two years as the result of increasing number of transistors stored in a single CPU (known as the Moore’s law). This implies that clusters can take advantage of the super-fast modern CPUs and provide considerable computational power at moderate costs. In the current research research, we take advantage of cluster systems, as high-performance computational tools, to conduct the computations required for numerical simulation of turbulent flows at high Reynolds numbers.

### 3.4.2 Message passing interface

In order to use a supercomputer with parallel computing capability for solving a fluid flow problem, it is required to provide the software background consistent to the architecture of the specific supercomputer. This implies that the main problem should be broken into several sub-problems (the so-called decomposition process) to be solved by each single processor of the supercomputer when using a cluster system. Two common types of decomposition are functional and domain decompositions [164]. In the functional decomposition, which is often used in weather forecasting programs,

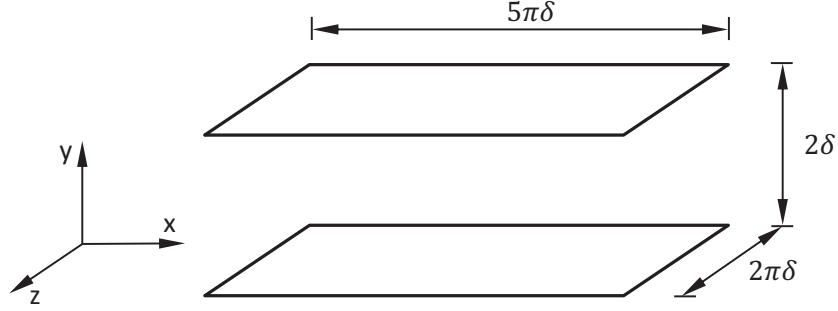


FIGURE 3.2: Schematic of the physical domain of a plane channel.

TABLE 3.1: Details of the domain size and grid resolution for the plane channel flow.

	$Re_\tau = 300$	$Re_\tau = 2000$
$L_x \times L_y \times L_z$	$5\pi\delta \times 2\delta \times 2\pi\delta$	$5\pi\delta \times 2\delta \times 2\pi\delta$
$N_x \times N_y \times N_z$	$160 \times 64 \times 160$	$160 \times 64 \times 160$
$\Delta x^+$	29.4	196.3
$\Delta y^+$	5.4 -11.4	36 -76
$\Delta z^+$	11.8	78.5

each processor is assigned a different type of data operation according to a different model (e.g., atmospheric model, oceanic model and etc.). However, in the domain decomposition approach, processors are assumed to perform similar computations and the physical domain is divided to several sub-domains which are distributed and assigned to different processors.

In the current thesis, the second approach (i.e., domain decomposition) has been selected for decomposition of the problems and the computational code is parallelized using the libraries of Message-passing interface (MPI). MPI is a standard and portable message-passing system whose first version was released in 1994, as MPI-1, by a group of researchers mainly from US and Europe. The MPI libraries are supported by several programming languages including C, C++ and FORTRAN. MPI has been tried to be an optimum design for being expressive, efficient and portable [165]. One of the advantages of MPI over other message-passing libraries is its portability as it has been implemented on many distributed-memory architectures. As a summary, MPI is an attempt to collect the best features of different message-passing systems, improve them where appropriate and standardize them [165].

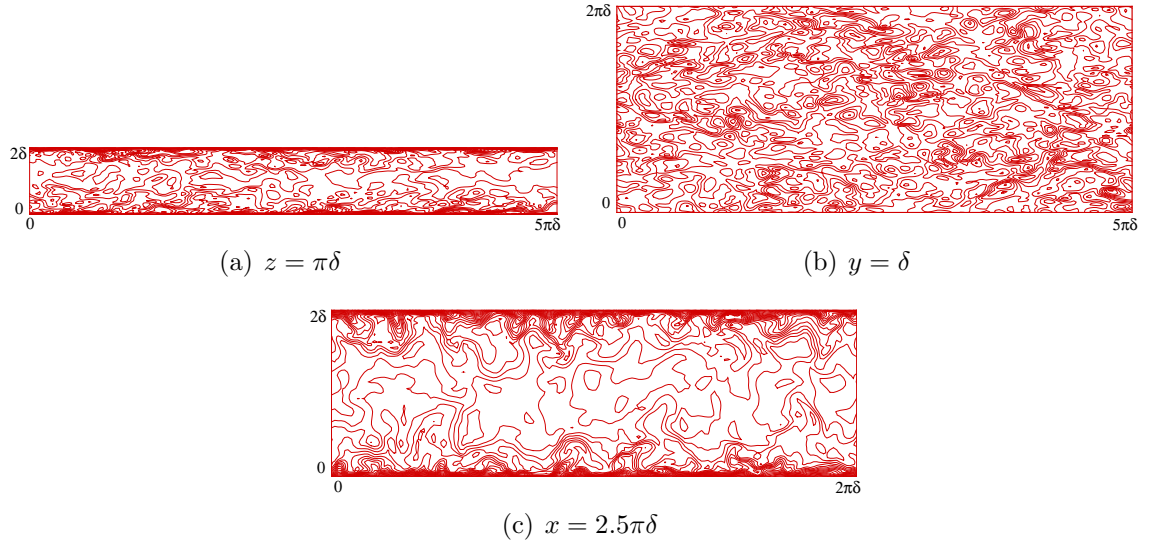


FIGURE 3.3: Isopleths of the streamwise velocity in three typical  $x$ - $y$ ,  $x$ - $z$  and  $y$ - $z$  planes, respectively, at  $Re_\tau = 300$ .

### 3.4.3 Parallel efficiency

The parallel code speedup result can be evaluated using equation  $S = T_1/T_N$ , where  $T_1$  is the execution time of the code on one processor and  $T_N$  is the execution time running on  $N$  processors. In order to measure the parallel efficiency of the code, a plane channel flow at a relatively high grid resolution has been chosen to conduct the tests and measure the scalability of the code. The results of the speedup tests has been shown in Fig. 3.1. The optimal line corresponds to a 1-to-1 speedup. The figure shows that the code scales fairly well (with the tested grid resolution) up to at least 128 processors. The speedup does not exhibit a limiting value or negative slope. If higher grid resolution is chosen (e.g., the cases which have been studied in follow up chapters), higher number of processors can be used for lower execution time. For the grid system of  $160^3$  when using 128 processors, as is evident in Fig. 3.1, the speedup is 94.6 times the nominal execution time using a single processor.

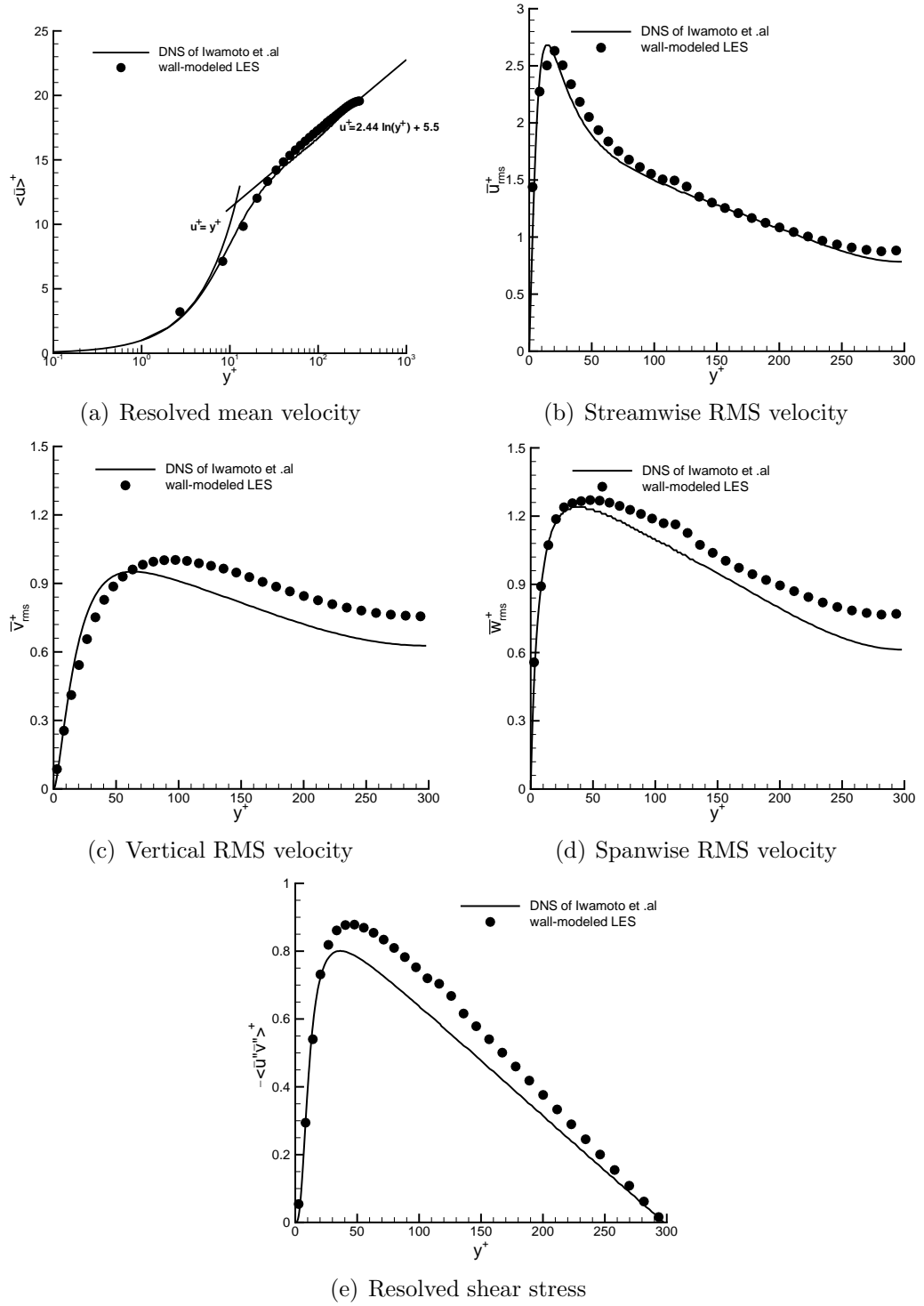


FIGURE 3.4: Comparison of the resolved first- and second-order turbulence statistics obtained from wall-modeled LES with the DNS results at  $Re_\tau = 300$ .

### 3.5 Preliminary tests based on plane channel flow

In this section, a geometrically simple wall-bounded turbulent flow has been chosen as the first benchmark test case to ensure about the performance of the computational code and to conduct some preliminary validation studies. Fully-developed turbulent plane channel flow (turbulent flow between two parallel infinite planes) has been selected as the benchmark test case. There are a vast number of studies conducted by different researchers based on turbulent plane channel flow and a rich knowledge of the physics of turbulent flow in plane channels is available in the literature. Although it has a simple geometry and is homogeneous in two directions, turbulent plane channel flow is a sensitive test case for testing LES codes and accurate prediction of its turbulent statistics is a challenging problem. Figure 3.2 schematically shows the geometry and coordinate system of a plane channel.

The flow is considered to be homogeneous in  $x$  and  $z$  directions and the boundaries in  $y$  direction are supposed to be solid walls. Thus, periodic boundary condition has been considered for the domain boundaries in  $x$  and  $z$  directions and wall boundary condition is assumed for the lower and upper walls. The DSM (equation 2.13 in section 2.2.2) has been used as the SGS stress model and the stress-balance model (equation 3.28) is considered as the wall model. In order to conduct the simulation, a relatively coarse grid ( $160 \times 64 \times 160$  in  $x$ ,  $y$  and  $z$  directions respectively) has been considered for domain discretization. Table 3.1 summarizes the grid data based on wall coordinate system for two Reynolds numbers tested. To conduct an assessment on the accuracy of the numerical simulation, the flow field and the first- and second-order turbulence statistics at Reynolds number  $Re_\tau = 300$  (based on the friction velocity and half channel height) have been presented and compared with the DNS results of Iwamoto *et al.* [166].

Figure 3.3 shows the isopleths of the resolved streamwise velocity extracted from a typical instantaneous snapshot in three perpendicular planes. In these figures, the irregular pattern of the flow structures and the evolution of turbulent patches from wall regions to the central region of the channel are qualitatively observable.

Figure 3.4 compares the first- and second-order turbulence statistics obtained from wall-modeled LES with those of DNS study of Iwamoto *et al.* [166]. As shown in Fig. 3.4a, for the mean streamwise velocity, there is an excellent agreement between the LES and DNS results and they both collapse on the classical law of the wall. This shows that the computational code is functioning properly and its different parts (e.g., discretization, solver, communication, post processing and etc.) have been consistently implemented. With respect to the fact that the LES-predicted values at the first grid point off the wall and also at grid points in the core region of the channel are in very good agreement with the DNS results, it can be concluded that the wall model and the SGS stress model are properly functioning and well implemented into the computational code. In Figs. 3.4b-d, profiles of the non-dimensionalized streamwise, wall-normal and spanwise root-mean-square (RMS) velocities have been presented. As shown in Fig. 3.4b, the resolved streamwise RMS velocity obtained from LES has a very good agreement with the DNS result and the difference between LES and DNS results for the wall-normal and spanwise RMS velocities are less than 10%. Figure 3.4e, presents the profile of the non-dimensionalized resolved Reynolds stress  $-\langle \bar{u}''\bar{v}'' \rangle^+$  and compares it with the Reynolds stress computed by DNS. Good agreement between the LES and DNS results can be observed. The value of the resolved shear stress in the wall region and in the central region of the channel are in very good agreement with the DNS results and the maximum value of the shear stress has been slightly overpredicted by LES. In general, the errors associated with low grid resolution, and the modeling effects are responsible for the difference between the LES and DNS results. It is worth to mention that these differences between LES and DNS results are indeed the costs that should be paid to gain the vast computational savings arising from the coarser grid requirement in LES compared to DNS.

Since there exists an analytical solution for the mean streamwise velocity of the turbulent plane channel flow (the law of the wall), a very high Reynolds number (i.e.,  $Re_\tau = 2,000$ ) has been also simulated to test and compare the resolved mean streamwise velocity profile against the analytical solution. The same domain configuration used for the previous case at  $Re_\tau = 300$  is used for  $Re_\tau = 2,000$ ,

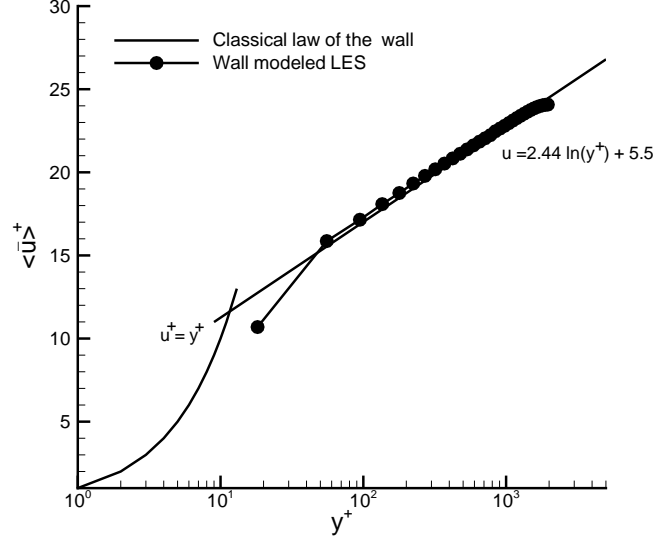


FIGURE 3.5: Resolved mean streamwise velocity at  $Re_\tau = 2,000$ .

while corresponding driving force (pressure gradient) has been adjusted to achieve the desired Reynolds number. This, in turn, means that a much lower grid resolution is used for the higher Reynolds number. The details of the grid resolution are given in table 3.1. Figure 3.5 presents the non-dimensionalized resolved mean streamwise velocity ( $\langle \bar{u} \rangle^+$ ) obtained from wall-modeled LES and compares it with the standard law of the wall. As is evident in Fig. 3.5, the profile of the resolved mean streamwise velocity has a very good agreement with the standard law of the wall at the high Reynolds number  $Re_\tau = 2,000$ . The value of  $\langle \bar{u} \rangle^+$  at the first node agrees well with the blended linear-log law profile and the value of  $\langle \bar{u} \rangle^+$  at the next grid-points fully collapse on the log-law line.

It should be noted that the purpose of this section and the presented results was not to thoroughly investigate the physics associated with turbulent plane channel flow and only preliminary assessment of the computational code was intended. Thus, with the numerical tests conducted on the turbulent channel flow at two Reynolds numbers, the general performance of our in-house code in simulating turbulent flows has been confirmed. In the next chapters, more rigorous tests will be conducted in the context of more geometrically complex flow domains and the results will be compared against the available wind-tunnel and water-channel measurement data.

## Chapter 4

# Wall-resolved LES of turbulent wake behind a surface-mounted square cylinder

Wall-resolved LES of turbulent flow and structures dynamically evolving around a square cylinder represents an interesting and challenging topic in computational fluid dynamics. Owing to the need to resolve fine-scale viscous motions in the vicinity of solid surfaces and to precisely calculate the dynamic interactions between the tip and Kármán vortices, the computational cost involved in a wall-resolved LES procedure is typically demanding which makes the use of parallel processing necessary. As the aspect ratio of the square cylinder increases, the vortical motions of the flow become more energetic and complex, which demands a significant increase in the size of the computational domain in order to properly capture the temporal and spatial evolution of all energy containing eddies.

The current chapter aims at investigating the turbulent wake behind a wall-mounted square cylinder with  $AR = 4$  using wall-resolved LES. In comparison with the classical cube flow case (for  $AR = 1$ ) of Yakhot *et al.* [45, 46], the relatively high aspect ratio ( $AR = 4$ ) of the cylinder in the current test case based on the recent wind-tunnel experiments of Bourgeois *et al.* [17, 18] and Sattari *et al.* [19] results in more energetic vortex motions and interactions, which further imposes a greater challenge to numerical simulations to capture properly eddy motions of all relevant scales with a much larger computational domain. This test case has been identified non-trivial in term of computational efforts and used as one of two “challenge cases” in two

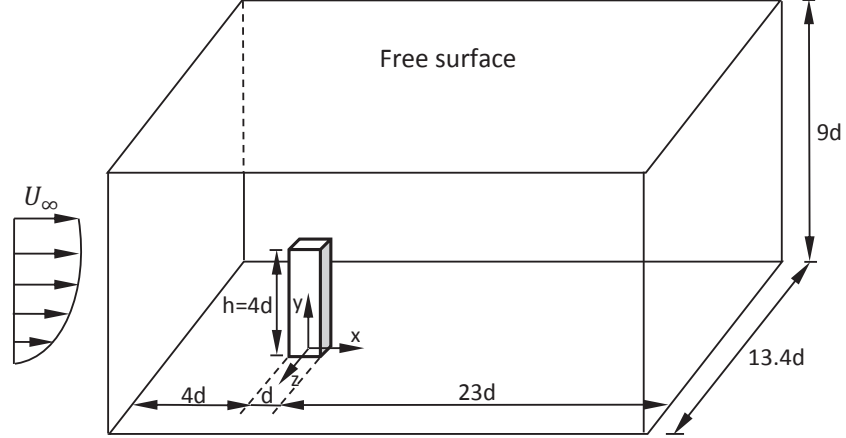


FIGURE 4.1: Schematic of the computational domain and coordinate system for the wall-mounted square cylinder flow.

consecutive Annual Conferences of the CFD Society of Canada hosted in Canmore, Alberta in 2012, and in Sherbrooke, Quebec in 2013.

## 4.1 Test case and computational domain

The test case for current LES is based on an experiment recently conducted by Bourgeois *et al.* [17,18] and Sattari *et al.* [19] in a boundary-layer wind tunnel. In their experiment, a free-stream flow with velocity of  $U_\infty = 15 \text{ m/s}$  and 0.8% turbulence intensity struck the sharp leading edge of a flat plate on which the obstacle was mounted. The obstacle had a square cross-section with a side length of  $d = 0.0127 \text{ m}$  and height of  $h = 4d$ . The Reynolds number based on the free-stream velocity and obstacle side length was 12,000. The obstacle was located  $4h$  downstream of the flat plate leading edge such that it was partially submerged in a thin boundary layer. The boundary-layer thickness at the obstacle location was approximately  $0.18h$  on a similar flat-plate with no obstacle. The aspect ratio for the square cylinder was  $AR = 4$ , which is significantly larger than that of the classical cube flow case (for  $AR = 1$ ) tested by Rodi [52], Shah and Ferziger [57] and Yakhot *et al.* [45,46]. Owing to the relatively high  $AR$  value and high Reynolds number tested, the interaction between the flow and the cylinder becomes very intense. As a result, energetic tip

and Kármán vortices are generated from the top and two sides of the cylinder, which dynamically evolve and highly interact with each other in the downstream region of the cylinder.

In order to conduct our LES, the energetic motions and flow structures have to be directly resolved. This requirement dictates the dimension of the domain to be large enough to include the largest eddies of the flow (which is of the order of the obstacle size in this case). Therefore, a relatively large computational domain is chosen for conducting the simulation. The schematic of the domain, surface-mounted cylinder and coordinate system are shown in Fig. 4.1. The obstacle is located along the central line of the domain,  $6.2d$  away from each side boundary in the spanwise direction,  $5d$  below the free surface of the flow in the vertical direction,  $4d$  downstream of the inlet and  $23d$  upstream of the outlet. It should be noted that the outlet boundary should be sufficiently far from the obstacle to avoid any interference on the result in the wake region. In the classical work of Shah and Ferziger [57] and Yakhot *et al.* [45, 46] on a single wall-mounted cube, the outlet was placed  $7d$  and  $10d$  downstream of the cylinder, respectively. However, in their parametric study of a 2-D of cylinder, Sohankar *et al.* [167] indicated that the outlet should be placed at least  $20d$  from the obstacle when Neumann boundary condition is used in the simulation.

Since in our simulation the distance between the obstacle and the inflow boundary is set to  $4d$ , the inflow boundary condition needs to be carefully treated in order to reproduce the exact boundary-layer thickness at the obstacle location (i.e.,  $0.18h$  at the location  $4d$  downstream of the inlet) observed during the experiments [17–19]. In view of this, the inlet turbulent velocity profile is approximated using a power law at the inlet boundary to generate the desired boundary-layer thickness, viz.

$$\begin{cases} \text{if } y < 0.15h, & \langle \bar{u} \rangle = U_\infty \left( \frac{y}{0.15h} \right)^{0.16}, \\ \text{if } y \geq 0.15h, & \langle \bar{u} \rangle = U_\infty \quad , \end{cases} \quad (4.1)$$

where  $y$  is the vertical distance from the ground and  $U_\infty = 15 \text{ m/s}$  is the free-stream velocity. This inlet condition ensures that the boundary-layer thickness is  $0.18h$  at the

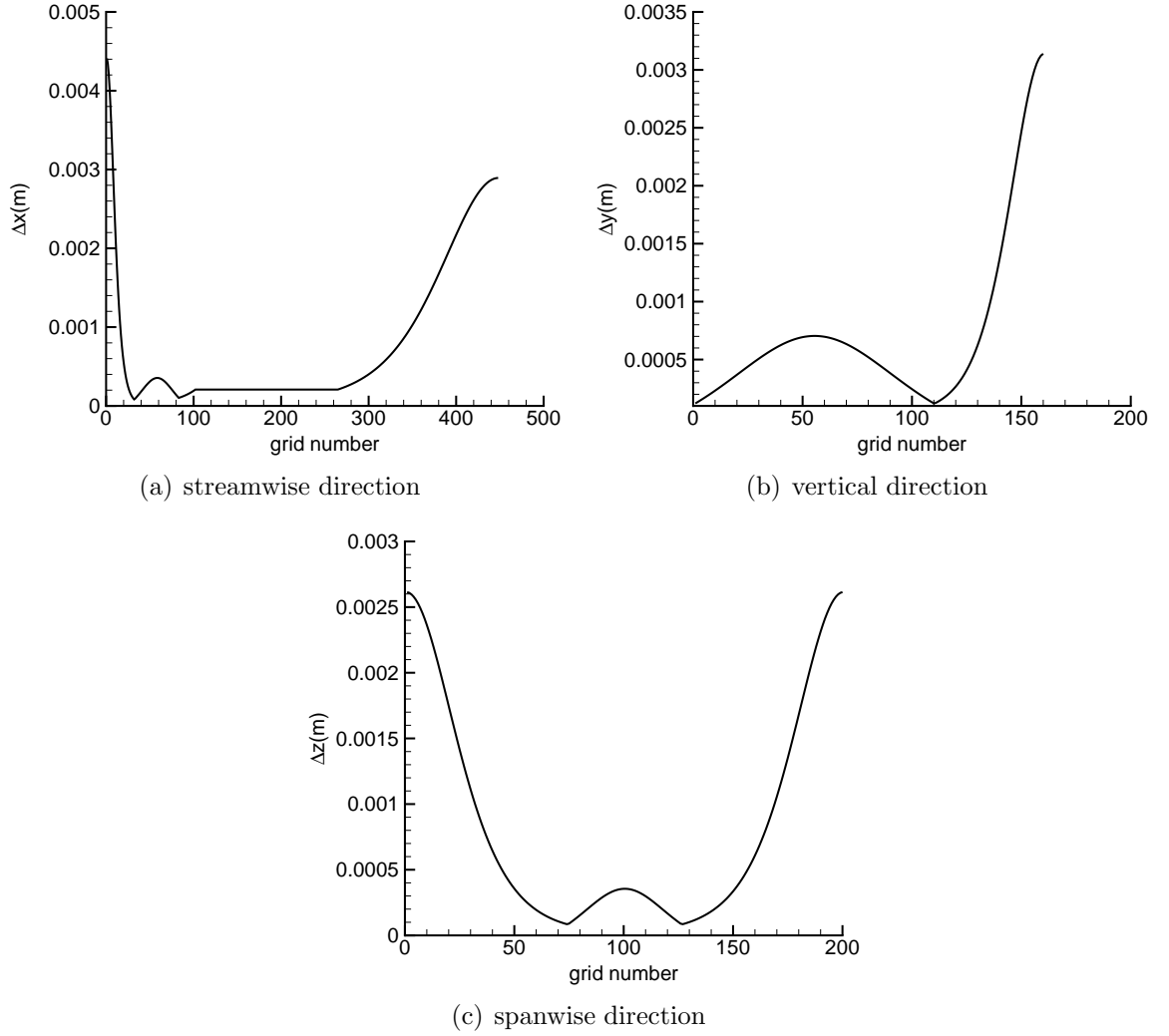


FIGURE 4.2: Grid distribution in streamwise, vertical and spanwise directions.

obstacle location to match the measured value. In order to synthesize the turbulence intensity level (0.8%) of the approaching flow in the experiment, time-correlated random fluctuations with zero mean, standard deviation of one and magnitude of 0.8% of the local mean velocity have been superimposed onto the inlet velocity profile (for all three components) following the method of Hanna *et al.* [68] and Shi *et al.* [69]. At the outlet and free surface, zero-gradient boundary condition is applied. Periodic boundary conditions are applied to the side boundaries in the spanwise direction. No-slip boundary condition is applied to all solid surfaces of the square cylinder and bottom plate.

The dynamic Smagorinsky model (DSM) of Lilly [93] and Germano *et al.* [94] (equation 2.13 in section 2.2.2) has been used as the subgrid-scale model to close the system of filtered mass and momentum equations. The computational domain was discretized using 14.3 million computational cells ( $448 \times 160 \times 200$  in  $x$ ,  $y$  and  $z$  directions, respectively). In order to perform parallel computing, the computational domain was divided into  $4 \times 5 \times 5$  sub-domains (in  $x$ ,  $y$  and  $z$  directions, respectively). Correspondingly, 100 processors were used to solve the flow field at each time step. All the computations were performed using the computer cluster based on Intel Xeon X5650 2.66 GHz chip technology. The total computing time spent on solving the flow field and collecting the statistics was over 40,000 CPU-hours. Before the flow statistics are collected, it is important to ensure that the flow has reached a statistically stationary state. In our simulation, the code was first run for approximately 3 flow-through times (the time required for the mean flow to travel from the obstacle location to the outlet plane) to allow the flow field to fully evolve to a statistically stationary state. Then the flow statistics were collected through a course of approximately 5.5 flow-through times. During the simulation, the time step was  $1 \times 10^{-6}$  s and the maximum CFL number was approximately 0.26. The convergence criterion for the solution of governing equations was set to  $1 \times 10^{-6}$  for the maximum difference in each velocity component (normalized by the spatially-averaged value of the same velocity component obtained in the previous time step).

Figures 4.2a-4.2c show the grid distribution in the streamwise, vertical and spanwise directions, respectively. As the distance from the wall increases, the grid size is stretched gradually with a stretching rate kept less than 10%. A slow growth rate of the grid size is required in general in order to maintain a global second-order truncation error in non-uniform grid systems [168]. To effectively resolve the anisotropic and small-scale flow motions near solid surfaces, the wall coordinate value for the first node off all the solid surfaces has been kept less than one (specifically, 0.80, 0.59 and 0.51 for  $\Delta x^+$ ,  $\Delta y^+$  and  $\Delta z^+$ , respectively).

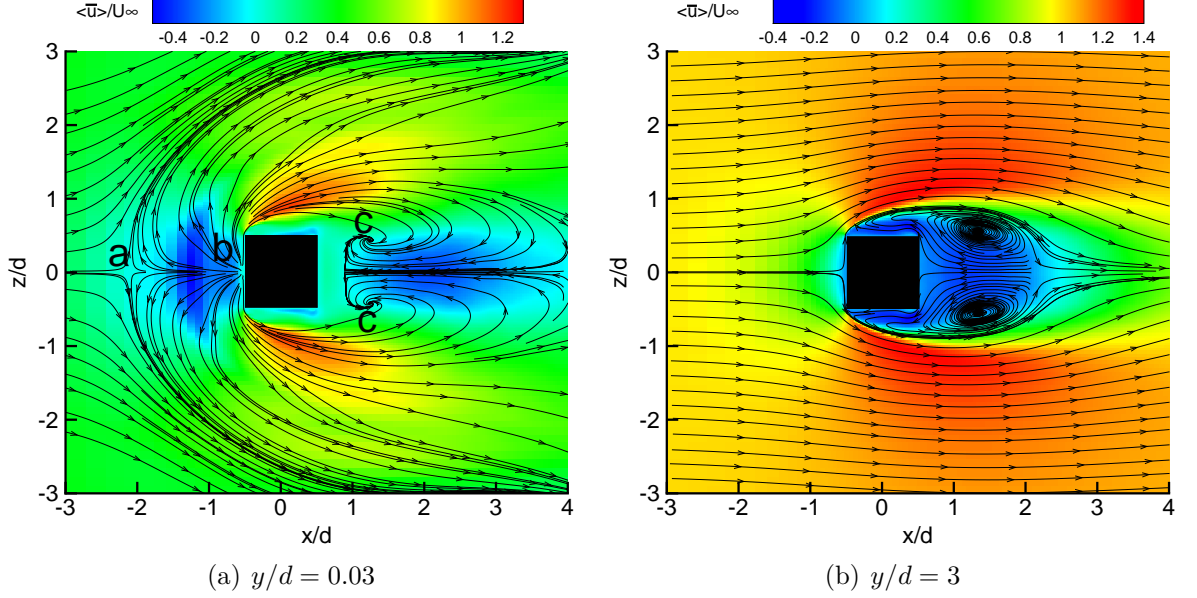


FIGURE 4.3: Time-averaged streamlines and contours of non-dimensionalized resolved streamwise velocity in  $x$ - $z$  planes at two different elevations for  $y/d = 0.03$  and  $y/d = 3$ .

## 4.2 Results and discussions

In this section, the qualitative and quantitative results obtained from the numerical simulation are thoroughly analyzed. Characteristics of the instantaneous pressure field, time-averaged streamlines and boundary limits of the recirculation region behind the cylinder, turbulence kinetic energy (TKE) production rate and its distribution in the domain, SGS kinetic energy dissipation rate and SGS viscosity are investigated. The first- and second-order turbulence statistics obtained from the simulations are also compared against the experimental results of Bourgeois *et al.* [17,18] and Sattari *et al.* [19].

### 4.2.1 Flow structures

Since the geometry of the domain and flow conditions are symmetrical in the spanwise direction, the mean flow field is expected to be symmetrical as well. In order to obtain a statistically stationary mean flow field, the sampling time for collecting turbulence

statistics should be long enough to take all turbulent motions of different temporal and spatial scales into account. In the present work, the sampling time is approximately 12 shedding periods (or, approximately 5.5 flow-through times). Figure 4.3 shows the time-averaged streamlines and the resolved streamwise velocity contours (top view) in the  $x$ - $z$  plane at two different elevations. As shown in both figures, the time-averaged resolved velocity field is symmetrical with respect to the central line of the domain ( $z/d = 0$ ). Figure 4.3a shows that very close to the wall (at  $y/d = 0.03$ ), an apparent horseshoe vortex pattern is formed in front of the obstacle. The horseshoe vortex is due to the adverse pressure gradient in front of the obstacle and is one of the major characteristics of a bluff body flow. The appearance of the so-called saddle, nodal and focal points in the horseshoe vortex (marked as points ‘a’, ‘b’ and ‘c’, respectively) is consistent with the previous classical experimental and numerical studies on the formation of horseshoe vortex around bluff bodies [5, 44, 169]. Figure 4.3b shows the streamlines at an elevation well above the lower ground ( $y/d = 3$ ). In comparison with Fig. 4.3a, it is clear that the time-averaged streamline pattern is sensitive to the elevation for a cylinder with large AR value. As shown in Fig. 4.3b, at a higher elevation, the horseshoe vortex pattern is no longer apparent, instead, there are two large counter-rotating vortices in the rear region of the obstacle and two small vortices adjacent to the side walls.

In order to develop a deeper understanding of the flow pattern shown in Fig. 4.3b, Figs. 4.4a and 4.4b are used to present the instantaneous and time-averaged vector plots of the resolved velocity field in the  $x$ - $z$  plane located at the same elevation for  $y/d = 3$ . The highly intermittent velocity field and interactions of turbulent eddies at different scales are apparent in Fig. 4.4a. Also, the strong shear layers issued by the two sides of the cylinder (located at  $z/d = \pm 0.5$ ) and the vortex shedding downstream of the cylinder are evident in this figure. From the time-averaged vector plot shown in Fig. 4.4b, two small recirculation regions adjacent to the side walls of the cylinder and two large counter-rotating vortices behind the cylinder are clearly observed. Furthermore, the boundary of the recirculation region can be readily identified based on the velocity vector patterns.

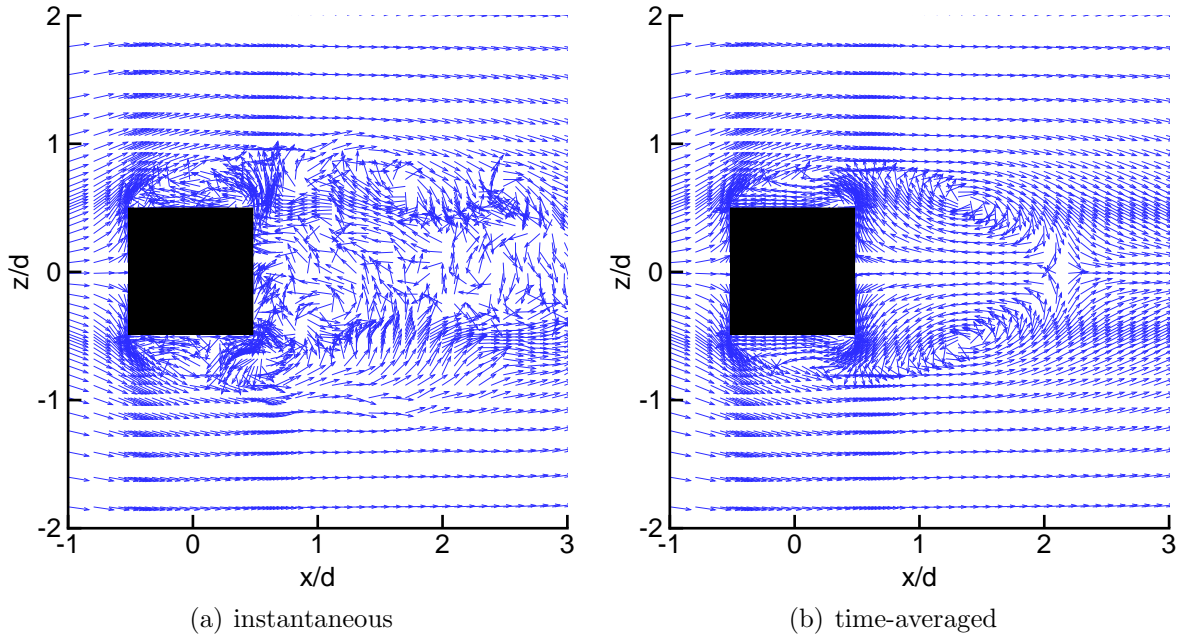


FIGURE 4.4: Top view of the instantaneous and time-averaged vector plots of the resolved velocity field in the  $x$ - $z$  plane at elevation  $y/d = 3$ .

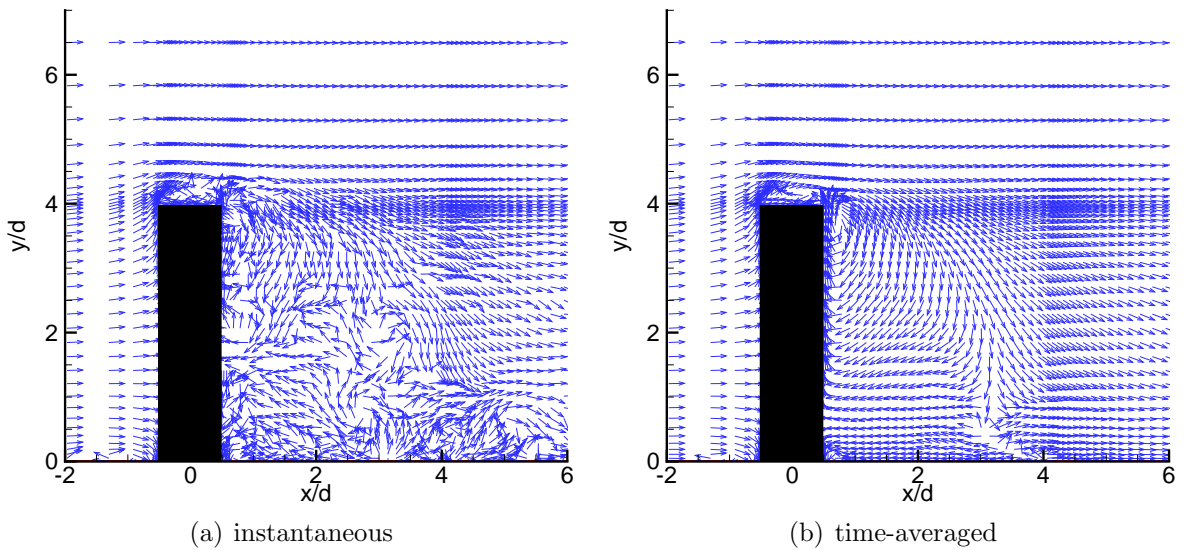


FIGURE 4.5: Side view of the instantaneous and time-averaged vector plots of the resolved velocity field in the central  $x$ - $y$  plane at  $z/d = 0$ .

The instantaneous and time-averaged vector plots of the resolved velocity field in the central  $x$ - $y$  plane of the domain (located at  $z/d = 0$ ) are shown in Fig. 4.5. The turbulent flow pattern downstream of the cylinder shown in Fig. 4.5a is a direct result of interactions between the downwash flow induced by the cylinder free-end

and Kármán vortices issued by the cylinder sides. Also, a shear layer formed on the rooftop of the cylinder is clearly observed in this figure. The time-averaged vector plot shown in Fig. 4.5b, demonstrates the large recirculation region behind the cylinder and the interactions of downwash, upwash and the reverse flow near the ground. Both Figs. 4.5a and 4.5b show that there exists a small recirculation region on the cylinder top, which is formed due to the direct strike of the free-stream flow at the cylinder top front edge and follow-up separation of the boundary layer from the top surface.

In Figs. 4.6a, 4.6b and 4.6c (corresponding to elevations  $y/d = 1, 2$  and  $3$ , respectively), the spanwise profiles of the mean resolved streamwise velocity at multiple downstream locations of the obstacle are compared. Through a careful analysis of these figures, the boundary of the recirculation region behind the obstacle can be identified. As previously shown in Fig. 4.3b, there is a recirculation bubble in the rear region of the obstacle where two large counter-rotating vortices are present. Inside the recirculation bubble and along the central streamline ( $z/d = 0$ ), there is a reverse flow with negative streamwise velocities. As the downstream distance from the cylinder increases, the magnitude of the reverse velocity decreases, and right at the boundary of the recirculation bubble along the central streamline, the mean streamwise velocity is zero. This boundary of the recirculation bubble varies with the elevation. As shown in Fig. 4.6a, at  $y/d = 1$ , the boundary of the recirculating bubble where the value of the mean streamwise velocity is zero is located at  $x/d = 3.5$ . However, as shown in Figs. 4.6b and 4.6c, for elevations  $y/d = 2$  and  $y/d = 3$ , this boundary is located at  $x/d = 3.2$  and  $x/d = 2.3$ , respectively. As such, it is clear that the bubble is larger at a lower elevation and becomes smaller at a higher elevation. Right at the wall (zero elevation), this boundary is at  $x/d = 3.8$ , which is the location of the so-called reattachment point. The formation and size of the recirculation bubble are primarily due to the effect of tip vortices shed from the free-end of the cylinder and further extended along with the downwash flow caused by the pressure difference between the front and rear regions of the cylinder.

Figure 4.7 shows the time-averaged streamlines and contours of the resolved streamwise velocity in the central  $x$ - $y$  plane located at  $z/d = 0$ . This figure clearly

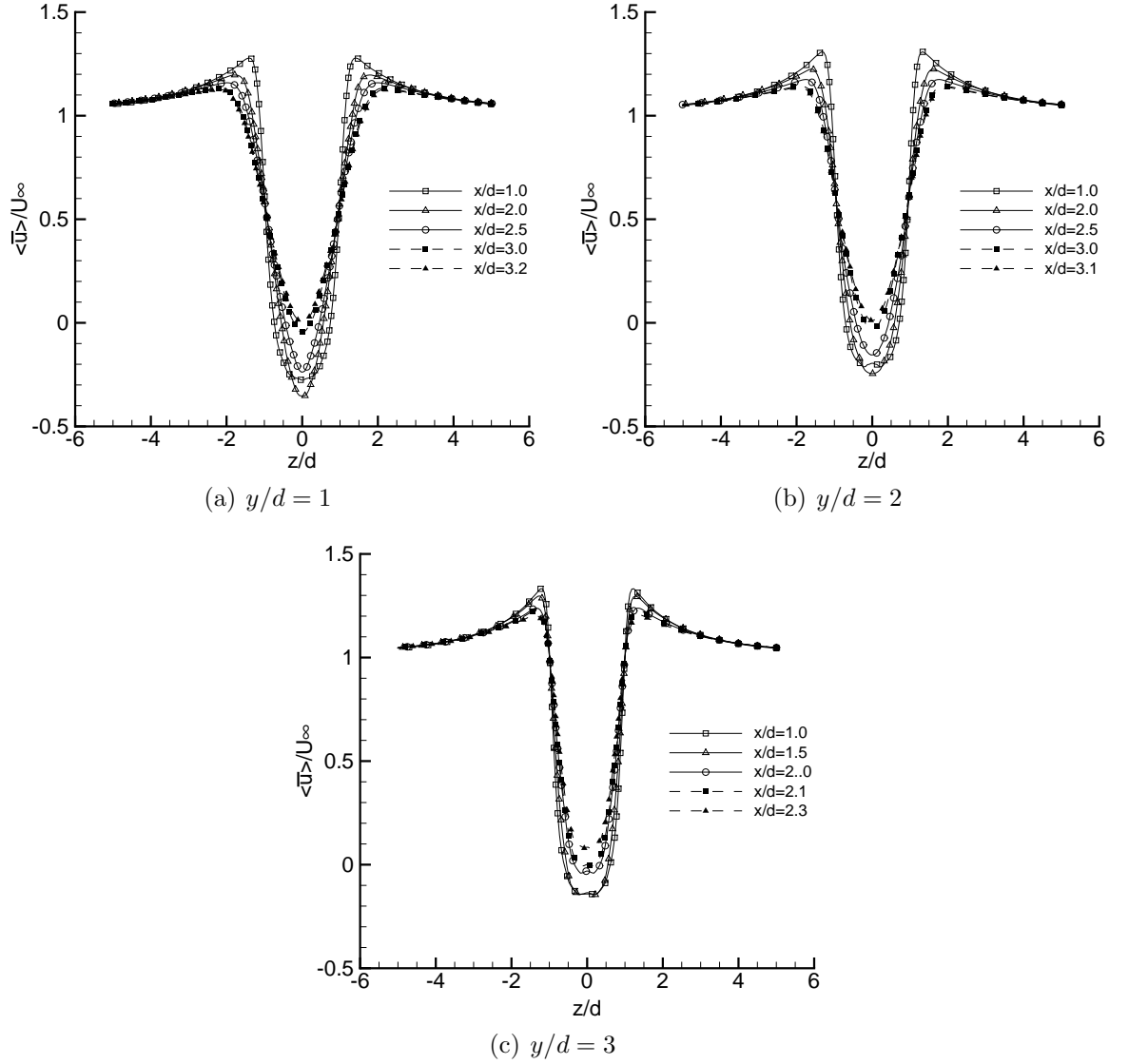


FIGURE 4.6: Spanwise profiles of the mean resolved streamwise velocity at 3 different elevations and multiple streamwise locations within the recirculation region (in order to make the figure more readable, data points are labeled using symbols at segments with the length of 3% of the total height of the frame).

grasps the low and negative velocity region and the large vortex formed behind the cylinder. The recirculation bubble boundary inferred previously from Fig. 4.6 is now vividly demonstrated by the streamlines. Clearly, the boundary of the recirculation region extends from higher to lower elevations  $z$  associated with the downwash of the flow behind the cylinder.

Figure 4.8 shows the instantaneous resolved pressure field in the central  $x$ - $y$  plane

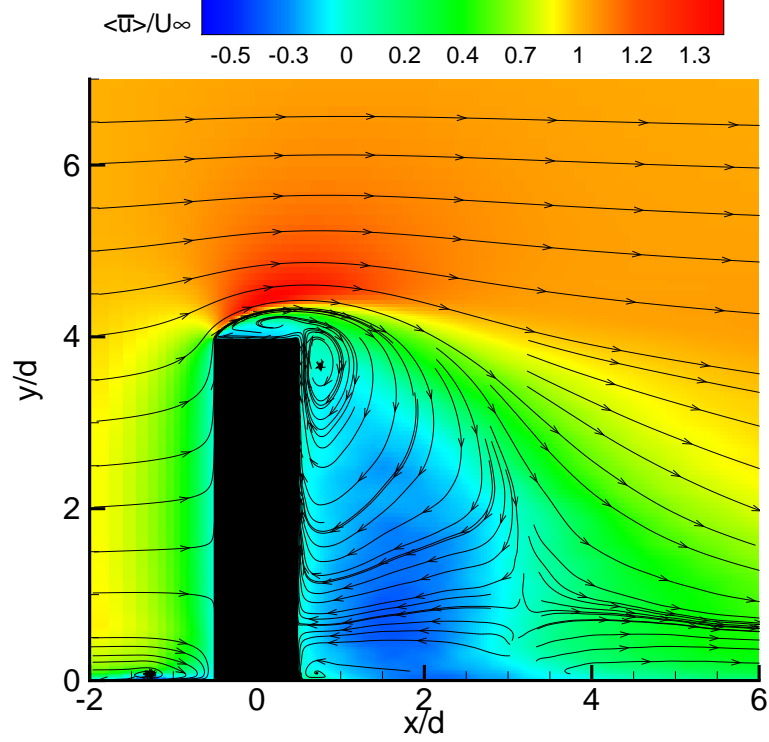


FIGURE 4.7: Time-averaged streamlines and contours of the mean resolved streamwise velocity in the central  $x$ - $y$  plane located at  $z/d = 0$ .

(located at  $z/d = 0$ ) at two different moments of time. The resolved pressure is non-dimensionalized as  $C_p = (\bar{p} - \bar{p}_\infty)/q_\infty$ , where  $\bar{p}_\infty$  is the free-stream resolved static pressure,  $q_\infty$  is the free-stream dynamic pressure defined as  $q_\infty = \frac{1}{2}\rho U_\infty^2$  and  $C_p$  represents the resolved pressure coefficient. This figure vividly shows that the flow strikes the top front edge of the cylinder and tip vortices are generated on the top (free-end) surface. These tip vortices then entrain the wake region behind the obstacle where the recirculation flow patterns dominate. Three distinct pressure regions are observable in Figs. 4.8a and 4.8b: firstly, the stagnation region which is formed in front of the obstacle due flow impingement and has the highest static pressure; secondly, the recirculation wake region into which the tip vortices are shed and is located immediately behind the obstacle and features the lowest pressure of the flow field; and thirdly, the outer region which is located above the recirculation region and has a pressure similar to the free-stream pressure. The pressure difference between front and rear surfaces causes a net form drag acting on the cylinder and makes the high

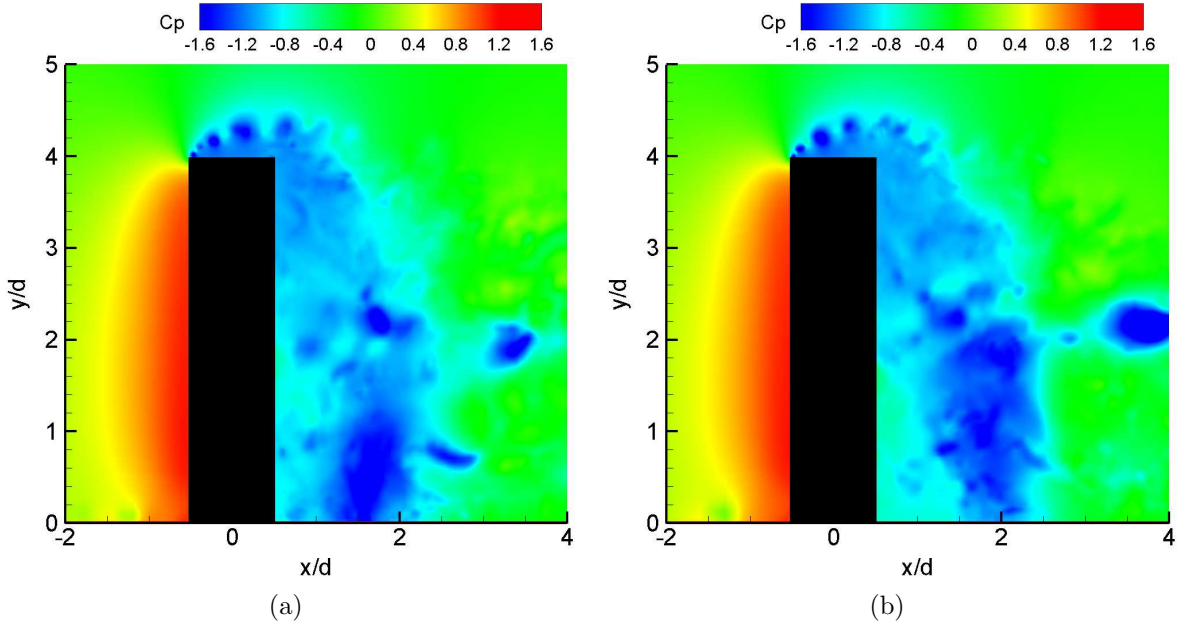


FIGURE 4.8: Tip vortex shedding visualized using the instantaneous non-dimensionalized resolved pressure field in the central  $x$ - $y$  plane located at  $z/d = 0$  (the pressure coefficient is defined as  $C_p = (\bar{p} - \bar{p}_\infty)/q_\infty$ ). The time step between the two snapshots is  $0.004$  s.

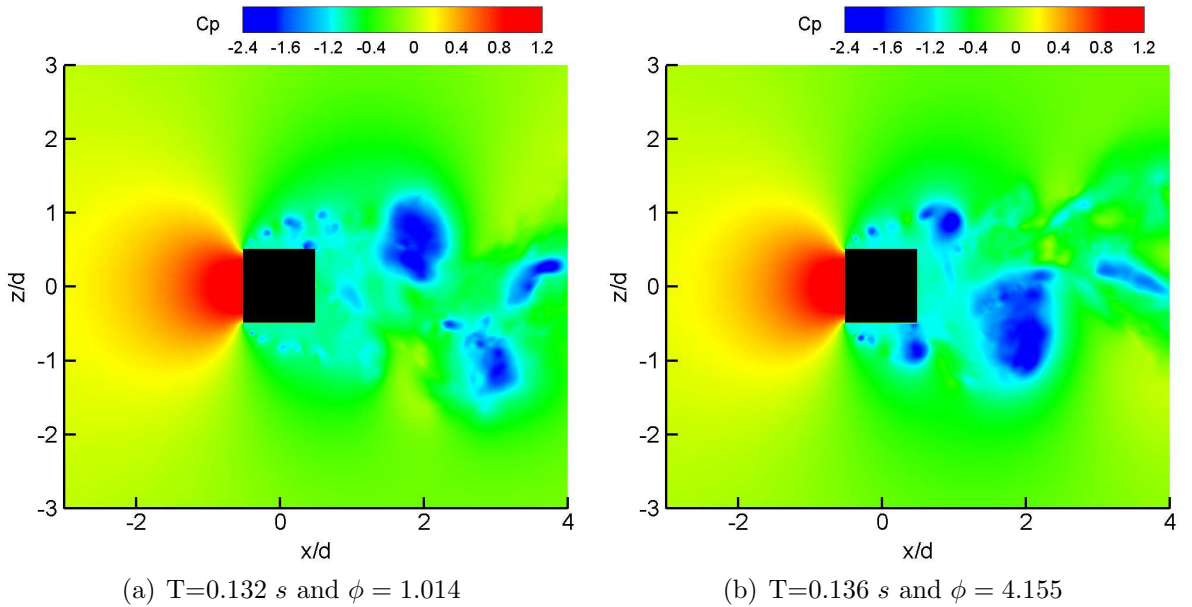


FIGURE 4.9: Kármán vortex shedding visualized using the instantaneous non-dimensionalized resolved pressure field near the cylinder in the  $x$ - $z$  plane located at  $y/d = 1$  (the pressure coefficient is defined as  $C_p = (\bar{p} - \bar{p}_\infty)/q_\infty$ ).

pressure fluid entrain the low pressure regions which further triggers flow instability to produce complex alternating vortical patterns in the downstream region.

Figures 4.9a and 4.9b show two instantaneous snapshots of the non-dimensionalized pressure field in the horizontal  $x$ - $z$  plane at  $y/d = 1$ . The time and phase differences between these two snapshots are  $\Delta t = 0.004$  s and  $\Delta\phi = \pi$  rad, respectively. Following the method of Bourgeois *et al.* [17, 18], to define the shedding period, the pressure signal on the side surface of the cylinder (specifically, at point  $x/d = 0$ ,  $y/d = 1$  and  $z/d \approx 0.5$ ) has been extracted and analyzed. A vortex shedding period/cycle is then defined based on the time difference between two consecutive peaks of the instantaneous pressure. Once a vortex shedding period is defined, the instantaneous shedding phase,  $\phi \in [0, 2\pi)$ , can be determined accordingly. The presence of the Kármán vortex street is evident in both figures. The low pressure vortices are shed into the wake region at frequency  $f = 125$  Hz. Corresponding to this characteristic frequency, the Strouhal number (based on the free-stream velocity and cylinder side length) is  $Sr = \frac{fd}{U_\infty} = 0.106$ , which is in agreement with the experimental result of Bourgeois *et al.* [17, 18].

Figure 4.10 shows the 3-D vortical structures formed around the edges and behind the cylinder visualized using low pressure iso-surfaces. As is evident in Figs. 4.10a and 4.10b, two alternating vortex tubes (designated as “low pressure tubes 1 and 2” in these two figures) are shed from the two cylinder sides, twist around each other and gradually approach the ground plane as they are carried by the main stream. Near the ground, where the first half loop of the low pressure tubes is just completed, the vortex tubes interact with the boundary layer and their rotation axes are deflected off the ground to start the second half loop pattern. The vortical structures observed in these figures are consistent with the experimental results reported by Bourgeois *et al.* [17, 18]. In Fig. 4.10c, the vortex tubes generated at the sharp edges of the cylinder are demonstrated. As shown in this figure, the vortex tubes evolve spatially and shed to the rear region of the cylinder. The coherent structures downstream of the cylinder and the complex vortex patterns are results of motions and interactions of tip vortices from the cylinder free-end, Kármán vortices shed from the cylinder side walls, and the developing and separating boundary layers from solid surfaces.

In order to obtain more physical insights into the flow behavior in the wake

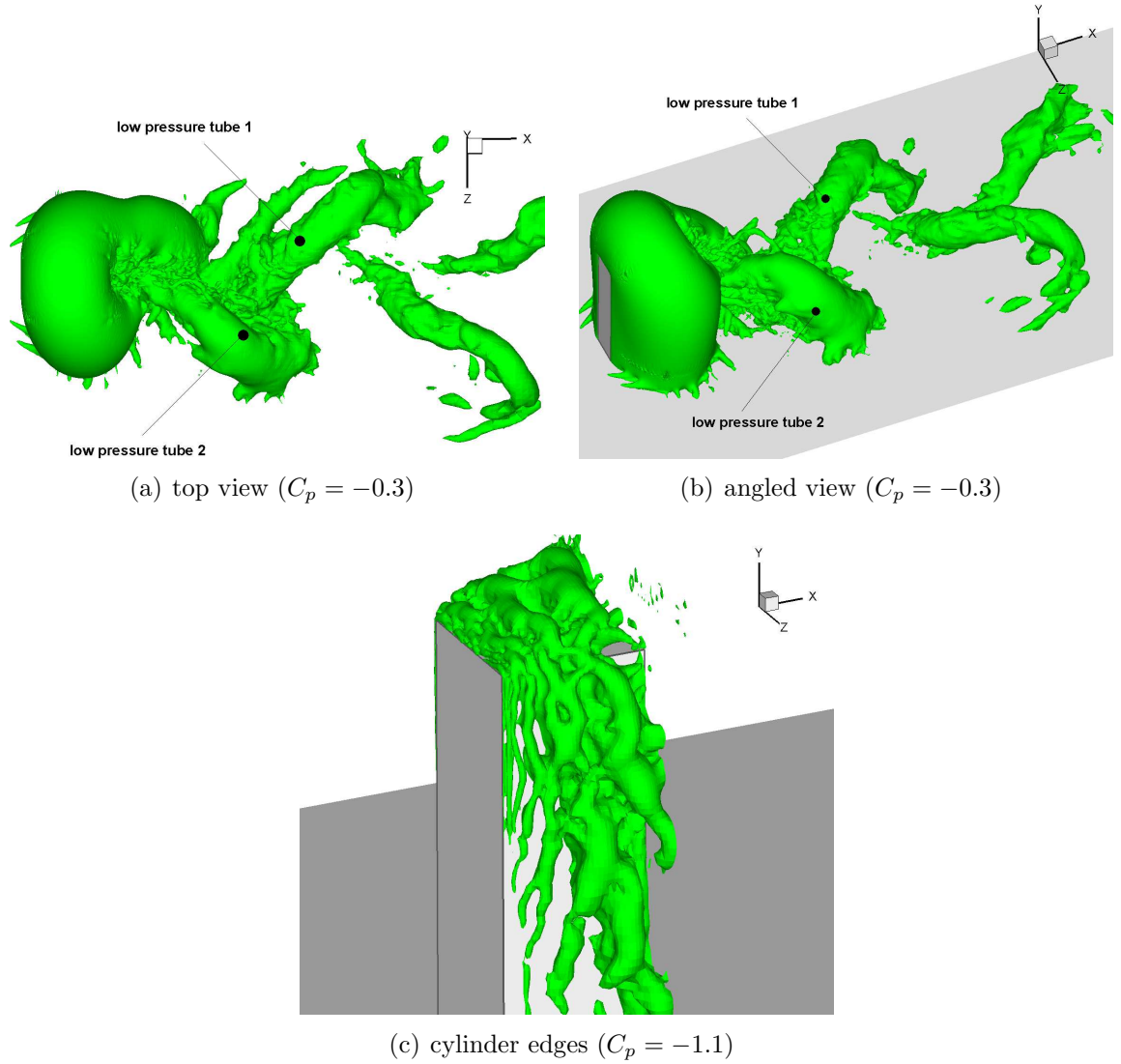


FIGURE 4.10: Three-dimensional vortical structures in the wake region and around the cylinder edges visualized using instantaneous resolved low pressure iso-surfaces (the pressure field has been non-dimensionalized and is represented by the pressure coefficient defined as  $C_p = (\bar{p} - \bar{p}_\infty)/q_\infty$ ).

region, instantaneous resolved pressure contours in 12 consecutive  $y$ - $z$  planes behind the cylinder are demonstrated in Figs. 4.11a-4.11l. All the planes are extracted from a single snapshot at locations which vary uniformly from  $x/d = 0.5$  to  $x/d = 6$ . The most striking feature in all figures relates to the negative pressure regions inside the wake. These low pressure spots represent the cores of vortices shed from the cylinder. It should be clarified here that a negative resolved pressure refers to a resolved pressure

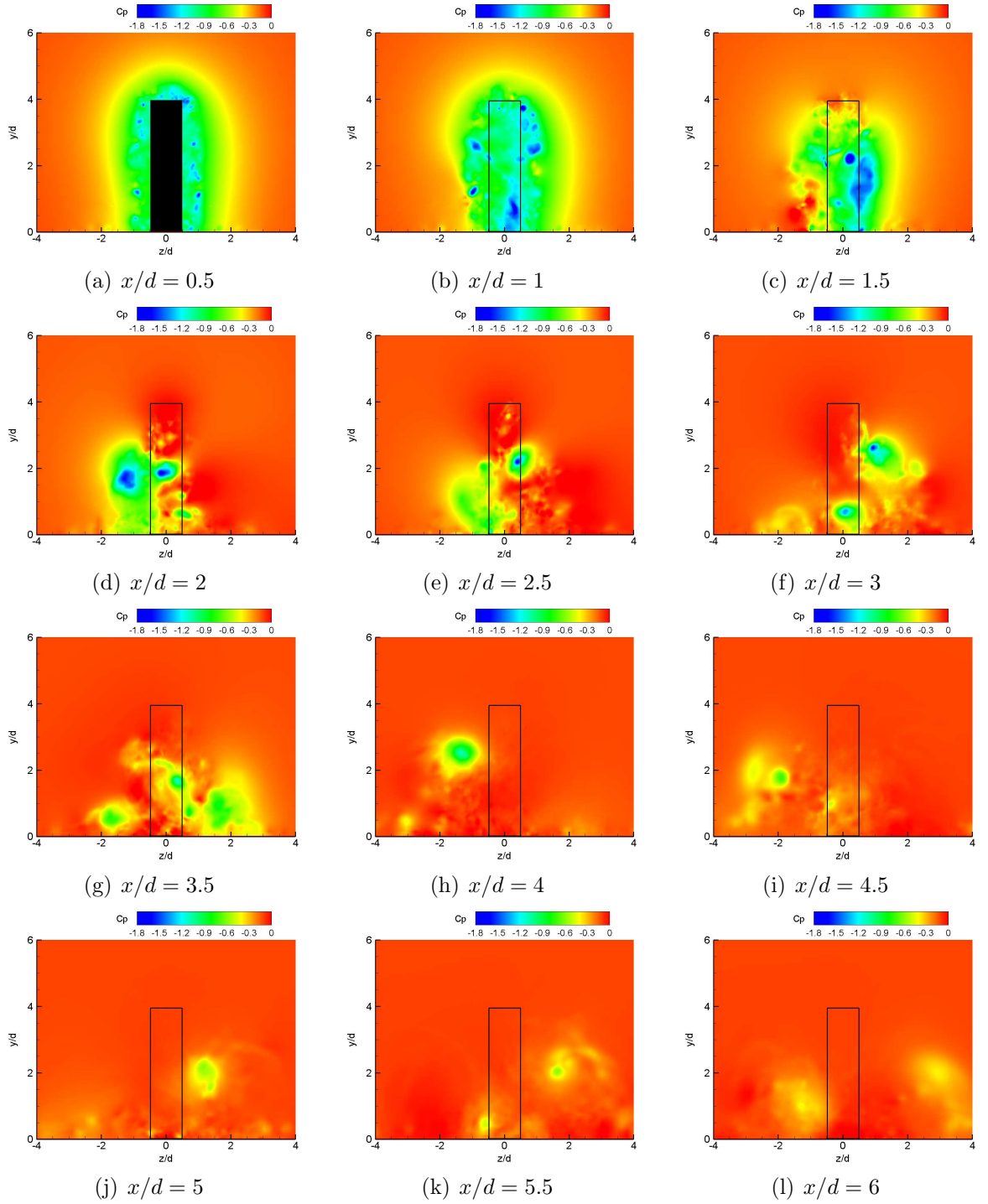


FIGURE 4.11: Contours of instantaneous non-dimensionalized resolved pressure in  $y$ - $z$  planes at 12 consecutive streamwise locations (the pressure coefficient is defined as  $C_p = (\bar{p} - \bar{p}_\infty)/q_\infty$ ).

lower than the free-stream static resolved pressure  $\bar{p}_\infty$ . The negative pressure behind the cylinder creates a suction effect and forms the recirculation bubble (due to the difference between the local pressure and the static pressure of the approaching free-stream flow, i.e.  $(\bar{p} - \bar{p}_\infty)$ ). In the remainder of the thesis, the negative resolved pressure on the leeward side of the cylinder will be also referred to as suction. In Fig. 4.11, the suction varies from  $-1.8q_\infty$  to 0. As shown in Fig. 4.11a, at  $x/d = 0.5$ , a band of low resolved pressure with suction of approximately  $-0.8q_\infty$  is formed around the cylinder. Clearly shown in Fig. 4.11, as the distance from the cylinder increases, the low resolved pressure band becomes more and more irregular in shape. The location of the low resolved pressure spots alternates from side to side reflecting the vortex shedding dynamics. As shown in Fig. 4.11d, at  $x/d = 2$ , a large suction effect is observed, where large fluid parcels entrain the recirculation bubble. Further downstream of the cylinder for  $x/d > 2$ , the suction strength decreases gradually and the low resolved pressure band around the cylinder gradually merges with the main stream background. This process continues until  $x/d = 4$ , where the negative resolved pressure band almost vanishes, indicating that the end of the recirculation region has been reached. In far downstream regions for  $x/d > 4$ , the alternating vortex shedding patterns are still apparent, however, the flow becomes dominated by the main stream and the strength of low-pressure vortices has significantly decayed due to turbulent mixing, diffusion and dissipation.

For sustainable turbulence, it is required that TKE is generated through turbulent motions in order to balance the viscous dissipation effects. The local resolved TKE production rate is defined as  $P_r = -\langle \bar{u}_i'' \bar{u}_j'' \rangle \frac{\partial \langle \bar{u}_i \rangle}{\partial x_j}$  in which  $\langle \bar{u}_i'' \bar{u}_j'' \rangle$  is the resolved Reynolds stress tensor and  $\frac{\partial \langle \bar{u}_i \rangle}{\partial x_j}$  is the resolved velocity gradient tensor based on time-averaged resolved velocity components. Figures 4.12a and 4.12b show the contours of the resolved TKE production rate (non-dimensionalized using the maximum resolved TKE production rate) in two typical lateral and horizontal planes. In order to demonstrate the effects of sharp edges of the cylinder on the  $P_r$  level, the contour patterns have been magnified locally in small figure panels based on different contour legend scales. As is evident in Fig. 4.12a, the maximum resolved TKE production

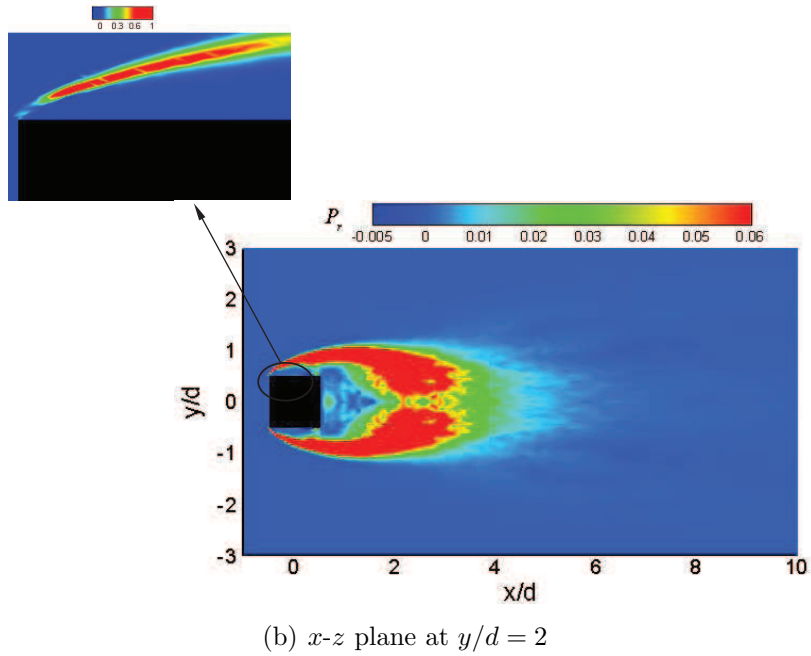
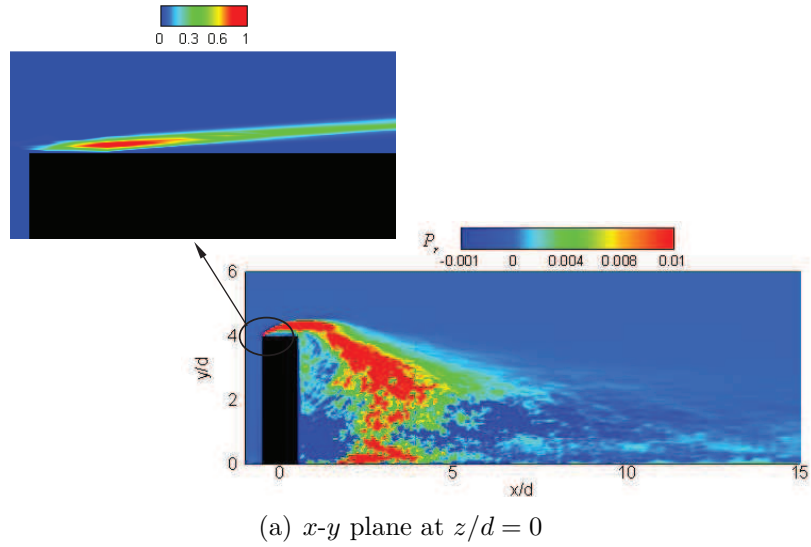


FIGURE 4.12: Contours of the resolved TKE production rate in two typical  $x$ - $y$  and  $x$ - $z$  planes (non-dimensionalized using the maximum resolved TKE production rate in the same planes, respectively).

rate occurs at the top front edge of the cylinder where tip vortex shedding starts. At this special location, the flow directly strikes the obstacle and the top front edge of the cylinder. The shear layer separates and further triggers flow instability. As the flow goes forward, the strength of the resolved TKE production rate reduces but remains significant in the wake region behind the cylinder. Figure 4.12b shows the

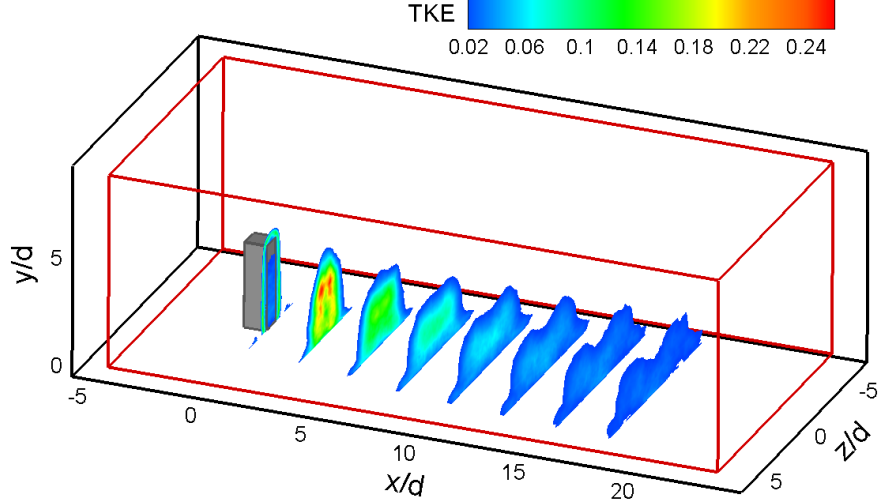


FIGURE 4.13: Slices of resolved TKE contours along the streamwise direction (the resolved TKE value has been non-dimensionalized using  $U_\infty^2$ ).

contours of the resolved TKE production rate in a horizontal plane located at half cylinder height ( $y/d = 2$ ). Similarly, the sharp side edges of the cylinder create the maximum resolved TKE production rate. The shear layer separation occurs on both sides, which further triggers flow instability leading to the Kármán vortex shedding pattern. Owing to the strong shear layers on both sides of the cylinder and active vortex motions and interactions, the level of  $P_r$  remains high downstream of the cylinder. As shown in Fig. 4.12b, the distribution of  $P_r$  is symmetrical in the cross-stream direction, reflecting its intrinsic time-averaged property (by definition) and geometrical symmetry of the domain. As the distance from the cylinder increases, the strength of  $P_r$  decreases, indicating a reduced turbulence level and well-mixed eddy motions in the far downstream region of the cylinder.

Figure 4.13 demonstrates the spatial evolution of the resolved TKE (defined as  $k = \frac{1}{2}(\langle \bar{u}''^2 \rangle + \langle \bar{v}''^2 \rangle + \langle \bar{w}''^2 \rangle)$  with  $\bar{u}''$ ,  $\bar{v}''$  and  $\bar{w}''$  being resolved fluctuating velocities) in the streamwise direction. In the figure, the resolved TKE value has been non-dimensionalized using  $U_\infty^2$ . The slices are distributed uniformly in the streamwise direction, and in order to effectively demonstrate energetic eddy motions (with high TKE levels) in the low TKE background, the lowest resolved TKE threshold used for plotting contours was set to  $0.02U_\infty^2$ . As shown in this figure, at  $x/d = 0$ , there

is a thin layer in proximity of the obstacle where the resolved TKE level is up to  $0.06U_\infty^2$ . This layer is produced due to the strong resolved TKE production rate on the top and two sides of the cylinder and triggering of the energetic vortices shown previously in Figs. 4.12a and 4.12b. As the downstream distance from the cylinder increases, the spread of the resolved TKE becomes wide in the cross-stream direction primarily due to the interactions and motions of eddies. Also, there is a downwash of resolved TKE to the wall in the wake region immediately behind the cylinder. The maximum resolved TKE occurs at approximately  $x/d = 4.0$  and  $y/d = 2.0$ , and has a value about  $0.22U_\infty^2$ . Further downstream of the cylinder, due to the dissipation and spatial transport of TKE, the peak value of the resolved TKE keeps decreasing until it drops below  $0.02U_\infty^2$  for  $x/d > 18d$ . By comparing Figs. 4.12 and 4.13, it is clear that the maximum values of the resolved TKE  $k$  and resolved TKE production rate  $P_r$  are tightly coupled. The exact relationship between these two quantities is described by the transport equation of the resolved TKE. Although the production term contributes significantly to the resolved TKE level, there are other influencing factors such as the advection and diffusion mechanisms. For this reason, the exact locations for the maximum values of  $P_r$  and  $k$  shown in Figs. 4.12 and 4.13, do not fully overlap.

## 4.2.2 Turbulence statistics

In this subsection, the first- and second-order turbulence statistics obtained from the numerical simulation are analyzed to further understand the dynamics of the wake of the cylinder flow. The obtained numerical results are compared against the available wind-tunnel experimental data of Bourgeois *et al.* [17, 18] and Sattari *et al.* [19].

Figures 4.14a-4.14d compare the mean streamwise and spanwise velocity profiles (non-dimensionalized using the free-stream velocity  $U_\infty$ ) obtained from the numerical simulation with experimental data [17–19] at two locations (corresponding to two streamwise locations  $x/d = 2$  and  $x/d = 3.5$  and the same elevation  $y/d = 3$ ). Based on the size of the recirculation bubble discussed in the previous subsection, the first

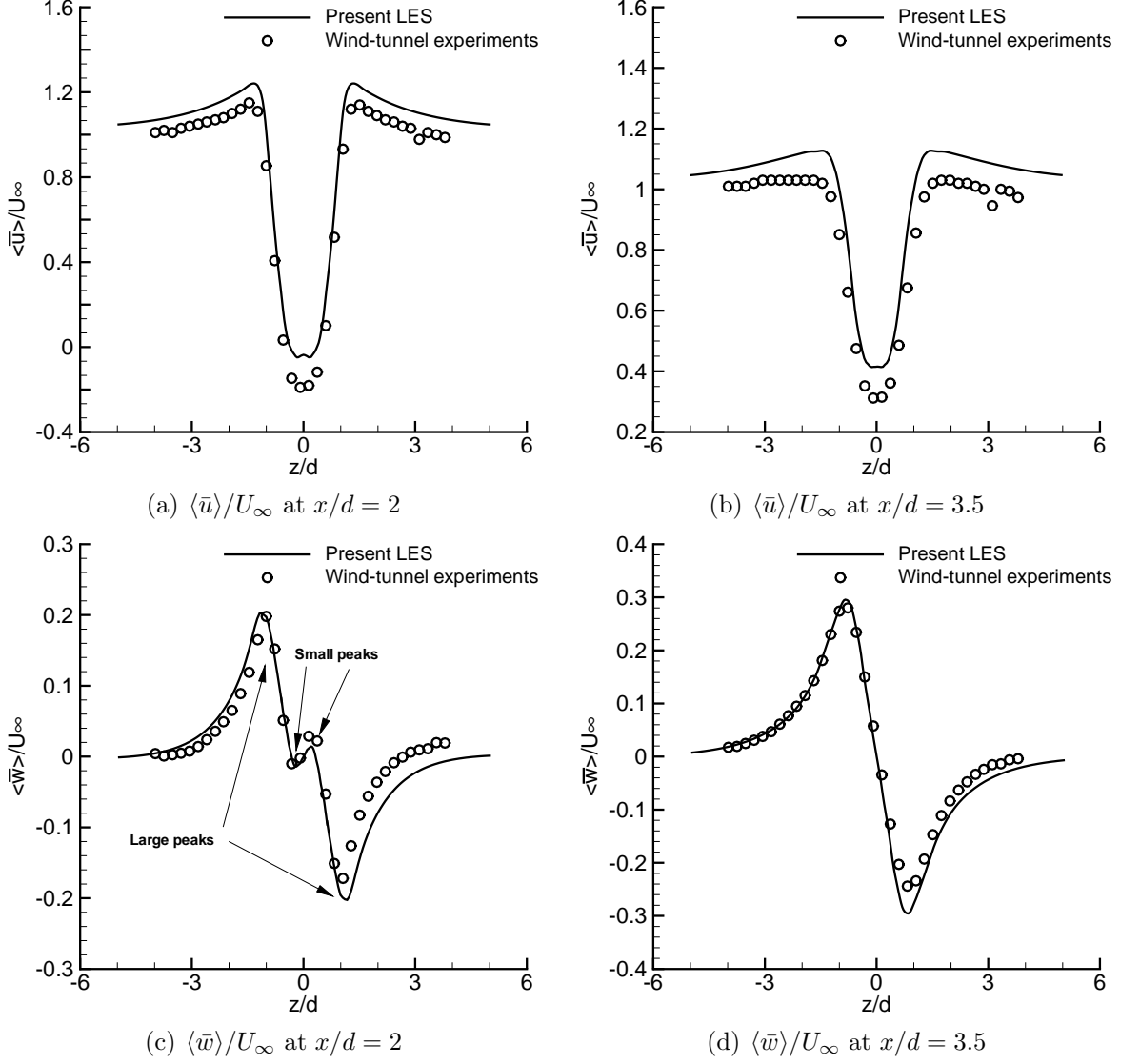


FIGURE 4.14: Time-averaged resolved streamwise and spanwise velocity profiles downstream of the obstacle at elevation  $y/d = 3$ , and two streamwise locations for  $x/d = 2$  and  $x/d = 3.5$ .

location ( $x/d = 2$  and  $y/d = 3$ ) is in the middle of the recirculation bubble and the second location ( $x/d = 3.5$  and  $y/d = 3$ ) is outside of the recirculation bubble (see also Figs. 4.3, 4.6 and 4.7). As shown in Fig. 4.14, the streamwise and spanwise profiles are symmetrical and anti-symmetrical, respectively, about the central plane of the domain ( $z/d = 0$ ). From Fig. 4.14a, it is seen that at location  $x/d = 2$ , the resolved streamwise velocity ( $\langle \bar{u} \rangle / U_\infty$ ) is negative (with a small magnitude) within  $-0.5 < z/d < 0.5$ , reflecting the recirculation pattern inside the cylinder wake.

However as exhibited in Fig. 4.14b, no negative value is observed in the mean resolved streamwise velocity profile at  $x/d = 3.5$ , indicating that the location is outside of the recirculation bubble. There are two pairs of peaks in Fig. 4.14c. The pair of outer large peaks of  $\langle \bar{w} \rangle / U_\infty$  shows the deviation of streamlines from the straight path in side regions of the obstacle and the pair of inner small peaks of  $\langle \bar{w} \rangle / U_\infty$  indicates the presence of counter-rotating vortices in the wake region. The magnitudes of small peaks are one order smaller than that of large peaks, indicating a relatively low velocity magnitude inside the recirculation bubble. However, at  $x/d = 3.5$ , only one pair of peaks are observed in Fig. 4.14d, indicating that the counter-rotating vortices are no longer present outside the recirculation bubble. These results are consistent with the previous observations in Figs. 4.3 and 4.7. As shown in Fig. 4.14, the profiles obtained from numerical simulation are in general agreement with the experimental measurements, especially for the resolved spanwise velocity component. However, as shown in Figs. 4.14a and 4.14b, the mean resolved streamwise velocity is slightly overpredicted by numerical simulation outside the range  $-1 < z/d < 1$ .

Figures 4.15a-4.15d compare the resolved streamwise and spanwise RMS velocities (or turbulence intensities) with the wind-tunnel measurement data of Bourgeois *et al.* [17,18] and Sattari *et al.* [19] at the elevation  $y/d = 3$  and streamwise locations  $x/d = 2$  and  $x/d = 3.5$ . The RMS velocities have been non-dimensionalized using  $U_\infty$ . Figures 4.15a and 4.15b compare the predicted and measured averaged cross-stream profiles of the streamwise RMS velocity inside and outside of the recirculation bubble (at the same elevation  $y/d = 3$ ), respectively. As shown in Figs. 4.15a and 4.15b, at location  $x/d = 2$  and  $x/d = 3.5$ , the resolved streamwise RMS velocity profiles clearly exhibit dual-peak patterns. As shown in these two figures, the peaks (corresponding to the highest streamwise turbulence intensity component) are located approximately at  $z/d = 1$  and  $z/d = -1$  ( $0.5d$  away from the cylinder side walls). The profiles of  $\bar{u}_{rms}/U_\infty$  are symmetrical about the central  $x$ - $y$  plane ( $z/d = 0$ ) due to the symmetry of the computational domain and statistically stationary alternating vortex shedding patterns from both sides of the cylinder. By comparing Figs. 4.15a with 4.15b, it is clear that as the location moves from  $x/d = 2$  (inside the recirculation bubble) to

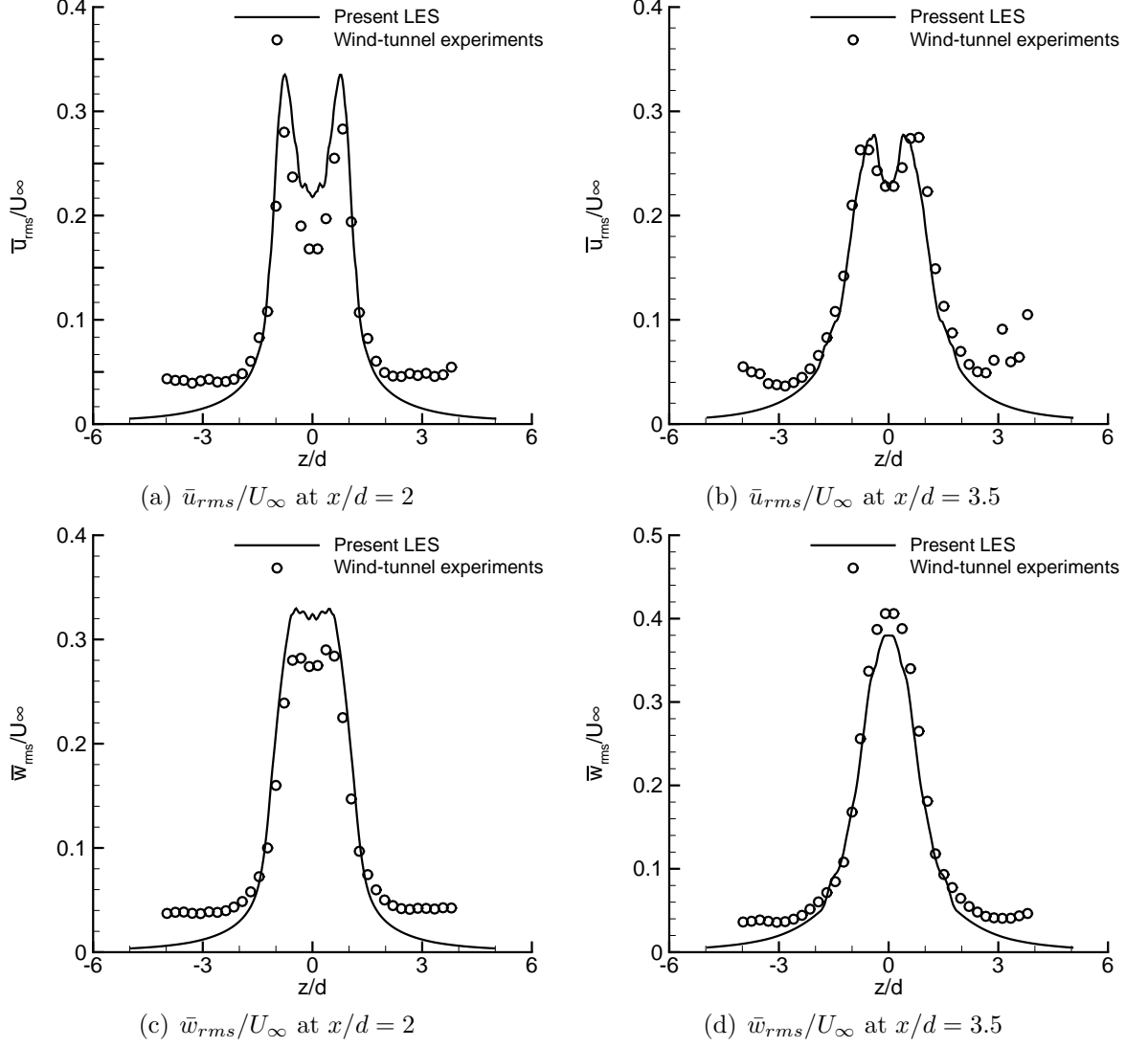


FIGURE 4.15: Cross-stream profiles the resolved streamwise and spanwise RMS velocities at elevation  $y/d = 3$ , and two streamwise locations for  $x/d = 2$  and  $x/d = 3.5$ .

$x/d = 3.5$  (outside the recirculation bubble), the resolved streamwise RMS velocity profile still keeps its dual-peak pattern, however the magnitude of the peaks have become attenuated. Figures 4.15c and 4.15d compare the predicted averaged cross-stream profiles of  $\bar{w}_{rms}/U_\infty$  with the measured spanwise RMS velocity inside and outside the recirculation bubble, respectively. As shown in Fig. 4.15c, the dual-peaks observed in the profile of  $\bar{u}_{rms}/U_\infty$  also exist in the profile of  $\bar{w}_{rms}/U_\infty$ , however, their magnitude is much reduced. Outside the recirculation bubble, as shown in Fig. 4.15d, the dual-peak pattern vanishes and the profile of  $\bar{w}_{rms}/U_\infty$  exhibits a Gaussian

pattern. It should be indicated that in Figs. 4.15a-4.15d, although the predicted resolved RMS velocities ( $u_{rms}/U_\infty$  and  $\bar{w}_{rms}/U_\infty$ ) are in good agreement with the measurement data in the central region, their magnitudes have been underpredicted in two far side regions (for  $|z/d| > 2$ ). The small discrepancies in the far side regions may be contributed by the differences in the blockage ratio and domain size between the experiment and numerical simulation. Figure 4.15 compares the cross-stream resolved RMS velocity profiles with the experimental data at only two streamwise locations (for  $y/d = 3$ ). A comprehensive presentation of the evolution of cross-stream resolved RMS velocity profiles at 10 different streamwise locations will be presented later in Fig. 4.17.

In Fig. 4.16, the streamwise profiles of the non-dimensionalized resolved streamwise mean and RMS velocities (i.e.,  $\langle \bar{u} \rangle / U_\infty$  and  $\bar{u}_{rms} / U_\infty$ ) in the central  $x$ - $y$  plane ( $z/d = 0$ ) are compared against the experimental measurements at two different elevations. As is evident in Figs. 4.16a and 4.16b, a negative velocity region is observed at both elevations reflecting the presence of the recirculating flow immediately behind the cylinder. The exact point at which the velocity is zero indicates the boundary of the recirculating region, which is  $x/d \approx 3.5$  at  $y/d = 1$  and  $x/d \approx 2.3$  at  $y/d = 3$  (consistent with the previous discussion of the size of the recirculation bubble). The velocity then increases until it reaches the free-stream velocity in the far downstream region. For the resolved streamwise RMS velocities shown in Figs. 4.16c and 4.16d, it is observed that at both elevations, the maximum resolved streamwise RMS velocity (or turbulence intensity) occurs at  $x/d \approx 2.5$  and then smoothly decays as the streamwise distance from the cylinder increases. In comparison with the first-order statistics (mean velocity) shown in Fig. 4.16a and 4.16b, the agreement between numerical and experimental results on the second-order statistics (RMS velocity) is less satisfactory in Figs. 4.16c and 4.16d. In comparison with the measurement data, the value of  $\bar{u}_{rms}$  at its peak location has been very well reproduced by LES. However, in the region far downstream of the cylinder (where the turbulence level is attenuated), the value of  $\bar{u}_{rms}$  has been underpredicted at a lower elevation ( $y/d = 1$ ) and slightly overpredicted at a higher elevation ( $y/d = 3$ ) by the numerical simulation. The above

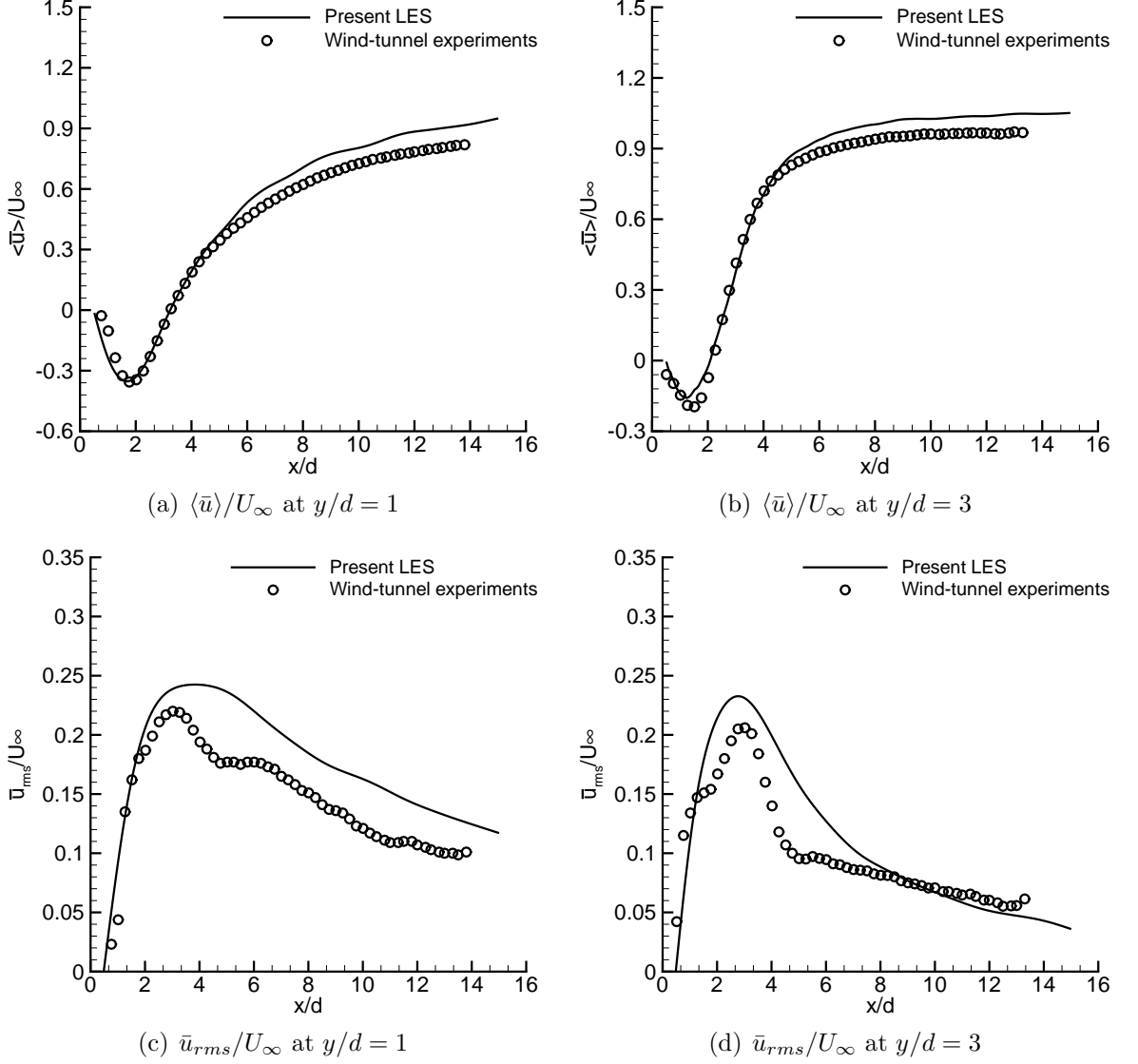


FIGURE 4.16: Streamwise profiles of the resolved streamwise mean and RMS velocities at two different elevations in the central  $x$ - $y$  plane ( $z/d = 0$ ).

characteristics of the streamwise and spanwise RMS velocity profiles (associated with Figs. 4.15 and 4.16) are intriguing, and in the following text, efforts will be made towards a detailed analysis of the streamwise evolution of the RMS velocity profiles and physical mechanisms underlying their characteristics.

Figures 4.17a-4.17d demonstrate the resolved mean streamwise and spanwise RMS velocities in the recirculation and far downstream regions (at elevation  $y/d = 2$ ). As shown in Fig. 4.17a, in the recirculation region, there is an apparent dual-peak pattern in the resolved streamwise RMS velocity profiles. The peaks in  $\bar{u}_{rms}/U_\infty$  are

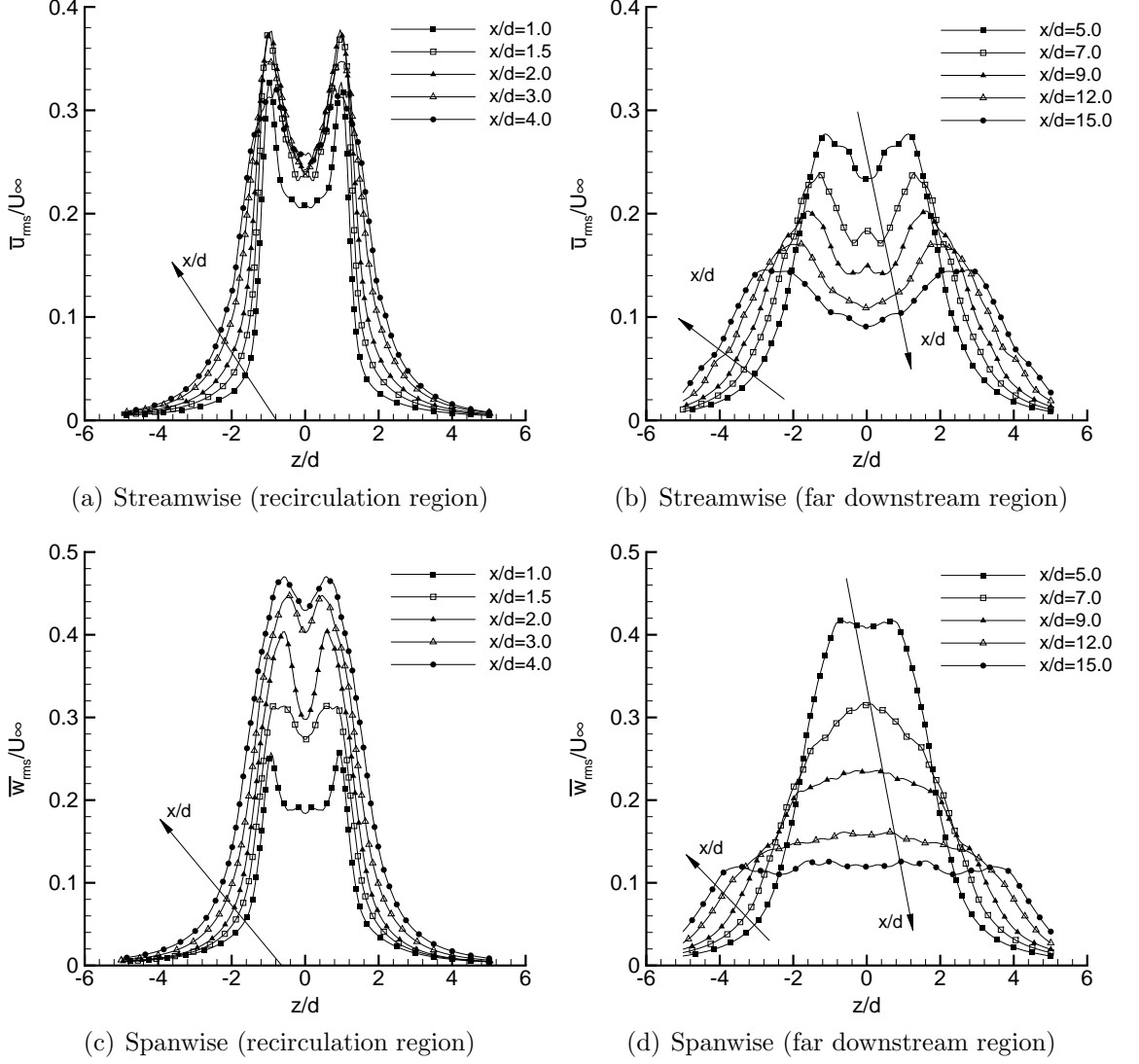


FIGURE 4.17: Cross-stream profiles of the resolved streamwise and spanwise RMS velocities in the recirculation and far downstream regions at elevation  $y/d = 2$ . Data points are labeled using symbols at segments with the length of 3% of the total height of the frame.

results of the strong shear layers formed on both sides of the cylinder, where large mean velocity gradients ( $\partial\langle\bar{u}_i\rangle/\partial x_j$ ) and high turbulent shear stress levels are present. This inevitably leads to a high TKE production rate on both sides of the cylinder, resulting in dual-peak patterns in the cross-stream profiles of  $u_{rms}/U_\infty$  in Fig. 4.17a. The very low level of the predicted resolved RMS velocities in the outer flow region (for  $|z/d| > 2$ ) is a result of the low production rate  $P_{ii} = -2\langle\bar{u}_i''\bar{u}_k''\rangle\frac{\partial\langle\bar{u}_i\rangle}{\partial x_k}$  (summation convention is applied to  $k$  but not to  $i$ ). The small values of Reynolds shear stress

components and small mean velocity gradients in the far side regions directly result in a low level of the production term  $P_{ii}$ , which further leads to a low level in resolved RMS velocities for  $|z/d| > 2$ .

As shown in Fig. 4.17b, in the far downstream region, the dual-peak pattern is still preserved. However, as the distance from the cylinder increases (as the value of  $x/d$  increases), the distance between the dual peaks in the cross-stream direction increases too. Furthermore, it is interesting to observe that the magnitude of  $\bar{u}_{rms}/U_\infty$  decreases in the central region but increases in the far side regions (for  $|z/d| > 2$ ). This is because as the flow evolves streamwise, the flow TKE spreads in the cross-stream direction due to the turbulent, pressure and viscous diffusion mechanisms.

Figure 4.17c shows the profile of the non-dimensional resolved spanwise RMS velocity ( $\bar{w}_{rms}/U_\infty$ ) in the recirculation region. In comparison with Fig. 4.17a, it is observed that the maximum value of  $\bar{w}_{rms}/U_\infty$  which occurs at  $x/d = 4.0$ , is approximately 30% higher than the maximum value of  $\bar{u}_{rms}/U_\infty$ . This is consistent with the previous discussion of Fig. 4.13 that the peak value of TKE occurs also at  $x/d = 4.0$ , indicating that the spanwise velocity fluctuations make the most significant contribution to TKE at this special streamwise location. Furthermore, it is observed from Fig. 4.17c that the dual-peak pattern is only strongly expressed in the immediate downstream region of the square cylinder. As shown in Fig. 4.17c, as the distance from the cylinder increases, the magnitude of  $\bar{w}_{rms}/U_\infty$  increases monotonically within the recirculation region. However, as the boundary of the recirculation bubble is approached (see Fig. 4.7), the dual-peak pattern becomes less apparent. As shown in Fig. 4.17d, this trend continues in the far downstream region, and in effect, the profile of  $\bar{w}_{rms}/U_\infty$  becomes exclusively Gaussian-like. Similar to Fig. 4.17b, as the value of  $x/d$  increases, the magnitude of  $\bar{w}_{rms}/U_\infty$  decreases in the central region and increases in the two far side regions due to diffusion mechanisms.

Figures 4.18a and 4.18b compare the numerical predictions and experimental measurements of the non-dimensionalized mean resolved Reynolds stress component  $\langle \bar{u}''\bar{w}'' \rangle$ , at two streamwise locations  $x/d = 2$  and  $x/d = 3.5$ , at the same elevation

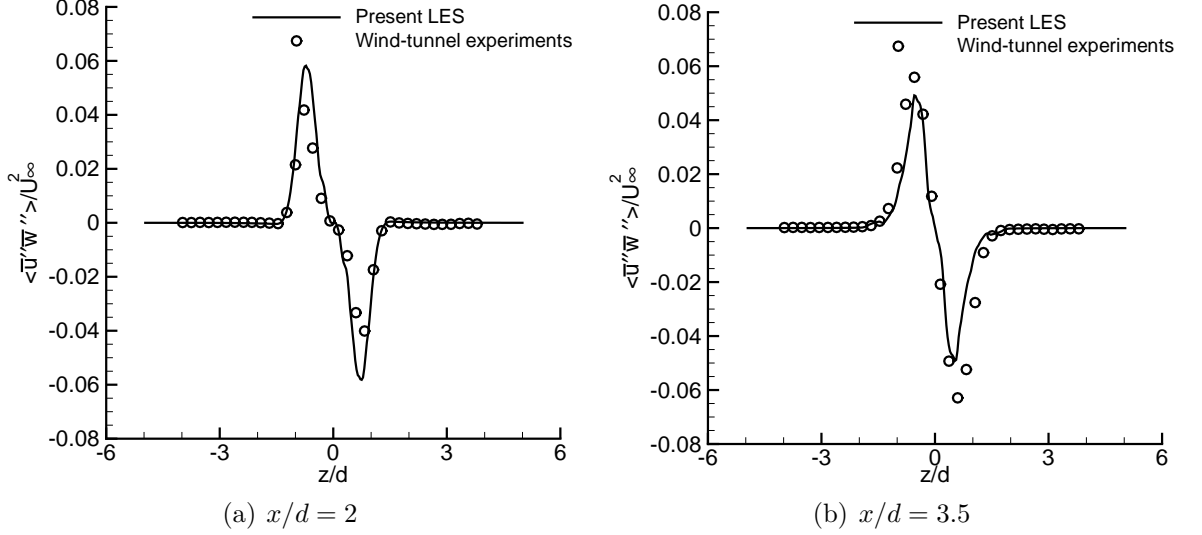


FIGURE 4.18: Cross-stream profiles of the non-dimensionalized mean resolved Reynolds stress component  $\langle \bar{u}''\bar{w}'' \rangle$  at elevation  $y/d = 3$ , and two streamwise locations for  $x/d = 2$  and  $x/d = 3.5$ .

$y/d = 3$ . The profiles are anti-symmetric about the central plane of the domain ( $z/d = 0$ ). An excellent agreement between numerical and experimental results is observed. From both figures, it is observed that the maximum Reynolds stress occurs at the same location where the maximum turbulence intensity exists ( $z/d \approx \pm 1$ ) and the shear production is the strongest due to boundary-layer development and separation from both side walls (associated with Kármán vortices). In two side regions far from the cylinder ( $|z/d| > 2$ ),  $\langle \bar{u}''\bar{w}'' \rangle$  becomes very small, which clearly indicates that the turbulent shear stresses are closely related to vortex motions and interactions, and strong shear layers immediately downstream of the two cylinder sides. In the following context, the streamwise evolution of the resolved Reynolds shear stress will be analyzed in a detailed manner.

Figure 4.19 shows the cross-stream profiles of the non-dimensionalized resolved Reynolds stress component  $\langle \bar{u}''\bar{w}'' \rangle$  in the recirculation and far downstream regions, respectively (at elevation  $y/d = 2$ ). In total, 10 different streamwise locations are selected to conduct the comparative study, which ranges from  $x/d = 1$  to 15. For all the streamwise locations studied, the maximum resolved Reynolds stress occurs at the spanwise locations  $z/d \approx \pm 1$  and decays significantly at  $z/d \approx \pm 2$ . As shown in

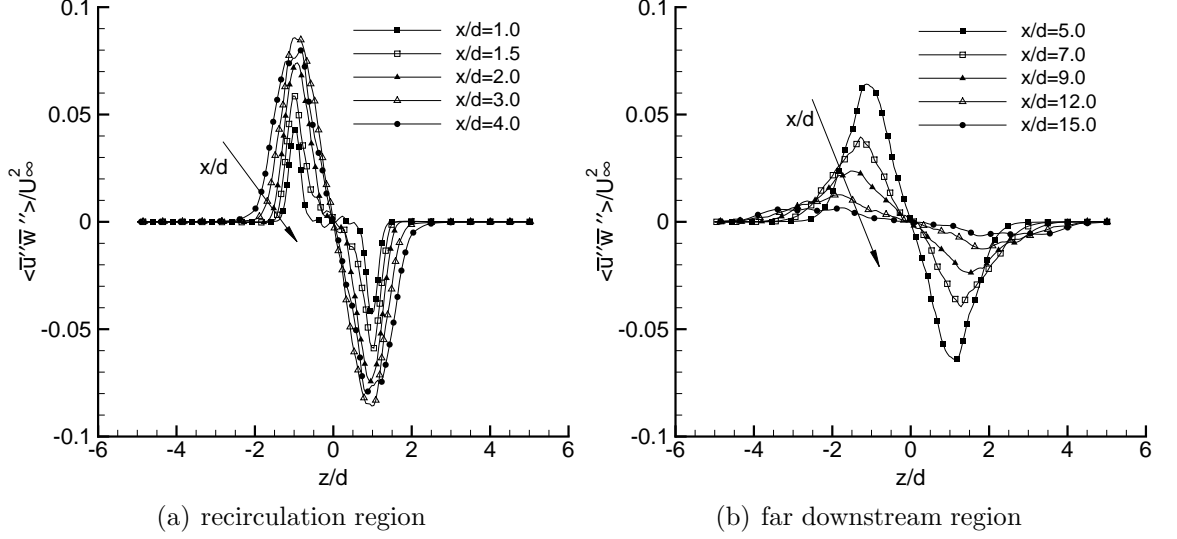


FIGURE 4.19: Cross-stream profiles of the non-dimensionalized mean resolved Reynolds stress component  $\langle \bar{u}''\bar{w}'' \rangle$  in the recirculation and far downstream regions at elevation  $y/d = 2$ . Data points are labeled using symbols at segments with the length of 3% of the total height of the frame.

Fig. 4.19a, the maximum resolved Reynolds stress occurs at the streamwise location  $x/d = 3.0$ . In the far downstream region, (see Fig. 4.19b), the profile of  $\langle \bar{u}''\bar{w}'' \rangle$  still keeps its dual-peak pattern at all locations, however, the magnitude of its peak values keeps decaying as the distance from the cylinder increases. This trend continues and eventually at  $x/d = 15$ , the resolved Reynolds shear stress becomes trivial across the domain, indicating that the energetic turbulent motions and interactions induced by the cylinder decay gradually and turbulence level eventually drops to the background level in the far downstream region.

The time frequency spectra  $E_{ij}$  of the resolved instantaneous turbulent flow can be determined through the following equation

$$E_{ij}(f) = \frac{2}{\pi} \int_0^{f_c} R_{ij}(s) \cos(fs) ds \quad , \quad (4.2)$$

where  $f$  represents the frequency,  $f_c$  is the cut-off frequency,  $R_{ij}(s) \stackrel{\text{def}}{=} \langle \bar{u}_i''(t)\bar{u}_j''(t+s) \rangle$  is the so-called temporal autocovariance, and  $s$  is the time interval based on which the autocovariance is calculated. The equation implies that the resolved turbulence kinetic energy (TKE)  $k$  is equal to one half the integral of the trace of  $E_{ij}$  (i.e.,  $E_{ii}$ ,

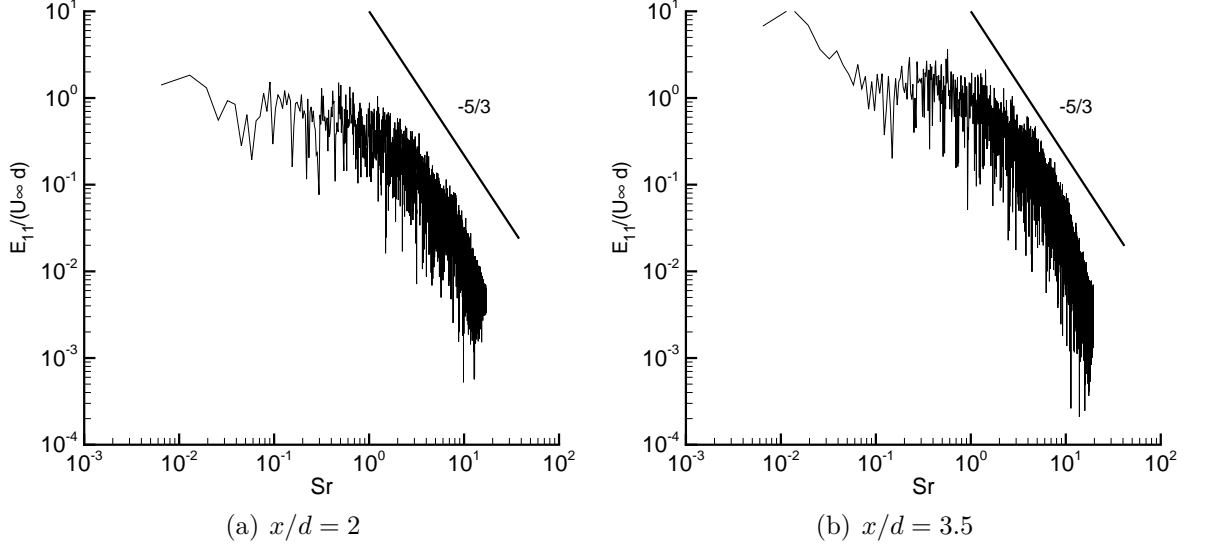


FIGURE 4.20: Non-dimensionalized temporal energy spectra for the resolved streamwise velocity component in the central plane ( $z/d = 0$ ), at the elevation  $y/d = 4$  and two streamwise locations  $x/d = 2$  and  $x/d = 3.5$ .

the temporal energy spectra) over the entire range of resolved frequencies, viz.

$$k = \frac{1}{2} \langle \bar{u}_i''(t) \bar{u}_i''(t) \rangle = \frac{1}{2} R_{ii}(0) = \frac{1}{2} \int_0^{f_c} E_{ii}(f) df \quad . \quad (4.3)$$

Figures 4.20a and 4.20b show the temporal energy spectra for the resolved streamwise velocity fluctuations at the elevation  $y/d = 1$  and streamwise locations  $x/d = 2$  and  $x/d = 3.5$  in the central plane of the domain ( $z/d = 0$ ). In the figure, the energy spectra has been non-dimensionalized as  $E_{ii}/(U_\infty d)$ . The frequency has also been non-dimensionalized and is represented by the Strouhal number defined as  $Sr = fd/U_\infty$ . According to Tennekes and Lumley [138], three distinct subranges are expected to appear in the energy spectra: the first subrange contains the flow TKE at very small time frequencies (spatially, corresponding to energetic large-scale eddy motions); the second part is the so-called inertial subrange where the energy cascade conserves across each frequency and the spectrum slope features a constant value,  $-5/3$ , following the well-known ‘‘Kolmogorov’s  $-5/3$  law’’ (or, ‘‘K41 theory’’); and the third part is the viscous dissipation subrange corresponding to high-frequency turbulent motions (spatially, corresponding to less energetic small-scale eddy motions). By comparing

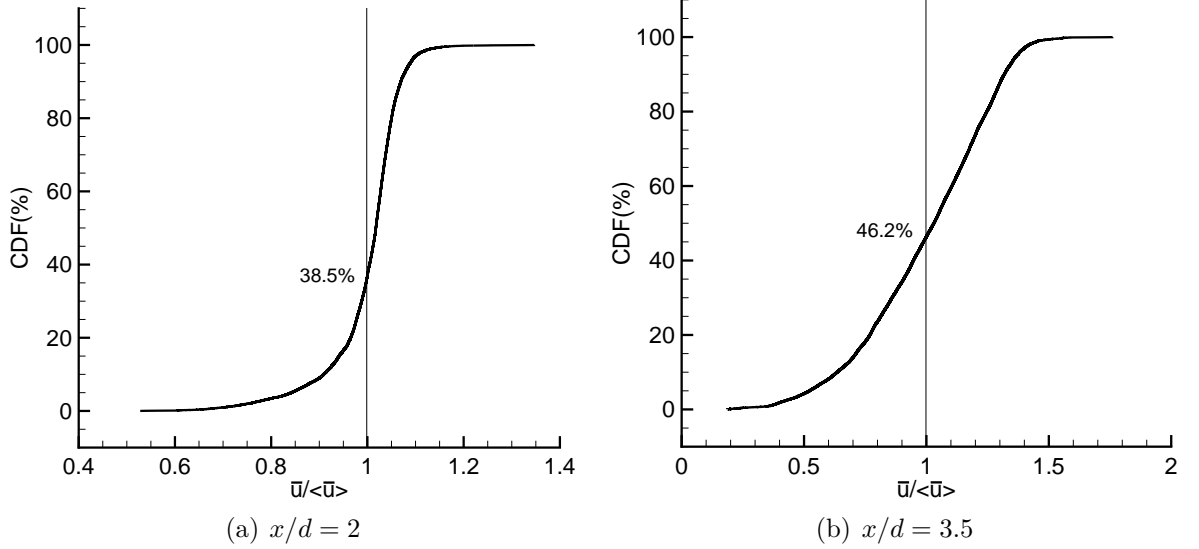


FIGURE 4.21: Cumulative distribution function for the resolved streamwise velocity component in the central plane ( $z/d = 0$ ), at the elevation  $y/d = 4$  and two streamwise locations  $x/d = 2$  and  $x/d = 3.5$ .

Figs. 4.20a and 4.20b, it is observed that the patterns of the spectra of the resolved streamwise velocity fluctuations at two locations  $x/d = 2$  and  $x/d = 3.5$  are similar to each other, however, the resolved TKE level of the streamwise contributions at  $x/d = 3.5$  is higher than that at  $x/d = 2$ , especially at low frequencies. As is evident in Figs. 4.20a and 4.20b, the spectra at both locations show that the energy cascades from large- to small-scales eddies, going through the inertial subrange. This indicates that the simulation has been able to resolve most of the energy of turbulent eddies (i.e., energy containing eddies), implying that the resolution is fine enough to capture the dominant flow features.

The resolved instantaneous velocity field analyzed above based on the temporal energy spectra can be further studied using the cumulative distribution function (CDF) defined as

$$F_{\alpha}(\beta) = \int_{-\infty}^{\beta} f_{\alpha}(\gamma) d\gamma \quad , \quad (4.4)$$

where CDF  $F_{\alpha}(\beta)$  is the integral of the probability density function (PDF)  $f_{\alpha}$  of a random variable  $\alpha$ , which describes the probability that the value of  $\alpha$  is less than or equal to  $\beta$  (i.e.,  $F_{\alpha}(\beta) = P(\alpha \leq \beta)$ ). Figures 4.21a and 4.21b show the CDF for

the streamwise velocity component at same locations used for Fig. 4.20. As shown in Fig. 4.21a, the CDF corresponding to  $\bar{u} = \langle \bar{u} \rangle$ , is 38.5%. This indicates that at  $x/d = 2$ , the number of fluctuations causing the instantaneous resolved streamwise velocity below the mean value  $\langle \bar{u} \rangle$  is smaller than that causing  $\bar{u}$  to be above the mean value. As a consequence, the amplitudes of oscillations causing  $\bar{u}$  to be below  $\langle \bar{u} \rangle$  must be larger than those causing  $\bar{u}$  to be above  $\langle \bar{u} \rangle$ . This further implies that a significant portion of the streamwise contribution to the TKE comes from oscillations causing the instantaneous resolved velocity  $\bar{u}$  to be below the mean value  $\langle \bar{u} \rangle$  (with higher oscillating amplitudes). As shown in Fig. 4.21b, at  $x/d = 3.5$ , the CDF corresponding to  $\bar{u} = \langle \bar{u} \rangle$  is 46.2%. This shows that as the streamwise distance increases from  $x/d = 2$  to 3.5, the CDF gradually evolves towards a symmetric shape and the numbers of fluctuations causing  $\bar{u}$  to be below and above the mean value are close to each other. Through a perusal of Figs. 4.21a and 4.21b, it is evident that the tails of the CDF profile at  $x/d = 2$  are much flatter in comparison with those at  $x/d = 3.5$ . This indicates that at  $x/d = 2$ , the magnitude of velocity fluctuations are very close to that of the mean value and all the velocity fluctuations are trapped through a very narrow band. However, at  $x/d = 3.5$ , oscillations with higher amplitudes are permitted. This is consistent with the previous analysis of the energy spectra that the TKE level at  $x/d = 3.5$  is higher than that at  $x/d = 2$ .

### 4.2.3 SGS effects

In this subsection, the SGS dynamics and the effect of SGS modeling on the resolved flow are studied. The streamwise evolution of the SGS stress and SGS viscosity, and the kinetic energy transfer rate between the resolved and subgrid scales are thoroughly analyzed.

Figure 4.22 shows the cross-stream profiles of the non-dimensionalized mean SGS stress component  $\langle \tau_{13} \rangle$  (as the SGS counterpart of the resolved Reynolds stress component  $\langle \bar{u}''\bar{w}'' \rangle$  previously shown in Fig. 4.19) in same locations as for Fig. 4.19. Among all the streamwise locations studied, the highest magnitude of the SGS stress

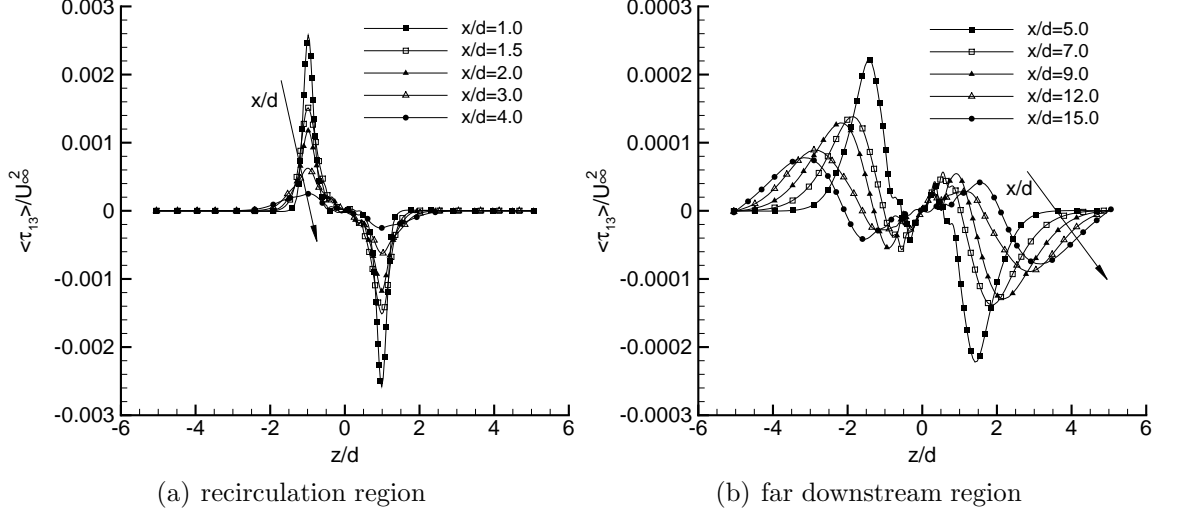


FIGURE 4.22: Cross-stream profiles of the non-dimensionalized mean SGS shear stress  $\tau_{13}$  in the recirculation and far downstream regions at elevation  $y/d = 2$ . Data points are labeled using symbols at segments with the length of 3% of the total height of the frame.

is up to 8% of the local resolved Reynolds stress  $\langle \bar{u}''\bar{w}'' \rangle$ . As shown in Fig. 4.22a, the maximum value of the SGS stress  $\langle \tau_{13} \rangle$  occurs at  $x/d = 1.0$  and its magnitude continues to decrease as the streamwise distance from the cylinder increases. In the recirculation region, the highest magnitude of the SGS stress occurs at  $z/d \approx \pm 1$  and decays significantly in the far side region for  $|z/d| > 2$  (similar to the trend observed in the profile of the resolved Reynolds stress in Fig. 4.19). This indicates that far from the cylinder in the spanwise direction, the effects of the turbulent shear layers induced by the two sides of the cylinder is much reduced, and consequently, both the resolved turbulent shear stresses and the SGS shear stresses decay significantly. In the far downstream region (see Fig. 4.22b), the magnitudes of the peak values of  $\langle \tau_{13} \rangle$  decrease and the corresponding peak locations move in the spanwise direction from  $z/d = \pm 1.5$  to  $z/d = \pm 3.5$  as the streamwise distance from the cylinder increases from  $x/d = 5$  to  $x/d = 15$ . As the flow runs downstream, the turbulent shear layers and eddy motions triggered by the cylinder spread in the cross-stream direction, which further facilitates the transport SGS shear stresses in the spanwise direction.

The SGS kinetic energy (KE) dissipation rate is defined as  $\varepsilon_{sgs} \stackrel{\text{def}}{=} -\tau_{ij}^* \bar{S}_{ij}$ , which represents the local transfer of KE between the filtered and subgrid scales, functioning

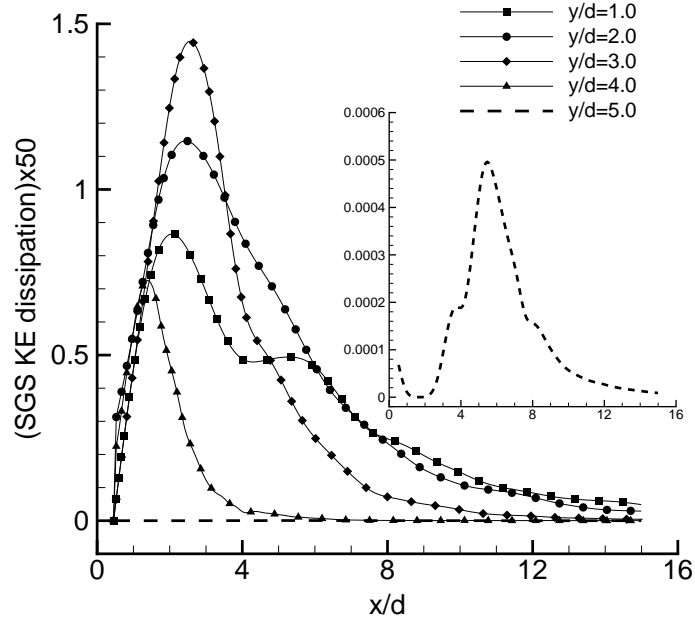


FIGURE 4.23: Streamwise profiles of the mean SGS KE dissipation rate  $\langle \varepsilon_{sgs} \rangle$  at different elevations downstream of the cylinder in the central plane (located at  $z/d = 0$ ). All the quantities shown in the figure have been non-dimensionalized using  $U_\infty^3/d$ . Data points are labeled using symbols at segments with the length of 3% of the total height of the frame.

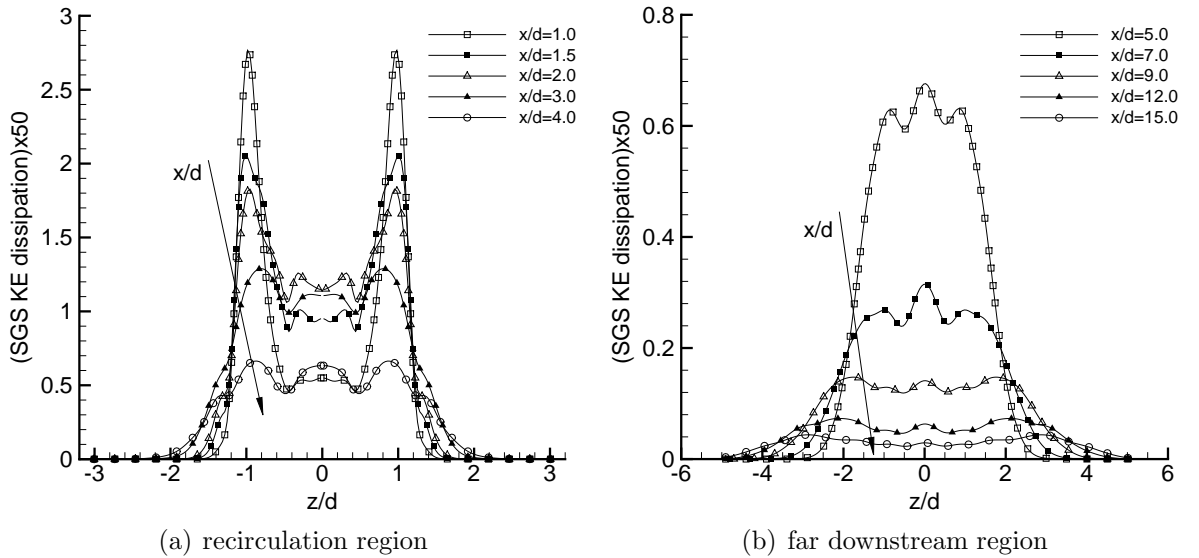


FIGURE 4.24: Cross-stream profiles of the mean SGS KE dissipation rate  $\langle \varepsilon_{sgs} \rangle$  in the recirculation and far downstream regions at elevation  $y/d = 2$ . All the quantities shown in the figure have been non-dimensionalized using  $U_\infty^3/d$ . Data points are labeled using symbols at segments with the length of 3% of the total height of the frame.

as a KE sink to the large resolved motions and a KE source to the SGS motions. Figure 4.23 demonstrates the streamwise evolution of the mean SGS dissipation rate  $\langle \varepsilon_{sgs} \rangle$  at different elevations in the central  $x$ - $y$  plane (located at  $z/d = 0$ ). In the figure, the mean SGS KE dissipation rate has been non-dimensionalized using  $U_\infty^3/d$ . A general feature shown in Fig. 4.23 is that the streamwise profiles peak in the immediate downstream region of the obstacle and then decay gradually in the streamwise direction. By definition, the magnitude of  $\varepsilon_{sgs}$  is directly influenced by  $\tau_{ij}^*$  (which reflects the SGS activities and turbulence level) and  $\bar{S}_{ij}$  (which reflects the gradients of the resolved velocities). From the previous analysis, we understand that the flow dynamics in the immediate downstream region of the obstacle feature a low pressure recirculation pattern and are affected significantly by the three strong shear layers issued by the top and two side surfaces of the cylinder. These three strong shear layers trigger flow instability, enhance local turbulence level and create large velocity gradients around them. As a consequence, the value of  $\langle \varepsilon_{sgs} \rangle$  peaks in rear of the cylinder. From the figure, the highest peak is observed at location  $y/d = 3$  and  $x/d \approx 3.1$ . As shown previously in Fig. 4.7, this particular location is close to the envelope of the recirculation bubble, where the flow is highly turbulent and velocity gradients are large. As a result, the KE transfer between the large resolved and subgrid scales is maximized at this location. Above the cylinder at  $y/d = 5$ , the values of  $\langle \varepsilon_{sgs} \rangle$  is much reduced in comparison with those at lower elevations. In order to clearly demonstrate its trend, the streamwise profile of  $\langle \varepsilon_{sgs} \rangle$  at  $y/d = 5$  is enlarged separately using a subfigure. Figure. 4.23 clearly shows that the mean local KE transfer rate (as represented by  $\langle \varepsilon_{sgs} \rangle$ ) between the resolved and subgrid scales is the highest within the immediate wake of the cylinder (for  $y/d < 4$  and  $x/d < 6$ ). However, in the region above or far downstream of the cylinder, the value of  $\langle \varepsilon_{sgs} \rangle$  decays significantly, implying that the SGS activities are much reduced in the background turbulence. This further clearly indicates that the enhanced SGS activities in this flow is a direct result of the turbulent wake induced by the cylinder, whose strength decays as the distance from (or above) the cylinder increases.

Figure 4.24 shows the spanwise profiles of the non-dimensionalized mean SGS

dissipation rate  $\langle \varepsilon_{sgs} \rangle$  in the recirculation and far downstream regions (at elevation  $y/d = 2$ ). As shown in Fig. 4.24a, in the recirculation region, a strong dual-peak pattern (with peak locations at  $z/d \approx \pm 1$ ) is observed, which is a direct consequence of two strong shear layers issued by the two cylinder sides accompanied with Kármán vortex shedding. The highest peak of  $\langle \varepsilon_{sgs} \rangle$  occurs at  $x/d = 1$ , and as the streamwise distance from the cylinder increases, the magnitude of the dual peaks decays monotonically. As is evident in Fig. 4.24b, in the far downstream region, as the streamwise distance from the cylinder increases from  $x/d = 5$  to  $x/d = 15$ , the magnitude of  $\langle \varepsilon_{sgs} \rangle$  decreases significantly, which is consistent with the pattern shown in Fig. 4.23. Furthermore, in comparison with the profiles of  $\langle \varepsilon_{sgs} \rangle$  shown in Fig. 4.24a, the distribution of  $\langle \varepsilon_{sgs} \rangle$  becomes much wider in the spanwise direction and the dual-peak pattern becomes less apparent in Fig 4.24b, indicating that as the streamwise distance from the cylinder increases, the flow becomes less turbulent and gradually recovers spanwise homogeneity (as for an open channel flow without cylinder). As a result, the SGS activities as indicated by  $\langle \varepsilon_{sgs} \rangle$  also become reduced in magnitude and homogeneous in spanwise direction in the far downstream region.

In order to further evaluate the strength of SGS activities and how it varies in the downstream region of the cylinder, the magnitude of the SGS viscosity relative to the kinematic viscosity of the fluid can be studied. For the DSM tested, the SGS kinematic viscosity can be defined as  $\nu_{sgs} \stackrel{\text{def}}{=} C_s \bar{\Delta}^2 |\bar{S}|$ . Figure 4.25 shows the streamwise profiles of  $\langle \nu_{sgs} \rangle / \nu$  at different elevations downstream of the cylinder. As shown in the figure, right on the leeward surface ( $x/d = 0.5$ ) of the cylinder, the value of  $\langle \nu_{sgs} \rangle / \nu$  is zero, identically. This is because  $\tau_{ij} \equiv 0$  right on a solid surface. Under the cylinder height ( $y/d \leq 4$ ) in the immediate downstream region ( $0.5 < x/d < 6$ ) of the cylinder, the SGS shear stress level increases significantly due to enhanced turbulent activities (see Fig. 4.22 for the streamwise evolution of the SGS stresses). The pattern that the SGS stress level (as well as the value of  $\langle \nu_{sgs} \rangle / \nu$ ) enhances and peaks within the immediate wake of the cylinder (for  $y/d < 4$  and  $x/d < 6$ ) is consistent with previous observation of the increased local KE flux from large resolved to subgrid scales in Fig. 4.23. However, in the region above (for  $y/d = 5$ ) or far downstream

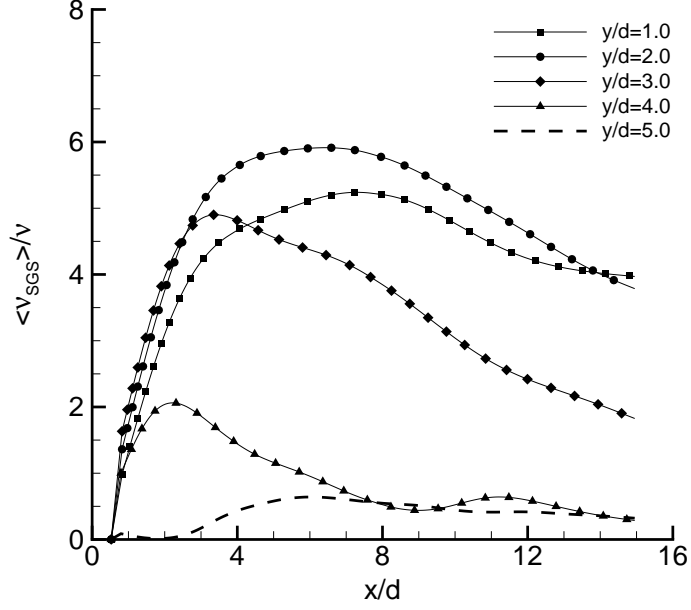


FIGURE 4.25: Streamwise profiles of the ratio of the SGS viscosity to the kinematic viscosity of the fluid ( $\langle \nu_{sgs} \rangle / \nu$ ) at different elevations downstream of the cylinder in the central plane (located at  $z/d = 0$ ). Data points are labeled using symbols at segments with the length of 3% of the total height of the frame.

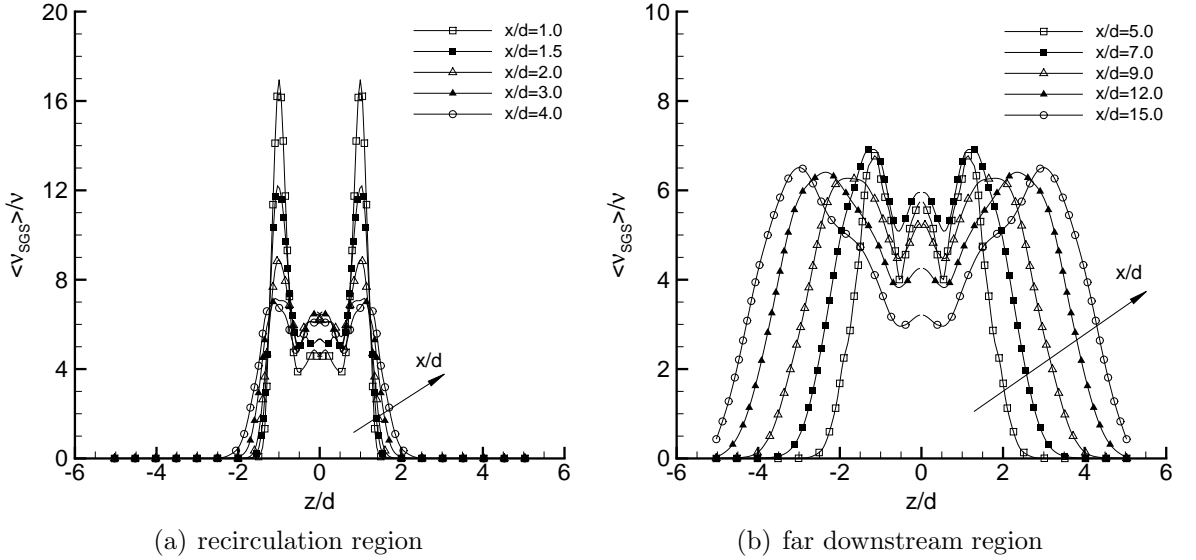


FIGURE 4.26: Cross-stream profiles of the ratio of the SGS viscosity to the kinematic viscosity of the fluid ( $\langle \nu_{sgs} \rangle / \nu$ ) at elevation  $y/d = 2$ . Data points are labeled using symbols at segments with the length of 3% of the total height of the frame.

(for  $x/d > 10$ ) of the cylinder, both the SGS stress level and the value of  $\langle \nu_{sgs} \rangle / \nu$  decrease, reflecting much reduced SGS activities in these regions. It should be noted that although the grid resolution becomes coarser in the far downstream region of the

cylinder which tends to increase the value of  $\nu_{sgs}$ , the turbulence level significantly drops in this region which tends to decrease the value of  $\nu_{sgs}$ .

Figure 4.26 demonstrates the spanwise profiles of  $\langle \nu_{sgs} \rangle / \nu$  in the recirculation and far downstream regions (at elevation  $y/d = 2$ ). Similar to the pattern shown previously in Fig. 4.24a for the mean SGS dissipation rate  $\langle \varepsilon_{sgs} \rangle$ , a dual-peak pattern is evident in Fig. 4.26a. The highest value of SGS viscosity occurs at  $x/d = 1.0$  and  $z/d \approx \pm 1$ , which is about  $\langle \nu_{sgs} \rangle / \nu \approx 17$ , indicating that the SGS effects are substantial in comparison with the viscous effects. These two peaks are due to the strong shear layers issued by both vertical sides of the obstacle, which significantly enhance local turbulent and SGS activities. As shown in Fig. 4.26a, at the same streamwise location ( $x/d = 1$ ), the value of  $\langle \nu_{sgs} \rangle$  becomes trivial for  $|z/d| > 2$ . This implies that at this downstream location, in regions far away from the cylinder sides, the flow is not influenced by the vortex shedding and both the turbulence level and SGS viscosity value are relatively low. As shown in Fig. 4.26b, as the distance from the cylinder increases, the peak value of  $\langle \nu_{sgs} \rangle$  decreases monotonically and its profile spreads wider in the spanwise direction as a result of the growth of turbulent wake.

### 4.3 Closure

Wall-resolved LES of turbulent wake behind a wall-mounted square cylinder with aspect ratio 4 and Reynolds number 12,000 has been performed. In comparison with the classical single cube flow case (for  $AR = 1$ ) of Rodi [52], Shah and Ferziger [57] and Yakhot *et al.* [45, 46], the current test case represents a challenging case for LES because of its relatively high aspect ratio and Reynolds number. Owing to the high aspect ratio of the cylinder, the flow is highly unsteady and exhibits complex vortex dynamics due to the motions and interactions of tip vortices from the cylinder free-end, Kármán vortices shed from the cylinder sides, and the developing and separating boundary layers over solid surfaces.

The instantaneous and mean structures of the resolved flow have been investigated

using a variety of visualization methods based on the instantaneous resolved pressure and velocity fields and TKE and TKE production rate. The frequency of Kármán vortex shedding has been well captured in the simulation and the predicted Strouhal number is 0.106, which is in excellent agreement with the reported measurement value [17–19]. In regions close to the sharp edges of the cylinder (top front edge and side edges), the resolved TKE production rate reaches its maximum. This is because in these special regions, the flow directly strikes the sharp edges of the cylinder, which generates large mean velocity gradients, triggers flow instability and shear layer separations, induces tip and Kármán vortices, and hence, increases the resolved Reynolds stress levels and the resolved TKE production rate. The resolved TKE level of the flow is tightly coupled with the resolved TKE production rate, and the maximum value of resolved TKE occurs behind the obstacle at  $x/d = 4.0$  and  $y/d = 2.0$ .

In a horizontal plane very close to the ground (at  $y/d = 0.03$ ), a horseshoe vortex has been observed based on time-averaged streamlines, which is an important feature for cylinder flows. The so-called saddle, nodal and focal points inside the horseshoe vortex are consistent with the previous classical studies on the formation of horseshoe vortex around bluff bodies [5, 44, 169]. However, at a higher elevation ( $y/d = 3$ ), two large counter-rotating vortices in the wake region and two small vortices adjacent to the obstacle side walls have been observed (based on time-averaged streamlines). The spatial extension of the recirculation bubble has been carefully investigated. It is observed that the streamwise length of the recirculation region increases as the ground wall is approached. Within the recirculation bubble, the largest suction effect (with the maximum negative pressure) occurs at  $x/d = 2.0$ . However, as the distance from the cylinder increases, the suction strength decreases gradually and the band of low resolved pressure around the cylinder gradually merges with the main background stream. In far downstream regions for  $x/d > 4$ , the alternating vortex shedding patterns are still apparent, however, the flow is mainly dominated by the main stream and the strength of low-pressure vortices decays significantly due to turbulent mixing, diffusion and dissipation.

Turbulence statistics including the resolved mean velocity profiles, Reynolds shear stress and turbulence intensities obtained from the simulation have been carefully compared against the experimental data of Bourgeois *et al.* [17, 18] and Sattari *et al.* [19]. Profiles of the non-dimensionalized resolved Reynolds stress component  $\langle \bar{u}''\bar{w}'' \rangle$  have been investigated in the recirculation and far downstream regions. It is observed that a dual-peak pattern consistently appears in the profile of  $\langle \bar{u}''\bar{w}'' \rangle$  at all the streamwise locations. The maximum resolved Reynolds stress occurs at  $z/d \approx \pm 1$  where the shear production is the strongest due to the presence of the large velocity gradient, and boundary-layer development and separation from the two side walls. However, the resolved Reynolds stress decays quickly in the cross-stream direction as the distance from the cylinder increases. In far side regions of the cylinder (for  $|z/d| > 2$ ), the value of  $\langle \bar{u}''\bar{w}'' \rangle$  is significantly reduced. Furthermore, the maximum stress decays as the streamwise distance from the cylinder increases, and eventually for  $x/d \geq 15$ , the resolved Reynolds shear stress becomes trivial. This indicates that significant turbulent shear stress levels are direct consequences of the interactions of the flow with the cylinder, which however, all decay (together with the strengths of induced vortices and TKE production rate) to the background turbulence level in the far downstream regions.

In the recirculation region, the resolved streamwise RMS velocity ( $\bar{u}_{rms}$ ) profile exhibits a dual-peak pattern as a result of the formation and separation of the strong shear layers on both sides of the cylinder. However, in the far downstream region, as the distance from the cylinder increases, the distance between the dual peaks in the cross-stream direction also increases. For the resolved spanwise RMS velocity ( $\bar{w}_{rms}$ ) profile, it is observed that the dual-peak pattern is only strongly expressed in the immediate downstream region of the cylinder. As the distance from the cylinder increases, the magnitude of  $\bar{w}_{rms}$  increases monotonically within the recirculation region. However, as the boundary of the recirculation bubble is approached, the dual-peak pattern in  $\bar{w}_{rms}$  profile becomes less apparent, indicating that alternating vortices generated from the two sides of the cylinder have spread spatially and reached a fully interactive and mixing state. For both streamwise and

spanwise RMS velocity profiles in the far downstream region, it is observed that the magnitude of RMS velocities decreases in the central region but increases in the far side regions, indicating that the flow TKE spreads in the cross-stream direction due to the turbulent, pressure and viscous diffusion mechanisms. It is observed that the maximum value of the resolved spanwise RMS velocity is approximately 30% higher than that of the streamwise RMS velocity, and the maximum resolved TKE and the maximum resolved spanwise RMS velocity occur approximately at the same location ( $x/d = 4.0$ ). This indicates that the spanwise velocity fluctuations make the most significant contribution to the resolved TKE at this special location.

By analyzing streamwise profiles of the mean SGS dissipation rate ( $\langle \varepsilon_{sgs} \rangle$ ) in the central  $x$ - $y$  plane downstream of the cylinder, it was observed that at different elevations, the peak value of  $\langle \varepsilon_{sgs} \rangle$  is located within the immediate wake of the cylinder. It is observed that the streamwise profiles peak in the immediate downstream region of obstacle and then decay gradually in the streamwise direction. This is mainly due to the large velocity gradients created by the strong shear layers issued by the top and two sides of the cylinder. The highest peak of  $\langle \varepsilon_{sgs} \rangle$  occurred at location  $y/d = 3$  and  $x/d \approx 3.1$  which is close to the envelope of the recirculation zone, where the flow is highly turbulent and velocity gradient is large. Among the horizontal profiles for elevations lower than or equal to the cylinder height (i.e.,  $y/d \leq 4$ ), the profile at the elevation  $y/d = 4$  has the lowest peak which is approximately 50% of the highest peak at  $y/d = 3$ . Above the cylinder at  $y/d = 5$ , the value of  $\langle \varepsilon_{sgs} \rangle$  is much reduced in comparison with those at lower elevations. This indicates that the enhanced SGS activities in this flow are direct results of the turbulent wake induced by the cylinder. For the spanwise profiles of  $\langle \varepsilon_{sgs} \rangle$ , a strong dual-peak pattern is observed which is a direct consequence of two strong shear layers issued by the two cylinder sides accompanied with Kármán vortex shedding. As the streamwise distance from the cylinder increases, the dual-peak pattern of the SGS dissipation profiles decays monotonically and the distribution of  $\langle \varepsilon_{sgs} \rangle$  becomes much wider in the spanwise direction. This indicates that as the streamwise distance from the cylinder increases, the flow becomes less turbulent and gradually recovers spanwise homogeneity (as

for an open channel flow). As a result, the SGS activities as indicated by  $\langle \varepsilon_{sgs} \rangle$  also become reduced in magnitude and homogeneous in spanwise direction in the far downstream region.

## Chapter 5

# Wall-modeled LES of turbulent flow over a matrix of wall-mounted cubes submerged in a simulated atmospheric boundary layer

In this chapter, we aim at performing wall-modeled LES of turbulent flow over an array of 3-D wall-mounted obstacles using the wall model proposed by Wang and Moin [75]. The matrix of cubes is fully submerged in a modeled urban atmospheric boundary layer (ABL). An inlet boundary condition has been proposed to reproduce the high turbulence level of the approaching flow based on generation of grid turbulence. The spatial evolution of flow structures and temporal cascades of the kinetic energies have been examined in terms of their transport equations and resolved spectra. In order to validate the LES approach, numerical predictions of turbulence statistics have been thoroughly validated against a set of comprehensive water-channel measurement data.

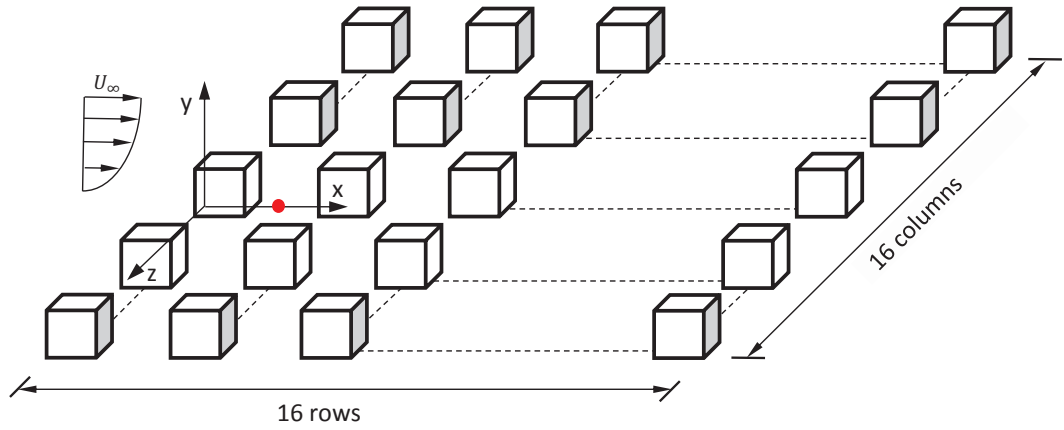


FIGURE 5.1: Schematic of the matrix of  $16 \times 16$  wall-mounted cubes and the coordinate system. The side length of the cube is  $d = 31.75$  mm.

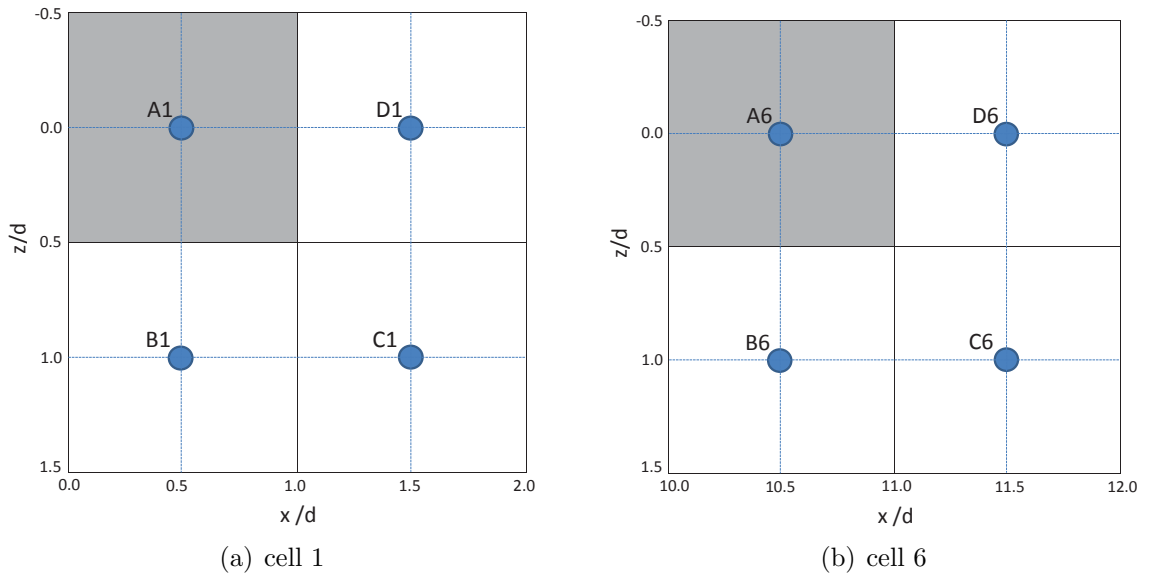


FIGURE 5.2: Locations in cell 1 and cell 6 selected for comparison of the predicted and measured velocity profiles. The non-dimensional coordinate ( $x/d$ ) in these two subfigures specifies the streamwise location with respect to the coordinate system defined in Fig. 5.1.

## 5.1 Test case and computational domain

The test case is based on the water-channel experiments of Yee *et al.* [24] and Hilderman and Chong [25]. In their experiments, a regular array of  $16 \times 16$  wall-mounted cubes with side length of  $d = 31.75$  mm were immersed in an emulated neutrally stratified urban ABL. Figure 5.1a shows the schematic of the array of wall-mounted cubes in the water-channel experiment. The cubes were strictly aligned with a uniform spacing of  $d$  in the streamwise and spanwise directions. The Reynolds number based on the cube’s side length and free-stream velocity ( $U_\infty = 0.38$  m/s) was  $Re \stackrel{\text{def}}{=} \frac{U_\infty d}{\nu} = 12,005$ . Here,  $\nu$  is the kinematic viscosity of the fluid.

The velocity field was measured using a 4-beam 2-component TSI fiber-optic LDA powered by an argon-ion laser. Titanium dioxide was used as seed particles for the LDA, and the data rate for the LDA measurements was typically 50–500 Hz. Velocity measurements (including mean and fluctuating velocities) were made along vertical lines at different locations in two central cells in the first and sixth rows. Here, a “cell” represents the repeating unit required for generating the regular array of obstacles which occupies an area of  $2d \times 2d$  in the  $x$ - $z$  plane with the cube placed in its upper-left quadrant. Four locations in the first- and sixth-row cells have been chosen for comparison of the predicted and measured velocity profiles. Figure 5.2 schematically shows the first- and sixth-row cells and the selected four measurement locations. In Fig. 5.2a, point A1, represents the location on top of the obstacles, points B1 and C1 represent locations in the streamwise canyon street and point D1 is inside the canyon at the midpoint between the first and second rows of obstacle. Here, subscript 1 refers to cell 1. Similar measurement locations in cell 6 are demonstrated in Fig. 5.2b and subscript 6 is used to indicate cell 6.

Given the fact that the flow conditions are symmetric in the spanwise direction and in order to moderate the computational cost, only the 5 central columns of cubes have been considered in the simulation. The range of the computational domain is:  $x/d \in [-22.5, 47]$ ,  $y/d \in [0, 7]$  and  $z/d \in [-5, 5]$ . This implies that an inlet fetch of  $22.5d$  is added before the first row of cubes, and an outlet fetch of  $16d$  is considered

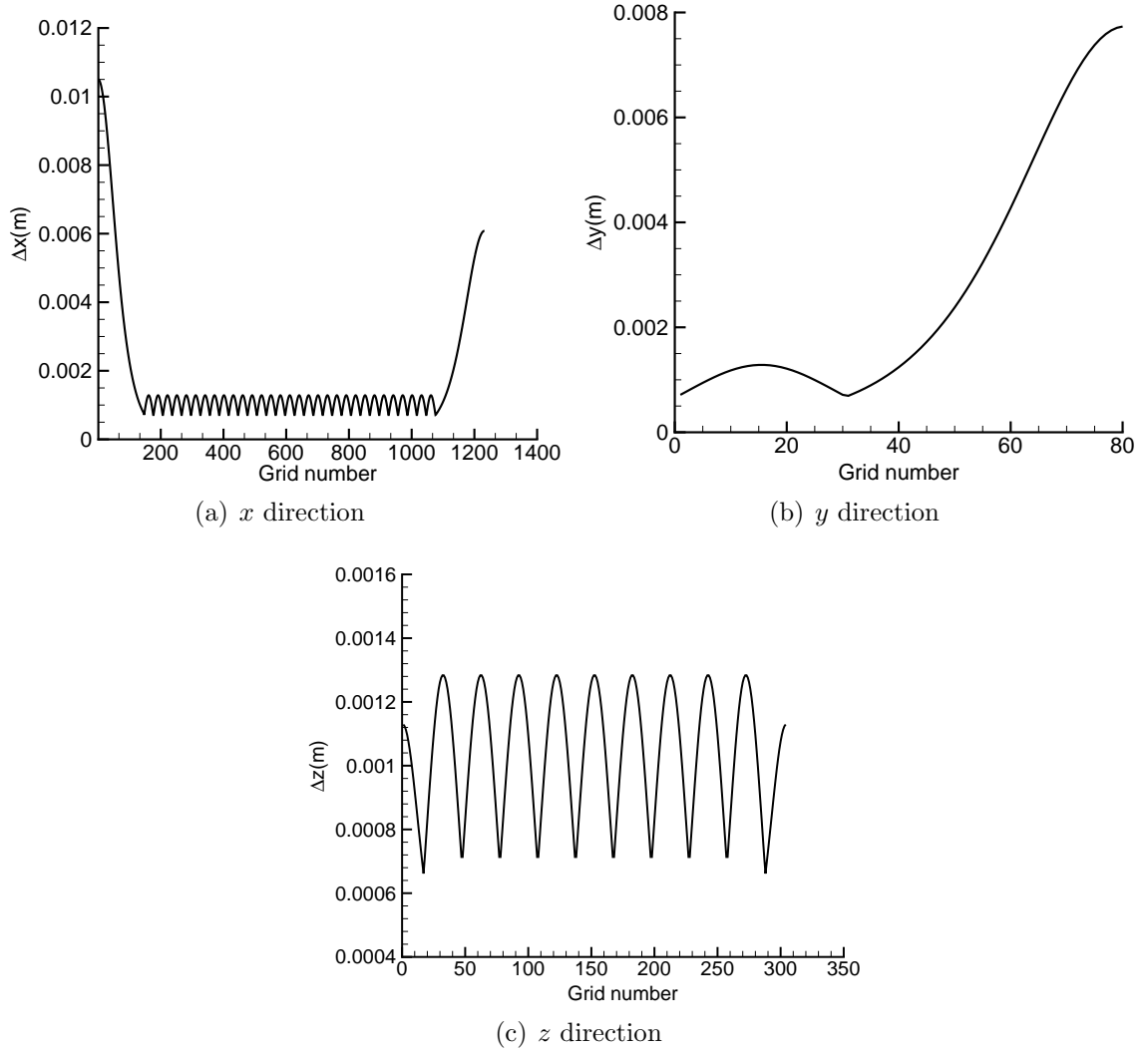


FIGURE 5.3: Grid distribution in streamwise, vertical and spanwise directions, respectively.

after the last row of cubes. In total,  $1232 \times 80 \times 304$  grid points have been used to discretize the domain in the streamwise, vertical and spanwise directions, respectively. Figure 5.3 shows the non-uniform grid distribution in the streamwise, vertical and spanwise directions. As demonstrated in this figure, the grid resolution is refined near all solid surfaces in all three directions, and the grid size is smoothly stretched (with a stretching rate kept less than 10% to avoid numerical instabilities arising from sudden change in the grid sizes). According to Madabhushi and Vanka [168], a slow growth rate of the grid size is required in order to maintain a global second-order

truncation error in non-uniform grid systems. In order to perform parallel computing, the computational domain is divided into  $11 \times 10 \times 2$  sub-domains in the  $x$ ,  $y$  and  $z$  directions, respectively, and 220 processors have been used accordingly.

The SGS stress model used for closure of the system of filtered mass and momentum equations is the dynamic non-linear model (DNM) (equation 2.15 in section 2.2.2) proposed by Wang and Bergstrom [95]. In this simulation, the code was first run for approximately 2 flow-through times (the time required for the mean flow to travel throughout the domain) to allow the flow field to fully evolve to a statistically stationary state. The flow statistics were then collected through a course of approximately 10 flow-through times. During the simulation, the time step was set to  $3 \times 10^{-4}$  s and the maximum CFL number was approximately 0.3. The convergence criterion for the solution of flow governing equations was set to  $10^{-6}$  for the maximum difference between two time steps in each quantity in calculation (i.e.,  $\bar{u}$ ,  $\bar{v}$  and  $\bar{w}$ ) normalized by its spatially-averaged value obtained in the previous time step. The simulation was conducted on a local 252-core computer cluster. In total, more than 100,000 CPU-hours have been spent to perform the simulation and collect the statistics.

### 5.1.1 Boundary conditions

In order to estimate the wall shear stress, the wall model of Wang [134] and Wang and Moin [75] (equation 3.29 in section 3.3.1.1) has been applied to solid surfaces.

Since the purpose of the original water-channel experiment was to simulate a modeled rough-wall ABL, the approaching flow had an exceptionally high turbulence level. In fact, the lowest turbulence intensity at the inlet and above the cubes was approximately 10% of the magnitude of the mean flow velocity. Indeed, reproducing such high turbulence level typical of a developing urban ABL of practical interests using numerical method is a very challenging topic. As reviewed in chapter 3, many research works have been devoted on developing effective inflow conditions for DNS and LES, based on either synthetic turbulence [144, 146–150, 153], or deterministic

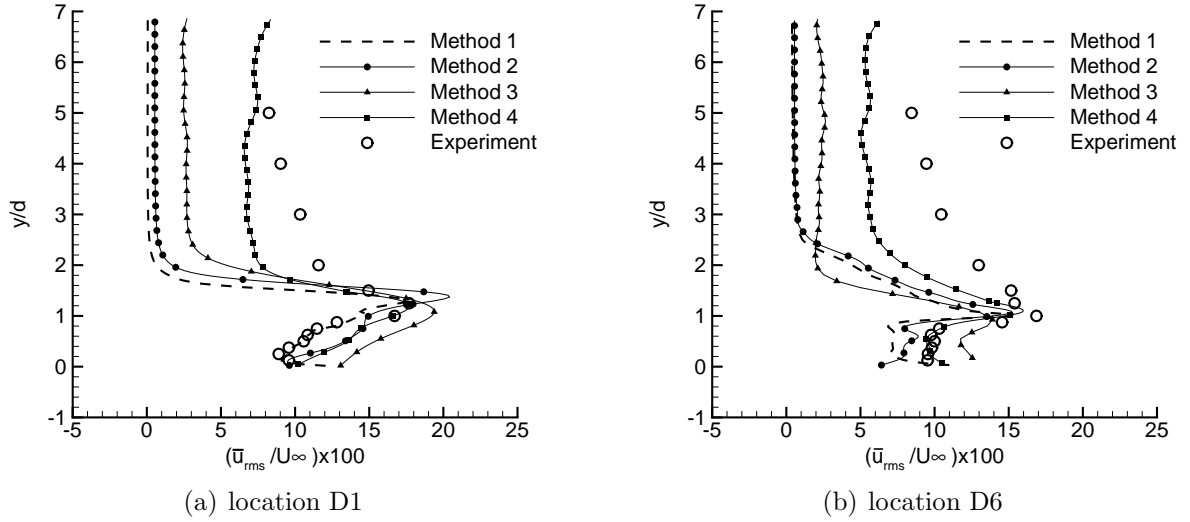


FIGURE 5.4: Effects of 4 different inlet conditions on the predicted streamwise RMS velocity level at the measurement locations D1 and D6.

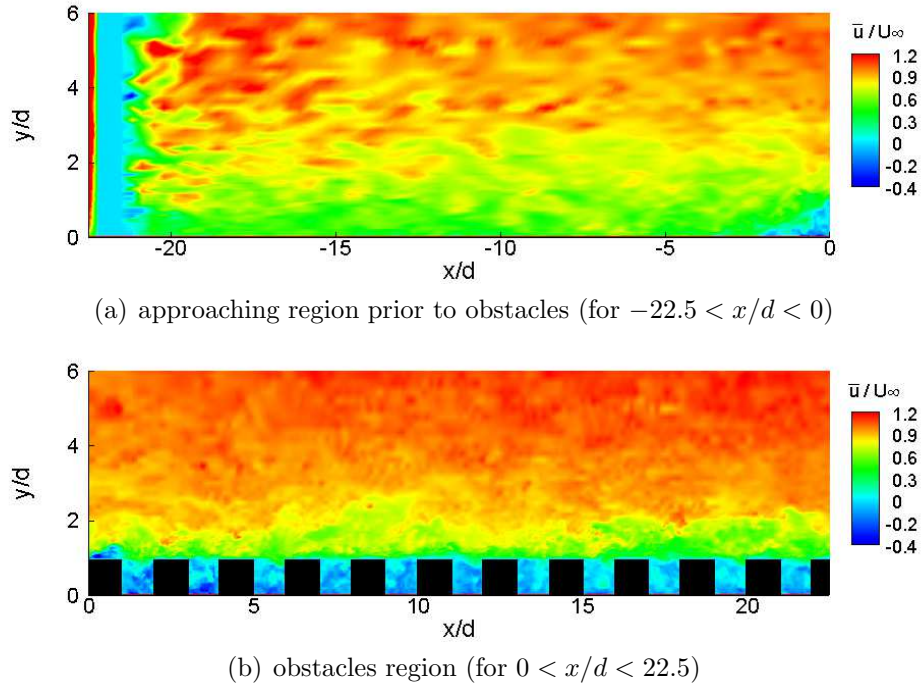


FIGURE 5.5: Contours of the resolved instantaneous streamwise velocity in the central  $x$ - $y$  plane (located at  $z/d = 0$ ).

computations using precursor simulations and rescaling methods [145, 157, 159–162].

In the context of urban flow simulation, a simple treatment is to assume that the flow is fully-developed such that a periodic boundary condition can be used in the streamwise direction (e.g., Cheng *et al.* [53], Xie and Castro [56], Coceal *et al.* [49]

and Nićeno *et al.* [67]). However, it will be demonstrated in the following context that this simplified treatment method significantly underestimates the TKE level for an urban ABL flow of practical interests, which typically features high turbulence levels (10% and above) and is typically developing (rather than fully-developed) in the streamwise direction. In order to mimic such high turbulence level of a realistic developing urban ABL flow, it is seen in literature that some unphysical perturbations are superimposed to the flow field. For instance, in the studies of Hanna *et al.* [68] and Shi *et al.* [69], at the inlet of the boundary-layer flow, time-correlated random fluctuations are prescribed. In contrast to the previous methods based on either periodic boundary conditions or unphysical perturbations, in the present work, we aim at generating a simulated highly turbulent urban ABL flow by using a physical inlet conditions. In order to refine the research, a comparative study is conducted, which includes tests of four different inlet boundary conditions: 1) prescribing the mean turbulent velocity profile with no fluctuations following the approach of Schlüter *et al.* [161]; 2) applying periodic boundary condition to the streamwise direction following the approach of Cheng *et al.* [53]; 3) using a turbulent plane channel flow simulation as a precursor following the approach of Lund *et al.* [159]; and 4) using a solid grid at the inlet plane to trigger the flow transition and facilitate turbulent fluctuations. The solid grid placed at the inlet consists of a set of horizontal and vertical lines fitted on the computational grid. In this research, the blockage ratio for the grid was approximately 19%.

In order to evaluate the performances of these four inlet boundary condition methods, the profiles of the resolved streamwise RMS velocity predicted by LES at position D1 (at  $x/d = 1.5$ , in cell 1) and D6 (at  $x/d = 11.5$ , in cell 6) are compared against the experimental data. As is evident in Figs. 5.4a and 5.4b, classical methods 1 and 2 totally failed in a sense that they were not able to produce more than 0.5% of turbulence in regions above the cubes. Also as a classical approach, method 3 performed slightly better than methods 1 and 2, and was able to generate up to 3% of turbulence level in regions above the cubes. In contrast to the unsatisfactory performances of classical methods 1, 2 and 3, the proposed method (i.e.,method 4)

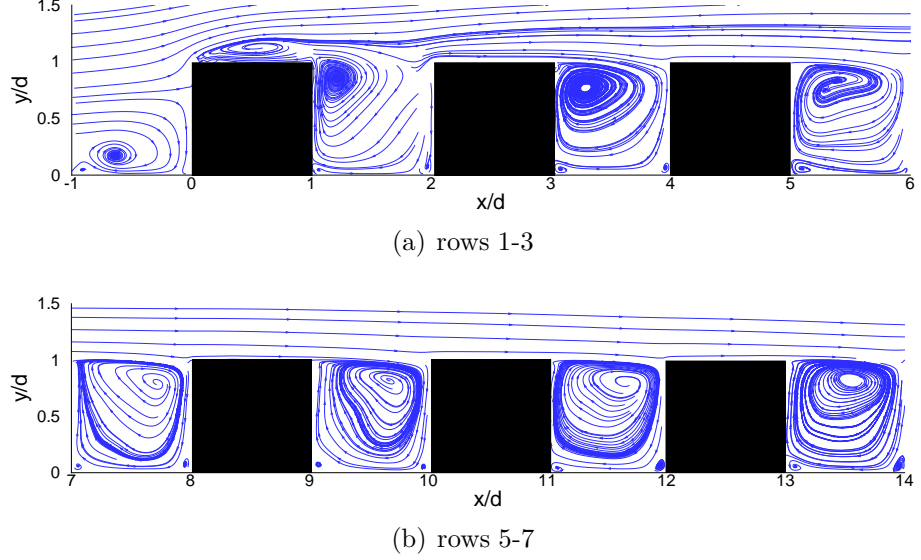


FIGURE 5.6: Time-averaged streamlines around obstacles in different rows, demonstrated in the central  $x$ - $y$  plane at  $z/d = 0$ .

was able to produce the highest turbulence intensity (up to 7%) in the present work. For method 4, it is needed to extend the approaching fetch of the domain (between the inlet and the first row of the cubes) long enough to avoid any direct interference of the immediate wakes produced at the inlet plane with the wall-mounted cubes, and also to allow the flow to reach to a sustainable turbulence level. Once a sustaining turbulence level is achieved, the time-averaged velocity profile obtained is expected to match to the measured one, with the presence of a constant level of fluctuations. Based on several numerical experiments, it is observed that the required distance between the inlet and the first row of cubes should be kept at least  $20d$ . However, since the grid resolution in the approaching region does not require to be considerably high, the additional computational cost arising from the extended inlet fetch is only approximately 10%. Figures 5.5a and 5.5b show the instantaneous streamwise velocity contour in the central  $x$ - $y$  plane located at  $z/d = 0$  in the approaching and cube regions, respectively. As is evident in Fig. 5.5a, significant turbulence is triggered right behind the solid grid located at  $x/d \approx -22$ , reaching a stable sustainable level. As the distance from the inlet increases, the turbulent patches quickly become uniform. Then, at the  $x/d = 0$ , the turbulent flow starts to strike the first row of obstacles.

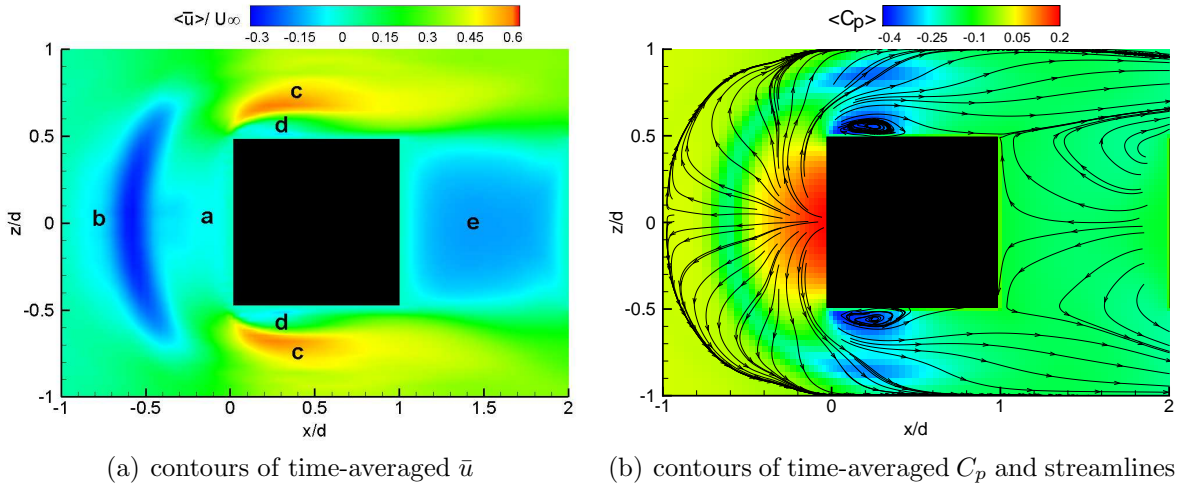


FIGURE 5.7: Horseshoe vortex in front of the first-row obstacle in the central column, visualized using time-averaged resolved streamwise velocity, pressure coefficient and streamlines in the  $x$ - $z$  plane at elevation  $y/d = 0.25$ .

The outlet boundary has been located  $16d$  away from last row of the cubes and the Neumann boundary condition has been applied to the outlet boundary. Slip condition has been considered for the upper free-surface boundary.

## 5.2 Results and discussions

In this section, the LES results will be presented to analyze characteristics of the instantaneous and mean flow field. The flow structures and their evolution and transport of kinetic energies will be thoroughly studied. Turbulence flow statistics obtained from the numerical simulation will be also compared against the available water-channel measurement data of Yee *et al.* [24] and Hilderman and Chong [25].

### 5.2.1 General description of the flow field

The characteristics of the highly-disturbed flow within and above the cubic obstacles have been demonstrated vividly using the contours of the resolved instantaneous velocity in Fig. 5.5b, which has been briefly discussed in the previous subsection. From the viewpoint of boundary-layer theory, the flow field studied here can be

classified as a ‘d’-type rough-wall flow (or, a skimming flow), since the ratio of the downstream pitch (or, length of a cell) to the height of cubes arrays is only  $2d/d = 2$ . Above the canopy, the high-speed flow is highly turbulent and quickly skims over the cubic obstacle array. Within the canopy, however, the speed of the flow is much reduced and recirculation patterns may exhibit (indicated by negative streamwise velocities). These features can be better viewed in Fig. 5.6, which shows the time-averaged streamlines in the central  $x$ - $y$  plane around the first seven rows of obstacles. As shown in Fig. 5.6a, a large vortex is observed in the stagnant region (impinging zone) in front of the first row of obstacles. This is the signature of the horseshoe vortex formed in front of the first row of obstacles, which will be thoroughly discussed in the next paragraph. Also, a small recirculation region has been formed only above the rooftop of the first obstacle which is due to the strike of the flow at the sharp front edge of the obstacle. At the rooftop of the first obstacle, a strong shear layer and large mean velocity gradient form, which further trigger flow instability and induce boundary layer separation. It is also clearly observed in Figs. 5.6a and 5.6b that the vortical structures (in terms of the location and size of recirculating vortices between the cubes) in the canyon regions gradually evolve towards a self-similar state as the distance from the first row increases. The size and pattern of recirculating vortices between two adjacent cubic obstacles become increasingly similar after the fifth row.

In order to analyze the structure of the horseshoe vortex formed around the first row of cubes, a top view of contours of the time-averaged resolved streamwise velocity  $\langle \bar{u} \rangle$  in the central column (for  $-1 < x/d < 2$  and  $-1 < z/d < 1$ ) at elevation  $y/d = 0.25$  is shown in Fig. 5.7a. In Fig. 5.7b, contours of the time-averaged pressure coefficient in the same location is demonstrated, superimposed with time-averaged streamlines. As is evident in Fig. 5.7a, there are five distinct flow zones around the first-row obstacles: a) a stagnant zone formed in the immediate adjacency of the windward face of the first-row obstacles due to the impingement of the flow onto the obstacle; b) an arch-shaped negative velocity zone located in front of the stagnant region; c) a pair of acceleration zones formed symmetrically on the two sides of the obstacle, in which the streamwise velocity drastically increases due to the local

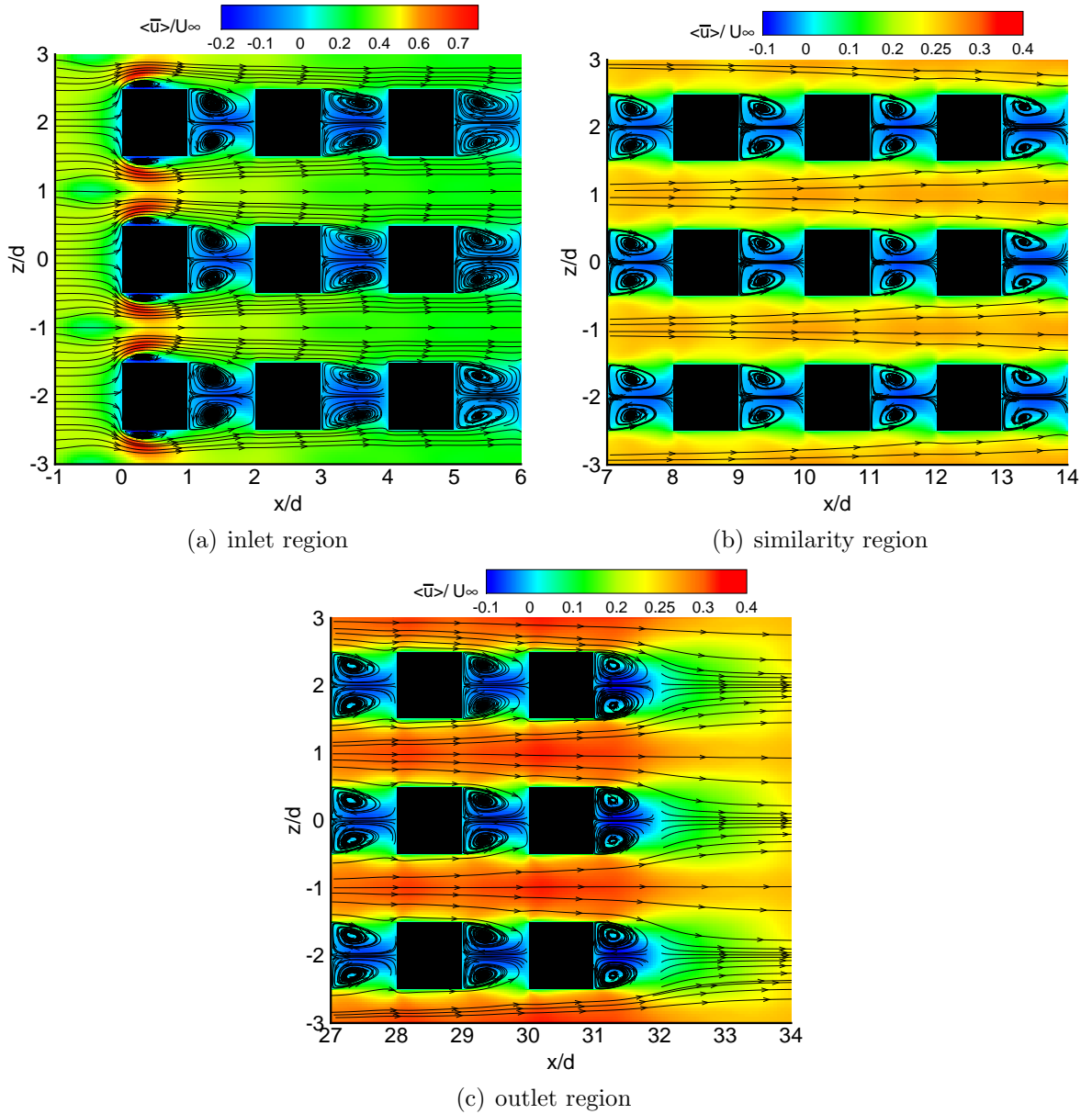


FIGURE 5.8: Contours of the time-averaged resolved streamwise velocity and time-averaged streamlines in  $x$ - $z$  planes at elevation  $y/d = 0.5$  and different streamwise regions.

blockage effects; d) a pair of small recirculation zones formed immediately adjacent to the side walls (under the acceleration zones) due to boundary layer separation; and e) a large recirculation zone formed behind the obstacles. The five flow regions mentioned above and the characteristic horseshoe vortex pattern around a first-row obstacle are also clearly shown using time-averaged streamlines in Fig. 5.7b. Corresponding to the five flow regions shown in Fig. 5.7a, the pressure distribution

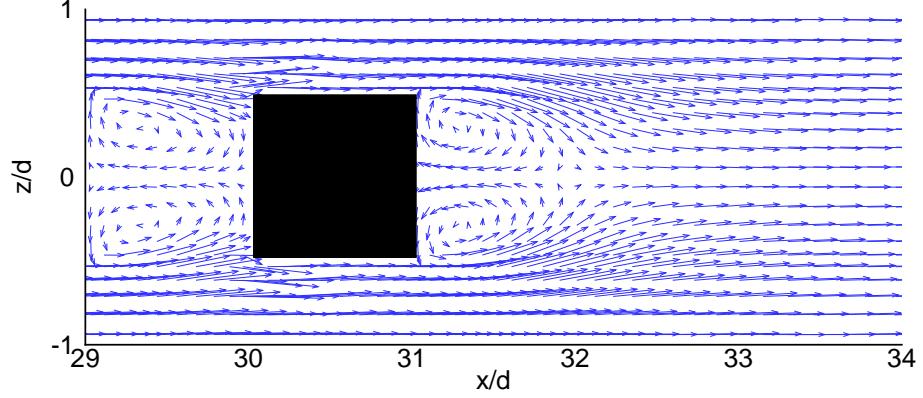


FIGURE 5.9: Top view of the time-averaged vector plot of the resolved velocity field around the last-row obstacle of the central column, in the  $x$ - $z$  plane at elevation  $y/d = 0.5$ .

shown in Fig. 5.7b exhibits an opposite trend in terms of its magnitude. Zone a centers around the stagnation point, where the pressure reaches the highest value. The high stagnation pressure then causes the reverse flow towards zone b. It shows intuitively in Fig. 5.7b that the horseshoe streamline pattern in the front of the obstacle is a result of this reverse flow and the approaching flow from the upstream. Also from Fig. 5.7b, it is clear that due to the acceleration of the flow on both sides of the obstacle, the pressure value drops significantly in zone c. Further according to Prandtl's classical boundary-layer theory, the pressure gradient in the  $z$ -direction (vertical to the mean flow direction) is trivial within the boundary layer. As such, the pressure in zone d is close to that in zone c, and therefore, also maintains at a low level. In comparison with the high pressure level in zone a, the pressure level in zone e is much lower. This pressure difference between the front and the rear of the obstacle is the exact cause of the form drag in building aerodynamics and wind engineering.

Figure 5.8 shows the time-averaged resolved streamwise velocity contours and time-averaged streamlines in the horizontal plane at half-cube height ( $y/d = 0.5$ ) in three streamwise regions (inlet, self-similarity and outlet regions). In Fig. 5.8a, the time-averaged streamlines shows that the free-stream flow strikes at the first-row obstacles, and vortical structures behind the cubes gradually evolve towards a

self-similar state. The local acceleration of the flow caused by the blockage of the first-row obstacles in their side regions is well captured by the mean streamwise velocity contours. From the figure, it is also observed that the boundary layer separation on the two sides of the first-row obstacles induces two small recirculation bubbles. In Fig. 5.8b, it is evident that the flow has reached a self-similar state and a repeating pattern in the recirculation flows behind the cubes is clearly observed. Figure 5.8c shows the streamlines around the last two rows of obstacles. Due to a lack of a downstream restriction, the counter-rotating vortices behind the last-row obstacles are apparently different than those in the upstream region between two rows of cubes. The streamlines passing through the streets diverge towards the recirculation region behind the last row of obstacles, exhibiting a clustered and parallel pattern. Meanwhile, this local divergent pattern of the streamlines results in a local deceleration along the streamwise street canyons immediately downstream of the last row of obstacles. In order to refine the study of the flow field in the outlet region, the vector plot around the cubic obstacle of the last row in the central column is shown in Fig. 5.9. The counter-rotating vortex pairs before and behind this obstacle can be clearly identified in the figure. The deceleration of the flow in the street canyon and redirection of the mass towards the wake region of the obstacle are consistent with the pattern observed previously in Fig. 5.8c.

In order to obtain more physical insights into the canyon flow in the self-similar region, the instantaneous and time-averaged vector plots and streamlines of the resolved velocity field between rows 7 and 8 in the central plane ( $z/d = 0$ ) are displayed in Fig. 5.10. As shown in Fig. 5.10a, the high-speed flow skimming over the obstacles interacts intensively with the windward face of the cube (especially around the top edge), creating turbulent eddies and a downwash flow pattern. This downwash flow along the windward face further drives the flow to recirculate within the canyon. In Fig. 5.10b, four stable vortices are observed, with one large vortex (or primary vortex) marked as ‘a’ in Fig. 5.10b, and three small vortices (or secondary vortices) at three corners marked with ‘b’, ‘c’ and ‘d’. The four eddies observed in Fig. 5.10b can be better visualized using streamlines shown in Fig. 5.10c. The formation of these

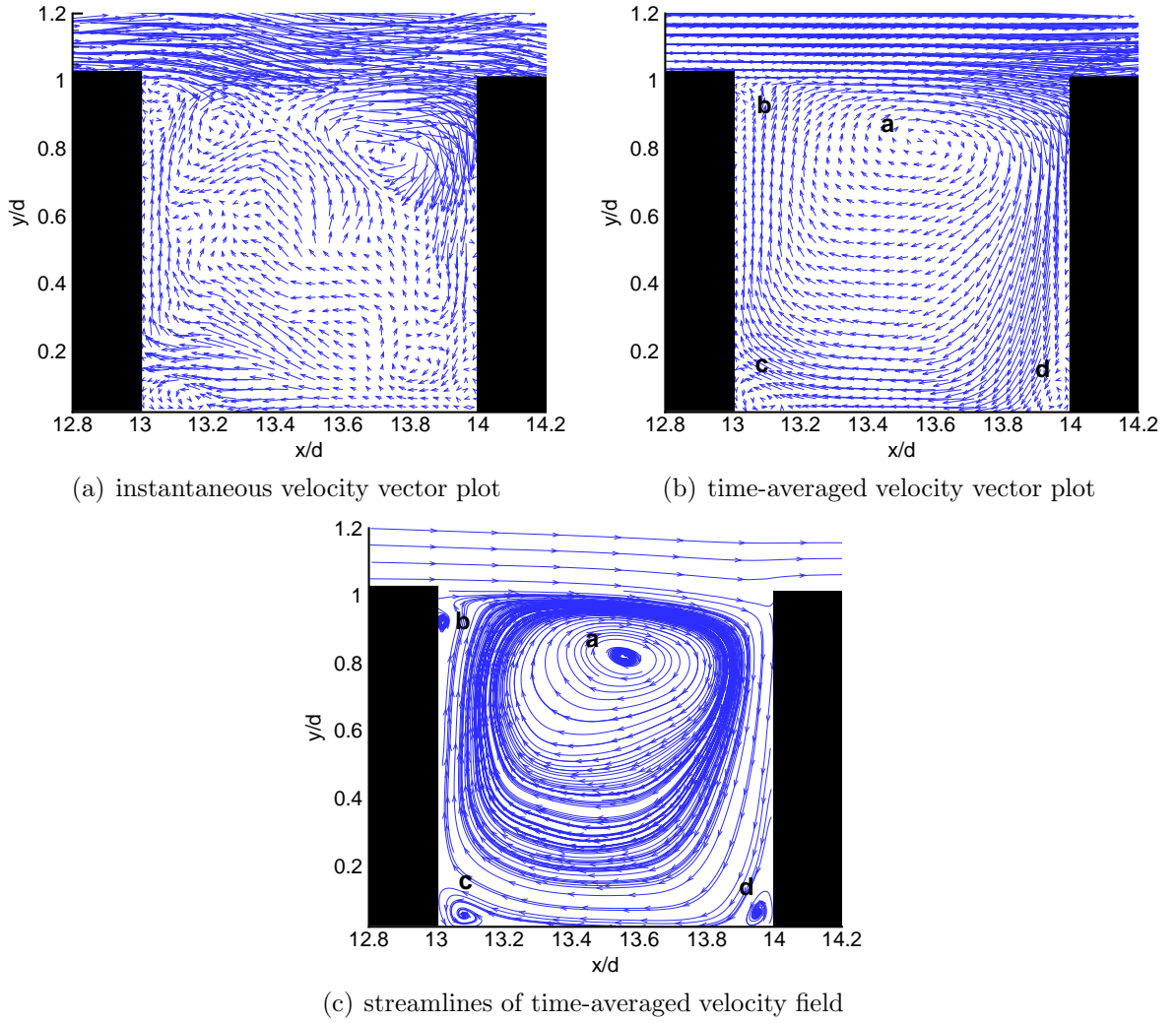


FIGURE 5.10: Lateral view of the instantaneous and time-averaged vector plots and streamlines of the resolved velocity field inside the canyon in the self-similar region (between rows 7 and 8). The plots are made in the central  $x$ - $y$  plane located at  $z/d = 0$ .

four vortices in the canyon region resembles the classical rectangular lid-driven cavity flow which have been well studied by many researchers (e.g., Ghia *et al.* [170] and Shankar and Deshpande [171]).

Figures 5.11a-5.11c show the temporal energy spectra for the streamwise, vertical and spanwise resolved velocity fluctuating components, respectively, at position  $x/d = 13.5$ ,  $y/d = 1$  and  $z/d = 0$  (located in the central plane of the domain between rows 7 and 8 at the rooftop elevation). At this point, flow has reached the self-similar state and is dominated by a very strong shear layer formed from the rooftop of the

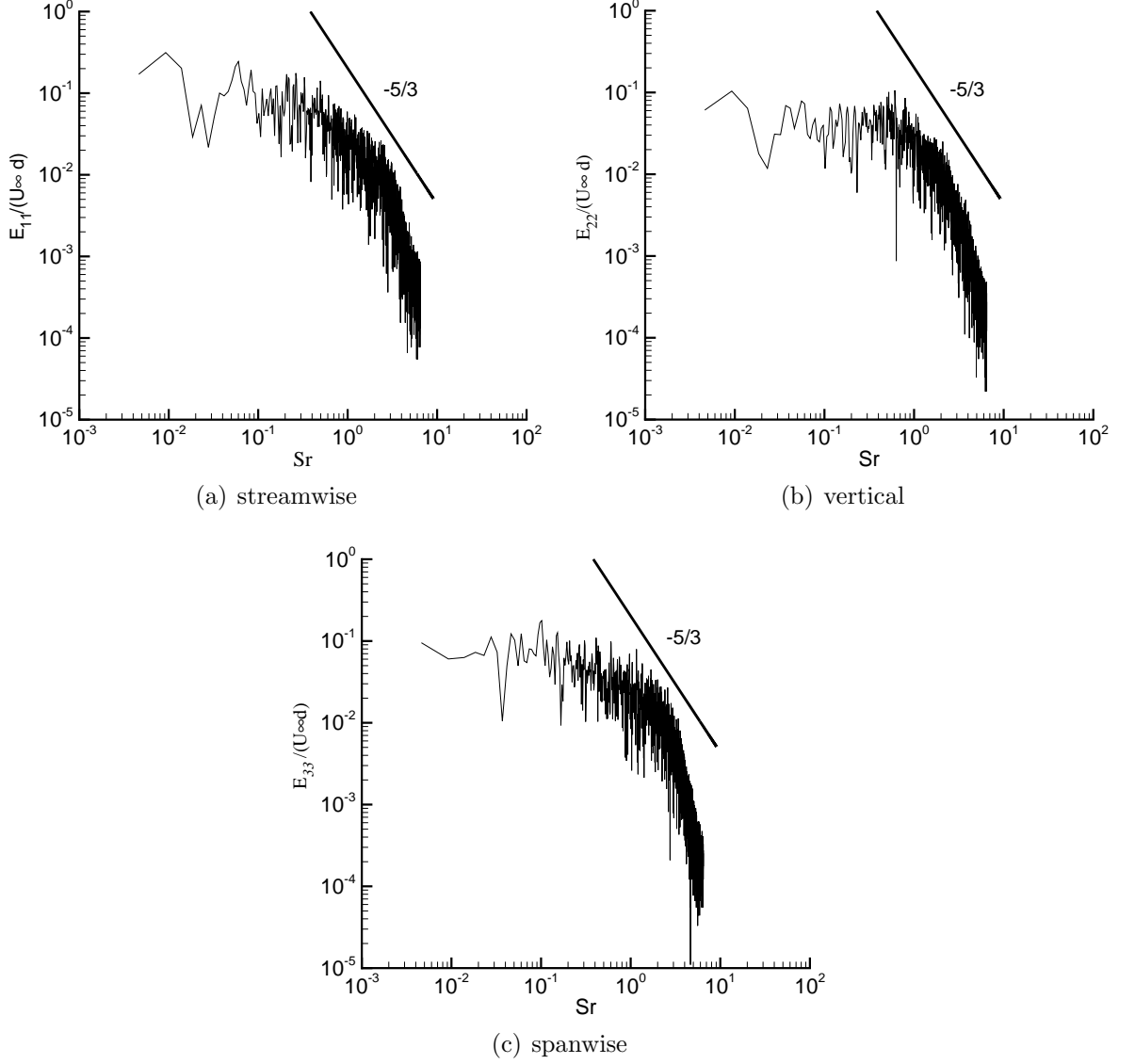


FIGURE 5.11: Non-dimensionalized temporal energy spectra for the streamwise, vertical and spanwise velocity components at position  $x/d = 13.5$ ,  $y/d = 1$  and  $z/d = 0$  (located within the self-similar region between rows 7 and 8 at the rooftop elevation in the central plane of the domain).

upstream (seventh row) obstacle. In the figure, the energy spectra has been non-dimensionalized as  $E_{ii}/(U_{\infty}d)$ . The frequency has also been non-dimensionalized and is represented using the Strouhal number defined as  $Sr = fd/U_{\infty}$ . By comparing Figs. 5.11a-5.11c, it is observed that the pattern of the spectra of three resolved velocity fluctuation components is similar to each other; however, the resolved TKE level of the streamwise component is slightly higher than those of the vertical and

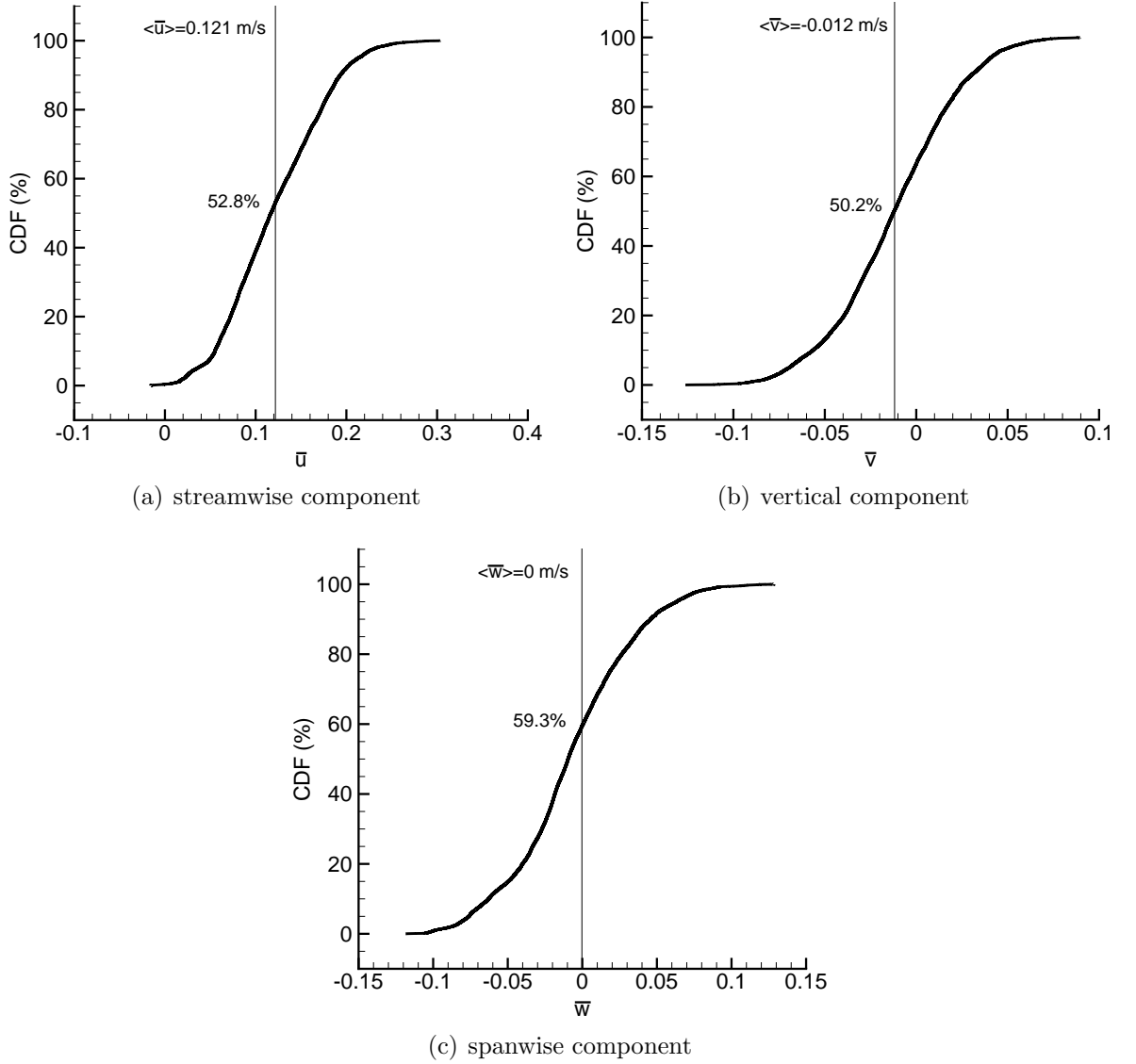


FIGURE 5.12: Cumulative distribution function for the streamwise, vertical and spanwise velocity components, respectively, at  $x/d = 13.5$ ,  $y/d = 1$  and  $z/d = 0$ .

spanwise components, especially at low frequencies. As is evident in Figs. 5.11a-5.11c, the spectra of all three resolved TKE components show that the energy cascades from large- to small-scales eddies, going through the inertial subrange. This indicates that the simulation has been able to resolve most of the energy of turbulent eddies (i.e., energy containing eddies), implying that the resolution in all directions is fine enough to capture the dominant flow features at the selected position.

Figures 5.12a-5.12c show the CDF for the streamwise, vertical and spanwise

velocity components, respectively. As shown in Fig. 5.12a, the CDF corresponding to  $\bar{u} = \langle \bar{u} \rangle$ , is 52.8%. This indicates that the streamwise velocity component fluctuates above and below its mean value with approximately an equal number of random events, implying that the magnitude of oscillations below and above the mean value are of approximately equal strength and contribute equally to TKE. For the vertical velocity component, as shown in Fig. 5.12b, the CDF corresponding to  $\bar{v} = \langle \bar{v} \rangle$ , is 50.2%. This also indicates that for the vertical velocity component, the numbers of fluctuations below and above the mean value are approximately equal. However, since the mean value of the vertical velocity component is negative, a portion (approximately 25%) of the fluctuations above the mean value (i.e.,  $\bar{v} > \langle \bar{v} \rangle$ ) still have amplitudes lower than the mean amplitude ( $|\bar{v}| < |\langle \bar{v} \rangle|$ ). As a consequence, the oscillations below the mean value must have higher amplitude than those above the mean value. This further implies that for the vertical velocity component, a significant portion of its contribution to the TKE comes from oscillations below the mean value with higher oscillating amplitude. For the spanwise velocity component, the CDF corresponding to  $\bar{w} = \langle \bar{w} \rangle$ , is 59.3%. This implies that for the spanwise velocity component, the number of random fluctuations below the mean value is slightly higher than that above the mean value.

## 5.2.2 Statistics of the velocity field

In this subsection, the predicted first- and second-order flow statistics are analyzed and validated against the available experimental data. The measurement locations (A-D) for the mean velocity and its root-mean-square (RMS) values in two cells (i.e., cells 1 and 6) of the cubic obstacle array in the water-channel experiment have been introduced previously in section 4.1 (see Fig. 5.2 for the geometries). Figures 5.13 and 5.14 compare the numerical predictions of the resolved time-averaged streamwise velocity against the measurement data in cells 1 and 6, respectively. As is evident in both figures, the LES predictions match very well with the experimental data. Figure 5.13a shows the profile of  $\langle \bar{u} \rangle / U_\infty$  at location A1 (which is on the rooftop

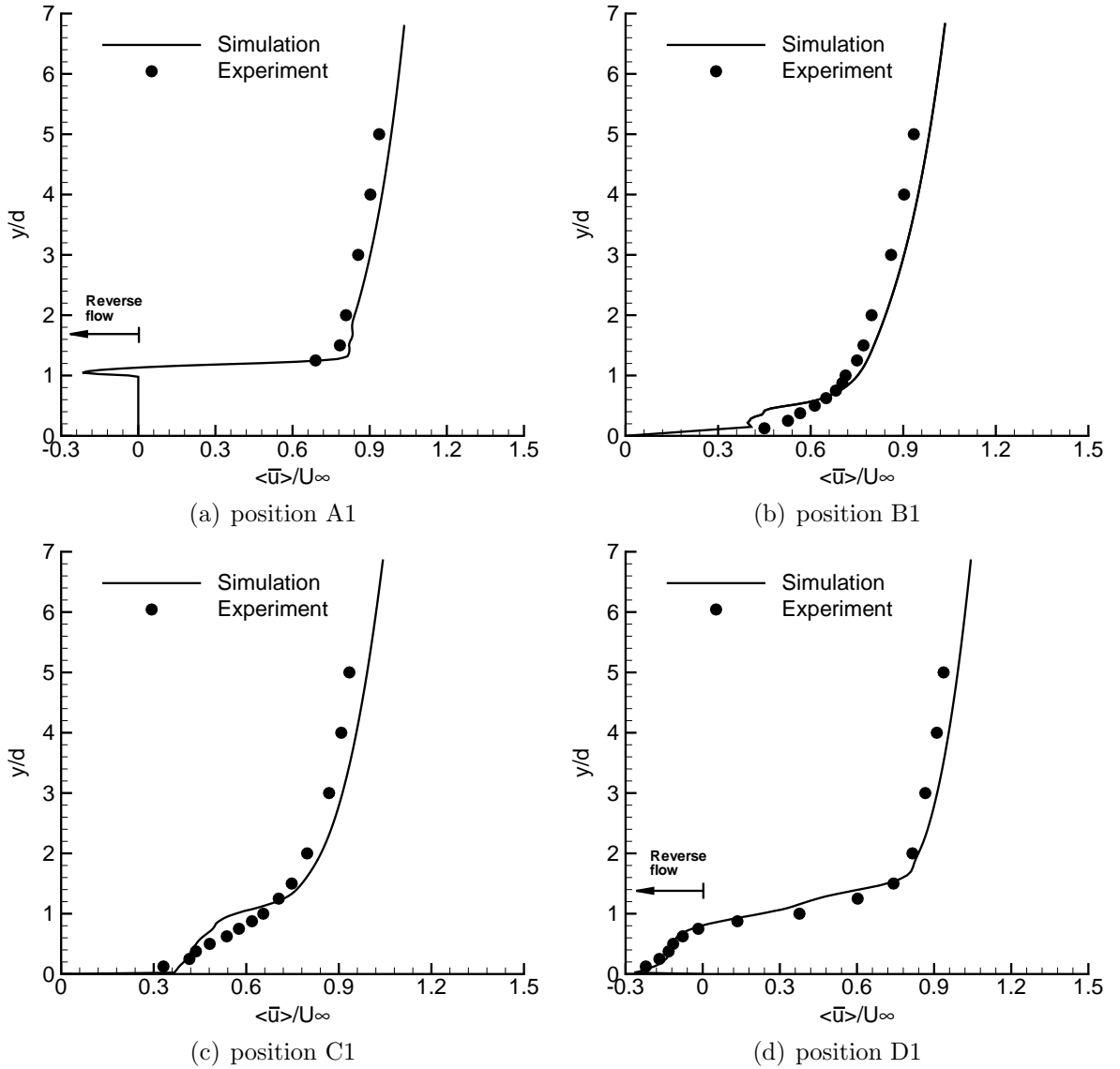


FIGURE 5.13: Vertical profiles of the non-dimensionalized mean streamwise velocity at different locations in cell 1.

of the first-row obstacle). From the figure, it is observed that in the vicinity of the top surface of the obstacle ( $y/d \approx 1$ ), a small region with negative mean velocities is predicted by LES, which is consistent with the previous analysis of the boundary layer separation and the concomitant recirculation pattern near the rooftop of the first-row obstacle demonstrated in Fig. 5.6. Immediately above this small recirculation region, a very strong shear layer (corresponding to a sharp vertical velocity gradient  $\frac{d\langle \bar{u} \rangle}{dy}$ ) appears, which has been well captured by LES. Figures 5.13b and 5.13c show the velocity profiles in the street canyon at locations B1 and C1. Figure 5.13d shows the

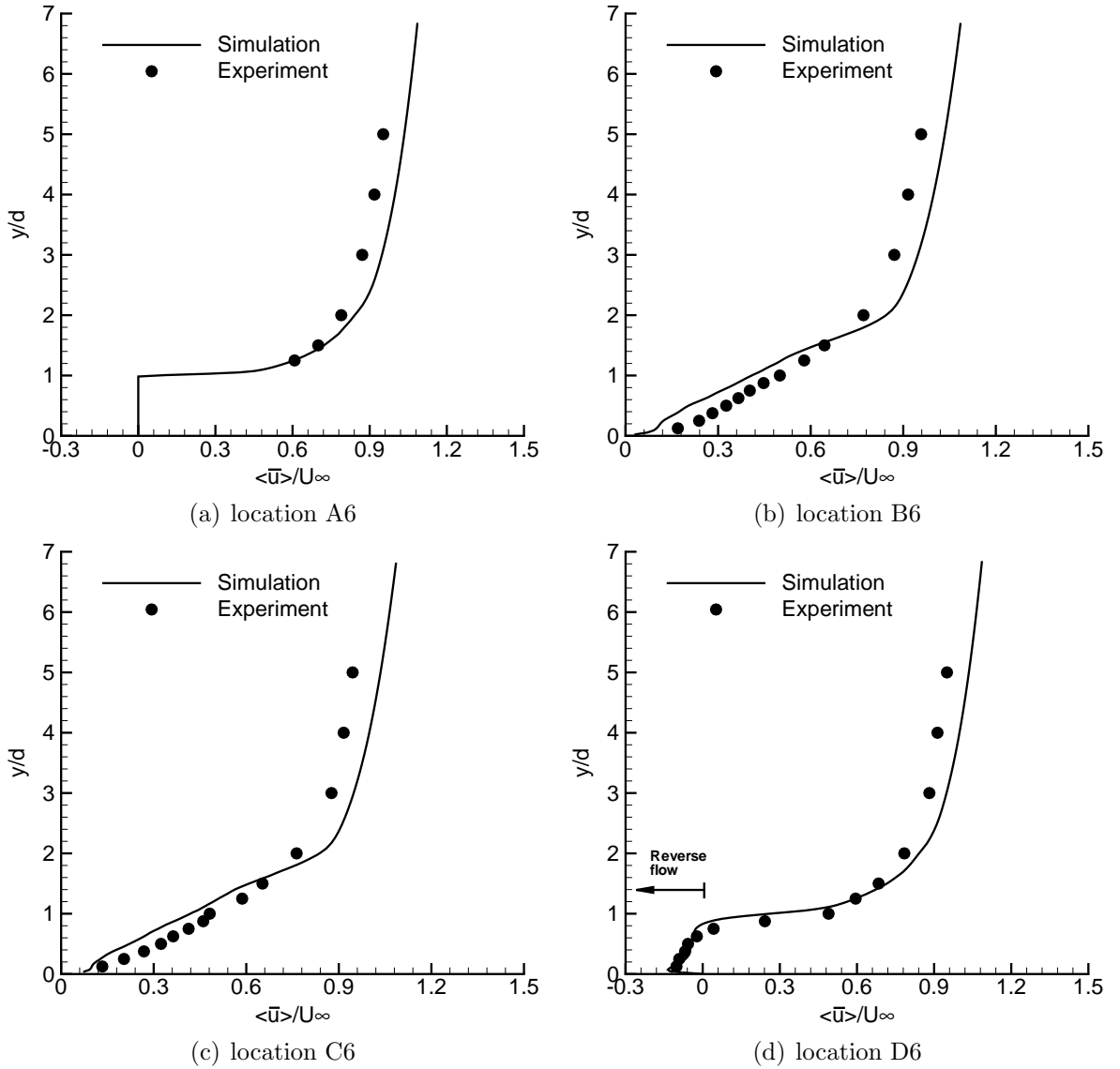


FIGURE 5.14: Vertical profiles of the non-dimensionalized mean streamwise velocity at different locations in cell 6.

mean velocity profile at location D1. As is evident in this figure, the reverse flow (for  $\langle \bar{u} \rangle / U_\infty < 0$ ) under the canopy (for  $y/d < 1$ ) has been correctly predicted by LES, which is consistent with the analysis of the recirculation pattern shown previously in Figs. 5.6a, 5.7a and 5.8a. Figures 5.14a-5.14d compares the predicted and measured velocity profiles at four locations (A-D) in cell 6 (which is located in the self-similar region of the flow). Although Figs. 5.13 and 5.14 share some general flow features, a careful comparison of these two figures indicates that some differences present in the mean velocity profiles between cells 1 and 6. Specifically, as shown in Fig. 5.14a,

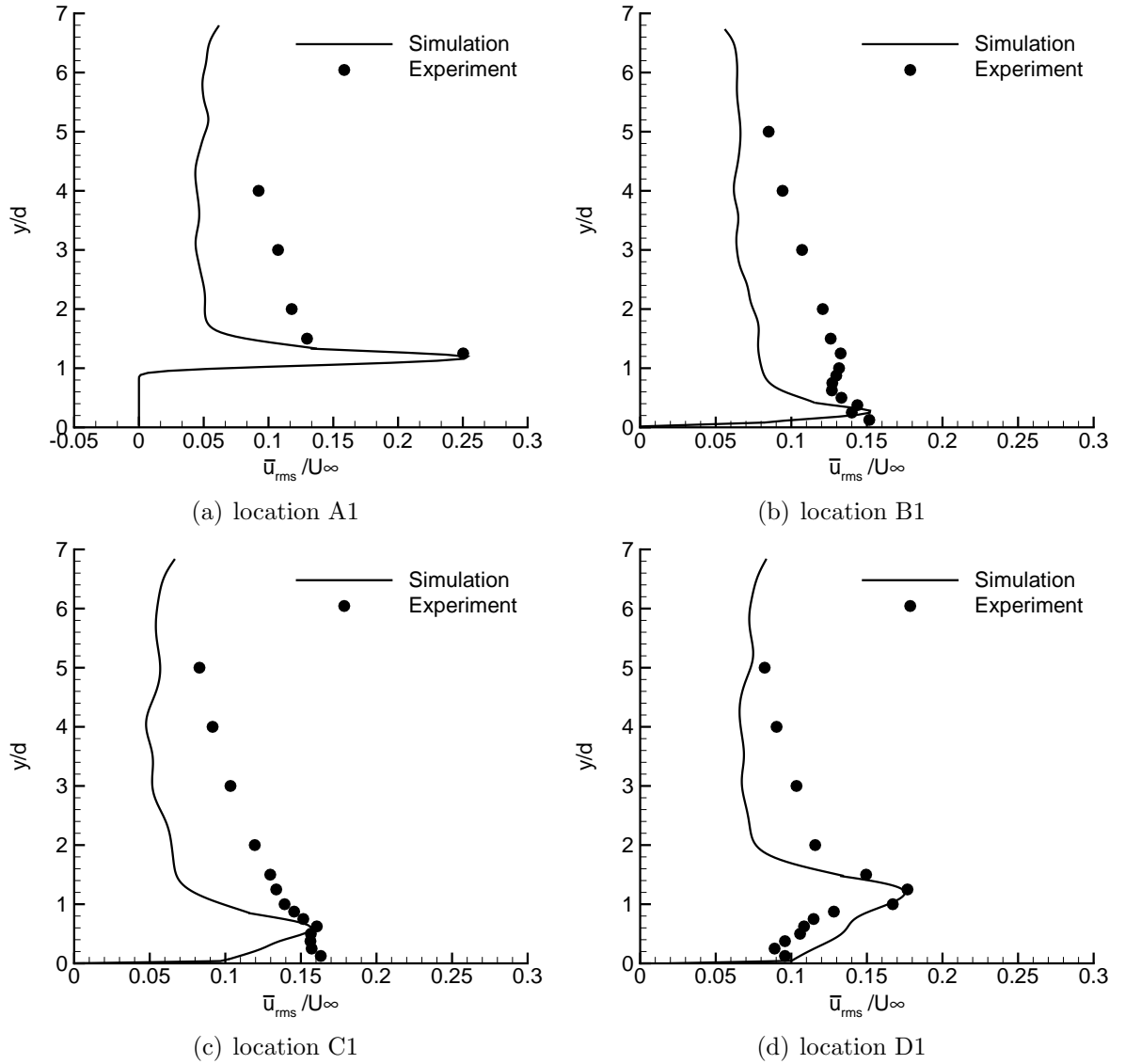


FIGURE 5.15: Vertical profiles of the non-dimensionalized RMS streamwise velocity at different locations in cell 1.

the small recirculation region near the rooftop of the first-row obstacle (at location A1 in cell 1) observed in Fig. 5.13a is no longer present at location A6 in cell 6. This indicates that the boundary-layer separation which leads to flow recirculation on rooftop of the first-row obstacle is a result of direct strike of the approaching free-stream flow at the sharp-edged cubic obstacle. This striking and blockage effect is much attenuated in the following-up downstream rows, and the mean flow gradually becomes self-similar to reflect the characteristics of a fully-developed d-type rough-wall boundary layer. This observation is consistent with the streamwise velocity

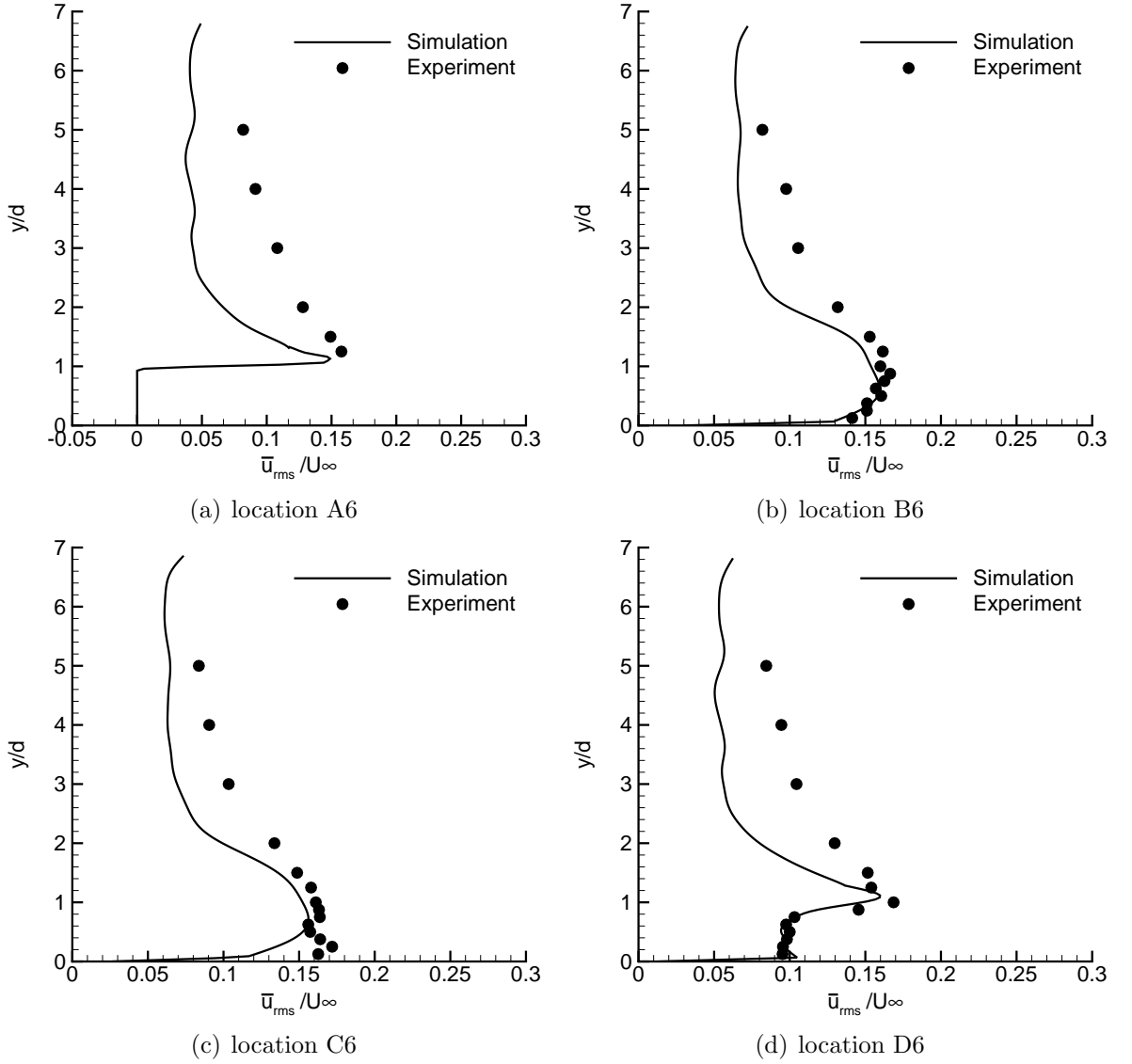


FIGURE 5.16: Vertical profiles of the non-dimensionalized RMS streamwise velocity at different locations in cell 6.

contours presented in Fig. 5.5 and streamline pattern shown in Fig. 5.6.

Figures 5.15 and 5.16 compare the profiles of the non-dimensionalized resolved streamwise RMS velocity  $\bar{u}_{rms}/U_\infty$  at four different locations in cells 1 and 6, respectively. As is evident in Fig. 5.15a, the RMS velocity reaches its maximum around the top of the canopy ( $y/d = 1$ ). The large mean velocity gradient at the rooftop (shown previously in Fig. 5.13a) results in a strong shear production rate for TKE, which then drastically increases the TKE level. As such, the magnitude of RMS velocity peaks at this special elevation at both location A1 (cf. Fig. 5.15a)

and its downstream location D1 (cf. Fig. 5.15d). Because of the vertical spreading and dissipation of TKE, the elevation of the peak increases while the magnitude of the peak decreases as the fluid flows from location A1 to location D1. By comparing the numerical results with the water-channel measurement data, it is seen that this physical feature has been reproduced by the simulation. It is especially satisfying to see in Fig. 5.15a that both the elevation (near the top of the canopy) and magnitude of the maximum RMS velocity have been correctly reproduced in the simulation. However, in regions above the cubes ( $y/d > 1$ ), the magnitude of the RMS velocity has been underpredicted by the simulation. This is due to the exceptionally high turbulence level in this region discussed in section 5.1.1. As shown in Figs. 5.15b and 5.15c, the maximum value of the RMS velocity has been shifted down to the ground-level at locations B1 and C1. Owing to vertical turbulent dispersion of the TKE, the elevation of the peak at location C1 is higher than that at its upstream location B1. In Figs. 5.16a-5.16d, the profiles of the streamwise RMS velocity at four measurement locations in cell 6 are presented. In general, the profiles of the streamwise RMS velocity in cell 6 are similar to those at corresponding measurement locations in cell 1 presented in Fig. 5.15, except that the magnitude of the maximum RMS velocity peak in location A6 is about 40% lower than that in location A1, and shape of peaks at B6 and C6 is wider than that at B1 and C1. This is consistent with the previous discussion that the free-stream flow strikes the windward side and rooftop of the obstacles of the first row much more intensely than does the sixth row, resulting in a stronger shear layer (see Figs. 5.13a and 5.14a) and boundary-layer separation at the rooftop of the first-row obstacles. After all, as flow passes from cell 1 to cell 6, spatial transport of TKE takes place due to convection, diffusion and dissipation, and inevitably, the profiles of the RMS velocity evolve in the streamwise direction due to these mechanisms.

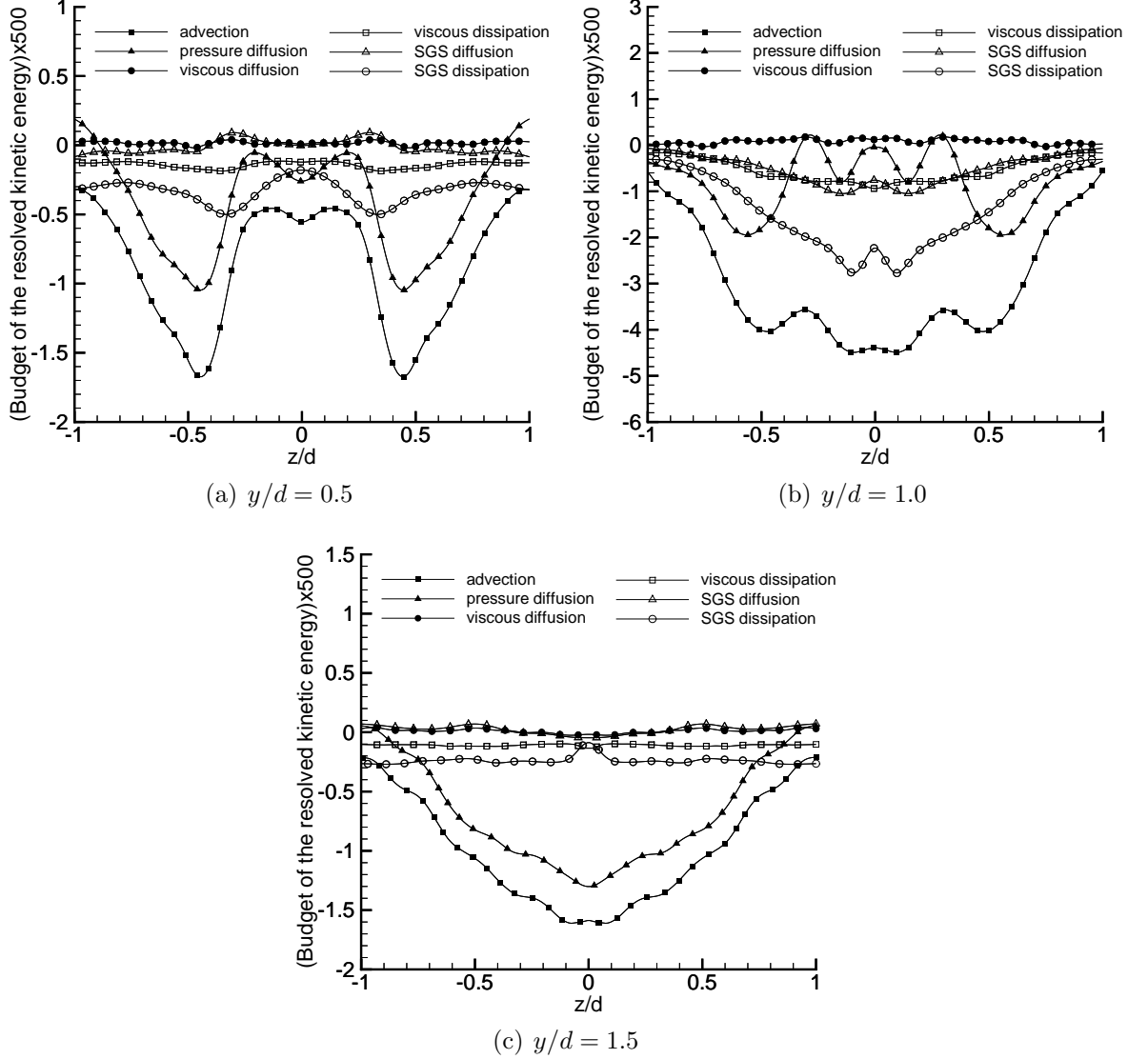


FIGURE 5.17: Budget of the time-averaged resolved kinetic energy ( $k_r$ ) at  $x/d = 13.5$  within  $-1 < z/d < 1$ , at three different elevations. All the quantities shown in the figures have been non-dimensionalized using  $U_\infty^3/d$ .

### 5.2.3 Budget of the resolved kinetic energy

In the previous subsection, the resolved turbulent fluctuations in terms of the profiles of the streamwise RMS velocity have been analyzed. In this subsection, we further extend this discussion by investigating the transport process and budget balance of the resolved kinetic energy (KE) and TKE of the flow. The filtered KE of the flow (defined as  $\overline{E} \stackrel{\text{def}}{=} \frac{1}{2} \overline{u_i u_i}$ ) can be decomposed into the resolved and SGS kinetic energy

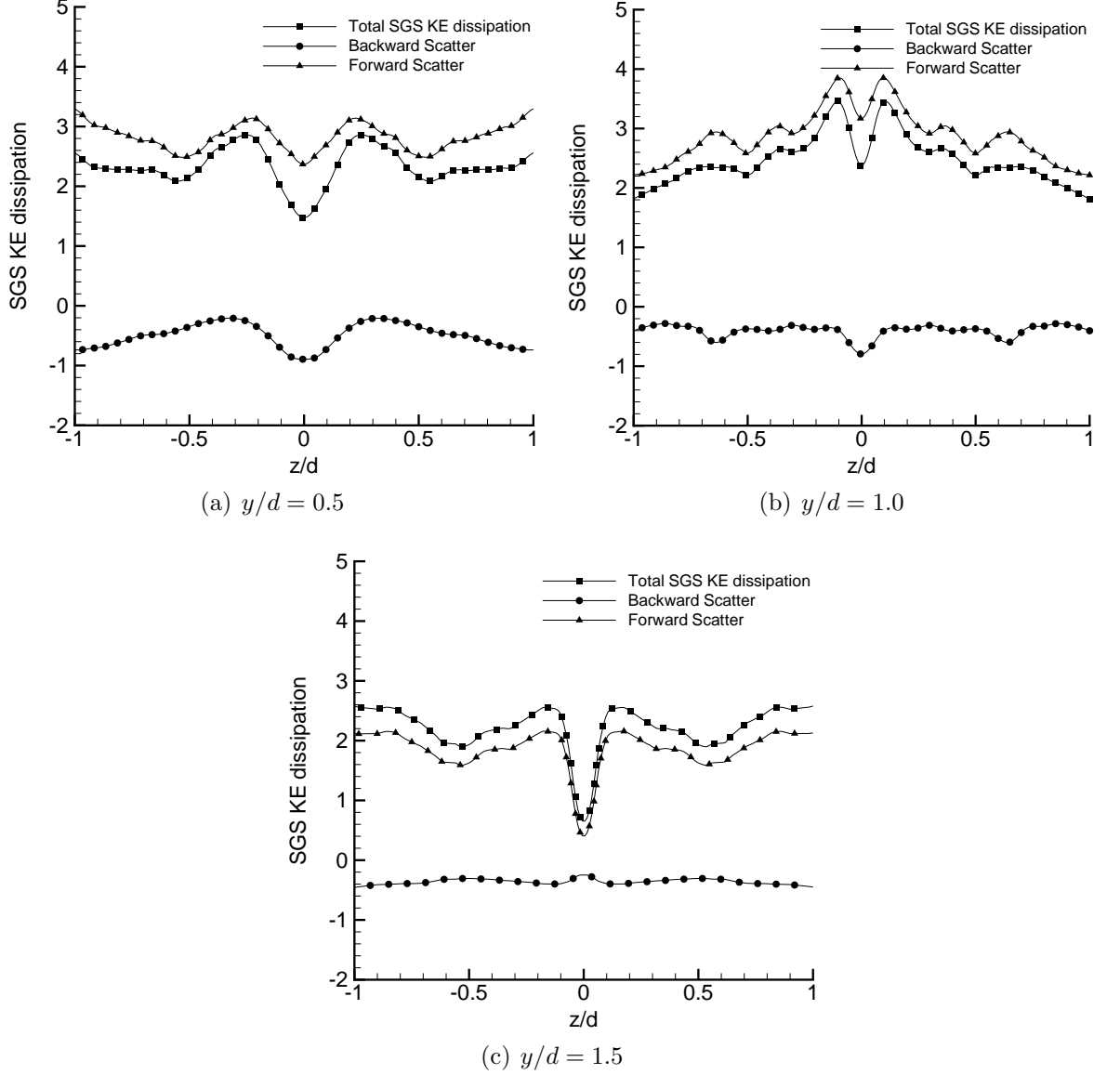


FIGURE 5.18: Profiles of the time-averaged SGS KE dissipation rates ( $\langle \varepsilon_{sgs} \rangle$ ) at  $x/d = 13.5$  within  $-1 < z/d < 1$ , at three different elevations. All the quantities shown in the figures have been non-dimensionalized using the averaged viscous dissipation rate  $2\nu \langle \bar{S}_{ij} \bar{S}_{ij} \rangle$ .

as

$$\bar{E} = k_r + k_{sgs} \quad , \quad (5.1)$$

in which  $k_r \stackrel{\text{def}}{=} \frac{1}{2} \bar{u}_i \bar{u}_i$  is the resolved KE of the flow and  $k_{sgs} \stackrel{\text{def}}{=} \frac{1}{2} (\overline{u_i u_i} - \bar{u}_i \bar{u}_i)$  is the SGS KE. It can be shown that the transport equation for the time-averaged resolved

KE of the flow takes the following form [97]

$$\underbrace{\left\langle \bar{u}_j \frac{\partial k_r}{\partial x_j} \right\rangle}_{\text{advection}} = - \underbrace{\frac{1}{\rho} \left\langle \bar{u}_j \frac{\partial \bar{p}}{\partial x_j} \right\rangle}_{\text{pressure diffusion}} + \underbrace{2\nu \left\langle \frac{\partial \bar{S}_{ij} \bar{u}_i}{\partial x_j} \right\rangle}_{\text{viscous diffusion}} - \underbrace{2\nu \langle \bar{S}_{ij} \bar{S}_{ij} \rangle}_{\text{viscous dissipation}} - \underbrace{\left\langle \frac{\partial \tau_{ij}^* \bar{u}_i}{\partial x_j} \right\rangle}_{\text{SGS diffusion}} + \underbrace{\langle \tau_{ij}^* \bar{S}_{ij} \rangle}_{\text{SGS dissipation}}. \quad (5.2)$$

Figures 5.17a-5.17c show the budget balance of  $k_r$  across the stream in the self-similarity region at mid-point ( $x/d = 13.5$ ) between rows 7 and 8 and behind the central column ( $-1 < z/d < 1$ ) at three different elevations for  $y/d = 0.5, 1$  and  $1.5$  (at the half-cube height, rooftop and above the canopy, respectively). All the terms shown in these figures have been non-dimensionalized using  $U_\infty^3/d$ . Also, all the budget terms on the right-hand side (RHS) of Eq. 5.2 shown in Figs. 5.17a-5.17c have included the addition/subtraction signs in Eq. 5.2. As such, the pressure diffusion, viscous dissipation and SGS diffusion terms shown in the budget balance in these figures are  $-\frac{1}{\rho} \left\langle \bar{u}_j \frac{\partial \bar{p}}{\partial x_j} \right\rangle$ ,  $-2\nu \langle \bar{S}_{ij} \bar{S}_{ij} \rangle$  and  $-\left\langle \frac{\partial \tau_{ij}^* \bar{u}_i}{\partial x_j} \right\rangle$ , respectively. As shown in Fig. 5.17a, at elevation  $y/d = 0.5$ , the advection, pressure diffusion and SGS dissipation rate are the dominant terms in the transport equation of  $k_r$ , and furthermore, the advection term is primarily balanced by the pressure diffusion and SGS dissipation terms. The peak values of advection and pressure diffusion occur at  $z/d \approx \pm 0.5$ , directly downstream of the two sides of the obstacle. At these locations, the flow in the canyons strikes the two vertical side edges of the cubic obstacle, forming a strong shear layer on each side which further triggers the flow instability and entrains the recirculating region immediately behind the cube. As a consequence of the enhanced turbulence level due to the pressure difference between side and rear regions of the obstacle and strong shear layers formed on both sides of the obstacle, the magnitudes of the pressure diffusion and advection terms peak around  $z/d \approx \pm 0.5$ . The highest value in the magnitude of the SGS dissipation rate occurs at  $z/d \approx \pm 0.35$ , which is slightly displaced from the location of the advection and pressure diffusion peaks towards the recirculation bubble behind the obstacle. As shown previously in Fig. 5.8, at these special locations, strong shear layers intensely interact with a pair of counter rotating recirculating vortices. At  $z/d = 0$  (inside the recirculation region), the level

of the advection and pressure diffusion are generally low while the SGS dissipation rate reaches its absolute minimum. This is because all these three dominant terms respond positively to high turbulence levels caused by pressure difference, convection, shear instability and intense interaction of eddies of different scales, and all these effects are relatively weak at the center of the recirculation bubble trapped between two cubes (see, Fig. 5.10). The overall influence of viscous diffusion and viscous dissipation rate are not significant in comparison with other terms, because this flow (with exceptionally high free-stream turbulence level and strong disturbances from cubes) is dominated by inertial forces rather than viscous forces. LES is an excellent tool for simulating this flow which features high TKE levels at large resolved scales. As shown in Fig. 5.17a, the level of SGS diffusion is much smaller than that of SGS dissipation. This is because the SGS dissipation term  $\langle \tau_{ij}^* \bar{S}_{ij} \rangle$  represents KE transfer between the large resolved and small subgrid scales, or interaction of eddy motions of these two different scales. The cascade of KE can be positive and negative, representing backward and forward scatter of energy between the two scales. The effect of SGS dissipation becomes stronger as the Reynolds number increases. The SGS dissipation rate reflects a major feature of SGS dynamics, as it represents a key physical quantity that determines the cascade of energy in LES. In contrast, the SGS diffusion represents diffusion (or, re-distribution) of KE due to SGS shear stresses (which are much smaller than resolved turbulent shear stresses), and its value is expected to be smaller than that of the SGS dissipation rate. The SGS dissipation rate will be further thoroughly investigated later in this subsection.

Figure 5.17b shows the cross-stream budget balance of the resolved kinetic energy  $k_r$  at the same streamwise location but at the rooftop elevation  $y/d = 1$ . At this elevation, the three separated boundary layers from the rooftop and two sides of cube interact with the reverse flow in the canyon region and significantly enhance turbulent mixing. As shown in Fig. 5.17b, the advection, pressure diffusion and SGS dissipation rates dominate the transport process of  $k_r$ , which is similar to that observed in Fig. 5.17a (under the canopy for  $y/d = 0.5$ ). As mentioned above, these three terms reflect enhanced turbulence activities caused by pressure gradients,

convection, shear instability and intense mixing of eddies of different scales, and all these effects are strong at this special location. The cascade of the resolved TKE as a result of eddy motions and interactions at this special location has been analyzed using the energy spectra shown previously in Fig. 5.11. Although in both Figs. 5.17a and 5.17b, the transport of  $k_r$  is dominated by advection, pressure diffusion and SGS dissipation terms, the profiles of these three dominant terms exhibit different patterns at these two elevations (for  $y/d = 0.5$  and 1). The magnitude of the advection term is the largest among all terms. By comparing Figs. 5.17b and 5.17a, it is observed that although two local maxima are still preserved at  $z/d \approx \pm 0.5$  to reflect strong instable shear layers from both cube sides, the largest peak of the advection term appears around the midspan (at  $z/d = 0$ ) for  $y/d = 1$ , which is in sharp contrast to Fig. 5.17a (in which the advection term reaches its local minimum around the midspan). This largest peak in the magnitude of the advection term is a consequence of the strong instable shear layer from the rooftop (at  $y/d = 1$ ) and accompanied boundary-layer separation and turbulent mixing at the top of the canopy. Also by comparing Fig. 5.17b with 5.17a, it is interesting to observe that the value of the advection term has generally increased by a factor of approximately 2.5, indicating that as the elevation increases from  $y/d = 0.5$  to 1, the convection and its effects on the transport of  $k_r$  has increased drastically, especially around the midspan. Also as a response to the enhanced convection level at the top of the canopy, the magnitude of the SGS and viscous dissipation rates have also increased in comparison with their counterparts at the half cube height shown in Fig. 5.17a.

In Fig. 5.17c, the cross-stream budget balance of  $k_r$  is shown at an elevation above the canopy ( $y/d = 1.5$ ). As is evident in Fig. 5.17c, the advection term is primarily balanced by the pressure diffusion term. The impact of the SGS dissipation rate on the transport of  $k_r$  still ranks the third, however, its magnitude has reduced as the elevation increases from  $y/d = 1$  to 1.5. In this figure, the effects of the shear layers from the cube sides is much reduced in comparison with those shown in Figs. 5.17a and 5.17b, and no local maxima are observed for the advection and pressure diffusion terms around the cube sides located at  $z/d \approx \pm 0.5$ . However, there is an increasing

trend in the across-stream distribution of the advection and pressure diffusion terms that their magnitudes reach maximum in the midplane ( $z/d = 0$ ). This indicates that at this elevation above the canopy, in terms of the transport of  $k_r$ , the flow is still significantly influenced by the strong instable shear layer formed on the rooftop (through vertical spreading), but no longer directly sees the two strong instable shear layers formed by the two cube side faces (as they are buried deeply under the canopy). It is interesting to observe that the profile of the SGS dissipation term is evolving towards a horizontal line, implying that the eddy motions and interactions represented by this SGS term are becoming increasingly homogeneous in the spanwise direction above the canopy. Furthermore, in comparison with Fig. 5.17b, it is observed that the value of the advection term has significantly increased at the ‘boundaries’ (center of the street canyon on both sides of the cube, at  $z/d = \pm 1$ ) in Fig. 5.17c, indicating that although the advection term is still influenced by the rooftop, it also tends to become homogeneous in the spanwise direction as the elevation increases. The flow is highly disturbed by the cubes and is highly heterogeneous under the canopy; however, the influence of cubes is expected to reduce as the elevation above the canopy increases, and eventually vanishes allowing the flow to reach a spanwise homogeneity state in regions far above the canopy.

The local KE transfer between the resolved and unresolved (subgrid) scales can be quantified using the SGS KE dissipation rate, which appears in both the resolved KE ( $k_r$ ) equation (i.e., Eq. 5.2) as  $\tau_{ij}^* \bar{S}_{ij}$  and the SGS KE ( $k_{sgs}$ ) equation as  $-\tau_{ij}^* \bar{S}_{ij}$ . As such, it functions as a KE sink term to the large resolved motions and a KE source term to the SGS motion. Define  $\varepsilon_{sgs} \stackrel{\text{def}}{=} -\tau_{ij}^* \bar{S}_{ij}$ . The value of  $\varepsilon_{sgs}$  can be either positive or negative, representing forward and backward scatter of local KE between the resolved and subgrid scale motions, respectively. In Figs. 5.18a-5.18c, the time-averaged cross-stream profiles of SGS KE dissipation rate  $\langle \varepsilon_{sgs} \rangle$  are displaced at streamwise location  $x/d = 13.5$ , across the spanwise range of  $-1 < z/d < 1$  at three elevations for  $y/d = 0.5, 1$  and  $1.5$ . In order to gain some deeper insights into the relative strength of the SGS and viscous dissipation rates, the value of the SGS dissipation rate has been non-dimensionalized with the value of the local viscous

dissipation rate  $2\nu\langle\bar{S}_{ij}\bar{S}_{ij}\rangle$  (see, Eq. 5.2). In the context of the conventional SGS eddy viscosity (Smagorinsky) modeling approach, it can be shown that the ratio between the SGS dissipation rate and the viscous dissipation rate is equivalent to the ratio between the SGS and molecular viscosities (i.e.,  $\nu_{sgs}/\nu$ ). Although the concept of SGS eddy viscosity is not directly applicable to the SGS stress model (DNM) used in this research, this ratio reflects the effective SGS dissipation rate over the viscous dissipation rate [97]. In Fig. 5.18, the forward scatter ( $\langle\varepsilon_{sgs}^+\rangle$ ) and backscatter ( $\langle\varepsilon_{sgs}^-\rangle$ ) of local KE flux have been separated. Naturally, these two quantities must verify  $\langle\varepsilon_{sgs}\rangle = \langle\varepsilon_{sgs}^+\rangle + \langle\varepsilon_{sgs}^-\rangle$ . As shown in Figs. 5.18a-5.18c, the magnitude of the forward scatter is approximately 4 times larger than that of the backward scatter, resulting in a net KE transfer from the resolved to unresolved scales. At the half cube height ( $y/d = 0.5$ ), as shown in Fig. 5.18a, the maximum value of the SGS dissipation rate and forward scatter occurs at  $z/d \approx \pm 0.3$ . As shown in Figs. 5.18b and 5.18c, as the elevation increases to  $y/d = 1.0$  and  $1.5$ , the location for the maximum values approaches the center of the domain (at  $z/d \approx 0$ ). Under the canopy, as shown in Fig. 5.18a, the local KE flux is significantly influenced by the two strong shear layers formed on two vertical sides of the cube (at  $z/d = \pm 0.5$ ) and their interactions with the recirculating zone behind the cube (see, Fig. 5.8). This is the reason that the KE flux peaks exhibit a symmetrical pattern in the spanwise direction behind the cube. However, these two vertical shear layers are immersed under the canopy and their influence on flow decreases significantly in regions above the canopy (when  $y/d > 1$ ). In the region at or immediately above the canopy, the flow is influenced by the shear layer formed at the rooftop of the cube and the concomitant intense eddy motions associated with it. As shown in Fig. 5.18b, this mechanism tends to elevate the KE flux magnitudes (in comparison with the KE flux magnitudes under the canopy shown in Fig. 5.18a).

In order to complement the discussion of the resolved KE transport equation, we can also analyze the transport of the resolved TKE. Different from the resolved KE  $k_r$  and SGS KE  $k_{sgs}$ , the resolved TKE of the flow is defined as  $k \stackrel{\text{def}}{=} \frac{1}{2}\langle\bar{u}_i''\bar{u}_i''\rangle$  where  $\bar{u}_i''$  is the resolved fluctuating velocity obtained based on the following general

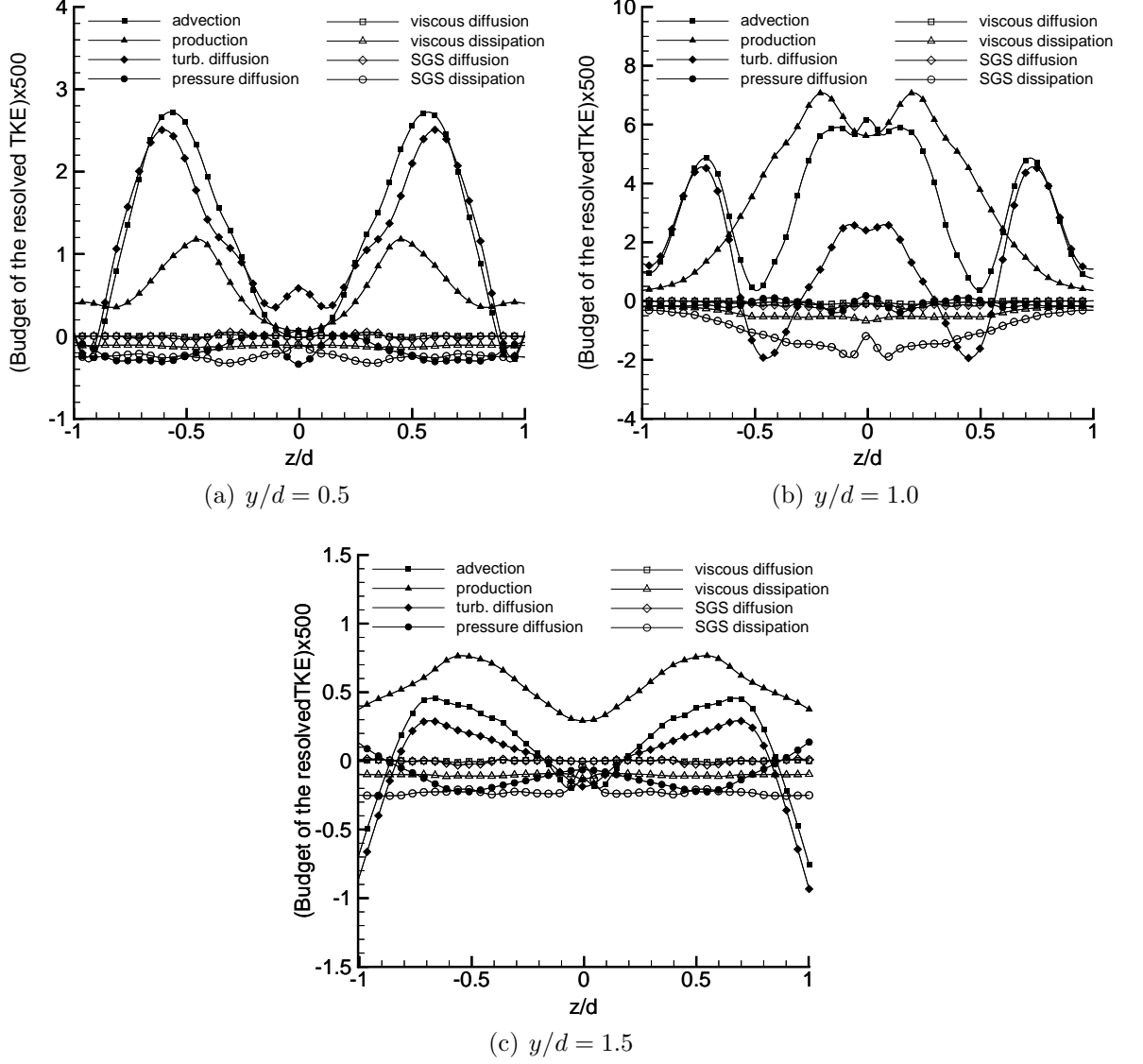


FIGURE 5.19: Budget of the time-averaged resolved TKE ( $k$ ) at  $x/d = 13.5$  within  $-1 < z/d < 1$ , at three different elevations. All the quantities shown in the figures have been non-dimensionalized using  $U_\infty^3/d$ .

decomposition method for a filtered variable  $\phi$

$$\bar{\phi}'' = \bar{\phi} - \langle \bar{\phi} \rangle \quad . \quad (5.3)$$

The time-averaged resolved KE  $\langle k_r \rangle$  relates to the resolved TKE  $k$  as

$$\langle k_r \rangle = \frac{1}{2} \langle \bar{u}_i \bar{u}_i \rangle + k \quad . \quad (5.4)$$

It can be shown that the transport equation of  $k$  takes the following form

$$\begin{aligned}
\underbrace{\langle \bar{u}_j \rangle \frac{\partial k}{\partial x_j}}_{\text{advection}} &= - \underbrace{\langle \bar{u}_i'' \bar{u}_j'' \rangle \frac{\partial \langle \bar{u}_i \rangle}{\partial x_j}}_{\text{production}} - \underbrace{\frac{1}{2} \frac{\partial}{\partial x_j} \langle \bar{u}_i'' \bar{u}_i'' \bar{u}_j'' \rangle}_{\text{turbulent diffusion}} - \underbrace{\frac{1}{\rho} \left\langle \bar{u}_j'' \frac{\partial \bar{p}''}{\partial x_j} \right\rangle}_{\text{pressure diffusion}} \\
&+ \underbrace{2\nu \frac{\partial}{\partial x_j} \langle \bar{S}_{ij}'' \bar{u}_i'' \rangle}_{\text{viscous diffusion}} - \underbrace{2\nu \langle \bar{S}_{ij}'' \bar{S}_{ij}'' \rangle}_{\text{viscous dissipation}} - \underbrace{\frac{\partial}{\partial x_j} \langle \bar{u}_i'' \tau_{ij} \rangle}_{\text{SGS diffusion}} + \underbrace{\langle \tau_{ij}^* \bar{S}_{ij}'' \rangle}_{\text{SGS dissipation}} . \quad (5.5)
\end{aligned}$$

Figures 5.19a-5.19c show the budget balance of  $k$  at the streamwise location  $x/d = 13.5$  across the spanwise range  $-1 < z/d < 1$  at three elevations for  $y/d = 0.5, 1$  and  $1.5$ . All the budget terms on the RHS of Eq. 5.5 shown in Figs. 5.19a-5.19c have included the addition/subtraction signs in Eq. 5.5. For instance, the production term and the viscous dissipation term shown in the budget balance in Fig. 5.19 are  $-\langle \bar{u}_i'' \bar{u}_j'' \rangle \frac{\partial \langle \bar{u}_i \rangle}{\partial x_j}$  and  $-2\nu \langle \bar{S}_{ij}'' \bar{S}_{ij}'' \rangle$ , respectively. At  $y/d = 0.5$ , as shown in Fig. 5.19a, the advection term is primarily balanced with the production, turbulent diffusion, pressure diffusion and SGS dissipation terms. The maximum TKE production rate occurs at  $z/d \approx \pm 0.5$ , directly downstream of the two vertical sides of the obstacle. At this special location, strong shear layer with sharp velocity gradients is formed on each side of the cube which triggers the flow instability and increases the TKE production rate. As shown in Figs. 5.19a-5.19c, at all three elevations, there are three local minima in the cross-stream profile of the TKE production rate, which are located at  $z/d = 0$  (corresponding to the central  $x$ - $y$  plane of the domain) and  $z/d \approx \pm 1$  (corresponding to the central  $x$ - $y$  plane of the neighboring street canyon). At these three special spanwise locations, the cross-stream mean velocity profile is locally symmetrical, and therefore, the spanwise mean velocity gradient is trivial. This further results in a significant reduction in the TKE production rate. As shown in Fig. 5.19b, the magnitudes of the turbulent advection, TKE production and SGS dissipation rate have been increased by a factor of approximately 3 at the rooftop level (for  $y/d = 1$ ) in comparison with their values at half cube height ( $y/d = 0.5$ ). This is an indication of increased turbulent activities as the elevation is increased from  $y/d = 0.5$  to  $y/d = 1.0$  (consistent with the vertical profiles of  $\bar{u}_{rms}/U_\infty$  in the

self-similar region shown in Fig. 5.16). The locations of the peak values of pressure diffusion, TKE production and SGS dissipation rates have been shifted towards the center of the domain (to  $z/d \approx \pm 0.3$ ,  $z/d \approx \pm 0.2$  and  $z/d \approx \pm 0.1$ , respectively). At this elevation ( $y/d = 1$ ), the separated shear layers from the side edges and top surface of the cube both considerably contribute to transport of resolved TKE, and all these three shear layers interact directly with the recirculation zone behind the cubic obstacle. Above the canopy at  $y/d = 1.5$ , as shown in Fig. 5.19c, the magnitudes of different terms of the TKE transport equation have decreased by a factor of approximately 6 in comparison with their counterparts at  $y/d = 1$ . This is an indication of decayed turbulence activities above the cube's rooftop, which is in agreement with the previous observation of decreased streamwise turbulence intensity levels in the vertical profiles of  $\bar{u}_{rms}/U_\infty$ . As the elevation increases above the canopy, the disturbances from the cubes are much reduced and flow becomes increasingly homogeneous in the spanwise direction.

In general, it can be concluded from the analysis of the KE and TKE transport equations that at the half-cube height, the flow in the canyon region is mainly influenced by the instable shear layers and boundary layer separation formed on the side edges of the cube, while at the rooftop level, the dominant dynamic phenomenon is the separated boundary layer from the cube's rooftop surface. At higher elevations, however, the level of turbulence activities are significantly reduced as the obstacles have no direct and dominant influence of the flow field.

### 5.3 Closure

Turbulent flow over a matrix of wall-mounted cubic obstacles at Reynolds number 12,005 has been studied using wall-modeled LES. The statistics and spectra of the turbulent flow field, spatial evolution of flow structures, and transport mechanisms of the kinetic energy have been thoroughly analyzed. One of the major challenges involved in the simulation is to reproduce the highly turbulent (with turbulence intensity of

at least 10%) approaching boundary layer of the water-channel experiment using the numerical method. Based on a comparative study of four inlet boundary conditions, we selected a method that utilizes a solid grid at the inlet of the computational domain to trigger the flow instability and produce physical perturbations. This approach enabled us to generate a highly turbulent boundary layer similar to that in the water-channel experiment with a stable sustainable turbulence level up to approximately 7% in regions above the wall-mounted cubes.

Due to the intense interaction of the approaching highly turbulent boundary layer with the cubic obstacles, the flow exhibits complex patterns, which dynamically evolve within and above the cubic obstacle array and have a significant impact on the transport of the momentum. The spatial flow evolution has been carefully analyzed using the time-averaged resolved velocity contours, streamlines and vector plots. A horseshoe vortex is observed in front of the first-row obstacles at low elevations (e.g.,  $y/d \approx 0.25$ ) as a result of the adverse pressure gradient in the windward face of obstacles in the first row. Five different zones have been observed in the horseshoe vortex region: a) a stagnant zone formed in the immediate adjacency of the windward faces of the first-row obstacles; b) an arch shape negative velocity region in front of zone a; c) a pair of acceleration zones in side regions of the obstacles; d) a pair of small recirculation zones in the immediate adjacency of the side walls; and e) a large recirculation zone formed behind the obstacles. It is observed that after the fifth row of obstacles, the flow quickly reaches a self-similar state featuring a repeating pattern in time-averaged vortical structures around an obstacle.

The first- and second-order flow statistics obtained from the simulation have been compared against the available experimental measurement data. Excellent agreement are observed between the predicted and measured mean velocities at different locations in the first- and sixth-row cells. Above the rooftop and behind the cubes, the strong shear layer is formed at  $y/d \approx 1$ . However, at different locations in the streamwise street, the shear layer is shifted down to the ground level ( $y/d \approx 0$ ) due to absence of any solid obstacle. For the streamwise RMS velocity (or turbulence intensity), the magnitude and location of the peak values are correctly captured by

the simulation. However, the simulation shows underprediction for the RMS velocity in regions above the obstacles which is due to the exceptionally high turbulence level in the original experiment.

The resolved instantaneous flow field in the self-similar region, at a point inside the canyon region and at the rooftop level, is analyzed using energy spectra and CDF. The so-called inertial subrange where the spectrum slope features a constant value of  $-5/3$  is well captured for all three velocity components. It is observed from the analysis of the CDF of the instantaneous velocity field that for the streamwise and spanwise velocity components, the random fluctuations occurring below and above their mean value have approximately equal contribution to the TKE. However, for the vertical velocity component, a significant portion of its contribution to the TKE comes from oscillations below the mean value with higher oscillating amplitude.

Different terms of the resolved KE and TKE transport equations have been analyzed behind a typical obstacle located in the self-similar region at three different elevations. For the transport of the resolved KE of the flow at half cube height ( $y/d = 0.5$ ), the advection term is mainly balanced with the pressure diffusion and SGS dissipation rate. Also, the peak values of advection and pressure diffusion occur at  $z/d \approx \pm 0.5$  due to the separated shear layers from the cube sides which trigger the flow instability and entrain the recirculating region immediately behind the cube. However, at the rooftop elevation, the largest peak in the magnitude of the advection term occurs at  $z/d \approx 0$  due to the strong instable shear layer formed on the rooftop and accompanied boundary-layer separation and turbulent mixing on top of the canopy. The magnitude of the SGS dissipation rate in the middle of the canyon region is lower than that at the rooftop elevation. It is also observed that the magnitudes of the advection, pressure diffusion and SGS dissipation terms increase by a factor of approximately 2.5, as the elevation increases from  $y/d = 0.5$  to 1, indicating that the convection and its effects on the transport of  $k_r$  increase drastically, especially around the midspan. Above the canopy at  $y/d = 1.5$ , the advection term is primarily balanced by the pressure diffusion term. The impact of the SGS dissipation rate on the transport of  $k_r$  is still important, however, its magnitude reduces as the elevation

increases from  $y/d = 1$  to 1.5. In other word, at this elevation, the effect of the separated shear layer from the cube sides is much reduced in comparison with that at lower elevations.

The local KE transfer between the resolved and unresolved (subgrid) scales has been also studied at same elevations as for the resolved KE. Although the SGS dissipation rate has a higher value at the rooftop level compared to other elevations, the relative strength of the SGS dissipation rate to the viscous dissipation rate does not show a considerable change at different elevations. It is observed that at all three elevations tested, the magnitude of the forward scatter is approximately 4 times larger than that of the backward scatter resulting in a net KE transfer from the resolved to unresolved scales. By analyzing the budget balance of the TKE transport equation, it is found that the TKE advection is primarily balanced with turbulent diffusion, TKE production and SGS dissipation rate. Under the canopy at half-cube height, the peak values of the TKE production term occur at  $z/d \approx \pm 0.5$  directly downstream of the two vertical sides of the obstacle. At the rooftop level, the separated shear layers from the side edges interact intensely with that issued from the top surface of the cube, and all considerably contribute to the transport of resolved TKE. Above the canopy at  $y/d = 1.5$ , the magnitudes of all budgetary terms of the TKE transport equation decrease by a factor of approximately 6. This is an indication of the decay of turbulence activities as the elevation increases above the cube rooftop. As the elevation increases above the canopy, the disturbances from the cubes are much reduced and flow becomes increasingly homogeneous in the spanwise direction.

## Chapter 6

# LES of turbulent dispersion from a localized source within an urban canopy model

In this chapter, the results of the LES of turbulent dispersion of passive scalar within a matrix of wall-mounted cubes will be presented and analyzed. The concentration field is produced through a continuous release of a passive scalar from a ground-level point source located within the matrix of cubes. The configuration of the matrix of obstacles is the same as presented in the previous chapter shown in Fig. 5.1. The concentration field is analyzed based on the statistics of the instantaneous field of the first and second orders, temporal spectra, transport equation of the scalar energy, and the CDF of the resolved concentration. The numerical predictions are also validated against the available water-channel measurement data.

### 6.1 Test case and computational domain

The test case is based on the same water-channel experiments of Yee *et al.* [24] and Hilderman and Chong [25] presented in the previous chapter. The concentration field was generated by continuous release of sodium fluorescein dye from a ground-level point source located in the central (specifically, the eighth) column and between the first and second rows of obstacles. The schematic of the source location and

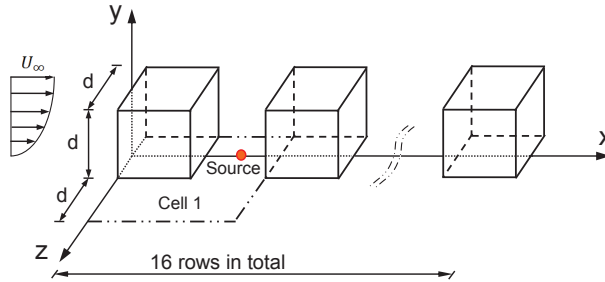


FIGURE 6.1: Schematic of the ground-level point source located in the central (or, eighth) column of the matrix of the obstacles.

coordinate system of the central column of the cubes are shown in Fig. 6.1. In the experiment, a one-dimensional (1-D) laser induced fluorescence (LIF) linescan system was used for measuring the instantaneous concentration field in the dispersing plume. Sodium fluorescein dye was continuously released from the point source at a rate of  $12 \text{ ml min}^{-1}$ , and illuminated using a laser beam powered by an argon-ion laser. The dye source was released from a small vertical stainless steel tube (with an inner diameter  $d_0 = 2.8 \text{ mm}$ ). A Dalsa monochrome digital linescan CCD camera ( $1024 \times 1$  pixels) with 12-bit (4,096 gray levels) amplitude resolution was used to measure the intensity of the dye fluorescence at a sampling rate of 300 Hz.

For simulating the concentration field, the scalar transport equation must be solved along with the flow governing equations whose solution was presented in the previous chapter. In order to close the filtered scalar transport equation, both dynamic eddy diffusivity model (EDM) of Moin *et al.* [102] (equation 2.17 in section 2.2.3) and dynamic full linear tensor diffusivity model (DFLTDM) of Wang *et al.* [103] (equation 2.19 in section 2.2.3) were tested for the current simulation. However, the EDM showed a more robust and stable behavior and consequently was used for modeling the the SGS scalar flux vector. The concentration release from the point source was activated when the flow had reached a fully-developed stage, and an additional period of approximately 2 flow-through times were spent to ensure that the scalar field had also become fully-developed. The concentration statistics were then collected through a course of approximately 10 flow-through times. The time step was  $3 \times 10^{-4} \text{ s}$  during the simulation. The convergence criterion for the solution

of the scalar transport equation was set to  $10^{-6}$  for the maximum difference between the new and old value of the scalar field ( $\bar{c}$ ) normalized by its spatially-averaged value obtained in the previous time step. In total, more than 100,000 CPU-hours have been spent to collect the concentration statistics.

In the simulation, the value of the scalar field has been set to zero at the inlet boundary. Zero-gradient condition has been assumed in the spanwise, upper and outlet boundaries of the domain. Zero-flux Neumann condition has been assumed at all solid surfaces to warrant the no-penetration condition.

## 6.2 Results and discussions

In this section, the concentration field is analyzed based on the statistics of the instantaneous field, temporal spectra, transport equation of the scalar energy, and CDF of the resolved concentration. The numerical predictions are also validated against a comprehensive water-channel measurement data.

### 6.2.1 General description of the concentration field

Figures 6.2a and 6.2b present a typical instantaneous snapshot of the concentration field (non-dimensionalized using the source strength  $c_s$ ) in the central  $x$ - $y$  plane (at  $z/d = 0$ ) and in the  $x$ - $z$  plane located at  $y/d = 0.5$ , respectively. As shown in both figures, as a passive scalar, the concentration field is significantly influenced by the turbulent flow patterns. From Fig. 6.2a, it is observed that a concentration boundary layer develops from the source location as the passive contaminant disperses through and above the cube array. Figure 6.2b vividly shows that under the canopy (at  $y/d = 0.5$ ), concentration carried by turbulent eddies dynamically meanders through the street canyons formed by cubes. In Fig. 6.3, the contours of the time-averaged concentration field (non-dimensionalized using the source strength  $c_s$ ) are displayed in  $x$ - $z$  planes at two different elevations under and above the canopy (for  $y/d = 0.5$  and 1.5, respectively). At both elevations, the concentration plume is symmetrical with

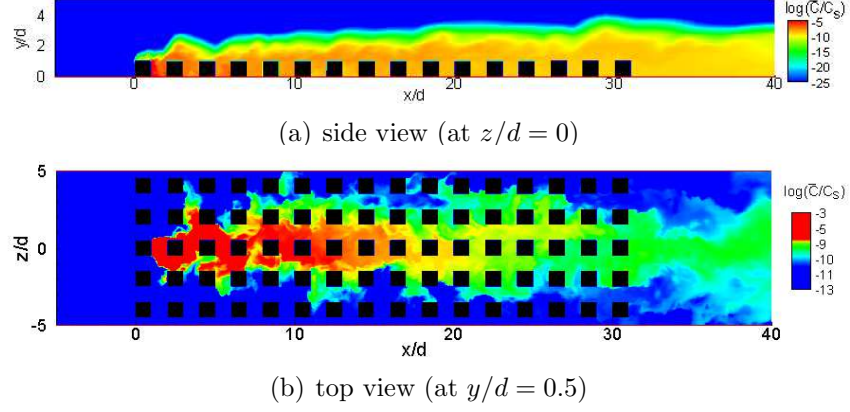


FIGURE 6.2: Contours of the instantaneous resolved concentration field ( $\bar{c}$ ) in the  $x$ - $y$  and  $x$ - $z$  planes located at  $z/d = 0$  and  $y/d = 0.5$ , respectively. The concentration field has been non-dimensionalized using the source strength  $c_s$ .

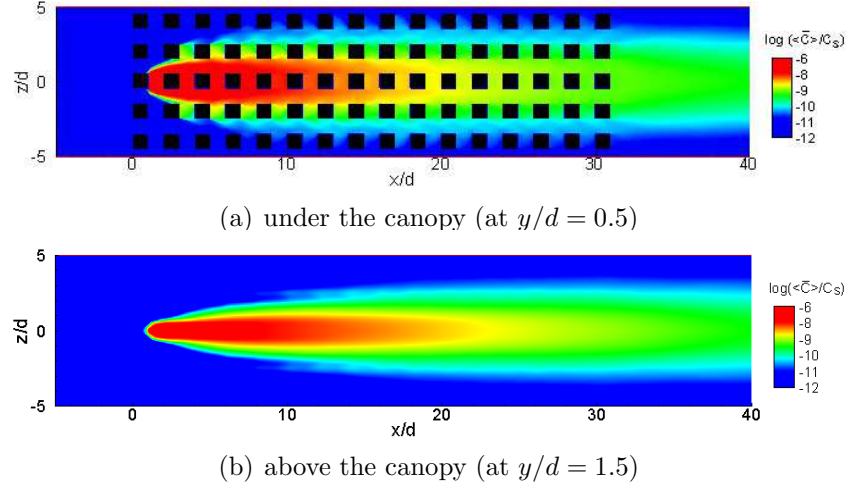


FIGURE 6.3: Contours of the time-averaged resolved concentration field ( $\langle \bar{c} \rangle$ ) in  $x$ - $z$  planes at two different elevations below and above the canopy. The concentration field has been non-dimensionalized using the source strength  $c_s$ .

respect to the central line of the domain ( $z/d = 0$ ). Above the canopy at  $y/d = 1.5$ , no direct interference between the obstacles and the concentration field occurs and the plume exhibits a typical Gaussian distribution across the stream.

Figure 6.4 shows the streamwise evolution of the vertical profiles of the mean and standard deviation of the concentration field (i.e.,  $\langle \bar{c} \rangle$  and  $\bar{c}_{rms} = \sqrt{\langle (\bar{c} - \langle \bar{c} \rangle)^2 \rangle}$ , respectively). The profiles are extracted from midpoint of 8 canyon regions starting from the second row ( $x/d = 3.5$ ) along the central column ( $z/d = 0$ ). In order to make the profiles at different locations comparable, concentrations and their standard

deviations have been non-dimensionalized using their local maximum values along each vertical line (that goes through the midpoint between two adjacent obstacles). The vertical position of the maximum concentration (corresponding to  $\langle \bar{c} \rangle / \langle \bar{c} \rangle_{max} = 1$ ) represents the centroid of the concentration plume, and as shown in Fig. 6.4a, it elevates as the streamwise distance from the point source increases. In fact, clean fluid packets (upstream or above the plume) entrain the plume and contaminated fluid packets engulf into the background clean fluid at the plume edge. This process results in the growth of the plume size. Also because of entraining and engulfing effects, the plume edge becomes highly intermittent, which significantly increases the level of concentration fluctuations. A similar trend is observed for the standard deviation profiles shown in Fig. 6.4b. However, by comparing Figs. 6.4a and 6.4b, it is evident that the peak values of the standard deviation are above those of the mean concentration at all streamwise locations. Similar observations have been made by Fackrell and Robins [172] for a point source in a turbulent boundary layer and by Lavertu and Mydlarski [173] for a line source in a turbulent plane channel flow. As is evident from Fig. 6.4a, the maximum vertical gradient of the mean concentration ( $d\langle \bar{c} \rangle / dy$ ) occurs at elevations immediately above that of the maximum mean concentration. This is related to the fact that the mean concentration gradient is typically the highest at the plume edge. As a consequence, the production rate of the concentration variance (i.e.,  $-2\langle \bar{u}_j'' \bar{c}'' \rangle \frac{\partial \langle \bar{c} \rangle}{\partial x_j}$ , where  $\bar{c}''$  is the resolved concentration fluctuation) is enhanced, further leading to an increase in the concentration variance at plume edges.

## 6.2.2 Concentration statistics

In the water-channel experiments of Yee *et al.* [24] and Hilderman and Chong [25], concentration statistics at three elevations are available, two under the canopy (for  $y/d = 0.25$  and  $0.5$ ) and one above the canopy (for  $y/d = 1.25$ ). In this section, the predicted and measured cross-stream profiles of the mean concentration at these three elevations are thoroughly compared through Figs. 6.5-6.7. As clearly shown

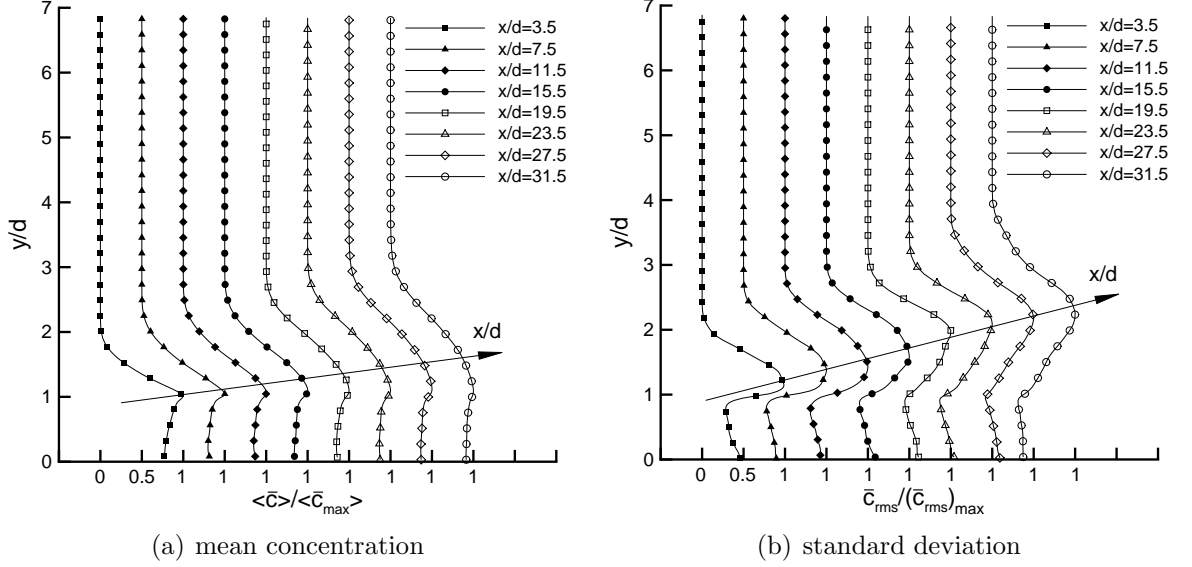


FIGURE 6.4: Streamwise evolution of vertical profiles of the mean and standard deviation of the concentration normalized by their local maximums along the vertical lines.

in these three figures, a good agreement between the numerical and experimental results is observed. Figures 6.5 and 6.6 show the mean concentration profiles at four streamwise locations under the canopy (for  $y/d = 0.25$  and  $0.5$ , respectively). From both Figs. 6.5 and 6.6, it is clear that as the distance from the source increases, the plume width increases in the cross-stream direction, however, its peak value decreases as a result of plume dispersion. At  $x/d = 3.5$ , the strong dual-peak pattern has been well captured by the numerical simulation. In fact, the dual-peak pattern is the direct result of the presence of the cube immediately behind the point source (which is located at  $x/d = 1.5$  in the central column). The cube introduces a local blockage into the concentration field such that the plume exhibits a distinct bimodal form as it sweeps around both sides of the cube. Then, the concentration disperses through the canyons on both sides of the cube. This results in a symmetric dual-peak pattern in the cross-stream concentration profile over a long sampling time. By comparing Fig. 6.7 with Fig. 6.6, it is clear that above the canopy ( $y/d = 1.25$ ), the plume width decreases apparently at the same streamwise locations, indicating a reduced amount of concentration at a higher elevation. Also, due to absence of obstacles, no apparent dual-peak pattern is observed at this elevation and the profiles tend to

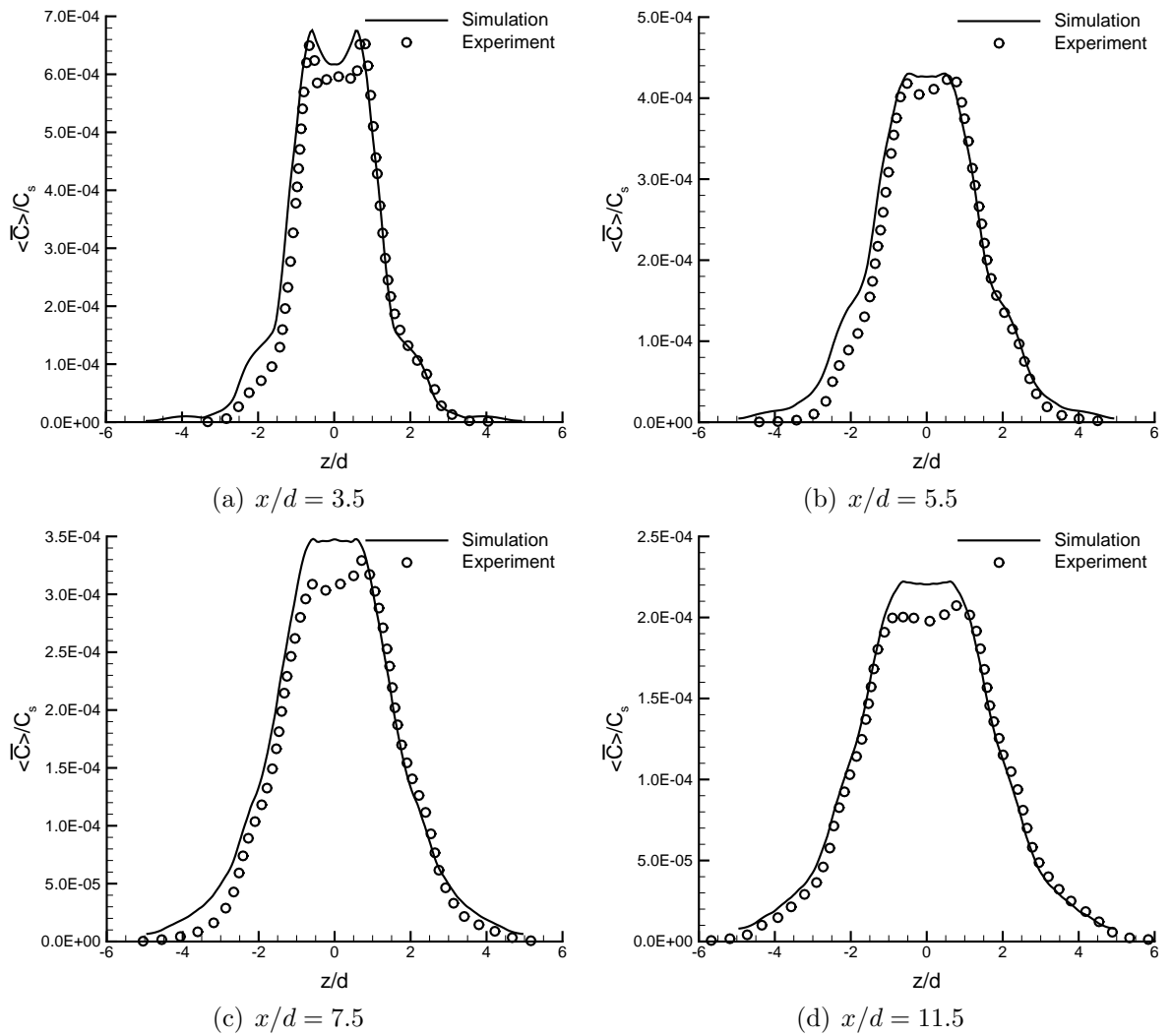


FIGURE 6.5: Cross-stream profiles of the non-dimensionalized mean concentration at the elevation  $y/d = 0.25$  and different streamwise locations.

exhibit a Gaussian distribution across the stream.

Figures 6.8-6.10 compare the predicted and measured cross-stream profiles of the standard deviation (or, RMS value) of the resolved concentration field at the same measurement locations as for the mean concentration presented previously in Figs. 6.5-6.7. In these figures, all the concentration variance values have been non-dimensionalized using the source strength  $c_s$ . By comparing the cross-stream profiles presented in Figs. 6.8-6.10, a general trend is observed in the streamwise evolution of the concentration RMS values: in regions close to the source location, the magnitude of  $\bar{c}_{rms}$  is high and the width of its profile is narrower, reflecting an intense turbulent

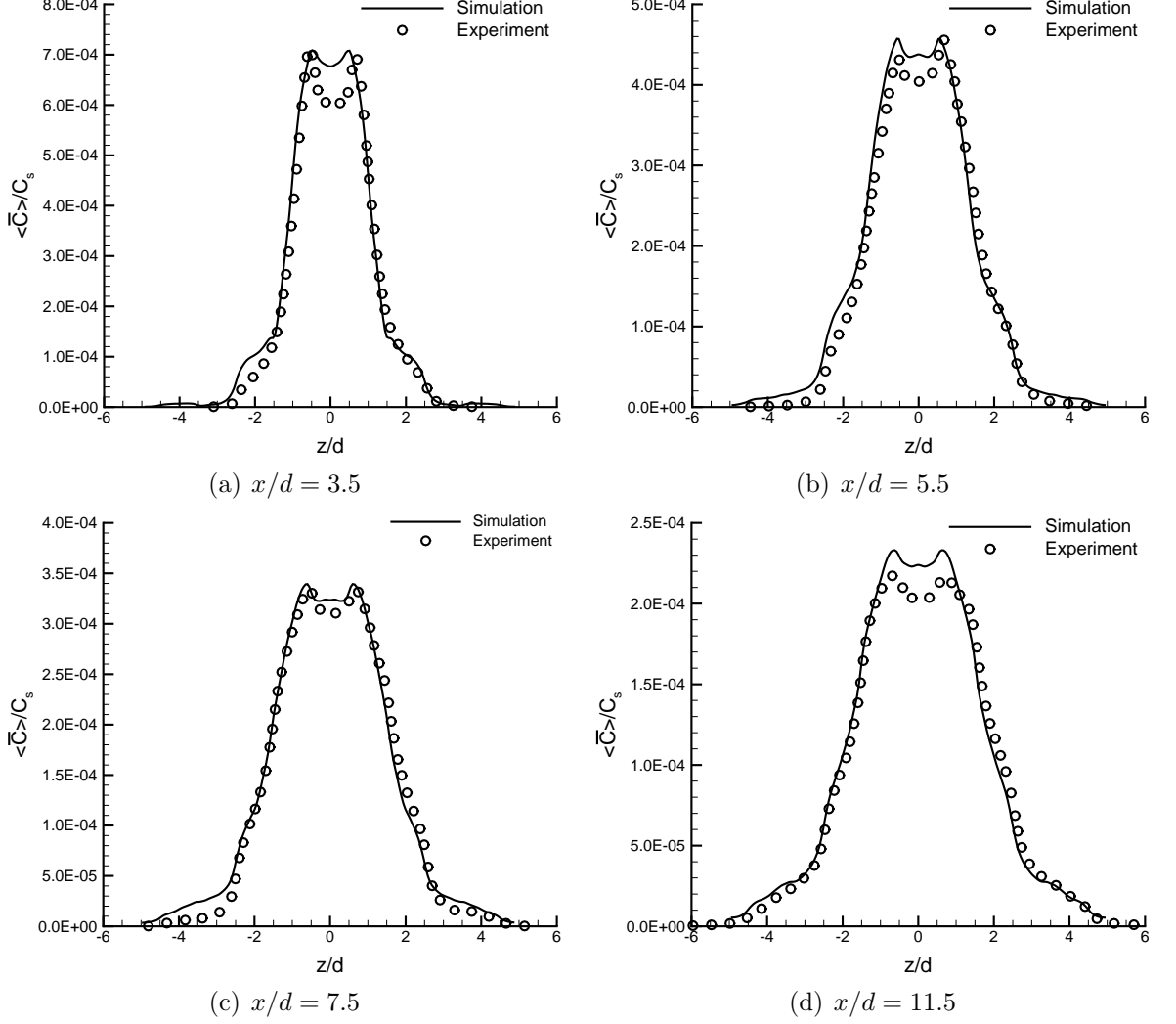


FIGURE 6.6: Cross-stream profiles of the non-dimensionalized mean concentration at the elevation  $y/d = 0.5$  and different streamwise locations.

fluctuation level; however, as the distance from the source increases, the peak value of  $\bar{c}_{rms}$  decays rapidly and its profile becomes wider in the cross-stream direction. As shown in Figs. 6.8 and 6.9, at elevations lower than the cube height (i.e.,  $y/d = 0.25$  and  $0.5$ ), a distinctive dual-peak pattern with a local minimum along the mean-plume centerline (at  $z/d = 0$ ) is observed which is well captured by the simulation. However, the simulation has underpredicted the magnitude of the peak values. The dual-peak pattern is due to the large vertical concentration gradient on two plume edges (see Figs. 6.5-6.7), which significantly increases the production rate for the concentration variance (i.e.,  $-2\langle \bar{u}_j' \bar{c}' \rangle \frac{\partial \langle \bar{c} \rangle}{\partial x_j}$ ). As shown in Figs. 6.10a-6.10d, above the

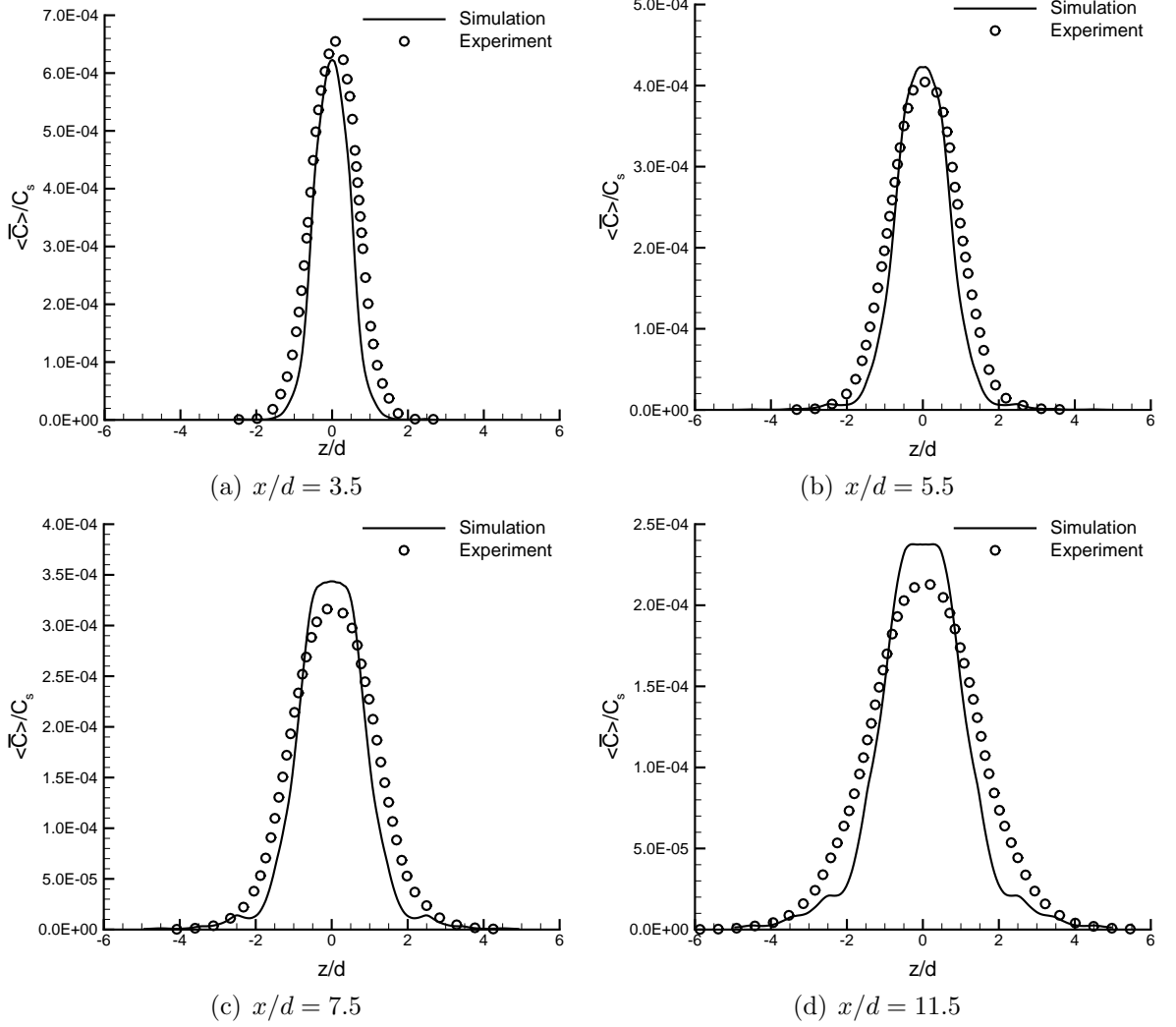


FIGURE 6.7: Cross-stream profiles of the non-dimensionalized mean concentration at the elevation  $y/d = 1.25$  and different streamwise locations.

canopy at elevation  $y/d = 1.25$ , the dual-peak pattern for the standard deviation is much less apparent in comparison with that shown at lower elevations, which is a direct consequence of the absence of cubic obstacles.

### 6.2.3 Spectra and scalar energy

Figure 6.11 shows the temporal spectra of concentration fluctuations at the same position ( $x/d = 13.5$ ,  $y/d = 1$  and  $z/d = 0$ , located in the central plane of the domain between rows 7 and 8 at the rooftop elevation) as for the velocity energy

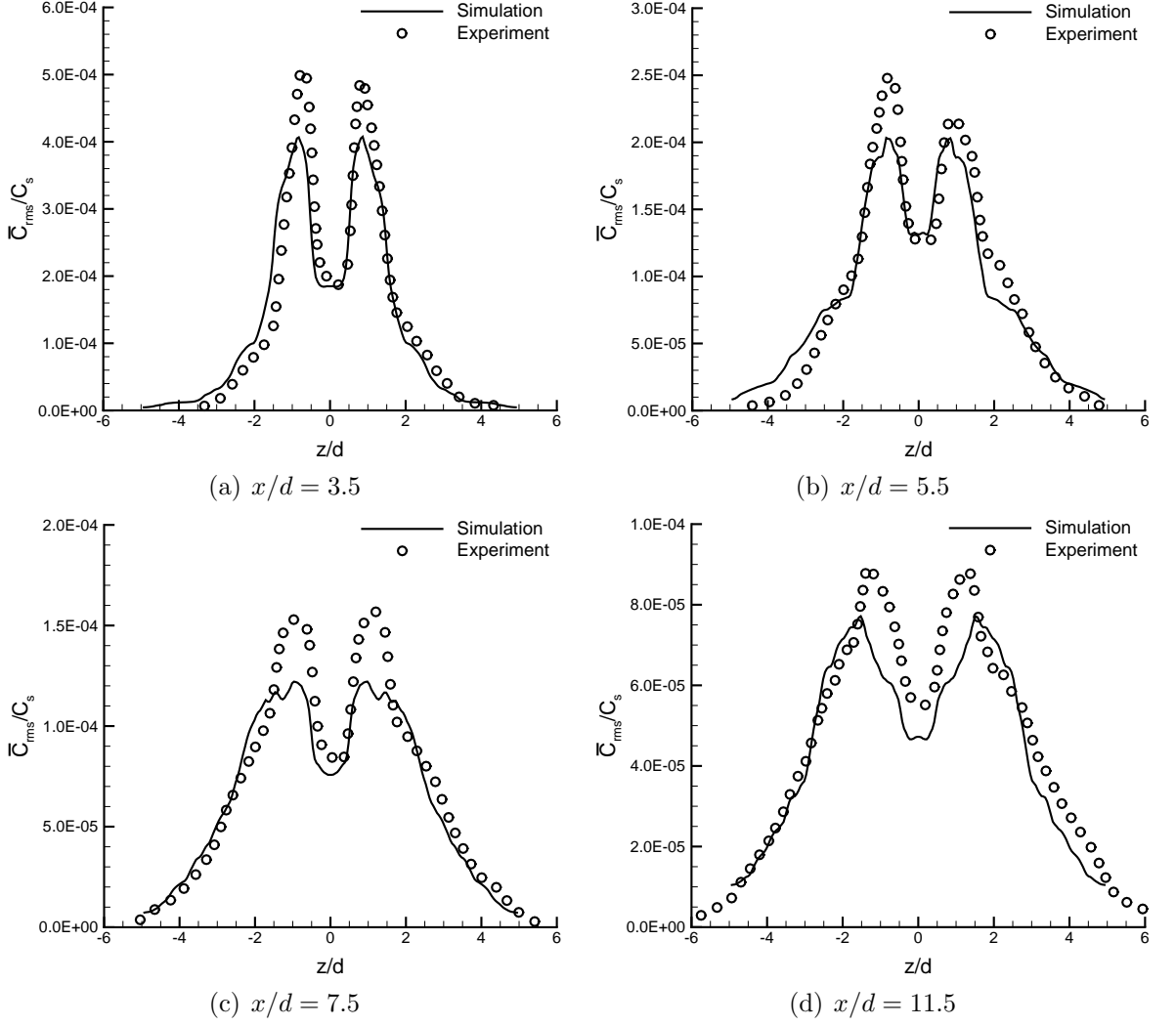


FIGURE 6.8: Cross-stream profiles of the non-dimensionalized standard deviation of the concentration at the elevation  $y/d = 0.25$  and different streamwise locations.

spectra plotted in Fig. 5.11. At this particular position, the flow has reached a self-similar state. Similar to Eq. 4.2, the spectra of concentration fluctuations relates to the resolved turbulent scalar energy as

$$k_s = \langle \bar{c}'' \bar{c}'' \rangle = \int_0^{f_c} E_{cc} df \quad , \quad (6.1)$$

where  $E_{cc}$  is the spectra of concentration fluctuations and  $k_s \stackrel{\text{def}}{=} \langle \bar{c}'' \bar{c}'' \rangle$  is the resolved turbulent scalar energy (or, scalar variance). In Fig. 6.11, the spectra is non-dimensionalized as  $E_{cc} U_\infty / (d \langle \bar{c} \rangle^2)$ . As indicated by Fackrell and Robins [172], similar

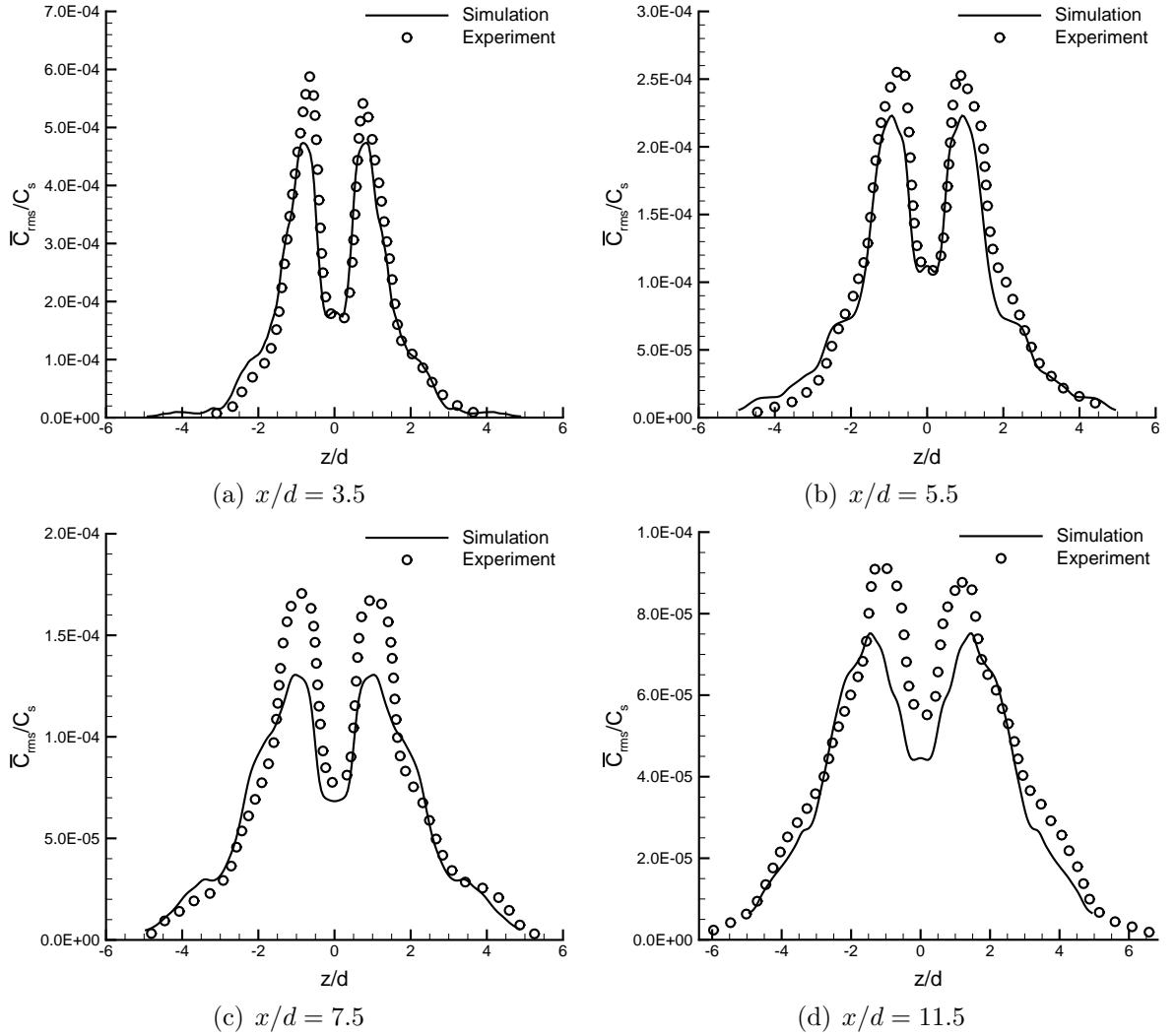


FIGURE 6.9: Cross-stream profiles of the standard deviation of the concentration at the elevation  $y/d = 0.5$  and different streamwise locations.

to temporal energy spectra for the velocity field, the inertial subrange for the turbulent scalar energy spectra also features the slope of  $-5/3$ . As shown in Fig. 6.11, the inertial subrange characteristic of the cascade of the turbulent scalar energy has been well captured by the current LES. This further implies that the inertial subrange and consequently the energetic motions and interactions of the concentration plume have been well captured by the simulation.

Figure 6.12 shows the CDF of the instantaneous concentration field extracted from the same location as for Fig. 6.11. As is evident in this figure, the CDF corresponding to  $\bar{c} = \langle \bar{c} \rangle$  is 51.8%. This shows that at this special position ( $x/d =$

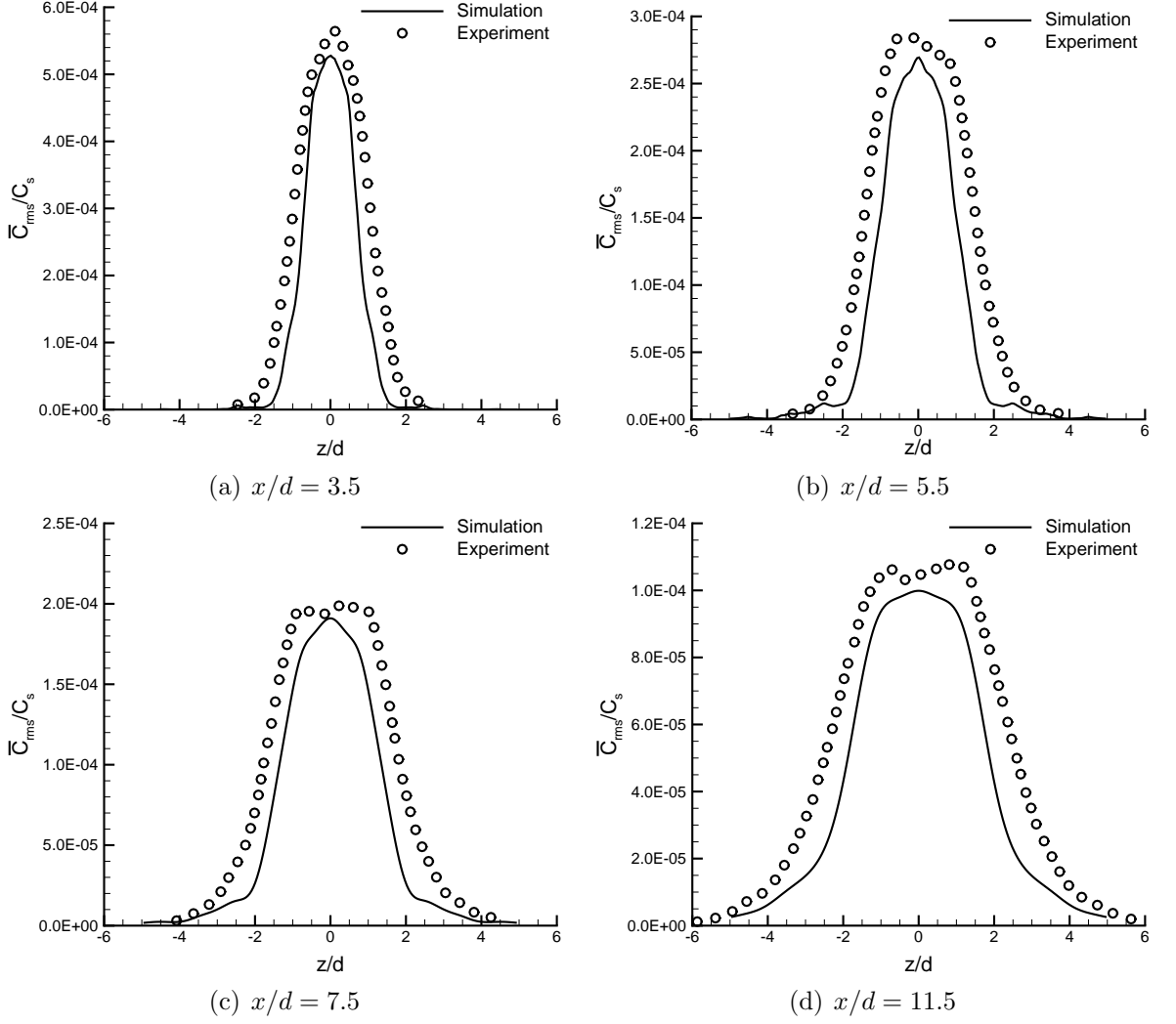


FIGURE 6.10: Cross-stream profiles of the standard deviation of the concentration at the elevation  $y/d = 1.25$  and different streamwise locations.

13.5,  $y/d = 1$  and  $z/d = 0$ ), the magnitude and number of random concentration fluctuations below and above the mean concentration value ( $\langle \bar{c} \rangle$ ) are almost identical. At this position (midpoint between rows 7 and 8 and at the cube height), there is a strong shear layer from the rooftop of the upstream cube, which results in intense concentration mixing and homogenizes the plume locally. As such, the CDF of the concentration field exhibits a steep symmetrical profile, which corresponds to a narrow Gaussian distribution about the mean concentration value.

Following Jiménez *et al.* [174], the so-called resolved scalar energy is defined as  $k_{r,s} \stackrel{\text{def}}{=} \bar{c}^2$ , which is analogous to the definition of the resolved KE  $k_r$  of the flow

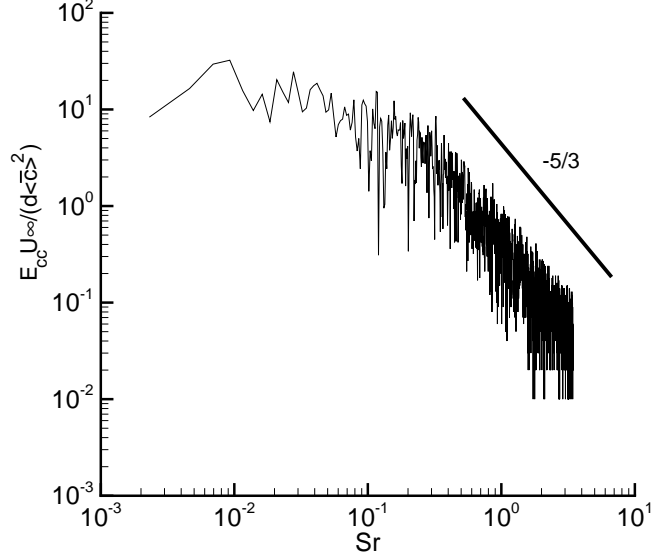


FIGURE 6.11: Non-dimensionalized temporal scalar energy spectra at  $x/d = 13.5$ ,  $y/d = 1$  and  $z/d = 0$ .

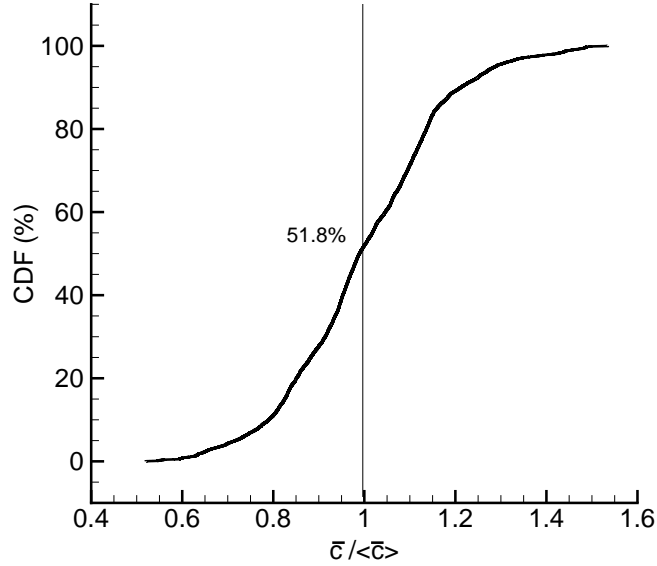


FIGURE 6.12: Cumulative distribution function for the resolved concentration at  $x/d = 13.5$ ,  $y/d = 1$  and  $z/d = 0$ .

field discussed previously in section 5.2.3. It can be shown that the time-averaged transport equation for the resolved scalar energy (SE) takes the following form

$$\underbrace{\left\langle \bar{u}_j \frac{\partial k_{rs}}{\partial x_j} \right\rangle}_{\text{advection}} = \alpha \underbrace{\left\langle \frac{\partial^2 k_{rs}}{\partial x_j \partial x_j} \right\rangle}_{\text{molecular diffusion}} - 2\alpha \underbrace{\left\langle \frac{\partial \bar{c}}{\partial x_j} \frac{\partial \bar{c}}{\partial x_j} \right\rangle}_{\text{molecular dissipation}} - 2 \underbrace{\left\langle \frac{\partial \bar{c} h_j}{\partial x_j} \right\rangle}_{\text{SGS diffusion}} + 2 \underbrace{\left\langle h_j \frac{\partial \bar{c}}{\partial x_j} \right\rangle}_{\text{SGS dissipation}} . \quad (6.2)$$

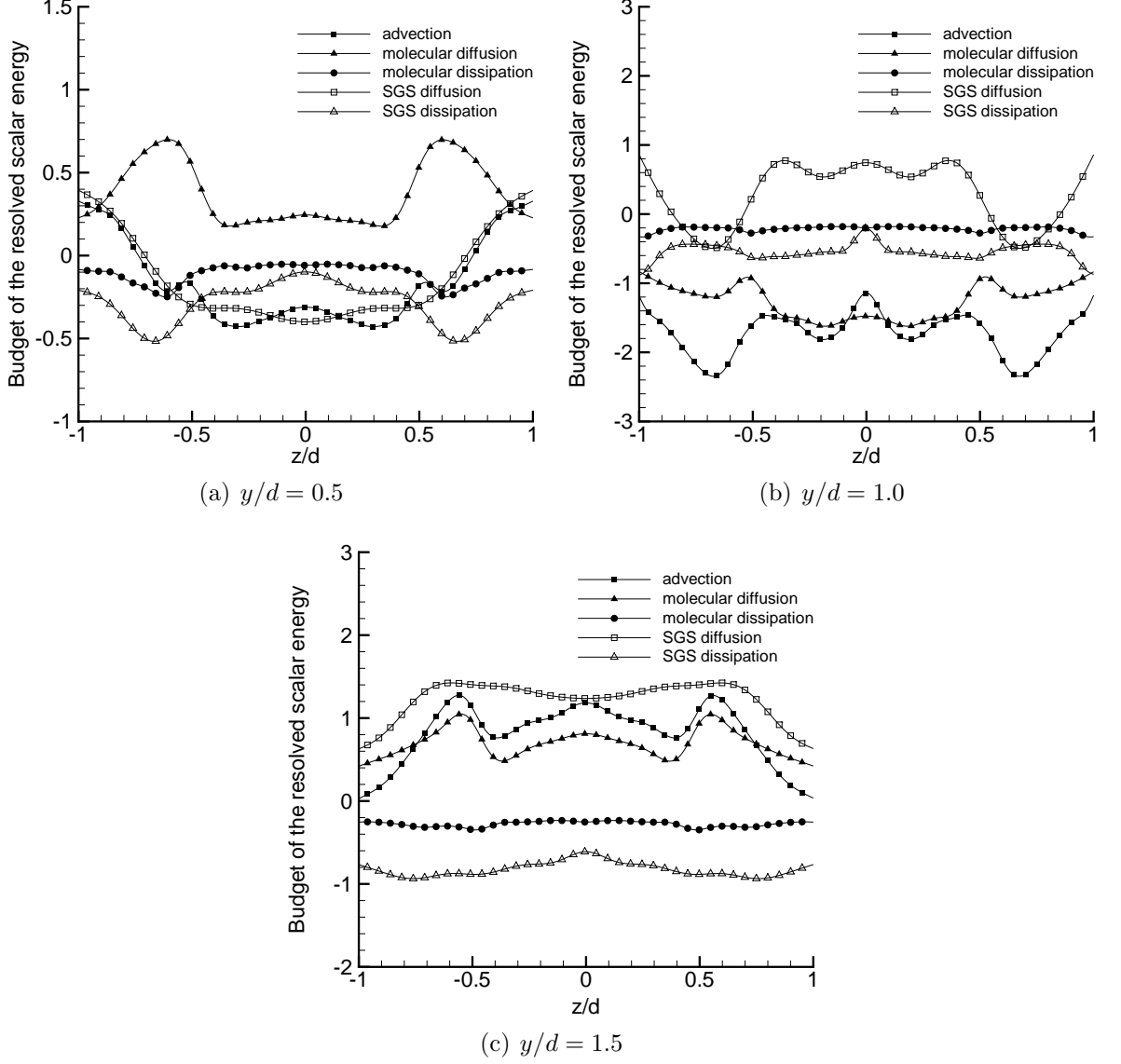


FIGURE 6.13: Budget of the time-averaged resolved scalar energy ( $k_{rs}$ ) at  $x/d = 13.5$  within  $-1 < z/d < 1$ , at three different elevations. All the terms are non-dimensionalized using  $U_\infty c_s^2/d$ .

Figures 6.13a-6.13c present the budget balance of the resolved SE  $k_{rs}$  at midpoint between rows 7 and 8 (for  $x/d = 13.5$ ) behind the central column (within  $-1 < z/d < 1$ ) at three different elevations (at the half-cube height, rooftop and above the canopy, for  $y/d = 0.5, 1$  and  $1.5$ , respectively). All the budget terms on the RHS of Eq. 6.2 shown in Figs. 6.13a-6.13c have included the addition/subtraction signs in Eq. 6.2. For instance, the molecular dissipation term and SGS diffusion term shown in the budget balance in Fig. 6.13 are  $-2\alpha \left\langle \frac{\partial \bar{c}}{\partial x_j} \frac{\partial \bar{c}}{\partial x_j} \right\rangle$  and  $-2 \left\langle \frac{\partial \bar{c} h_j}{\partial x_j} \right\rangle$ , respectively. In

Eq. 6.2, the molecular and SGS dissipation act as sink terms for the resolved SE. In Fig. 6.13, all the terms have been non-dimensionalized using  $U_\infty c_s^2/d$ . As shown in Fig. 6.13a, under the canopy at elevation  $y/d = 0.5$ , the advection term is negative (carrying the resolved SE away) within the range of  $|z/d| < 0.7$  and is positive (bringing in the resolved SE) for  $|z/d| > 0.7$ . This indicates that at the half-cube height, the effect of the mean velocity field is to carry the resolved SE out of the rear region of the cube (where the flow and concentration recirculate), and meanwhile, carries the resolved SE towards the two central canyon regions. At the rooftop level ( $y/d = 1$ ), however, the advection term is constantly negative, which indicates that the effect of the mean velocity field is to carry the resolved SE away. The minimum of the advection term occurs at  $z/d = \pm 0.65$ , where the contaminated fluid is dispersed away at the highest rate through convection mechanisms. As shown in Fig. 6.13c, above the canopy, the convection terms are exclusively positive, indicating that the resolved SE is carried to this elevation from ground level. In Figs. 6.13a-6.13c, the convection term exhibits extrema for  $z/d \in \pm[0.5 \sim 1.0]$ , which is due to the combined effects of the following two factors: (1) there are two strong shear layers issued by the two vertical sides of the cube (located at  $z/d = \pm 0.5$ ), which have significant impact on convection immediately downstream of them; and (2) the center of the street canyon is located at  $z/d = \pm 1.0$ , where the streamwise convection (streamwise velocity) is the highest under the canopy.

As shown in Fig. 6.13a, at the half canopy height ( $y/d = 0.5$ ), the molecular diffusion takes positive values across the spanwise direction. The concentration is released from a ground-level point source located at  $x/d = 1.5$ , which then channels through street canyons under the canopy. A positively valued molecular diffusion term is expected at this low elevation, which shows that the effect of molecular activities is to diffuse the resolved SE to other regions (i.e., transporting the concentration to a higher elevation). However, as shown in Fig. 6.13b, at the rooftop level ( $y/d = 1$ ), the molecular diffusion keeps negative across the channel, showing that the net effect of molecular activities is to carry the resolved SE  $\bar{c}^2$  towards this region. Negative molecular diffusion may be counterintuitive at first, which however, can

be well-explained through the advection-diffusion equation for  $\bar{c}^2$  (i.e, Eq. 6.2). As discussed in the previous paragraph, at the rooftop level, the flow and dispersion is much complicated by the three shear layers and their interactions with turbulent eddy motions. A negatively valued diffusion term is a direct consequence of a negatively valued advection term at this special position. Furthermore, as shown in Fig. 6.13c, above the canopy, both the advection and molecular diffusion terms maintain positive across the entire spanwise direction. This shows that in the region above canopy, the effect of cubic obstacles on plume dispersion is much reduced. Positively valued advection and molecular diffusion indicate that the contaminated fluid packets engulf into the clean background fluid in the region above canopy, which mechanism facilitates the growth of the plume size and elevation of its centroid in the streamwise direction. This is consistent with the previous observation in Fig. 6.4. Another interesting observation is that at this elevation ( $y/d = 1.5$ ), the cubes are deeply immersed under the canopy and their disturbances to the flow and dispersion are attenuated. As such, the profiles budget terms shown in Fig. 6.13c tend to recover spanwise homogeneity (as in an open channel), and this tendency is the most strongly expressed with the molecular and SGS dissipation terms.

As is evident Figs. 6.13a-6.13c, the SGS diffusion and dissipation terms play a significant role in balancing the advection term, and their magnitudes are much larger than that of the molecular dissipation term. Similar to the function of the SGS dissipation term  $\tau_{ij}^* \bar{S}_{ij}$  in Eq. 5.2 in the transport of the resolved KE, the SGS dissipation term  $2h_j \frac{\partial \bar{c}}{\partial x_j}$  reflects the local SE flux between the resolved and subgrid scale motions. As shown in Figs. 6.13a-6.13c, the value of  $2 \left\langle h_j \frac{\partial \bar{c}}{\partial x_j} \right\rangle$  remains negative across the stream at all three elevations, indicating a net forward scatter of SE from resolved to subgrid scales.

## 6.3 Closure

Turbulent dispersion of contaminant from a ground-level point source located within a modeled urban environment has been investigated using LES. The statistics and spectra of the concentration field, interactions of turbulent flow structures with the dispersing plume, and transport mechanisms of the scalar energy have been thoroughly analyzed.

By analyzing the cross-stream profiles of the mean and standard deviation of the concentration field, it is observed that in regions close to the source location, the magnitudes of  $\langle \bar{c} \rangle$  and  $\bar{c}_{rms}$  are high and their profiles are narrower, reflecting the high concentration zone and intense turbulent mixing close to the point source. However, as the distance from the source increases, the peak values of  $\langle \bar{c} \rangle$  and  $\bar{c}_{rms}$  decay rapidly and their profiles become wider in the cross-stream direction. A distinctive dual-peak pattern is observed in the cross-stream profiles of the mean concentration and its standard deviation at elevations lower than the cube height as a direct result of the presence of solid obstacles. The cube introduces a local blockage into the concentration field such that the plume exhibits a distinct bimodal form as it sweeps around both sides of the cube. However, above the canopy, a typical Gaussian pattern is observed for the cross-stream profiles of the mean concentration. The LES results on the cross-stream profiles of the mean concentration and concentration variance have been thoroughly compared against the available water-channel measurement data at different streamwise locations for three elevations (two under the canopy one above the canopy). The simulation predictions of the mean concentration field are in excellent agreement with the water-channel measurement data. The shapes of the cross-stream profiles of the concentration variance at different locations are also well captured by the simulation; however, their peak values are slightly underpredicted by the simulation under the canopy.

It is observed that the centroid of the concentration plume elevates as the downstream distance from the point source increases. At the plume edges, clean fluid packets (upstream or above the plume) entrain the plume and contaminated fluid

packets engulf into the background clean fluid. This process results in the growth of the plume size and makes plume edges become highly intermittent, which significantly increases the level of concentration fluctuations. At all streamwise locations, the peak values of the concentration variance  $\bar{c}_{rms}$  are above those of the mean concentration  $\langle \bar{c} \rangle$ . This is due to the fact that the mean concentration gradient is typically the highest at the plume edge. As a consequence, the production rate of the concentration variance is significantly enhanced at plume edges.

The temporal spectra of concentration fluctuations computed at a typical point in the flow self-similar region (midpoint between two consecutive cubes at the rooftop level) shows that the inertial subrange is well captured by the simulation. The CDF of the resolved instantaneous concentration field at this location reveals that the magnitude and the number of concentration fluctuations below and above the mean concentration value ( $\langle \bar{c} \rangle$ ) are almost identical. This further implies that the concentration plume has been developed enough such that the plume size is of the same order or larger than energetic turbulent eddies and fluctuations are purely from turbulent motions and internal mixing within the plume.

Through a careful analysis of the transport equation of the resolved SE  $\bar{c}^2$ , it is observed that under the canopy at the half-cube height, the effect of the mean velocity field is to carry the concentration out of the rear region of the cube, and meanwhile, carrying the concentration towards the two central canyon regions. At the rooftop level ( $y/d = 1$ ), however, the advection term is constantly negative, which indicates that the effect of the mean velocity field is to carry the resolved SE away. A positively valued molecular diffusion is observed at the half-cube height indicating that the effect of molecular activities is to diffuse the resolved SE to other regions (i.e., transporting the concentration to a higher elevation). However, at the rooftop level ( $y/d = 1$ ), the molecular diffusion keeps negative across the channel, showing that the net effect of molecular activities is to carry the resolved SE towards this region. Above the canopy, both the advection and molecular diffusion terms maintain positive across the entire spanwise direction which shows the reduced effect of cubic obstacles on plume dispersion. Positively valued advection and molecular diffusion indicates

that the contaminated fluid packets engulf into the clean background fluid in the region above canopy, which results to the growth of the plume size and elevation of its centroid in the streamwise direction.

# Chapter 7

## Conclusions and Future Works

### 7.1 Computational code

In this thesis, a 3-D finite difference CFD code written in FORTRAN 90/95 and parallelized with MPI libraries has been modified, developed and customized to be used in DNS/LES of turbulent flows and dispersion in complex geometries such as flow in urban environments and around bluff bodies. The second-order energy-conserving finite difference scheme of Ham *et al.* [106] has been employed for discretizing the flow governing equations. The four-step fractional step method of Choi and Moin [109] coupled with the second-order Crank-Nicolson scheme have been used to advance the velocity field over a single time step. A second-order TVD scheme [108] and the second-order central differencing scheme are used for discretizing the convective and diffusive terms of the scalar transport equation, respectively. The Crank-Nicolson scheme has been used for time advancement of the scalar transport equation.

The scalability of the code has been tested based on a plane channel flow with grid resolution of  $160^3$ . It is observed that for the mentioned grid system, the speedup of 94.6 can be achieved using 128 processors. In order to conduct the final simulations, several preliminary steps have been performed which are summarized in the following subsections.

### 7.1.1 SGS stress and scalar flux models

In order to close the system of filtered governing equations required for LES of turbulent flows, the so-called SGS stress tensor needs to be modeled. In view of this, different SGS stress models have been studied and tested in different flow configurations (e.g., the study of Saeedi *et al.* [92]) to be embedded into the computational code required for conducting wall-resolved and wall-modeled LES. In summary, with respect to different influential factors including the mathematical robustness, stability and self-calibrating mechanisms, two different SGS stress models (i.e., the DSM of Lilly [93] and Germano *et al.* [94] and the DNM of Wang and Bergstrom [95]) have been used for simulations of turbulent flows over a single and a group of wall-mounted obstacles. For the LES of turbulent dispersion arising from a continuous release of contaminant from a point source, the EDM of Moin *et al.* [102] has been used to model the scalar flux vector.

### 7.1.2 Wall models

With respect to the very high computational demand of wall-resolved LES for resolving the flow dynamics near solid surfaces, conducting wall-resolved LES for turbulent flow over a group of obstacles is indeed prohibitively expensive. Thus, we essentially need to model the near wall dynamics for simulating the flow in a computational domain which includes a large number of obstacles. Different wall models have been studied and the wall model of Wang and Moin [75] has been selected for the wall-modeled LES. This model is based on the simplified thin boundary layer equations which accounts for the changes of pressure gradient. Thus, compared to other simpler wall models, it can show a better performance for configurations with flow separations.

### 7.1.3 Inlet conditions

In order to successfully simulate turbulent flows over wall-mounted obstacles, one of the key factors is to prescribe realistic inlet boundary conditions. In fact, the approaching flow in real atmospheric boundary layers has a very high turbulence level. In this research, several inlet conditions reported in the literature are tested to prescribe the proper inflow condition. However, the desired turbulence level can not be reproduced using existing classical methods. Thus, a method based on generating grid turbulence at the inlet of the flow domain has been proposed which can substantially increase the turbulence level of the approaching flow.

### 7.1.4 Preliminary validation

The code was initially validated by solving turbulent plane channel flow at two Reynolds numbers  $Re_\tau = 300$  and  $Re_\tau = 2,000$ . Wall-modeled LES was conducted to simulate the turbulent flow in these two test cases. The results were compared against theory and also available DNS data of Iwamoto *et al.* [166]. Very good agreement between the LES predictions and available DNS data were observed. In the next sections, the results of more rigorous tests over more geometrically complex domains will be summarized.

## 7.2 Turbulent wake of a single wall-mounted obstacle

For studying the turbulent flow in complex geometries and specifically in build-up environments (as one of the primary objectives of this thesis), in the first step, turbulent flow over a single wall-mounted square cylinder with  $AR = 4$  at  $Re=12,000$  has been selected. This configuration is based on a recent wind-tunnel experiment of Bourgeois *et al.* [17, 18] and Sattari *et al.* [19]. In comparison with the classical cube flow case (for  $AR = 1$ ) of Rodi [52], Shah and Ferziger [57] and Yakhot *et*

*al.* [45, 46], this test case results in more energetic vortex motions and interactions, which further imposes a greater challenge to numerical simulations to properly capture eddy motions of all relevant scales with a much larger computational domain. This test case has been identified non-trivial in term of computational efforts and used as one of two “challenge cases” in two consecutive Annual Conferences of the CFD Society of Canada hosted in Canmore, Alberta in 2012, and in Sherbrooke, Quebec in 2013. Local flow separation, sharp velocity gradient in regions close to the cylinder edges and high Reynolds number are among the challenges associated for simulating this flow configuration.

Wall-resolved LES has been chosen to investigate the turbulent wake behind the cylinder. Over 40,000 CPU-hours have been spent to solve the flow field and collect the turbulence statistics. Very good agreement with the available experimental measurement data has been obtained and the flow structures have been thoroughly analyzed. With the aim of wall-resolved LES, we have been able to capture the sensitive flow dynamics and obtain detailed analysis of turbulent wake behind the wall-mounted high aspect ratio obstacle. The frequency of Kármán vortex shedding and its corresponding Strouhal number has been well captured in the simulation. It is revealed that the highest influence of the SGS model and consequently the energy transfer between the resolved and subgrid scales occurred within the immediate wake of the cylinder where interactions of shear layers separated from the top and side edges of the cylinder are highly enhanced.

### **7.3 Turbulent flow over a matrix of wall-mounted obstacles**

To extend our study of turbulent flows to a group of wall-mounted obstacles (which can more realistically represent an urban area and build-up environment) the water-channel experiment of Yee *et al.* [24] and Hilderman and Chong [25] has been selected as the test case. In their selected experiment, a regular matrix of  $16 \times 16$  wall-mounted

cubes was submerged in a simulated neutrally stratified atmospheric boundary layer. The Reynolds number based on the cube's side length and the free-stream velocity was 12,005. Due to the presence of several obstacles in the flow field (which means several solid surfaces in the flow domain), conducting wall-resolved LES for this test case, is extremely expensive. Therefore, wall-modeled LES has been selected for conducting the simulation. Given the fact that the flow conditions are symmetric in the spanwise direction and in order to moderate the computational cost, a regular matrix of  $5 \times 16$  cubes have been considered in the simulation. The SGS stress model of Wang and Bergstrom [95] and the wall model of Wang and Moin [75] have been used as the SGS stress and wall models, respectively. One of the main challenges of this problem is to realistically reproduce the highly turbulent (with turbulence intensity of at least 10%) approaching boundary layer. In order to select the proper inlet condition, a comparative study between four different inlet conditions has been conducted. Based on the performances of the studied approaches, a method based on mounting a solid grid at the inlet of the computational domain is selected to trigger the flow instability and produce physical perturbations. Following this approach enabled us to reproduce the turbulence level up to approximately 7% in regions above the wall-mounted cubes. In terms of the computational cost, over 100,000 CPU-hours have been spent for solving the flow field and collecting the statistics. Good agreement between the numerical prediction and experimental measurement data are obtained.

Based on the analysis of the budget balance of the resolved KE transport equation, it is observed that below the rooftop level, the advection term is mainly balanced with the pressure diffusion and SGS dissipation rate. The peak values of the advection and pressure diffusion terms occur directly downstream of the cube's side edges. This is due to the separated shear layers issued from the cube sides which trigger the flow instability and entrain the recirculating region immediately behind the cube. However, at the rooftop elevation, the largest peak of the advection term occur at  $z/d \approx 0$ . This is due to the strong unstable shear layer formed on the cube rooftop and the accompanied boundary-layer separation and turbulent mixing on top of the canopy. It is observed that at all different elevations studied, the magnitude of the

forward scatter is approximately  $3 \sim 4$  times larger than that of the backward scatter resulting in a net KE transfer from the resolved to unresolved scales.

## 7.4 Turbulent dispersion from a localized source

In order to study turbulent dispersion of contaminant in urban environments, we further extended our urban flow simulation and located a ground-level point source with continuous release of contaminant in the central column of obstacles at the midpoint between the first and second rows. The experimental measurement data of the concentration field was also available from the work of Yee *et al.* [24] and Hilderman and Chong [25]. The evolution of the mean concentration field and its RMS values have been well predicted by the simulation. Reasonable agreement between the numerical prediction and experimental measurement data is observed for the mean and standard deviation of the concentration field. In total, more than 100,000 CPU-hours have been spent to perform the simulation and collect the statistics.

By analyzing the streamwise evolution of the concentration plume, it is observed that the centroid of the concentration plume elevates as the downstream distance from the point source increases. Also, the peak values of the standard deviation are always located above those of the mean concentration. This is mainly because the maximum vertical gradient of the mean concentration is always located above the point for the maximum mean concentration which enhances the concentration variance production. The CDF of the resolved instantaneous concentration field at a typical point in the velocity self-similar region (inside the canyon region and at the rooftop level) reveals that the magnitude and the number of concentration fluctuations below and above the mean concentration value ( $\langle \bar{c} \rangle$ ) are almost identical. This further implies that the concentration plume has been developed enough such that the plume size is of the same order or larger than energetic turbulent eddies and fluctuations are purely from turbulent motions and internal mixing within the plume. By investigating the transport equation of the resolved SE, it is observed that under the canopy at the

half-cube height, the effect of the mean velocity field is to carry the concentration out of the rear of the cube, and meanwhile, carrying the concentration to this streamwise location through canyons besides the cube. At the rooftop level ( $y/d = 1$ ), however, the advection term is constantly negative, which indicates that the effect of the mean velocity field is to wash the concentration away. It is observed that at all elevations studied, the molecular and SGS dissipations act as sink terms for the resolved scalar energy.

## 7.5 Future works

To continue the current research on turbulent flow and dispersion in urban environments, the following suggestions are recommended:

- Investigating the effects of different influential parameters (e.g., Reynolds number, aspect ratios and inlet turbulence) on the turbulent wake of a single wall-mounted obstacle using wall-resolved and wall-modeled LES.
- Conducting comparative studies on the performance of different SGS stress models for simulating turbulent wake of wall-mounted obstacles.
- Simulating the flow field in different arrangements of wall-mounted obstacles including staggered array of cubes, obstacles with higher aspect ratios (rectangle obstacles rather than cubic obstacles) and a combination of obstacles with low and high aspect ratios.
- Studying the effects of different wind directions on the evolution of turbulent flow structures in different regions around the wall-mounted obstacles.
- Placing the point source at different locations including elevations below and above the canopy and also in different places in streamwise streets.
- Investigating the feasibility of employing a wall model for the simulation of the dispersion field.

- Studying the non-continuous release of the contaminant and puff release from the point source.
- Studying the dispersion field arising from multiple point sources in the flow domain.

## References

- [1] D. Sumner, J. L. Heseltine, and O. J. P. Dansereau, “Wake structure of a finite circular cylinder of small aspect ratio,” *Exper. Fluids*, vol. 37, pp. 720–730, 2004.
- [2] J. J. Miao, S. J. Wu, C. C. Hu, and J. H. Chou, “Low-frequency modulations associated with vortex shedding from flow over bluff body,” *AIAA J.*, vol. 42, pp. 1388–1397, 2004.
- [3] D. Sumner and J. L. Heseltine, “Tip vortex structure for a circular cylinder with a free end,” *J. Wind Eng. Ind. Aero.*, vol. 96, pp. 1185–1196, 2008.
- [4] I. P. Castro and A. G. Robins, “The flow around a surface-mounted cube in uniform and turbulent streams,” *J. Fluid Mech.*, vol. 79, pp. 307–335, 1977.
- [5] J. C. R. Hunt, C. J. Abell, J. A. Peterka, and H. Woo, “Kinematical studies of the flows around free or surface-mounted obstacles; applying topology to flow visualization,” *J. Fluid Mech.*, vol. 86, pp. 179–200, 1978.
- [6] C.-W. Park and S.-J. Lee, “Free end effects on the near wake flow structure behind a finite circular cylinder,” *J. Wind Eng. Ind. Aero.*, vol. 88, pp. 231–246, 2000.
- [7] M. S. Adaramola, O. G. Akinlade, D. Sumner, D. J. Bergstrom, and A. J.

- Schenstead, “Turbulent wake of a finite circular cylinder of small aspect ratio,” *J. Fluids Struct.*, vol. 22, pp. 919–928, 2006.
- [8] H. J. Hussein and R. J. Martinuzzi, “Energy balance for turbulent flow around a surface mounted cube placed in a channel,” *Phys. Fluids*, vol. 8, pp. 764–780, 1996.
- [9] H. F. Wang, Y. Zhou, C. K. Chan, and K. S. Lam, “Effect of initial conditions on interaction between a boundary layer and a wall-mounted finite-length-cylinder wake,” *Phys. Fluids*, vol. 18, pp. 065106, 1–12, 2006.
- [10] H. F. Wang and Y. Zhou, “The finite-length square cylinder near wake,” *J. Fluid Mech.*, vol. 638, pp. 453–490, 2009.
- [11] H. Wang, Y. Zhou, C. Chan, and T. Zhou, “Momentum and heat transport in a finite-length cylinder wake,” *Exper. Fluids*, vol. 46, pp. 1173–1185, 2009.
- [12] T. B. Araújo, C. Sicot, J. Borée, and R. J. Martinuzzi, “Influence of obstacle aspect ratio on tripped cylinder wakes,” *Int. J. Heat Fluid Flow*, vol. 35, pp. 109–118, 2012.
- [13] A. Okajima, “Strouhal numbers of rectangular cylinders,” *J. Fluid Mech.*, vol. 123, pp. 379–398, 1982.
- [14] H. C. Lim, I. P. Castro, and R. P. Hoxey, “Bluff bodies in deep turbulent boundary layers: Reynolds-number issues,” *J. Fluid Mech.*, vol. 571, pp. 97–118, 2007.
- [15] D. Sumner, M. D. Richards, and O. O. Akosile, “Strouhal number data for two staggered circular cylinders,” *J. Wind Eng. Ind. Aero.*, vol. 96, pp. 859–871, 2008.

- [16] R. Martinuzzi, M. Abuomar, and E. Savory, “Scaling of wall pressure field around surface-mounted pyramids and other bluff bodies,” *J. Fluids Eng.*, vol. 129, pp. 1147–1156, 2007.
- [17] J. A. Bourgeois, P. Sattari, and R. J. Martinuzzi, “Alternating half-loop shedding in the turbulent wake of a finite surface-mounted square cylinder with a thin boundary layer,” *Phys. Fluids*, vol. 23, pp. 095101, 1–15, 2011.
- [18] J. A. Bourgeois, B. R. Noack, and R. J. Martinuzzi, “Generalized phase average with applications to sensor-based flow estimation of the wall-mounted square cylinder wake,” *J. Fluid Mech.*, vol. 736, pp. 316–350, 2013.
- [19] P. Sattari, J. A. Bourgeois, and R. J. Martinuzzi, “On the vortex dynamics in the wake of a finite surface-mounted square cylinder,” *Exper. Fluids*, vol. 52, pp. 1149–1167, 2012.
- [20] R. J. Martinuzzi and B. Havel, “Vortex shedding from two surface-mounted cubes in tandem,” *Int. J. Heat Fluid Flow*, vol. 25, pp. 364–372, 2004.
- [21] K. J. Allwine, J. H. Shinn, G. E. Streit, K. L. Clawson, and M. Brown, “Overview of URBAN 2000: A multiscale field study of dispersion through an urban environment,” *Bull. Amer. Meteorol. Soc.*, vol. 83, pp. 521–536, 2002.
- [22] M. W. Rotach, S.-E. Gryning, E. Batchvarova, A. Christen, and R. Vogt, “Pollutant dispersion close to an urban surface—the BUBBLE tracer experiment,” *Meteorol. Atmos. Phys.*, vol. 87, pp. 39–56, 2004.
- [23] E. Yee and C. A. Biltoft, “Concentration fluctuation measurements in a plume dispersing through a regular array of obstacles,” *Boundary-Layer Meteorol.*, vol. 111, pp. 363–415, 2004.

- [24] E. Yee, R. M. Gailis, A. Hill, T. Hilderman, and D. Kiel, “Comparison of wind-tunnel and water-channel simulations of plume dispersion through a large array of obstacles with a scaled field experiment,” *Boundary-Layer Meteorol.*, vol. 121, pp. 389–432, 2006.
- [25] T. Hilderman and R. Chong, “A laboratory study of momentum and passive scalar transport and diffusion within and above a model urban canopy,” Tech. Rep. CRDC 00327, Coanda Research & Development Corporation, 2004. 70 pp.
- [26] M. J. Brown, R. E. Lawson, D. S. DeCroix, and R. L. Lee, “Comparison of centerline velocity measurements obtained around 2D and 3D building arrays in a wind tunnel,” Tech. Rep. LA-UR-01-4138, Los Alamos National Laboratory, 2001.
- [27] R. W. MacDonald, R. F. Griffiths, and D. J. Hall, “An improved method for the estimation of surface roughness of obstacle arrays,” *J. Atmos. Env.*, vol. 32, pp. 1857–1864, 1998.
- [28] R. W. MacDonald, “Modelling the mean velocity profile in the urban canopy layer,” *Boundary-Layer Meteorol.*, vol. 97, pp. 25–45, 2000.
- [29] S. Andronopoulos, D. Grigoriadis, A. Robins, A. Venetsanos, S. Rafailidis, and J. G. Bartzis, “Three-dimensional modelling of concentration fluctuations in complicated geometry,” *Env. Fluids Mech.*, vol. 1, pp. 415–440, 2002.
- [30] M. Milliez and B. Carissimo, “Computational fluid dynamical modelling of concentration fluctuations in an idealized urban area,” *Boundary-Layer Meteorol.*, vol. 127, pp. 241–259, 2008.

- [31] B.-C. Wang, E. Yee, and F.-S. Lien, “Numerical study of dispersing pollutant clouds in a built-up environment,” *Int. J. Heat Fluid Flow*, vol. 30, pp. 3–19, 2009.
- [32] B.-C. Wang, E. Yee, and F.-S. Lien, “Prediction of second-order concentration statistics for dispersing plumes in obstacle arrays,” *Prog. Comput. Fluid Dyn.*, vol. 10, pp. 252–262, 2010.
- [33] E. Yee, B.-C. Wang, and F.-S. Lien, “Probabilistic model for concentration fluctuations in compact-source plumes in an urban environment,” *Boundary-Layer Meteorol.*, vol. 130, pp. 169–208, 2009.
- [34] F. S. Lien, E. Yee, and Y. Cheng, “Simulation of mean flow and turbulence over a 2D building array using high-resolution CFD and a distributed drag force approach,” *J. Wind Eng. Ind. Aero.*, vol. 92, pp. 117–158, 2004.
- [35] F.-S. Lien and E. Yee, “Numerical modelling of the turbulent flow developing within and over a 3-D building array, part I: A high resolution Reynolds-averaged Navier-Stokes approach,” *Boundary-Layer Meteorol.*, vol. 112, pp. 427–466, 2004.
- [36] J. L. Santiago, A. Martilli, and F. Martín, “CFD simulation of airflow over a regular array of cubes. Part I: Three-dimensional simulation of the flow and validation with wind-tunnel measurements,” *Boundary-Layer Meteorol.*, vol. 122, pp. 609–634, 2007.
- [37] J.-J. Kim and J.-J. Baik, “A numerical study of the effects of ambient wind direction on flow and dispersion in urban street canyons using the RNG  $k-\epsilon$  turbulence model,” *J. Atmos. Env.*, vol. 38, pp. 3039–3048, 2004.

- [38] S. Majumdar and W. Rodi, “Three-dimensional computation of flow past cylindrical structures and model cooling towers,” *Bldg Envir.*, vol. 24, pp. 3–22, 1989.
- [39] K. J. Hsieh and F. S. Lien, “Conjugate turbulent forced convection in a channel with an array of ribs,” *Int. J. Numer. Meth. Heat Fluid Flow*, vol. 15, pp. 462–482, 2005.
- [40] L. E. Drain and S. Martin, “Two-component velocity measurements of turbulent flow in a ribbed-wall flow channel,” in *Proc. of 1st International Conference on Laser Anemometry, Advances and Applications*, 1985. Manchester - UK.
- [41] A. K. Saha, K. Muralidhar, and G. Biswas, “Vortex structures and kinetic energy budget in two-dimensional flow past a square cylinder,” *Comput. Fluids*, vol. 29, pp. 669–694, 2000.
- [42] A. K. Saha, G. Biswas, and K. Muralidhar, “Three-dimensional study of flow past a square cylinder at low Reynolds numbers,” *Int. J. Heat Fluid Flow*, vol. 24, pp. 54–66, 2003.
- [43] A. Sohankar, C. Norberg, and L. Davidson, “Simulation of three-dimensional flow around a square cylinder at moderate Reynolds numbers,” *Phys. Fluids*, vol. 11, pp. 288–306, 1999.
- [44] J.-Y. Hwang and K.-S. Yang, “Numerical study of vortical structures around a wall-mounted cubic obstacle in channel flow,” *Phys. Fluids*, vol. 16, pp. 2382–2394, 2004.
- [45] A. Yakhot, H. Liu, and N. Nikitin, “Turbulent flow around a wall-mounted cube: A direct numerical simulation,” *Int. J. Heat Fluid Flow*, vol. 27, pp. 994–1009, 2006.

- [46] A. Yakhot, T. Anor, H. Liu, and N. Nikitin, “Direct numerical simulation of turbulent flow around a wall-mounted cube: Spatio-temporal evolution of large-scale vortices,” *J. Fluid Mech.*, vol. 566, pp. 1–9, 2006.
- [47] M. Saeedi, P. LePoudre, and B.-C. Wang, “Direct numerical simulation of turbulent wake behind a wall-mounted cylinder,” *J. Fluids Struct.*, vol. 59, pp. 20–39, 2014.
- [48] V. Dousset and A. Poth erat, “Formation mechanism of hairpin vortices in the wake of a truncated square cylinder in a duct,” *J. Fluid Mech.*, vol. 653, pp. 519–536, 2010.
- [49] O. Coceal, T. G. Thomas, I. P. Castro, and S. E. Belcher, “Mean flow and turbulence statistics over groups of urban-like cubical obstacles,” *Boundary-Layer Meteorol.*, vol. 121, pp. 491–519, 2006.
- [50] J. H. Lee, H. J. Sung, and P.- . Krogstad, “Direct numerical simulation of the turbulent boundary layer over a cube-roughened wall,” *J. Fluid Mech.*, vol. 669, pp. 397–431, 2011.
- [51] A. Ashrafian, H. I. Andersson, and M. Manhart, “DNS of turbulent flow in a rod-roughened channel,” *Int. J. Heat Fluid Flow*, vol. 25, pp. 373–383, 2004.
- [52] W. Rodi, “Comparison of LES and RANS calculations of the flow around bluff bodies,” *J. Wind Eng. Ind. Aero.*, vol. 69, pp. 55–75, 1997.
- [53] Y. Cheng, F. S. Lien, E. Yee, and R. Sinclair, “A comparison of large eddy simulations with a standard  $k-\epsilon$  Reynolds-averaged Navier-Stokes model for the prediction of a fully developed turbulent flow over a matrix of cubes,” *J. Wind Eng. Ind. Aero.*, vol. 91, pp. 1301–1328, 2003.

- [54] S. M. Salim, R. Buccolieri, A. Chan, and S. D. Sabatino, “Numerical simulation of atmospheric pollutant dispersion in an urban street canyon: Comparison between RANS and LES,” *J. Wind Eng. Ind. Aero.*, vol. 99, pp. 103–113, 2011.
- [55] S. Schmidt and F. Thiele, “Comparison of numerical methods applied to the flow over wall-mounted cubes,” *Int. J. Heat Fluid Flow*, vol. 23, pp. 330–339, 2002.
- [56] Z. Xie and I. P. Castro, “LES and RANS for turbulent flow over arrays of wall-mounted obstacles,” *Flow, Turbul. Combust.*, vol. 76, pp. 291–312, 2006.
- [57] K. B. Shah and J. H. Ferziger, “A fluid mechanics view of wind engineering: Large eddy simulation of flow past a cubic obstacle,” *J. Wind Eng. Ind. Aero.*, vol. 67, pp. 211–224, 1997.
- [58] R. Martinuzzi and C. Tropea, “The flow around surface-mounted, prismatic obstacles placed in a fully developed channel flow,” *J. Fluids Eng.*, vol. 115, pp. 85–92, 1993.
- [59] J. Fröhlich, W. Rodi, P. Kessler, S. Parpais, J. P. Bertoglio, and D. Laurence, “Large eddy simulation of flow around circular cylinders on structured and unstructured grids,” *Note. Numer. Fluid Mech.*, vol. 66, pp. 319–338, 1998.
- [60] J. Fröhlich and W. Rodi, “LES of the flow around a circular cylinder of finite height,” *Int. J. Heat Fluid Flow*, vol. 25, pp. 537–548, 2004.
- [61] M. Breuer, “Large eddy simulation of the subcritical flow past a circular cylinder: Numerical and modeling aspects,” *Int. J. Numer. Meth. Fluids*, vol. 28, pp. 1281–1302, 1998.

- [62] M. Breuer, “A challenging test case for large eddy simulation: High Reynolds number circular cylinder flow,” *Int. J. Heat Fluid Flow*, vol. 21, pp. 648–654, 2000.
- [63] P. Catalano, M. Wang, G. Iaccarino, and P. Moin, “Numerical simulation of the flow around a circular cylinder at high Reynolds numbers,” *Int. J. Heat Fluid Flow*, vol. 24, pp. 463–469, 2003.
- [64] D.-H. Kim, K.-S. Yang, and M. Senda, “Large eddy simulation of turbulent flow past a square cylinder confined in a channel,” *Comput. Fluids*, vol. 33, pp. 81–96, 2004.
- [65] I. Afgan, C. Moulinec, R. Prosser, and D. Laurence, “Large eddy simulation of turbulent flow for wall mounted cantilever cylinders of aspect ratio 6 and 10,” *Int. J. Heat Fluid Flow*, vol. 28, pp. 561–574, 2007.
- [66] D. A. Lysenko, I. S. Ertesvåg, and K. E. Rian, “Large-eddy simulation of the flow over a circular cylinder at Reynolds number 3900 using the OpenFOAM toolbox,” *Flow, Turbul. Combust.*, vol. 89, pp. 491–518, 2012.
- [67] B. Ničeno, A. D. T. Dronkers, and K. Hanjalić, “Turbulent heat transfer from a multi-layered wall-mounted cube matrix: A large eddy simulation,” *Int. J. Heat Fluid Flow*, vol. 23, pp. 173–185, 2002.
- [68] S. R. Hanna, S. Tehranian, B. Carissimo, R. W. MacDonald, and R. Lohner, “Comparisons of model simulations with observations of mean flow and turbulence within simple obstacle arrays,” *J. Atmos. Env.*, vol. 36, pp. 5067–5079, 2002.
- [69] R. F. Shi, G. X. Cui, Z. S. Wang, C. X. Xu, and Z. S. Zhang, “Large eddy

- simulation of wind field and plume dispersion in building array,” *J. Atmos. Env.*, vol. 42, pp. 1083–1097, 2008.
- [70] C.-H. Liu, D. Y. C. Leung, and M. C. Barth, “On the prediction of air and pollutant exchange rates in street canyons of different aspect ratios using large-eddy simulation,” *J. Atmos. Env.*, vol. 39, pp. 1567–1574, 2005.
- [71] W. C. Cheng and C.-H. Liu, “Large-eddy simulation of flow and pollutant transports in and above two-dimensional idealized street canyons,” *Boundary-Layer Meteorol.*, vol. 139, pp. 411–437, 2011.
- [72] P. J. Mason and N. S. Callen, “On the magnitude of the subgrid-scale eddy coefficient in large-eddy simulations of turbulent channel flow,” *J. Fluid Mech.*, vol. 162, pp. 439–462, 1986.
- [73] U. Piomelli, J. Ferziger, P. Moin, and J. Kim, “New approximate boundary conditions for large eddy simulations of wall-bounded flows,” *Phys. Fluids A*, vol. 1, pp. 1061–1068, 1989.
- [74] U. Piomelli and E. Balaras, “Wall-layer models for large-eddy simulations,” *Annu. Rev. Fluid Mech.*, vol. 34, pp. 349–374, 2002.
- [75] M. Wang and P. Moin, “Dynamic wall modeling for large-eddy simulation of complex turbulent flows,” *Phys. Fluids*, vol. 14, pp. 2043–2051, 2002.
- [76] S. Kawai and J. Larsson, “Wall-modeling in large eddy simulation: Length scales, grid resolution, and accuracy,” *Phys. Fluids*, vol. 24, pp. 015105, 1–10, 2012.
- [77] E. Balaras, C. Benocci, and U. Piomelli, “Finite-difference computations of

- high Reynolds number flows using the dynamic subgrid-scale model,” *Theor. Comput. Fluid Dyn.*, vol. 7, pp. 207–216, 1995.
- [78] S. B. Mathieu and J. Scott, *An Introduction to Turbulent Flow*. Cambridge, UK: Cambridge Univ., 2000.
- [79] S. V. Patankar, *Numerical Heat Transfer and Fluid Flow*. New York: Hemisphere, 1980.
- [80] J. H. Ferziger and M. Perić, *Computational Methods for Fluid Dynamics*. Berlin: Springer, 2nd ed., 1999.
- [81] R. H. Pletcher, J. C. Tannehill, and D. A. Anderson, *Computational Fluid Mechanics and Heat Transfer*. New York: Taylor and Francis, 3rd ed., 2013.
- [82] P. Moin and J. Kim, “Numerical investigation of turbulent channel flow,” *J. Fluid Mech.*, vol. 118, pp. 341–387, 1982.
- [83] P. Sagaut and R. Grohens, “Discrete filters for large eddy simulation,” *Int. J. Numer. Meth. Fluids*, vol. 31, pp. 1195–1220, 1999.
- [84] J. Smagorinsky, “General circulation experiments with the primitive equations I. the basic experiment,” *Mon. Weath. Rev.*, vol. 91, pp. 99–164, 1963.
- [85] S. Liu, C. Meneveau, and J. Katz, “On the properties of similarity subgrid-scale models as deduced from measurements in a turbulent jet,” *J. Fluid Mech.*, vol. 275, pp. 83–119, 1994.
- [86] M. V. Salvetti and S. Banerjee, “A priori tests of a new dynamic subgrid-scale model for finite-difference large-eddy simulations,” *Phys. Fluids*, vol. 7, pp. 2831–2847, 1995.

- [87] Y. Morinishi and O. V. Vasilyev, “A recommended modification to the dynamic two-parameter mixed subgrid scale model for large eddy simulation of wall bounded turbulent flow,” *Phys. Fluids*, vol. 13, pp. 3400–3410, 2001.
- [88] B.-C. Wang and D. Bergstrom, “An integral-type dynamic localization two-parameter subgrid-scale model: Formulation and simulation,” *Int. J. CFD*, vol. 18, pp. 209–220, 2004.
- [89] T. Sayadi and P. Moin, “A comparative study of subgrid scale models for the prediction of transition in turbulent boundary layers,” *Center for Turbulence Research, Annual Research Briefs 2010*, pp. 237–247, 2010.
- [90] M. Saeedi and B.-C. Wang, “On the euler rotation angle and axis of a subgrid-scale stress model,” in *proc. of 2012 CTR Summer Program, Center for Turbulence Research, Stanford Univ.*, pp. 117–126, 2012.
- [91] M. Saeedi and B.-C. Wang, “Large-eddy simulation of turbulent flow over an array of wall-mounted cubic obstacles,” in *Direct and Large-Eddy Simulation 9 (DLES9)*, 2013 (in print). Dresden, Germany.
- [92] M. Saeedi, B.-C. Wang, and Z. Yang, “A comparative study of subgrid-scale stress models in the context of a transitional boundary layer,” *Acta Mechanica*, vol. 225, pp. 2595–2609, 2014.
- [93] D. K. Lilly, “A proposed modification of the Germano subgrid-scale closure method,” *Phys. Fluids A*, vol. 4, pp. 633–635, 1992.
- [94] M. Germano, U. Piomelli, P. Moin, and W. H. Cabot, “A dynamic subgrid-scale eddy viscosity model,” *Phys. Fluids A*, vol. 3, pp. 1760–1765, 1991.

- [95] B.-C. Wang and D. Bergstrom, “A dynamic nonlinear subgrid-scale stress model,” *Phys. Fluids*, vol. 17, pp. 035109, 1–15, 2005.
- [96] C. G. Speziale, “On nonlinear  $k-l$  and  $k-\varepsilon$  models of turbulence,” *J. Fluid Mech.*, vol. 178, pp. 459–475, 1987.
- [97] B.-C. Wang, E. Yee, D. Bergstrom, and O. Iida, “New dynamic subgrid-scale heat flux models for large-eddy simulation of thermal convection based on the general gradient diffusion hypothesis,” *J. Fluid Mech.*, vol. 604, pp. 125–163, 2008.
- [98] B.-C. Wang, E. Yee, J. Yin, and D. J. Bergstrom, “A general dynamic linear tensor-diffusivity subgrid-scale heat flux model for large-eddy simulation of turbulent thermal flows,” *Numer. Heat Trans.: Part B*, vol. 51, pp. 205–227, 2007.
- [99] B.-C. Wang, E. Yee, and D. Bergstrom, “Geometrical description of subgrid-scale stress tensor based on Euler axis/angle,” *AIAA J.*, vol. 44, pp. 1106–1110, 2006.
- [100] Q.-Q. Xun, B.-C. Wang, and E. Yee, “Large-eddy simulation of turbulent heat convection in a spanwise rotating channel flow,” *Int. J. Heat Mass Trans.*, vol. 54, pp. 698–716, 2011.
- [101] M. Molla, B.-C. Wang, and D. Kuhn, “Characteristics of pulsatile channel flows undergoing transition triggered by an idealized stenosis,” *Phys. Fluids*, vol. 24, pp. 121901, 1–25, 2012.
- [102] P. Moin, K. Squires, W. Cabot, and S. Lee, “A dynamic subgrid-scale model for compressible turbulence and scalar transport,” *Phys. Fluids A*, vol. 3, pp. 2746–2757, 1991.

- [103] B.-C. Wang, J. Yin, E. Yee, and D. Bergstrom, “A complete and irreducible dynamic SGS heat-flux modelling based on the strain rate tensor for large-eddy simulation of thermal convection,” *Int. J. Heat Fluid Flow*, vol. 28, pp. 1227–1243, 2007.
- [104] P. A. Durbin and B. A. Pettersson Rief, *Statistical Theory and Modeling for Turbulent Flows*. London: Wiley, 2nd ed., 2011.
- [105] C. R. Ethier and D. A. Steinman, “Exact fully 3D Navier-Stokes solutions for benchmarking,” *Int. J. Numer. Meth. Fluids*, vol. 19, pp. 369–375, 1994.
- [106] F. E. Ham, F. S. Lien, and A. B. Strong, “A fully conservative second-order finite difference scheme for incompressible flow on nonuniform grids,” *J. Comp. Phys.*, vol. 177, pp. 117–133, 2002.
- [107] Y. Morinishi, T. S. Lund, O. V. Vasilyev, and P. Moin, “Fully conservative higher order finite difference schemes for incompressible flow,” *J. Comp. Phys.*, vol. 143, pp. 90–124, 1998.
- [108] H. Versteeg and W. Malalasekera, *An Introduction To Computational Fluid Dynamics: The Finite Volume Method*. Essex, England: Pearson Education, 2nd ed., 2007.
- [109] H. Choi and P. Moin, “Effects of the computational time step on numerical solutions of turbulent flow,” *J. Comp. Phys.*, vol. 113, pp. 1–4, 1994.
- [110] P. Sagaut, *Large Eddy Simulation for Incompressible Flows: An Introduction*. Berlin: Springer, 2nd ed., 2002.
- [111] D. R. Chapman, “Computational aerodynamics development and outlook,” *AIAA J.*, vol. 17, pp. 1293–1313, 1979.

- [112] H. Choi and P. Moin, “Grid-point requirements for large eddy simulation: Chapman’s estimates revisited,” *Center for Turbulence Research, Annual Research Briefs 2011*, pp. 31–36, 2011.
- [113] P. R. Spalart, “Strategies for turbulence modelling and simulations,” *Int. J. Heat Fluid Flow*, vol. 21, pp. 252–263, 2000.
- [114] W. Cabot and P. Moin, “Approximate wall boundary conditions in the large-eddy simulation of high Reynolds number flow,” *Flow, Turbul. Combust.*, vol. 63, pp. 269–291, 1999.
- [115] U. Piomelli, “Wall-modeled large-eddy simulations: Present status and prospects,” in *Direct and Large-Eddy Simulation 7*, September 2008. Trieste - Italy.
- [116] U. Piomelli, “Wall-layer models for large-eddy simulations,” *Prog. Aerospace Science*, vol. 44, pp. 437–446, 2008.
- [117] P. R. Spalart, “Detached-eddy simulation,” *Annu. Rev. Fluid Mech.*, vol. 41, pp. 181–202, 2009.
- [118] P. R. Spalart, W.-H. Jou, M. Strelets, and S. R. Allmaras, “Comments on the feasibility of LES for wings, and on a hybrid RANS/LES approach,” in *1st AFOSR International Conference on DNS/LES*, August 1997. Ruston - LA.
- [119] R. Allen, F. Mendonça, and D. Kirkham, “RANS and DES turbulence model predictions of noise on the M219 cavity at  $M = 0.85$ ,” *Int. J. Aeroacoust.*, vol. 4, pp. 135–151, 2005.
- [120] M. L. Shur, P. R. Spalart, M. K. Strelets, and A. K. Travin, “A hybrid RANS-

- LES approach with delayed-DES and wall-modelled LES capabilities,” *Int. J. Heat Fluid Flow*, vol. 29, pp. 1638–1649, 2008.
- [121] A. Travin, M. Shur, M. Strelets, and P. Spalart, “Detached-eddy simulations past a circular cylinder,” *Flow, Turbul. Combust.*, vol. 63, pp. 293–313, 1999.
- [122] N. V. Nikitin, F. Nicoud, B. Wasistho, K. D. Squires, and P. R. Spalart, “An approach to wall modeling in large-eddy simulations,” *Phys. Fluids*, vol. 12, pp. 1629–1632, 2000.
- [123] J. Larsson and S. Kawai, “Wall-modeling in large eddy simulation: Length scales, grid resolution and accuracy,” *Center for Turbulence Research, Annual Research Briefs 2010*, pp. 39–46, 2010.
- [124] J. W. Deardorff, “A numerical study of three-dimensional turbulent channel flow at large Reynolds numbers,” *J. Fluid Mech.*, vol. 41, pp. 453–480, 1970.
- [125] J. Laufer, “Investigation of turbulent flow in a two-dimensional channel,” Tech. Rep. NACA TN 1053, National Advisory Committee for Aeronautics, 1950.
- [126] U. Schumann, “Subgrid scale model for finite difference simulations of turbulent flows in plane channels and annuli,” *J. Comp. Phys.*, vol. 18, pp. 376–404, 1975.
- [127] S. Rajagopalan and R. A. Antonia, “Some properties of the large structure in a fully developed turbulent duct flow,” *Phys. Fluids*, vol. 22, pp. 614–622, 1979.
- [128] G. Grötzbach, *Encyclopedia of Fluid Mechanics, Vol. 6*. West Orange, NJ: N. P. Cheremisinoff editor, Gulf, 1987.
- [129] W. Cabot, “Large-eddy simulations with wall models,” *Center for Turbulence Research, Annual Research Briefs 1995*, pp. 41–50, 1995.

- [130] W. Cabot, “Near-wall models in large eddy simulations of flow behind a backward-facing step,” *Center for Turbulence Research, Annual Research Briefs 1996*, pp. 199–210, 1996.
- [131] E. Balaras, C. Benocci, and U. Piomelli, “Two-layer approximate boundary conditions for large-eddy simulations,” *AIAA J.*, vol. 34, pp. 1111–1119, 1996.
- [132] S. Kawai and J. Larsson, “A dynamic wall model for large-eddy simulation of high Reynolds number compressible flows,” *Center for Turbulence Research, Annual Research Briefs 2010*, pp. 25–37, 2010.
- [133] S. Kawai and J. Larsson, “Wall modeling in large-eddy simulation: Predicting accurate skin friction at very high Reynolds number,” in *49th AIAA Aerospace Sciences Meeting*, January 2011. Orlando, FL.
- [134] M. Wang, “LES with wall models for trailing-edge aeroacoustics,” *Center for Turbulence Research, Annual Research Briefs 1999*, pp. 355–364, 1999.
- [135] Z. L. Chen, A. Devesa, S. Hickel, C. Stemmer, and N. A. Adams, “A wall model based on simplified thin boundary layer equations for implicit large eddy simulation of turbulent channel flow,” *Note. Numer. Fluid Mech.*, vol. 112, pp. 59–66, 2010.
- [136] F. Nicoud, J. S. Baggett, P. Moin, and W. Cabot, “Large eddy simulation wall-modeling based on suboptimal control theory and linear stochastic estimation,” *Phys. Fluids*, vol. 13, pp. 2968–2984, 2001.
- [137] T.-H. Shih, L. A. Povinelli, and N.-S. Liu, “Application of generalized wall function for complex turbulent flows,” *J. Turbul.*, vol. 4(15), pp. 1–16, 2003.

- [138] H. Tennekes and J. L. Lumley, *A First Course in Turbulence*. Cambridge, MA: MIT, 1972.
- [139] L. Castillo and T. G. Johansson, “The effects of the upstream conditions on a low Reynolds number turbulent boundary layer with zero pressure gradient,” *J. Turbul.*, vol. 3(31), pp. 1–19, 2002.
- [140] B. J. Boersma, G. Brethouwer, and F. T. M. Nieuwstadt, “A numerical investigation on the effect of the inflow conditions on the self-similar region of a round jet,” *Phys. Fluids*, vol. 10, pp. 899–909, 1998.
- [141] M. D. Slessor, C. L. Bond, and P. E. Dimotakis, “Turbulent shear-layer mixing at high Reynolds numbers: Effects of inflow conditions,” *J. Fluid Mech.*, vol. 376, pp. 115–138, 1998.
- [142] M. Saeedi and B.-C. Wang, “Investigation of the inlet effects on the wake of a wall-mounted cube using large-eddy simulation,” in *Proc. 21st Annual Conference of the CFD Society of Canada (CFD2013)*, 2013. Sherbrooke, Quebec, Canada.
- [143] G. R. Tabor and M. H. Baba-Ahmadi, “Inlet conditions for large eddy simulation: A review,” *Comput. Fluids*, vol. 39, pp. 553–567, 2010.
- [144] S. Lee, S. K. Lele, and P. Moin, “Simulation of spatially evolving turbulence and the applicability of Taylor’s hypothesis in compressible flow,” *Phys. Fluids A*, vol. 4, pp. 1521–1530, 1992.
- [145] H. Le, P. Moin, and J. Kim, “Direct numerical simulation of turbulent flow over a backward-facing step,” *J. Fluid Mech.*, vol. 330, pp. 349–374, 1997.

- [146] C. W. Li and J. H. Wang, “Large eddy simulation of free surface shallow-water flow,” *Int. J. Numer. Meth. Fluids*, vol. 34, pp. 31–46, 2000.
- [147] A. Smirnov, S. Shi, and I. Celik, “Random flow generation technique for large eddy simulations and particle-dynamics modeling,” *J. Fluids Eng.*, vol. 123, pp. 359–371, 2001.
- [148] M. Klein, A. Sadiki, and J. Janicka, “A digital filter based generation of inflow data for spatially developing direct numerical or large eddy simulations,” *J. Comp. Phys.*, vol. 186, pp. 652–665, 2003.
- [149] L. di Mare, M. Klein, W. P. Jones, and J. Janicka, “Synthetic turbulence inflow conditions for large-eddy simulation,” *Phys. Fluids*, vol. 18, pp. 025107, 1–11, 2006.
- [150] I. Veloudis, Z. Yang, J. J. McGuirk, G. J. Page, and A. Spencer, “Novel implementation and assessment of a digital filter based approach for the generation of LES inlet conditions,” *Flow, Turbul. Combust.*, vol. 79, pp. 1–24, 2007.
- [151] Z.-T. Xie and I. P. Castro, “Efficient generation of inflow conditions for large eddy simulation of street-scale flows,” *Flow, Turbul. Combust.*, vol. 81, pp. 449–470, 2008.
- [152] D. J. Glaze and S. H. Frankel, “Stochastic inlet conditions for large-eddy simulation of a fully turbulent jet,” *AIAA J.*, vol. 41, pp. 1064–1073, 2003.
- [153] N. D. Sandham, Y. F. Yao, and A. A. Lawal, “Large-eddy simulation of transonic turbulent flow over a bump,” *Int. J. Heat Fluid Flow*, vol. 24, pp. 584–595, 2003.

- [154] P. Druault, S. Lardeau, J.-P. Bonnet, F. Coiffet, J. Delville, E. Lamballais, J. F. Largeau, and L. Perret, “Generation of three-dimensional turbulent inlet conditions for large-eddy simulation,” *AIAA J.*, vol. 42, pp. 447–456, 2004.
- [155] P. Druault, J. F. Largeau, F. Coiffet, J. Delville, J. P. Bonnet, and S. Lardeau, “Numerical investigations of turbulent inflow condition generation for LES,” *J. Fluids Eng.*, vol. 127, pp. 945–948, 2005.
- [156] A. Keating, U. Piomelli, E. Balaras, and H.-J. Kaltenbach, “*A priori* and *a posteriori* tests of inflow conditions for large-eddy simulation,” *Phys. Fluids*, vol. 16, pp. 4696–4712, 2004.
- [157] Y. Na and P. Moin, “Direct numerical simulation of a separated turbulent boundary layer,” *J. Fluid Mech.*, vol. 374, pp. 379–405, 1998.
- [158] K. Mahesh, P. Moin, and S. K. Lele, “The interaction of a shock wave with a turbulent shear flow,” Tech. Rep. TF-69, Thermosciences Div., Dept. of Mech. Eng., Stanford University, 1996.
- [159] T. S. Lund, X. Wu, and K. D. Squires, “Generation of turbulent inflow data for spatially-developing boundary layer simulations,” *J. Comp. Phys.*, vol. 140, pp. 233–258, 1998.
- [160] A. Ferrante and S. E. Elghobashi, “A robust method for generating inflow conditions for direct simulations of spatially-developing turbulent boundary layers,” *J. Comp. Phys.*, vol. 198, pp. 372–387, 2004.
- [161] J. U. Schlüter, H. Pitsch, and P. Moin, “Large eddy simulation inflow conditions for coupling with Reynolds-averaged flow solvers,” *AIAA J.*, vol. 42, pp. 478–484, 2004.

- [162] X. Wu and P. Moin, “Direct numerical simulation of turbulence in a nominally zero-pressure-gradient flat-plate boundary layer,” *J. Fluid Mech.*, vol. 630, pp. 5–41, 2009.
- [163] X. Wu and P. Moin, “Transitional and turbulent boundary layer with heat transfer,” *Phys. Fluids*, vol. 22, pp. 085105, 1–8, 2010.
- [164] I. Foster, *Designing and Building Parallel Programs*. Boston: Addison-Wesley, 1995.
- [165] W. Gropp, E. Lusk, and A. Skjellum, *Using MPI, Portable Parallel Programming with the Message-Passing Interface*. Cambridge, MA: MIT, 2nd ed., 1999.
- [166] K. Iwamoto, Y. Suzuki, and N. Kasagi, “Reynolds number effect on wall turbulence: Toward effective feedback control,” *Int. J. Heat Fluid Flow*, vol. 23, pp. 678–689, 2002.
- [167] A. Sohankar, C. Norberg, and L. Davidson, “Low-Reynolds-number flow around a square cylinder at incidence: Study of blockage, onset of vortex shedding and outlet boundary condition,” *Int. J. Numer. Meth. Fluids*, vol. 26, pp. 39–56, 1998.
- [168] R. K. Madabhushi and S. P. Vanka, “Large eddy simulation of turbulence-driven secondary flow in a square duct,” *Phys. Fluids A*, vol. 3, pp. 2734–2745, 1991.
- [169] A. E. Perry and M. S. Chong, “A description of eddying motions and flow patterns using critical-point concepts,” *Annu. Rev. Fluid Mech.*, vol. 19, pp. 125–155, 1987.

- [170] U. Ghia, K. N. Ghia, and C. T. Shin, “High-Re solutions for incompressible flow using the Navier-Stokes equations and a multigrid method,” *J. Comp. Phys.*, vol. 48, pp. 387–411, 1982.
- [171] P. N. Shankar and M. D. Deshpande, “Fluid mechanics in the driven cavity,” *Annu. Rev. Fluid Mech.*, vol. 32, pp. 93–136, 2000.
- [172] J. E. Fackrell and A. G. Robins, “Concentration fluctuations and fluxes in plumes from point sources in a turbulent boundary layer,” *J. Fluid Mech.*, vol. 117, pp. 1–26, 1982.
- [173] R. A. Lavertu and L. Mydlarski, “Scalar mixing from a concentrated source in turbulent channel flow,” *J. Fluid Mech.*, vol. 528, pp. 135–172, 2005.
- [174] C. Jiménez, L. Valiño, and C. Dopazo, “*A priori* and *a posteriori* tests of subgrid scale models for scalar transport,” *Phys. Fluids*, vol. 13, pp. 2433–2436, 2001.

# Appendix A

## Derivation of the transport equations

Although the velocity, pressure and scalar fields can be fully determined by the solution of their governing equations (i.e., mass, momentum and scalar transport equations), there are some important quantities (e.g., turbulent kinetic energy) which are of significant interests to fluid dynamicists. Thus, an exact analysis of different physical mechanisms governing the transport of these quantities can be very attractive to scientists and engineers. Such analysis is possible through investigating the specific transport equation of the desired quantity. To derive a transport equation for a specific quantity, we need to refer to the original governing equations of the flow and scalar fields, apply the required mathematical operations and extract the desired equation. In this appendix, the transport equations of four important physical quantities in the context of LES of turbulent flows and scalar fields have been reviewed and their derivation procedures are presented. The transport equations are time- (or ensemble-) averaged.

### A.1 Resolved kinetic energy

The filtered continuity and momentum equations for an incompressible fluid flow can be written as

$$\frac{\partial \bar{u}_i}{\partial x_i} = 0 \quad , \quad (\text{A.1})$$

$$\frac{\partial \bar{u}_i}{\partial t} + \bar{u}_j \frac{\partial \bar{u}_i}{\partial x_j} = -\frac{1}{\rho} \frac{\partial \bar{p}}{\partial x_i} + 2\nu \frac{\partial \bar{s}_{ij}}{\partial x_j} - \frac{\partial \tau_{ij}}{\partial x_j} \quad , \quad (\text{A.2})$$

in which  $\bar{S}_{ij} = \frac{1}{2}(\partial\bar{u}_i/\partial x_j + \partial\bar{u}_j/\partial x_i)$  is the strain rate tensor. Multiplying both sides of the equation A.2 by  $\bar{u}_i$  yields

$$\bar{u}_i \frac{\partial \bar{u}_i}{\partial t} + \bar{u}_i \bar{u}_j \frac{\partial \bar{u}_i}{\partial x_j} = -\frac{1}{\rho} \bar{u}_i \frac{\partial \bar{p}}{\partial x_i} + 2\nu \bar{u}_i \frac{\partial \bar{S}_{ij}}{\partial x_j} - \bar{u}_i \frac{\partial \tau_{ij}}{\partial x_j} . \quad (\text{A.3})$$

Applying the chain rule to the derivatives and neglecting the divergence of the velocity according to the continuity equation ( $\frac{\partial \bar{u}_i}{\partial x_i} = 0$ ) will result in

$$\frac{\partial(\frac{1}{2}\bar{u}_i \bar{u}_i)}{\partial t} + \bar{u}_j \frac{\partial(\frac{1}{2}\bar{u}_i \bar{u}_i)}{\partial x_j} = -\frac{1}{\rho} \bar{u}_i \frac{\partial \bar{p}}{\partial x_i} + 2\nu \frac{\partial \bar{u}_i \bar{S}_{ij}}{\partial x_j} - 2\nu \bar{S}_{ij} \frac{\partial \bar{u}_i}{\partial x_j} - \frac{\partial \bar{u}_i \tau_{ij}}{\partial x_j} + \tau_{ij} \frac{\partial \bar{u}_i}{\partial x_j} . \quad (\text{A.4})$$

Rearranging the terms<sup>a</sup> and taking the average of the obtained equation will give us the transport equation of the resolved kinetic energy ( $k_r$ ) as

$$\underbrace{\left\langle \bar{u}_j \frac{\partial k_r}{\partial x_j} \right\rangle}_{\text{advection}} = -\frac{1}{\rho} \underbrace{\left\langle \bar{u}_j \frac{\partial \bar{p}}{\partial x_j} \right\rangle}_{\text{pressure diffusion}} + 2\nu \underbrace{\left\langle \frac{\partial \bar{S}_{ij} \bar{u}_i}{\partial x_j} \right\rangle}_{\text{viscous diffusion}} - 2\nu \underbrace{\langle \bar{S}_{ij} \bar{S}_{ij} \rangle}_{\text{viscous dissipation}} - \underbrace{\left\langle \frac{\partial \tau_{ij}^* \bar{u}_i}{\partial x_j} \right\rangle}_{\text{SGS diffusion}} + \underbrace{\langle \tau_{ij}^* \bar{S}_{ij} \rangle}_{\text{SGS dissipation}} . \quad (\text{A.5})$$

## A.2 Resolved turbulent kinetic energy

The filtered instantaneous velocity can be decomposed into the time-averaged and fluctuating part as  $\bar{u}_i = \langle \bar{u}_i \rangle + \bar{u}_i''$ . Inserting the decomposed form of the velocity into equation A.2 and taking the average of the obtained equation will result the transport equation of the resolved averaged-velocity as

$$\langle \bar{u}_k \rangle \frac{\partial \langle \bar{u}_i \rangle}{\partial x_k} = -\frac{1}{\rho} \frac{\partial \langle \bar{p} \rangle}{\partial x_i} + 2\nu \frac{\partial \langle \bar{S}_{ik} \rangle}{\partial x_k} - \frac{\partial \langle \bar{u}_i'' \bar{u}_k'' \rangle}{\partial x_k} - \frac{\partial \langle \tau_{ik} \rangle}{\partial x_k} . \quad (\text{A.6})$$

---

<sup>a</sup>Note the rearrangement for the viscous and SGS dissipation:

$$\begin{aligned} \bar{S}_{ij} \frac{\partial \bar{u}_i}{\partial x_j} &= (\bar{S}_{ij} \frac{\partial \bar{u}_i}{\partial x_j} + \bar{S}_{ji} \frac{\partial \bar{u}_j}{\partial x_i})/2 = (\bar{S}_{ij} \frac{\partial \bar{u}_i}{\partial x_j} + \bar{S}_{ij} \frac{\partial \bar{u}_j}{\partial x_i})/2 = \bar{S}_{ij} \bar{S}_{ij} \\ \tau_{ij} \frac{\partial \bar{u}_i}{\partial x_j} &= (\tau_{ij} \frac{\partial \bar{u}_i}{\partial x_j} + \tau_{ji} \frac{\partial \bar{u}_j}{\partial x_i})/2 = (\tau_{ij} \frac{\partial \bar{u}_i}{\partial x_j} + \tau_{ij} \frac{\partial \bar{u}_j}{\partial x_i})/2 = \tau_{ij} \bar{S}_{ij} \end{aligned}$$

Subtracting equation A.6 from equation A.2 will obtain the transport equation for the resolved fluctuating velocity as

$$\langle \bar{u}_k \rangle \frac{\partial \bar{u}_i''}{\partial x_k} + \bar{u}_k'' \frac{\partial \langle \bar{u}_i \rangle}{\partial x_k} + \bar{u}_k'' \frac{\partial \bar{u}_i''}{\partial x_k} - \frac{\langle \bar{u}_i'' \bar{u}_k'' \rangle}{\partial x_k} = -\frac{1}{\rho} \frac{\partial \bar{p}''}{\partial x_i} + 2\nu \frac{\partial \bar{s}_{ik}''}{\partial x_k} - \frac{\partial \tau_{ik}}{\partial x_k} + \frac{\partial \langle \tau_{ik} \rangle}{\partial x_k} . \quad (\text{A.7})$$

Multiplying equation A.7 by  $\bar{u}_j''$  and the corresponding equation of  $\bar{u}_j''$  by  $\bar{u}_i''$  and summation of the obtained equations will result the Reynolds stress transport equation as

$$\begin{aligned} \langle \bar{u}_k \rangle \frac{\partial \bar{u}_i'' \bar{u}_j''}{\partial x_k} + \bar{u}_j'' \bar{u}_k'' \frac{\partial \langle \bar{u}_i \rangle}{\partial x_k} + \bar{u}_i'' \bar{u}_k'' \frac{\partial \langle \bar{u}_j \rangle}{\partial x_k} + \bar{u}_k'' \frac{\partial \bar{u}_i'' \bar{u}_j''}{\partial x_k} - \bar{u}_i'' \frac{\langle \bar{u}_j'' \bar{u}_k'' \rangle}{\partial x_k} - \bar{u}_j'' \frac{\langle \bar{u}_i'' \bar{u}_k'' \rangle}{\partial x_k} = \\ -\frac{1}{\rho} \bar{u}_i'' \frac{\partial \bar{p}''}{\partial x_j} - \frac{1}{\rho} \bar{u}_j'' \frac{\partial \bar{p}''}{\partial x_i} + 2\nu \bar{u}_i'' \frac{\partial \bar{s}_{jk}''}{\partial x_k} + 2\nu \bar{u}_j'' \frac{\partial \bar{s}_{ik}''}{\partial x_k} - \\ \bar{u}_j'' \frac{\partial \tau_{ik}}{\partial x_k} - \bar{u}_i'' \frac{\partial \tau_{jk}}{\partial x_k} + \bar{u}_j'' \frac{\partial \langle \tau_{ik} \rangle}{\partial x_k} + \bar{u}_i'' \frac{\partial \langle \tau_{jk} \rangle}{\partial x_k} . \quad (\text{A.8}) \end{aligned}$$

Rearranging the terms and contracting the equation A.8 and dividing the result by 2, will give the transport equation of the resolved TKE ( $k$ ) as

$$\begin{aligned} \underbrace{\langle \bar{u}_j \rangle \frac{\partial k}{\partial x_j}}_{\text{advection}} = - \underbrace{\langle \bar{u}_i'' \bar{u}_j'' \rangle \frac{\partial \langle \bar{u}_i \rangle}{\partial x_j}}_{\text{production}} - \underbrace{\frac{1}{2} \frac{\partial}{\partial x_j} \langle \bar{u}_i'' \bar{u}_i'' \bar{u}_j'' \rangle}_{\text{turbulent diffusion}} - \underbrace{\frac{1}{\rho} \left\langle \bar{u}_j'' \frac{\partial \bar{p}''}{\partial x_j} \right\rangle}_{\text{pressure diffusion}} \\ + \underbrace{2\nu \frac{\partial}{\partial x_j} \langle \bar{S}_{ij}'' \bar{u}_i'' \rangle}_{\text{viscous diffusion}} - \underbrace{2\nu \langle \bar{S}_{ij}'' \bar{S}_{ij}'' \rangle}_{\text{viscous dissipation}} - \underbrace{\frac{\partial}{\partial x_j} \langle \bar{u}_i'' \tau_{ij} \rangle}_{\text{SGS diffusion}} + \underbrace{\langle \tau_{ij}^* \bar{S}_{ij}'' \rangle}_{\text{SGS dissipation}} . \quad (\text{A.9}) \end{aligned}$$

### A.3 Resolved scalar energy

The transport equation of the resolved scalar field takes the following form

$$\frac{\partial \bar{c}}{\partial t} + \frac{\partial}{\partial x_j} (\bar{u}_j \bar{c}) = \alpha \frac{\partial^2 \bar{c}}{\partial x_j \partial x_j} - \frac{\partial h_j}{\partial x_j} . \quad (\text{A.10})$$

Multiplying both sides of the equation A.10 by  $2\bar{c}$  will result

$$2\bar{c} \frac{\partial \bar{c}}{\partial t} + 2\bar{c} \frac{\partial}{\partial x_j} (\bar{u}_j \bar{c}) = 2\alpha \bar{c} \frac{\partial^2 \bar{c}}{\partial x_j \partial x_j} - 2\bar{c} \frac{\partial h_j}{\partial x_j} . \quad (\text{A.11})$$

Applying the chain rule to the derivatives and neglecting the divergence of the velocity according to the continuity equation ( $\frac{\partial \bar{u}_i}{\partial x_i} = 0$ ) will obtain

$$\frac{\partial \bar{c}^2}{\partial t} + \bar{u}_j \frac{\partial \bar{c}^2}{\partial x_j} = 2\alpha \bar{c} \frac{\partial^2 \bar{c}}{\partial x_j \partial x_j} - 2 \frac{\partial \bar{c} h_j}{\partial x_j} + 2 h_j \frac{\partial \bar{c}}{\partial x_j} . \quad (\text{A.12})$$

Rearranging the terms<sup>b</sup> and taking the average of the obtained equation will give the transport equation of the resolved scalar energy ( $k_{rs}$ ) as

$$\underbrace{\left\langle \bar{u}_j \frac{\partial k_{rs}}{\partial x_j} \right\rangle}_{\text{advection}} = \alpha \underbrace{\left\langle \frac{\partial^2 k_{rs}}{\partial x_j \partial x_j} \right\rangle}_{\text{molecular diffusion}} - 2\alpha \underbrace{\left\langle \frac{\partial \bar{c}}{\partial x_j} \frac{\partial \bar{c}}{\partial x_j} \right\rangle}_{\text{molecular dissipation}} - 2 \underbrace{\left\langle \frac{\partial \bar{c} h_j}{\partial x_j} \right\rangle}_{\text{SGS diffusion}} + 2 \underbrace{\left\langle h_j \frac{\partial \bar{c}}{\partial x_j} \right\rangle}_{\text{SGS dissipation}} . \quad (\text{A.13})$$

## A.4 Resolved scalar variance

The filtered instantaneous scalar field can be decomposed into the time-averaged and fluctuating part as  $\bar{c} = \langle \bar{c} \rangle + \bar{c}''$ . Inserting the decomposed form of the velocity, which was introduced before, and also the decomposed form of the scalar field into equation A.10 and taking the average of the obtained equation will result the transport equation of the resolved averaged-scalar field as

$$\frac{\partial \langle \bar{c} \rangle}{\partial t} + \langle \bar{u}_j \rangle \frac{\partial \langle \bar{c} \rangle}{\partial x_j} + \frac{\partial \langle \bar{u}_j'' \bar{c}'' \rangle}{\partial x_j} = \alpha \frac{\partial^2 \langle \bar{c} \rangle}{\partial x_j \partial x_j} - \frac{\partial \langle h_j \rangle}{\partial x_j} . \quad (\text{A.14})$$

Subtracting equation A.14 from equation A.10 will obtain the transport equation for the resolved fluctuating scalar field as

$$\frac{\partial \bar{c}''}{\partial t} + \bar{u}_j'' \frac{\partial \bar{c}''}{\partial x_j} + \langle \bar{u}_j \rangle \frac{\partial \bar{c}''}{\partial x_j} + \bar{u}_j'' \frac{\partial \langle \bar{c} \rangle}{\partial x_j} - \frac{\partial \langle \bar{u}_j'' \bar{c}'' \rangle}{\partial x_j} = \alpha \frac{\partial^2 \bar{c}''}{\partial x_j \partial x_j} - \frac{\partial h_j}{\partial x_j} + \frac{\partial \langle h_j \rangle}{\partial x_j} . \quad (\text{A.15})$$

---

<sup>b</sup>Note the rearrangement for the molecular diffusion and molecular dissipation:

$$2\alpha \bar{c} \frac{\partial^2 \bar{c}}{\partial x_j \partial x_j} = 2\alpha \left( \frac{\partial}{\partial x_j} \bar{c} \frac{\partial \bar{c}}{\partial x_j} - \frac{\partial \bar{c}}{\partial x_j} \frac{\partial \bar{c}}{\partial x_j} \right) = 2\alpha \left( \frac{\partial}{\partial x_j} \left( \frac{\partial \bar{c}^2}{2} \right) - \frac{\partial \bar{c}}{\partial x_j} \frac{\partial \bar{c}}{\partial x_j} \right) = \alpha \frac{\partial^2 \bar{c}^2}{\partial x_j \partial x_j} - 2\alpha \frac{\partial \bar{c}}{\partial x_j} \frac{\partial \bar{c}}{\partial x_j}$$

Multiplying equation A.15 by  $2\bar{c}''$  will result in

$$\begin{aligned} & \frac{\partial \bar{c}''^2}{\partial t} + 2\bar{c}''\bar{u}_j'' \frac{\partial \bar{c}''}{\partial x_j} + \langle \bar{u}_j \rangle \frac{\partial \bar{c}''^2}{\partial x_j} + 2\bar{c}''\bar{u}_j'' \frac{\partial \langle \bar{c} \rangle}{\partial x_j} - 2\bar{c}'' \frac{\partial \langle \bar{u}_j'' \bar{c}'' \rangle}{\partial x_j} = \\ & \alpha \frac{\partial^2 \bar{c}''^2}{\partial x_j \partial x_j} - 2\alpha \frac{\partial \bar{c}''}{\partial x_j} \frac{\partial \bar{c}''}{\partial x_j} - 2 \frac{\partial h_j \bar{c}''}{\partial x_j} + 2h_j \frac{\partial \bar{c}''}{\partial x_j} + \frac{\partial \langle h_j \bar{c}'' \rangle}{\partial x_j} - 2 \langle h_j \rangle \frac{\partial \bar{c}''}{\partial x_j} . \end{aligned} \quad (\text{A.16})$$

Taking the average of the above equation will obtain the transport equation of the resolve scalar variance ( $k_s$ ) as

$$\begin{aligned} \underbrace{\langle \bar{u}_j \rangle \frac{\partial k_s}{\partial x_j}}_{\text{advection}} &= - \underbrace{2 \langle \bar{u}_j'' \bar{c}'' \rangle \frac{\partial \langle \bar{c} \rangle}{\partial x_j}}_{\text{production}} - \underbrace{\frac{\partial}{\partial x_j} \langle \bar{u}_j'' \bar{c}'' \bar{c}'' \rangle}_{\text{turbulent diffusion}} + \underbrace{\alpha \frac{\partial^2 k_s}{\partial x_j \partial x_j}}_{\text{molecular diffusion}} \\ & - \underbrace{2\alpha \left\langle \frac{\partial \bar{c}''}{\partial x_j} \frac{\partial \bar{c}''}{\partial x_j} \right\rangle}_{\text{molecular dissipation}} - \underbrace{2 \frac{\partial}{\partial x_j} \langle h_j \bar{c}'' \rangle}_{\text{SGS diffusion}} + \underbrace{2 \left\langle h_j \frac{\partial \bar{c}''}{\partial x_j} \right\rangle}_{\text{SGS dissipation}} . \end{aligned} \quad (\text{A.17})$$

# Appendix B

## Discretization of the governing equations

In this appendix, we demonstrate the discretization algorithms used for the momentum, continuity and scalar transport equations. For the momentum and continuity equations, we follow the scheme of Ham *et al.* [106] based on the finite difference approach in a staggered grid arrangement. For the scalar transport equation, a classical total variation diminishing (TVD) scheme is used. It should be noted that in this appendix, we consider the original form of the continuity, momentum and scalar transport equations (without any filtering or averaging which is used for DNS) to demonstrate the procedure for extracting the algebraic equations required for the numerical solution. Further modifications to the governing equations (e.g., embedding the SGS models or wall models) can be applied based on the original discrete equations.

### B.1 Discretization of the momentum equation

The tensorial form of the momentum equation is

$$\frac{\partial u_i}{\partial t} + \frac{\partial}{\partial x_j}(u_i u_j) = -\frac{1}{\rho} \frac{\partial p}{\partial x_i} + \nu \frac{\partial^2 u_i}{\partial x_j \partial x_j} \quad , \quad (\text{B.1})$$

in which  $u_i$  and  $p$  represent the velocity and pressure fields, respectively,  $x_i$  represents coordinates, and  $\rho$  and  $\nu$  are the density and kinematic viscosity of the fluid, respectively. To demonstrate the algorithm, here, we consider the  $x$ -component equation (corresponding to the index  $i = 1$  in equation B.1). Similar procedure can be applied for other components of the momentum equation analogously. Thus,

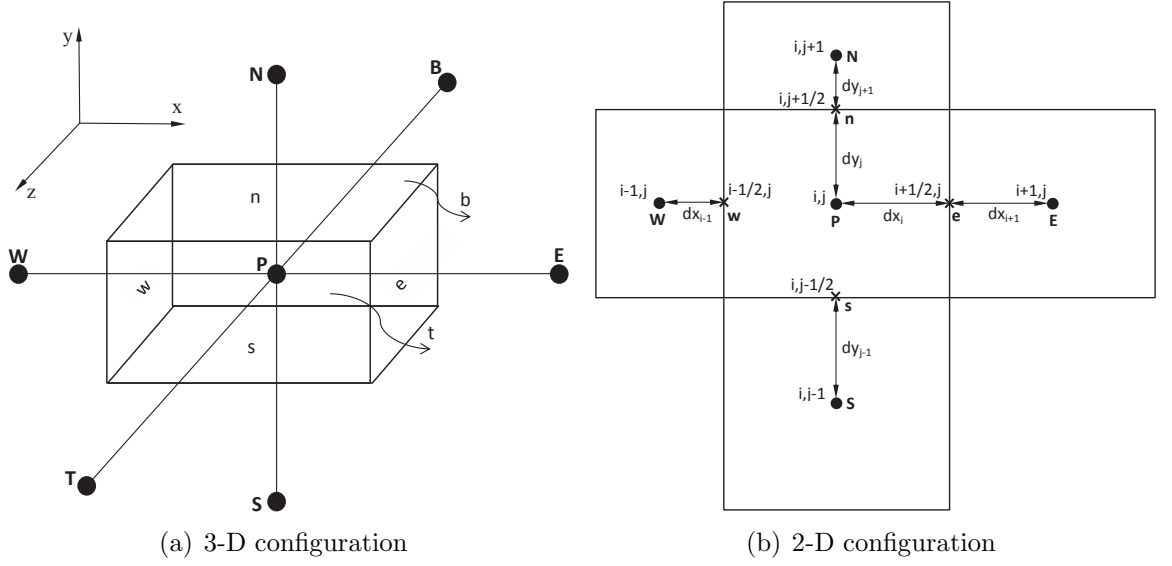


FIGURE B.1: Schematic of a typical computational cell, its node, faces, indices and neighbors in 2-D and 3-D configurations for the base grid. Note that in a staggered grid arrangement, the grids for storing velocity components ( $u$ ,  $v$  and  $w$ ) are half-cell shifted in  $x$ ,  $y$  and  $z$  directions, respectively.

the  $x$ -component of the momentum equation is given by

$$\frac{\partial u}{\partial t} + \frac{\partial uu}{\partial x} + \frac{\partial vu}{\partial y} + \frac{\partial wu}{\partial z} = -\frac{1}{\rho} \frac{\partial p}{\partial x} + \nu \left( \frac{\partial^2 u}{\partial x \partial x} + \frac{\partial^2 u}{\partial y \partial y} + \frac{\partial^2 u}{\partial z \partial z} \right) \quad . \quad (\text{B.2})$$

In the first step of the fractional step method used in this thesis, we need to solve the momentum equation for every single point in the discrete computational domain (i.e., computational nodes). Figure B.1a presents the schematic of a computational node (located in the center of a 3-D computational cell) and its neighbors in a Cartesian coordinate system. As a convention, the computational node is denoted by P, representing *point*, and the neighboring nodes are denoted by W, E, S, N, B, T, representing *west, east, south, north, bottom* and *top* directions. Lower case letters  $w$ ,  $e$ ,  $s$ ,  $n$ ,  $b$ , and  $t$  are used for the faces of the computational cell in same directions. To present the spacing and indices of the computational cell more clearly, Fig. B.1b shows the computational cells, nodes, faces and their indices in a 2-D configuration.

Following the fractional step method of Choi and Moin [109] coupled with a second-order Crank-Nicolson scheme, the  $x$ -momentum equation will be

$$\begin{aligned}
& \frac{u_p^* - u_p^n}{\Delta t} + \frac{1}{4} \left[ \frac{\partial(u^n + u^*)(u^n + u^*)}{\partial x} \right]_p \\
& \quad + \frac{1}{4} \left[ \frac{\partial(v^n + v^*)(u^n + u^*)}{\partial y} \right]_p \\
& \quad + \frac{1}{4} \left[ \frac{\partial(w^n + w^*)(u^n + u^*)}{\partial z} \right]_p \\
& \quad = -\frac{1}{\rho} \left( \frac{\partial p^n}{\partial x} \right)_p \\
& + \frac{\nu}{2} \left( \frac{\partial^2(u^n + u^*)}{\partial x \partial x} + \frac{\partial^2(u^n + u^*)}{\partial y \partial y} + \frac{\partial^2(u^n + u^*)}{\partial z \partial z} \right)_p, \tag{B.3}
\end{aligned}$$

in which the superscript  $n$  denotes the variable at the old time level and  $*$  represents the variable at time level  $n + \frac{1}{2}$ .

The convective terms are discretized as

$$\begin{aligned}
& \frac{1}{4} \left[ \frac{\partial(u^n + u^*)(u^n + u^*)}{\partial x} \right]_p = \\
& \frac{u_{i,j,k}^n + u_{i,j,k}^*}{2} + \frac{u_{i+1,j,k}^n + u_{i+1,j,k}^*}{2} - \frac{u_{i,j,k}^n + u_{i,j,k}^*}{2} + \frac{u_{i-1,j,k}^n + u_{i-1,j,k}^*}{2} \\
& \frac{u_{fe}}{dx_i + dx_{i+1}} - \frac{u_{fw}}{dx_i + dx_{i+1}} \tag{B.4}
\end{aligned}$$

$$\begin{aligned}
& \frac{1}{4} \left[ \frac{\partial(v^n + v^*)(u^n + u^*)}{\partial y} \right]_p = \\
& \frac{u_{i,j,k}^n + u_{i,j,k}^*}{2} + \frac{u_{i,j+1,k}^n + u_{i,j+1,k}^*}{2} - \frac{u_{i,j,k}^n + u_{i,j,k}^*}{2} + \frac{u_{i,j-1,k}^n + u_{i,j-1,k}^*}{2} \\
& \frac{v_{fn}}{dy_j + dy_j} - \frac{v_{fs}}{dy_j + dy_j} \tag{B.5}
\end{aligned}$$

$$\begin{aligned}
& \frac{1}{4} \left[ \frac{\partial(w^n + w^*)(u^n + u^*)}{\partial z} \right]_p = \\
& \frac{u_{i,j,k}^n + u_{i,j,k}^*}{2} + \frac{u_{i,j,k+1}^n + u_{i,j,k+1}^*}{2} - \frac{u_{i,j,k}^n + u_{i,j,k}^*}{2} + \frac{u_{i,j,k-1}^n + u_{i,j,k-1}^*}{2} \\
& \frac{w_{ft}}{dz_k + dz_k} - \frac{w_{fb}}{dz_k + dz_k} \tag{B.6}
\end{aligned}$$

in which

$$u_{fe} = \frac{dx_{i+1} \frac{u_{i+1,j,k}^n + u_{i+1,j,k}^*}{2} + dx_{i+1} \frac{u_{i,j,k}^n + u_{i,j,k}^*}{2}}{dx_{i+1} + dx_{i+1}}, \quad (\text{B.7})$$

$$u_{fw} = \frac{dx_i \frac{u_{i,j,k}^n + u_{i,j,k}^*}{2} + dx_i \frac{u_{i-1,j,k}^n + u_{i-1,j,k}^*}{2}}{dx_i + dx_i}, \quad (\text{B.8})$$

$$v_{fn} = \frac{dx_{i+1} \frac{v_{i+1,j+1,k}^n + v_{i+1,j+1,k}^*}{2} + dx_i \frac{v_{i,j+1,k}^n + v_{i,j+1,k}^*}{2}}{dx_i + dx_{i+1}}, \quad (\text{B.9})$$

$$v_{fs} = \frac{dx_{i+1} \frac{v_{i+1,j-1,k}^n + v_{i+1,j-1,k}^*}{2} + dx_i \frac{v_{i,j-1,k}^n + v_{i,j-1,k}^*}{2}}{dx_i + dx_{i+1}}, \quad (\text{B.10})$$

$$w_{ft} = \frac{dx_{i+1} \frac{w_{i+1,j,k+1}^n + w_{i+1,j,k+1}^*}{2} + dx_i \frac{w_{i,j,k+1}^n + w_{i,j,k+1}^*}{2}}{dx_i + dx_{i+1}}, \quad (\text{B.11})$$

$$w_{fb} = \frac{dx_{i+1} \frac{w_{i+1,j,k-1}^n + w_{i+1,j,k-1}^*}{2} + dx_i \frac{w_{i,j,k-1}^n + w_{i,j,k-1}^*}{2}}{dx_i + dx_{i+1}}. \quad (\text{B.12})$$

The discretization of diffusion terms will be

$$\frac{\nu}{2} \frac{\partial^2 (u^n + u^*)}{\partial x \partial x} = \nu \frac{\left(\frac{du}{dx}\right)_e - \left(\frac{du}{dx}\right)_w}{dx_i + dx_{i+1}}, \quad (\text{B.13})$$

$$\frac{\nu}{2} \frac{\partial^2 (u^n + u^*)}{\partial y \partial y} = \nu \frac{\left(\frac{du}{dy}\right)_n - \left(\frac{du}{dy}\right)_s}{dy_j + dy_j}, \quad (\text{B.14})$$

$$\frac{\nu}{2} \frac{\partial^2 (u^n + u^*)}{\partial z \partial z} = \nu \frac{\left(\frac{du}{dz}\right)_t - \left(\frac{du}{dz}\right)_b}{dz_k + dz_k}, \quad (\text{B.15})$$

in which

$$\left(\frac{du}{dx}\right)_e = \frac{\frac{u_{i+1,j,k}^n + u_{i+1,j,k}^*}{2} - \frac{u_{i,j,k}^n + u_{i,j,k}^*}{2}}{dx_{i+1} + dx_{i+1}}, \quad (\text{B.16})$$

$$\left(\frac{du}{dx}\right)_w = \frac{\frac{u_{i,j,k}^n + u_{i,j,k}^*}{2} - \frac{u_{i-1,j,k}^n + u_{i-1,j,k}^*}{2}}{dx_i + dx_i} , \quad (\text{B.17})$$

$$\left(\frac{du}{dy}\right)_n = \frac{\frac{u_{i,j+1,k}^n + u_{i,j+1,k}^*}{2} - \frac{u_{i,j,k}^n + u_{i,j,k}^*}{2}}{dy_{j+1} + dy_j} , \quad (\text{B.18})$$

$$\left(\frac{du}{dy}\right)_s = \frac{\frac{u_{i,j,k}^n + u_{i,j,k}^*}{2} - \frac{u_{i,j-1,k}^n + u_{i,j-1,k}^*}{2}}{dy_j + dy_{j-1}} , \quad (\text{B.19})$$

$$\left(\frac{du}{dz}\right)_t = \frac{\frac{u_{i,j,k+1}^n + u_{i,j,k+1}^*}{2} - \frac{u_{i,j,k}^n + u_{i,j,k}^*}{2}}{dz_{k+1} + dz_k} , \quad (\text{B.20})$$

$$\left(\frac{du}{dz}\right)_b = \frac{\frac{u_{i,j,k}^n + u_{i,j,k}^*}{2} - \frac{u_{i,j,k-1}^n + u_{i,j,k-1}^*}{2}}{dz_k + dz_{k-1}} , \quad (\text{B.21})$$

and the source term is discretized as

$$-\frac{1}{\rho} \frac{\partial p^n}{\partial x} = -\frac{\frac{p_{i+1,j,k}^n + p_{i+1,j,k}^*}{2} - \frac{p_{i,j,k}^n + p_{i,j,k}^*}{2}}{dx_i + dx_{i+1}} . \quad (\text{B.22})$$

The final algebraic form of the  $u$ -momentum equation takes the following form

$$A_p u_p^* = A_E u_E^* + A_W u_W^* + A_N u_N^* + A_S u_S^* + A_T u_T^* + A_B u_B^* + B_p , \quad (\text{B.23})$$

in which the neighbor coefficients are

$$\begin{aligned}
A_E &= -\frac{dx_{i+1} \frac{u_{i+1,j,k}^n + u_{i+1,j,k}^*}{2} + dx_{i+1} \frac{u_{i,j,k}^n + u_{i,j,k}^*}{2}}{4(dx_i + dx_{i+1})(dx_{i+1} + dx_{i+1})} \\
&\quad + \frac{\nu}{4dx_{i+1}(dx_i + dx_{i+1})} \quad , \\
A_W &= +\frac{dx_i \frac{u_{i,j,k}^n + u_{i,j,k}^*}{2} + dx_i \frac{u_{i-1,j,k}^n + u_{i-1,j,k}^*}{2}}{4(dx_i + dx_{i+1})(dx_i + dx_i)} \\
&\quad + \frac{\nu}{4dx_i(dx_i + dx_{i+1})} \quad , \\
A_N &= -\frac{dx_{i+1} \frac{v_{i+1,j+1,k}^n + v_{i+1,j+1,k}^*}{2} + dx_i \frac{v_{i,j+1,k}^n + v_{i,j+1,k}^*}{2}}{4(dy_j + dy_j)(dx_i + dx_{i+1})} \\
&\quad + \frac{\nu}{4dy_j(dy_{j+1} + dy_j)} \quad , \\
A_S &= +\frac{dx_{i+1} \frac{v_{i+1,j-1,k}^n + v_{i+1,j-1,k}^*}{2} + dx_i \frac{v_{i,j-1,k}^n + v_{i,j-1,k}^*}{2}}{4(dy_j + dy_j)(dx_i + dx_{i+1})} \\
&\quad + \frac{\nu}{4dy_j(dy_j + dy_{j-1})} \quad , \\
A_T &= -\frac{dx_{i+1} \frac{w_{i+1,j,k+1}^n + w_{i+1,j,k+1}^*}{2} + dx_i \frac{w_{i,j,k+1}^n + w_{i,j,k+1}^*}{2}}{4(dz_k + dz_k)(dx_i + dx_{i+1})} \\
&\quad + \frac{\nu}{4dz_k(dz_{k+1} + dz_k)} \quad , \\
A_B &= +\frac{dx_{i+1} \frac{w_{i+1,j,k-1}^n + w_{i+1,j,k-1}^*}{2} + dx_i \frac{w_{i,j,k-1}^n + w_{i,j,k-1}^*}{2}}{4(dz_k + dz_k)(dx_i + dx_{i+1})} \\
&\quad + \frac{\nu}{4dz_k(dz_k + dz_{k-1})} \quad ,
\end{aligned} \tag{B.24}$$

and the central coefficient is

$$\begin{aligned}
A_P = & \frac{1}{\Delta t} \\
& + \frac{dx_{i+1} \frac{u_{i+1,j,k}^n + u_{i+1,j,k}^*}{2} + dx_{i+1} \frac{u_{i,j,k}^n + u_{i,j,k}^*}{2}}{4(dx_i + dx_{i+1})(dx_{i+1} + dx_{i+1})} + \frac{\nu}{4dx_{i+1}(dx_i + dx_{i+1})} \\
& - \frac{dx_i \frac{u_{i,j,k}^n + u_{i,j,k}^*}{2} + dx_i \frac{u_{i-1,j,k}^n + u_{i-1,j,k}^*}{2}}{4(dx_i + dx_{i+1})(dx_i + dx_i)} + \frac{\nu}{4dx_i(dx_i + dx_{i+1})} \\
& + \frac{dx_{i+1} \frac{v_{i+1,j+1,k}^n + v_{i+1,j+1,k}^*}{2} + dx_i \frac{v_{i,j+1,k}^n + v_{i,j+1,k}^*}{2}}{4(dy_j + dy_j)(dx_i + dx_{i+1})} + \frac{\nu}{4dy_j(dy_{j+1} + dy_j)} \\
& - \frac{dx_{i+1} \frac{v_{i+1,j-1,k}^n + v_{i+1,j-1,k}^*}{2} + dx_i \frac{v_{i,j-1,k}^n + v_{i,j-1,k}^*}{2}}{4(dy_j + dy_j)(dx_i + dx_{i+1})} + \frac{\nu}{4dy_j(dy_j + dy_{j-1})} \\
& + \frac{dx_{i+1} \frac{w_{i+1,j,k+1}^n + w_{i+1,j,k+1}^*}{2} + dx_i \frac{w_{i,j,k+1}^n + w_{i,j,k+1}^*}{2}}{4(dz_k + dz_k)(dx_i + dx_{i+1})} + \frac{\nu}{4dz_k(dz_{k+1} + dz_k)} \\
& - \frac{dx_{i+1} \frac{w_{i+1,j,k-1}^n + w_{i+1,j,k-1}^*}{2} + dx_i \frac{w_{i,j,k-1}^n + w_{i,j,k-1}^*}{2}}{4(dz_k + dz_k)(dx_i + dx_{i+1})} + \frac{\nu}{4dz_k(dz_k + dz_{k-1})} ,
\end{aligned} \tag{B.25}$$

and the source term coefficient takes the following form

$$\begin{aligned}
B_p = & \frac{2u_P^n}{\Delta t} \\
& + A_E u_E^n + A_W u_W^n + A_N u_N^n + A_S u_S^n + A_T u_T^n + A_B u_B^n \\
& - \frac{\frac{p_{i+1,j,k}^n + p_{i+1,j,k}^*}{2} - \frac{p_{i,j,k}^n + p_{i,j,k}^*}{2}}{dx_i + dx_{i+1}} .
\end{aligned} \tag{B.26}$$

## B.2 Discretization of the continuity equation

In the third step of the fractional step method, we need to update the pressure field so that the velocity field in the new time step is divergence free (satisfies the continuity equation). This is accomplished by solving the following Poisson equation

$$\frac{\partial^2 p^{n+1}}{\partial x_i \partial x_i} = \frac{2\rho}{\Delta t} \frac{\partial u_i^{**}}{\partial x_i} \quad , \quad (\text{B.27})$$

which can be further expanded to

$$\frac{\partial^2 p^{n+1}}{\partial x \partial x} + \frac{\partial^2 p^{n+1}}{\partial x \partial x} + \frac{\partial^2 p^{n+1}}{\partial x \partial x} = \frac{2\rho}{\Delta t} \left( \frac{\partial u^{**}}{\partial x} + \frac{\partial v^{**}}{\partial y} + \frac{\partial w^{**}}{\partial z} \right) \quad . \quad (\text{B.28})$$

Applying the discretization for the first and second derivatives, a final algebraic equation of the following form will be obtained

$$A_p p_p^{n+1} = A_E p_E^{n+1} + A_W p_W^{n+1} + A_N p_N^{n+1} + A_S p_S^{n+1} + A_T p_T^{n+1} + A_B p_B^{n+1} + B_p \quad , \quad (\text{B.29})$$

where the neighbor coefficients are

$$\begin{aligned} A_E &= \frac{1}{(dx_i + dx_{i+1})(dx_i + dx_i)} \quad , \\ A_W &= \frac{1}{(dx_{i-1} + dx_i)(dx_i + dx_i)} \quad , \\ A_N &= \frac{1}{(dy_j + dy_{j+1})(dy_j + dy_j)} \quad , \\ A_S &= \frac{1}{(dy_{j-1} + dy_j)(dy_j + dy_j)} \quad , \\ A_T &= \frac{1}{(dz_k + dz_{k+1})(dz_k + dz_k)} \quad , \\ A_B &= \frac{1}{(dz_{k-1} + dz_k)(dz_k + dz_k)} \quad , \end{aligned} \quad (\text{B.30})$$

and the central coefficient is

$$\begin{aligned} A_P &= \frac{1}{(dx_i + dx_{i+1})(dx_i + dx_i)} \\ &+ \frac{1}{(dx_{i-1} + dx_i)(dx_i + dx_i)} \\ &+ \frac{1}{(dy_j + dy_{j+1})(dy_j + dy_j)} \\ &+ \frac{1}{(dy_{j-1} + dy_j)(dy_j + dy_j)} \\ &+ \frac{1}{(dz_k + dz_{k+1})(dz_k + dz_k)} \\ &+ \frac{1}{(dz_{k-1} + dz_k)(dz_k + dz_k)} \quad , \end{aligned} \quad (\text{B.31})$$

and the source term takes the following form

$$B_p = \frac{-2\rho}{\Delta t} \left[ \frac{u_{i,j,k}^{**} - u_{i-1,j,k}^{**}}{(dx_i + dx_i)} + \frac{u_{i,j,k}^{**} - u_{i,j-1,k}^{**}}{(dy_j + dy_j)} + \frac{u_{i,j,k}^{**} - u_{i,j,k-1}^{**}}{(dz_k + dz_k)} \right] . \quad (\text{B.32})$$

### B.3 Discretization of the scalar transport equation

If the solution of the concentration field is required, along with the continuity and momentum equations, the scalar transport equation also has to be solved at each time step. Scalar transport equation is a linear equation which takes the following form

$$\frac{\partial c}{\partial t} + \frac{\partial}{\partial x_j}(u_j c) = \alpha \frac{\partial^2 c}{\partial x_j \partial x_j} . \quad (\text{B.33})$$

Since the concentration is typically considered as a passive scalar, the transport equation for the flow and the scalar field are fully decoupled. Thus, after solving the the continuity and momentum equations, the obtained velocity field should be inserted into the discretized form of the scalar transport equation to form a system of linear algebraic equation. Different schemes can be used for discretizing the scalar transport equation out of which second order central difference scheme is a simple and common one. However, in problems with high local gradients (e.g., point source release of contaminant), central difference scheme will cause unphysical oscillations in the concentration field. Thus, a more stable scheme is required for this type of problems. For this purpose, a total variation diminishing (TVD) scheme has been applied to the discretization of the scalar transport equation which is demonstrated in the following.

The semi discretized form (discretized in time not in space) of the scalar transport equation presented in equation B.33 can be expressed as

$$\frac{c^{n+1} - c^n}{\Delta t} + \frac{\partial uc}{\partial x} + \frac{\partial vc}{\partial y} + \frac{\partial wc}{\partial z} = \alpha \left( \frac{\partial^2 c}{\partial x \partial x} + \frac{\partial^2 c}{\partial y \partial y} + \frac{\partial^2 c}{\partial z \partial z} \right) . \quad (\text{B.34})$$

The convective terms are discretized as

$$\frac{\partial uc}{\partial x} = f_e \frac{c_e^n + c_e^{n+1}}{2} - f_w \frac{c_w^n + c_w^{n+1}}{2} \quad , \quad (\text{B.35})$$

$$\frac{\partial vc}{\partial x} = f_n \frac{c_n^n + c_n^{n+1}}{2} - f_s \frac{c_s^n + c_s^{n+1}}{2} \quad , \quad (\text{B.36})$$

$$\frac{\partial wc}{\partial x} = f_t \frac{c_t^n + c_t^{n+1}}{2} - f_b \frac{c_b^n + c_b^{n+1}}{2} \quad , \quad (\text{B.37})$$

in which the superscripts  $n$  and  $n + 1$  represents values at the old and the current time steps, respectively. the convective fluxes are

$$f_e = \frac{\frac{u_{i,j,k}^n + u_{i,j,k}^{n+1}}{2}}{2dx_i} \quad , \quad f_w = \frac{\frac{u_{i-1,j,k}^n + u_{i-1,j,k}^{n+1}}{2}}{2dx_i} \quad , \quad (\text{B.38})$$

$$f_n = \frac{\frac{v_{i,j,k}^n + v_{i,j,k}^{n+1}}{2}}{2dy_j} \quad , \quad f_s = \frac{\frac{v_{i,j-1,k}^n + v_{i,j-1,k}^{n+1}}{2}}{2dy_j} \quad , \quad (\text{B.39})$$

$$f_t = \frac{\frac{w_{i,j,k}^n + w_{i,j,k}^{n+1}}{2}}{2dz_k} \quad , \quad f_b = \frac{\frac{w_{i,j,k-1}^n + w_{i,j,k-1}^{n+1}}{2}}{2dz_k} \quad , \quad (\text{B.40})$$

and the value of the scalar field at cell faces are evaluated as

$$c_e = \alpha_e \left[ c_P + \frac{1}{2} \psi(r_e^+) (c_E - c_P) \right] + (1 - \alpha_e) \left[ c_E + \frac{1}{2} \psi(r_e^-) (c_P - c_E) \right] \quad , \quad (\text{B.41})$$

$$c_w = \alpha_w \left[ c_W + \frac{1}{2} \psi(r_w^+) (c_P - c_W) \right] + (1 - \alpha_w) \left[ c_P + \frac{1}{2} \psi(r_w^-) (c_W - c_P) \right] \quad , \quad (\text{B.42})$$

$$c_n = \alpha_n \left[ c_P + \frac{1}{2} \psi(r_n^+) (c_N - c_P) \right] + (1 - \alpha_n) \left[ c_N + \frac{1}{2} \psi(r_n^-) (c_P - c_N) \right] \quad , \quad (\text{B.43})$$

$$c_s = \alpha_s \left[ c_S + \frac{1}{2} \psi(r_s^+) (c_P - c_S) \right] + (1 - \alpha_s) \left[ c_P + \frac{1}{2} \psi(r_s^-) (c_S - c_P) \right] \quad , \quad (\text{B.44})$$

$$c_t = \alpha_t \left[ c_P + \frac{1}{2} \psi(r_t^+) (c_T - c_P) \right] + (1 - \alpha_t) \left[ c_T + \frac{1}{2} \psi(r_t^-) (c_P - c_T) \right] \quad , \quad (\text{B.45})$$

$$c_b = \alpha_b \left[ c_B + \frac{1}{2} \psi(r_b^+) (c_P - c_B) \right] + (1 - \alpha_b) \left[ c_P + \frac{1}{2} \psi(r_b^-) (c_B - c_P) \right] \quad , \quad (\text{B.46})$$

TABLE B.1: Values of the  $\alpha$  coefficients for different flow directions

$\alpha_e = 1$	for	$f_e > 0$	and	$\alpha_e = 0$	for	$f_e < 0$
$\alpha_w = 1$	for	$f_w > 0$	and	$\alpha_w = 0$	for	$f_w < 0$
$\alpha_n = 1$	for	$f_n > 0$	and	$\alpha_n = 0$	for	$f_n < 0$
$\alpha_s = 1$	for	$f_s > 0$	and	$\alpha_s = 0$	for	$f_s < 0$
$\alpha_t = 1$	for	$f_t > 0$	and	$\alpha_t = 0$	for	$f_t < 0$
$\alpha_b = 1$	for	$f_b > 0$	and	$\alpha_b = 0$	for	$f_b < 0$

TABLE B.2: The ratio of gradients for different flow directions and cell faces

$r_e^+ = \frac{c_P - c_W}{c_E - c_P}$	$r_e^- = \frac{c_{EE} - c_E}{c_E - c_P}$	$r_w^+ = \frac{c_W - c_{WW}}{c_P - c_W}$	$r_w^- = \frac{c_E - c_P}{c_P - c_W}$
$r_n^+ = \frac{c_P - c_S}{c_N - c_P}$	$r_n^- = \frac{c_{NN} - c_N}{c_N - c_P}$	$r_s^+ = \frac{c_S - c_{SS}}{c_P - c_S}$	$r_s^- = \frac{c_N - c_P}{c_P - c_S}$
$r_t^+ = \frac{c_P - c_B}{c_T - c_P}$	$r_t^- = \frac{c_{TT} - c_T}{c_T - c_P}$	$r_b^+ = \frac{c_B - c_{BB}}{c_P - c_B}$	$r_b^- = \frac{c_T - c_P}{c_P - c_B}$

in which  $\alpha_{e,w,\dots}$  shows the flow directions,  $r$  is the ratio of the upstream to downstream gradients and  $\psi$  is the flux limiter function. The values of  $\alpha$  coefficients and the relationships for gradient ratios have been specified in tables B.1 and B.2, respectively.

The flux limiter function is chosen to be

$$\psi(r) = \frac{r + r^2}{1 + r^2} \quad . \quad (\text{B.47})$$

The diffusion terms are discretized as

$$\alpha \frac{\partial^2 c}{\partial x \partial x} = \alpha \frac{\left(\frac{dc}{dx}\right)_e - \left(\frac{dc}{dx}\right)_w}{2dx_i} = \alpha \frac{\frac{c_E^n + c_E^{n+1}}{2} - \frac{c_P^n + c_P^{n+1}}{2}}{dx_i + dx_{i+1}} - \frac{\frac{c_P^n + c_P^{n+1}}{2} - \frac{c_W^n + c_W^{n+1}}{2}}{dx_i + dx_{i-1}}}{2dx_i} \quad , \quad (\text{B.48})$$

$$\alpha \frac{\partial^2 c}{\partial y \partial y} = \alpha \frac{\left(\frac{dc}{dy}\right)_n - \left(\frac{dc}{dy}\right)_s}{2dy_j} = \alpha \frac{\frac{c_N^n + c_N^{n+1}}{2} - \frac{c_P^n + c_P^{n+1}}{2}}{dy_j + dy_{j+1}} - \frac{\frac{c_P^n + c_P^{n+1}}{2} - \frac{c_S^n + c_S^{n+1}}{2}}{dy_j + dy_{j-1}}}{2dy_j} \quad , \quad (\text{B.49})$$

$$\alpha \frac{\partial^2 c}{\partial z \partial z} = \alpha \frac{\left(\frac{dc}{dz}\right)_t - \left(\frac{dc}{dz}\right)_b}{2dz_k} = \alpha \frac{\frac{c_T^n + c_T^{n+1}}{2} - \frac{c_P^n + c_P^{n+1}}{2}}{dz_k + dz_{k+1}} - \frac{\frac{c_P^n + c_P^{n+1}}{2} - \frac{c_B^n + c_B^{n+1}}{2}}{dz_k + dz_{k-1}}}{2dz_k} \quad . \quad (\text{B.50})$$

Applying the above discretization to the scalar transport equation, the following algebraic equation will be obtained

$$A_p c_p^{n+1} = A_E c_E^{n+1} + A_W c_W^{n+1} + A_N c_N^{n+1} + A_S c_S^{n+1} + A_T c_T^{n+1} + A_B c_B^{n+1} + B_p \quad , \quad (\text{B.51})$$

in which the neighbor coefficients are

$$\begin{aligned} A_E &= \max(-f_e, 0) + \frac{\alpha}{4dx_i(dx_i + dx_{i+1})} \quad , \\ A_W &= \max(f_w, 0) + \frac{\alpha}{4dx_i(dx_{i-1} + dx_i)} \quad , \\ A_N &= \max(-f_n, 0) + \frac{\alpha}{4dy_j(dy_j + dy_{j+1})} \quad , \\ A_S &= \max(f_s, 0) + \frac{\alpha}{4dy_j(dy_{j-1} + dy_j)} \quad , \\ A_T &= \max(-f_t, 0) + \frac{\alpha}{4dz_k(dz_k + dz_{k+1})} \quad , \\ A_B &= \max(f_b, 0) + \frac{\alpha}{4dz_k(dz_{k-1} + dz_k)} \quad , \end{aligned} \quad (\text{B.52})$$

and the central coefficient is

$$\begin{aligned} A_P &= \frac{1}{\Delta t} \\ &+ A_E + A_W + A_N + A_S + A_T + A_B \\ &+ (f_e - f_w) + (f_n - f_s) + (f_t - f_b) \quad , \end{aligned} \quad (\text{B.53})$$

and the source term is

$$\begin{aligned}
B_P = & \left( \frac{2}{\Delta t} - A_P \right) c_P^n \\
& + A_E c_E^n + A_W c_W^n + A_N c_N^n + A_S c_S^n + A_T c_T^n + A_B c_B^n \\
& + \frac{1}{2} f_e \left[ (1 - \alpha_e) \psi(r_e^-) - \alpha_e \psi(r_e^+) \right] (c_E^n - c_P^n) \\
& + \frac{1}{2} f_w \left[ \alpha_w \psi(r_w^+) - (1 - \alpha_w) \psi(r_w^-) \right] (c_P^n - c_W^n) \\
& + \frac{1}{2} f_n \left[ (1 - \alpha_n) \psi(r_n^-) - \alpha_n \psi(r_n^+) \right] (c_N^n - c_P^n) \\
& + \frac{1}{2} f_s \left[ \alpha_s \psi(r_s^+) - (1 - \alpha_s) \psi(r_s^-) \right] (c_P^n - c_S^n) \\
& + \frac{1}{2} f_t \left[ (1 - \alpha_t) \psi(r_t^-) - \alpha_t \psi(r_t^+) \right] (c_T^n - c_P^n) \\
& + \frac{1}{2} f_b \left[ \alpha_b \psi(r_b^+) - (1 - \alpha_b) \psi(r_b^-) \right] (c_P^n - c_B^n) \quad . \tag{B.54}
\end{aligned}$$